NUMERICAL SIMULATION OF THE INFLUENCE OF THE LARGE-SCALE MONSOON FLOW ON THE DIURNAL WEATHER PATTERNS OVER KENYA

Joseph R. Mukabana

A thesis submitted in partial fulfillment of the requirements
for the degree of Doctor of Philosophy in Meteorology
University of Nairobi, Kenya.

August , 1992

This thesis is my original work and has not been presented for a degree in any other University.

Signature:...................................... August 3, 1912

JOSEPH R. MUKABANA

This thesis has been submitted for examination with our approval as University supervisors

Signature:.......................... August 3, 1992

Professor Roger A. Pielke
Colorado State University
Department of Atmospheric Science
Fort Collins, Colorado 80523
U.S.A.

Signature:.......................... 12/8/92

Professor Laban J. Ogallo
University of Nairobi
Department of Meteorology
P.O. Box 30197
NAIROBI, Kenya

TABLE OF CONTENTS

v

ABSTRACT

The influence of the large-scale monsoonal wind systems on the diurnal weather patterns over Kenya was investigated in this study using a three-dimensional limited-area model known as the Regional Atmospheric Modeling System (RAMS) which was developed at Colorado State University (CSU). The contribution of the mesoscale forcings and the interaction between the mesoscale and synoptic scale systems on the weather over Kenya were also investigated.

Three numerical experiments were performed in this study. Experiment 1 was devoted to investigating the influence of the large-scale monsoonal wind systems on the weather over Kenya through dry simulations of the dynamics and structure of these systems over the country. A "variable initialization" method was applied to the European Centre for Medium-range Weather Forecasts (ECMWF) data which was accessed from the National Center for Atmospheric Research (NCAR) to create the initial state of the atmosphere at 0 Z which was nudged with another set of data at 12 Z. Starting at 0 Z the model was integrated forward in time for 24 hours. Model outputs were generated at a frequency of one hour.

The second set of simulations (Experiment 2) examined the influence of the mesoscale circulations on the weather over Kenya in the absence of the large-scale monsoonal winds. The dry simulations were started from an atmosphere at rest. The initial field was procured from a one-station sounding data from Dagoretti weather station in Nairobi. A "horizontally homogeneous" technique was employed to create the initial fields for the

model at 0 Z. Model integration was also performed for 24 hours to simulate the diurnal patterns of circulations that were generated by the local features in the absence of the large-scale monsoonal winds. As in the first experiment, the frequency of the model output was one hour.

The model-generated mesoscale circulations (from Experiment 2) were "superimposed" on the prevailing large-scale flows at low levels (from Experiment 1) in order to examine the interaction between the mesoscale and the large-scale systems through the determination of possible areas of convergence/divergence over the domain in the course of the 24-hour simulations. The convergence zones were taken to be areas where the mesoscale circulation was in direct opposition to the prevailing large-scale flow while the divergence zones were considered to be the regions where the mesoscale circulations and the large-scale monsoonal flows at low levels were in the same direction.

The third set of simulations (Experiment 3) used the ECMWF data to generate precipitation in the convergence zones determined earlier, as explained above. This experiment also attempted to determine the control of the large-scale monsoonal winds on the space-time locations of the precipitation/convergence zones over the domain.

The results from the first experiment revealed the atmospheric structure over the country dominated with a shallow layer of the southeasterly monsoon winds at low levels, westerly winds at mid-levels, and easterly winds aloft. These features conformed with the observations of the case study day. The results also showed a rising motion in the low level southeasterlies (indicative of a vertical transfer of easterly momentum) including most parts of the mid-level westerlies going up to 12.0 km height, subsidence motion in the layer between 13 km and 16 km heights with an isothermal layer above to 23.0 km height. The ITCZ was absent at the lowest level of the model at $\sigma_z = 122$ m (≈ 990.7 mb) but appeared explicitly at $\sigma_z = 2.6$ km (≈ 741 mb) as a zone of confluence between two hemispheric air masses, namely, the southeasterly and the northeasterly trade winds. Low level pressure centers, vertical velocity, and relative vorticity fields accurately replicated regions of active weather over the domain. The East African Low Level Jet Stream (EALLJ) at the coast and the Turkana Jet Stream channelled in the Turkana-Marsabit corridor were also revealed in the

simulations. The large-scale moisture field at low levels ($\sigma_z = 122$ m) showed a maxima of 22.4 g kg^{-1} at the coastal region at 0600 UTC which spread inland advected by the large-scale winds in the course of the simulations.

The results from the second experiment signified the importance of the mesoscale circulations on the space-time characteristics of weather over Kenya. The results clearly identified the contributions of the local circulations comprising the sea/land and lake/land breeze circulations plus the upslope/downslope drainage winds. The dry simulations further helped to reveal the dynamics and structure of the atmosphere in the absence of the large-scale flow fields. The moisture maxima (19.2 g kg^{-1}) recorded at the coastal region (at $\sigma_z = 122$ m) spread inland advected by the sea breeze coupled with the upslope winds.

The results from the third experiment showed the space-time location of the precipitation generated in the convergence zones which were controlled and advected by the large-scale flow field. The results of this experiment revealed the diurnal characteristic patterns of weather over Kenya. The coastal region, the eastern slopes of the Kenyan Highlands, the Kenyan Highlands, and the Lake Victoria trough region depicted diurnal weather patterns that were related to the interactions between the local circulations such as the sea/land breeze circulations, upslope/downslope drainage winds with the prevailing southeast monsoon winds at low levels.

The model-generated results showed that although the local features like Lake Victoria, the Indian Ocean, orographic barriers, Turkana-Marsabit corridor, etc. have a strong influence on the local circulation patterns of weather, the large-scale monsoon winds contribute substantially to the inland transport of large amounts of moisture into Kenya.

Lastly, it was concluded from the results of this study that mesoscale and synoptic-scale weather systems together with their scale-interaction play a crucial role in the determination of the space-time characteristics of the weather observed over Kenya. Since no operational limited-area model is currently available in Kenya, this work gives both an insight as well as forming a major basis for the development or adoption of an operational limited-area model for Kenya. This will facilitate forecasts of the rainfall events over the region which may include thunderstorms, hailstorms, lightning, dry/wet spells,

strong winds, risk zones for the weather hazards, etc.   Such informations are crucial to the development, planning, and mitigation of all weather dependent activities, and will help the government to minimize the severe socio-economical implications of the adverse weather events.

LIST OF FIGURES

LIST OF SYMBOLS AND ACRONYMS

u –   zonal or east-west wind component

v –   meridional or north-south wind component

w –   vertical wind component

f –   Coriolis parameter

g –   gravity

ρ –   density

π –   total Exner function

π' –   perturbation pressure Exner function

p –   pressure

K_m –   eddy viscosity coefficient for momentum

K_h –   eddy viscosity coefficient for heat and moisture

θ_{il} –   ice-liquid water potential temperature

θ_v –   virtual potential temperature

γ_n –   water mixing ratio of total water, rain, pristine crystals, aggregates, and snow ($n = 1,2,...5$)

γ_t –   total water mixing ratio

con   –   subscript denoting tendency from convective parameterization

rad   –   subscript denoting tendency from radiation parameterization

res   –   subscript denoting tendency from resolvable scale microphysical parameterization

AMSL   –   Above Mean Sea Level

ECMWF   –   European Centre for Medium-range Weather Forecasts

CSU   –   Colorado State University

GCM   –   Global Circulation Model

GMT (or Z)   –   Greenwich Mean Time

GTS   –   Global Teleconnection System

ITCZ   –   Inter-Tropical Convergence Zone

NCAR   –   National Center for Atmospheric Research

RAMS   –   Regional Atmospheric Modeling System

UTC   –   Universal Time Coordinated   (equivalent to GMT ; for instance, Kenya Local Time is 3 hours ahead of GMT, or UTC)

NMC   –   National Meteorological Center

LIST OF TABLES

Chapter 1

INTRODUCTION

The importance of weather on human activities over Kenya, like elsewhere in the world, cannot be overstressed since weather affects our lives in different ways, including the food and water resources. Kenya, like most developing countries within the tropics, depends on agriculture for food and social-economic developments. The agricultural production greatly depends on the cumulative effects of weather characteristics. Accurate weather forecasting would therefore assist in the planning and management of the national agricultural production.

Accurate weather prediction, at both the short and long range, are also vital for optimum planning and management of all weather related activities like water-management, aviation safety, sea navigation, communication, environmental protection, and many others. Weather prediction through numerical methods is currently one of the major subjects on many studies on attempting to improve the accuracy of weather forecasting.

The daily weather forecasts used in Kenya (see Figure 1) are dependent on synoptic chart analysis. Under this method, all the weather observations which are taken simultaneously at various observatories at a range of heights are plotted on special charts and analyzed. The charts give the space-time pattern of weather in the form of areas of low/high pressure, rain, cloudiness, ITCZ fronts, etc. The systems sometimes move erratically, both in space and time, making it difficult to detect them from the synoptic charts. The method is also time consuming and depends largely on the space-time availability of the weather records from the synoptic stations.

It has been recognized that atmospheric equations form a "closed system" as an "Initial-Value-Problem". In other words, given accurate informations about the atmosphere
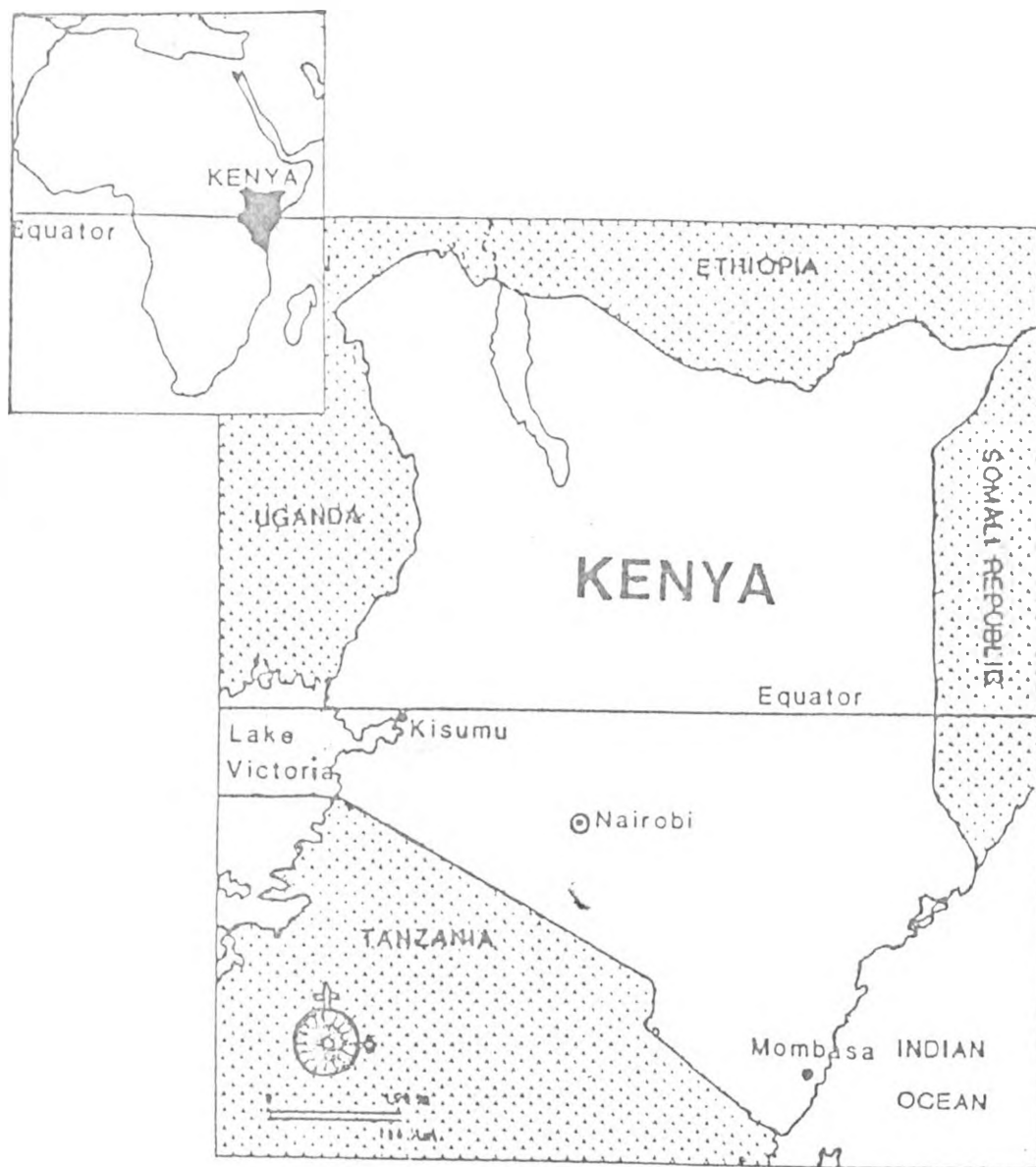
Figure 1: The study site (Kenya).

at an initial instant of time and a proper quantitative formulation of the physical processes operating, it is conceptually possible to forecast the future state of the atmosphere. This procedure is called the "Numerical Weather Prediction" method. Numerical models are currently being employed in many parts of the world to simulate observed weather processes such as the development of fog, clouds, microbursts, hailstorms, snow, tornadoes, flash-floods, storm-surges, tropical cyclones, atmospheric jets, easterly (or westerly) waves, environmental pollution and degradation, ozone layer depletion, climate change, etc.

Synoptic chart analysis, as used in Kenya, and the large-scale models with very coarse grid-mesh cannot give accurate predictions of rainfall in the tropics. This is because both methods cannot take into account the mesoscale systems, convective scale systems, and the topographic forcings which have a great impact on the weather of this region. Rainfall can only be predicted with accuracy using a fine grid-mesh as in limited-area models.

A number of investigators have utilized numerical mesoscale techniques to study some local circulation systems and their effects on the weather over Kenya (e.g., Fraederick, 1972; Okeyo, 1982, 1987). However, the contribution of the large-scale synoptic forcings have not been given much attention in the numerical studies over the country. Nevertheless, various researchers in observational studies have shown, through observational analysis, that most of the diurnal variations of weather in Kenya and other parts of East Africa is determined by the mesoscale flows, the synoptic-scale flows, convective instability, and by the interaction between the local mesoscale systems such as breeze circulations around large water bodies, upslope/downslope drainage winds due to orography with the large-scale monsoonal winds (e.g., Asnani and Kinuthia, 1979). These investigators assert that the large-scale winds interact with the local circulation systems to effect convergence/divergence zones with resultant rainfall. This study, therefore, intends to investigate the above assertion through numerical methods by simulating both the large-scale flows, mesoscale circulations plus precipitation over Kenya using a limited-area model whose details will be provided later in the text. Details of the objectives of the study are given in the next section.

1.1 Objectives of the Study

The major aim of this study is to determine the influence of the large-scale flow on the diurnal weather patterns over Kenya using a three-dimensional limited-area model, the Regional Atmospheric Modeling System, developed at Colorado State University. This study addresses the issue of scale-interaction between the large-scale monsoonal flow and the local mesoscale circulations that are generated and controlled by local features like Lake Victoria and the Indian Ocean, orographic barriers, the Turkana-Marsabit corridor, and the overall resultant effect on the diurnal weather patterns over Kenya. The aims of the study may be summarized as follows:

(i) To generate the large-scale synoptic (monsoon) flow, plus other large-scale weather parameters, over Kenya using a data set from the global ECMWF records of 14 April 1985. Rawinsonde, surface observations, topography, sea surface temperature, land-percentage, soil moisture and temperature, roughness parameter, and radiation are to be incorporated into the simulation in an attempt to establish and understand the dynamics of the region and the ITCZ position plus the vertical structure of the atmosphere over Kenya. This is done in an endeavor to determine the influence of the large-scale monsoonal winds on the weather patterns over Kenya.

(ii) To generate a purely mesoscale circulation over Kenya by excluding the large-scale winds in the model runs. This is done in an attempt to establish and to understand the control of the mesoscale features, both laterally and vertically, on the local circulation patterns in the absence of the large-scale synoptic winds. The features to be considered in the model to initiate and drive the local circulations are, among others, orographic barriers, Lake Victoria, Indian Ocean, Turkana-Marsabit corridor, radiation, roughness parameter, soil moisture and temperature. The influence of the mesoscale systems on the weather over Kenya are thus investigated.

(iii) To determine the contribution of the large-scale synoptic winds on the moisture incursion over Kenya by comparing the magnitudes of the moisture fields; one including the large-scale monsoon flows and the other without the large-scale flows in the model runs.

(iv) To determine zones of low level convergence/divergence over Kenya through "super-imposition" of the model outputs of the wind flow fields; one including the large-scale synoptic flows at low levels and the other with a purely mesoscale wind field. To further note the magnitudes of these opposing motions at low levels as a way of estimating the strength or intensity of the convergence/divergence.

(v) To generate moist convection in the model over the study domain and to use convective precipitation rates as indicators of locations or zones of precipitation over the country to establish:

(a) whether the low level convergence zones determined, through "superimposition" of the mesoscale circulations with the prevailing large-scale monsoonal flows at low levels are also active weather zones, where clouds and precipitation occur;

(b) the control of the large-scale monsoonal winds on the movement and locations of the precipitating zones over the country in the course of the simulation (the diurnal pattern of active weather over the country). Details of the literature review relevant to this work are presented in the next section.

1.2 Literature Review

A discussion of literature review has been subdivided into two sections, namely observational and theoretical works in the study area including some work done outside the region of study.

1.2.1 Observational Studies

The monsoons are defined as the seasonal reversal of the cross-equatorial winds that follow the overhead sun and the ITCZ. Kenya can be described as one of the land areas lying in the monsoon wind regime (see Fig. 2). Of the observational studies of atmospheric motion few studies exist for Kenya and the rest of the East African region. This is so despite the fact that it is important to have an adequate understanding of the flow characteristics of the precipitation-generating systems in the area. The only documented three-dimensional distribution of the tropospheric mean horizontal motion fields in the
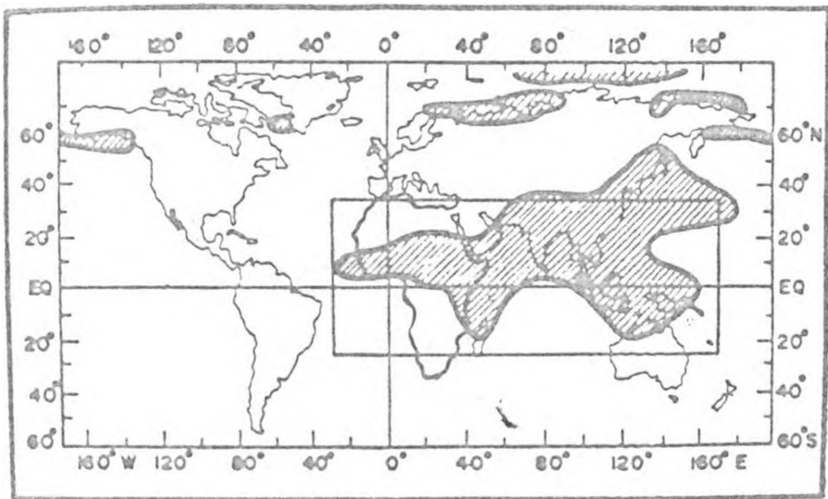
KEY

Monsoon regions of the world

Figure 2: The monsoons regime (from *Monsoon Meteorology* by Ramage, 1971).

region is found in Thompson (1965), Findlater (1968, 1971), Ramage and Raman (1972) and Anyamba (1984). With the exception of Anyamba (1984), data used in the other studies were from sparsely distributed observational networks and had limited duration, except perhaps Findlater's work which had about ten years of data.

The work of Findlater (1968, 1971) used only 10 stations in the region (8 in Kenya, 1 in Tanzania and 1 in Uganda). This meant that the tropospheric mean flow was not adequately resolved in space, especially in Uganda and Tanzania. Anyamba (1984) considered 31 pilot balloon stations in East Africa when studying the monthly mean lower tropospheric circulation and anomalous circulation during the 1961/1962 flood episode in East Africa.

The observational study of Kiangi et al. (1981) produced systematic documentations of the mean horizontal motion field in the East African atmosphere using the then available pilot balloon wind data during the two major rainy months of April and May. The four pressure levels considered were: 850 mb, 700 mb, 600 mb, and 500 mb. A total of 36 pilot balloon stations were used. These stations included 14 in Kenya, 14 in Tanzania, and 8 in Uganda. Data collection was done for a period of 10 years running from 1966 to 1975. This study greatly added to the knowledge of the mean flow over the region (see Figures 3, 4, 5 and 6).

Asnani and Kinuthia (1979) found from an observational analysis that the diurnal variation of the rainfall in East Africa was largely determined by the mesoscale flows, synoptic-scale flows, convective instability, and interaction between the mesoscale and synoptic-scale flows. Hence, the synoptic-scale monsoon winds are an important component to the development of the mesoscale and convective-scale systems in the area and deserve considerable attention for the improvement of model forecast products. Moreover, Majugu (1983) studied the mean and seasonal diurnal variation of precipitation in East Africa. The observational study contributed more to the knowledge of the large-scale flow fields, both in the morning and afternoon, over this region.

Rainfall characteristics in Kenya, as elsewhere in East Africa, have been given extensive observational studies unlike the atmospheric motions. Details concerning different
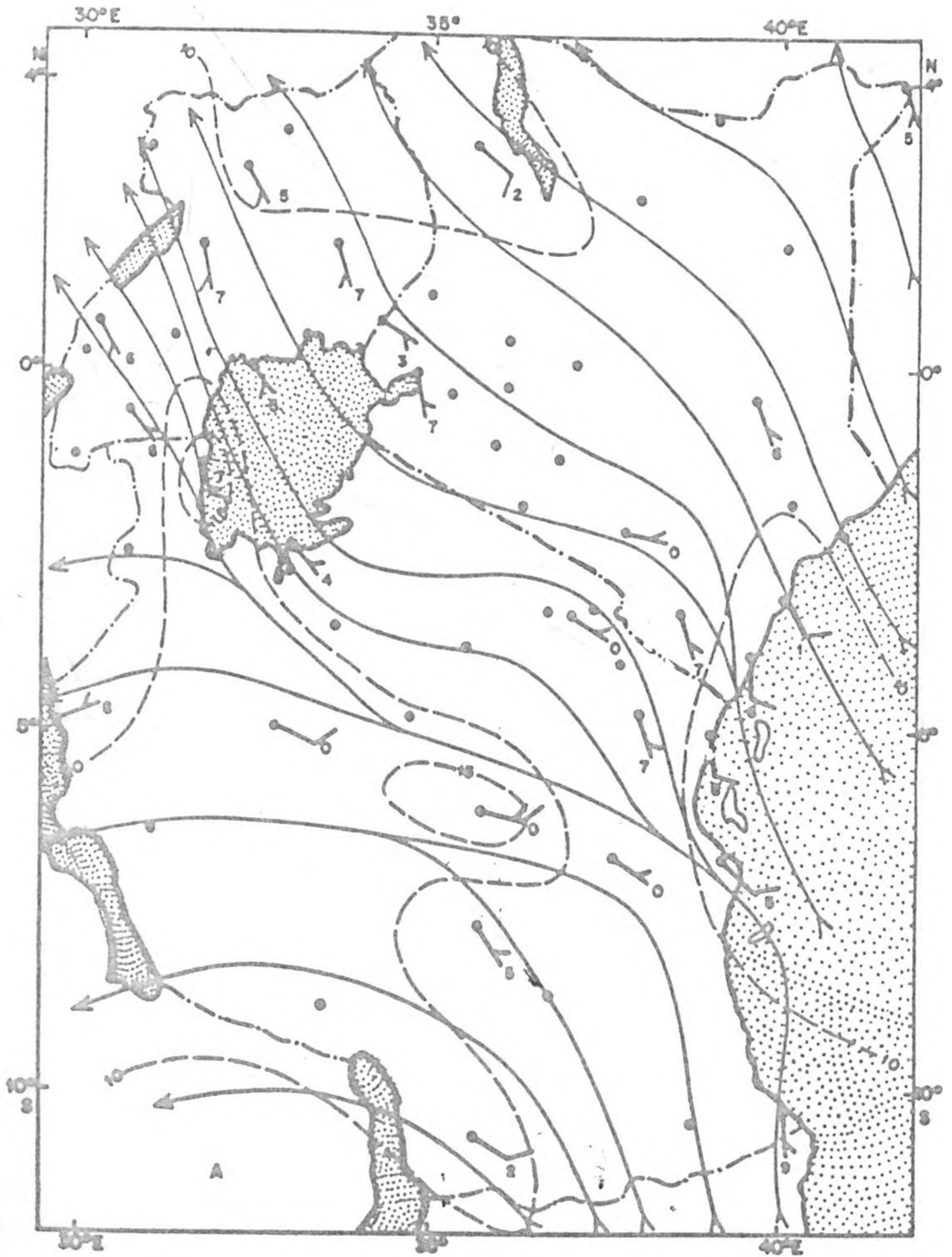
Figure 3: The resultant mean wind vectors (speed in knots) at 850 mb during April (from Kiangi et al., 1981).
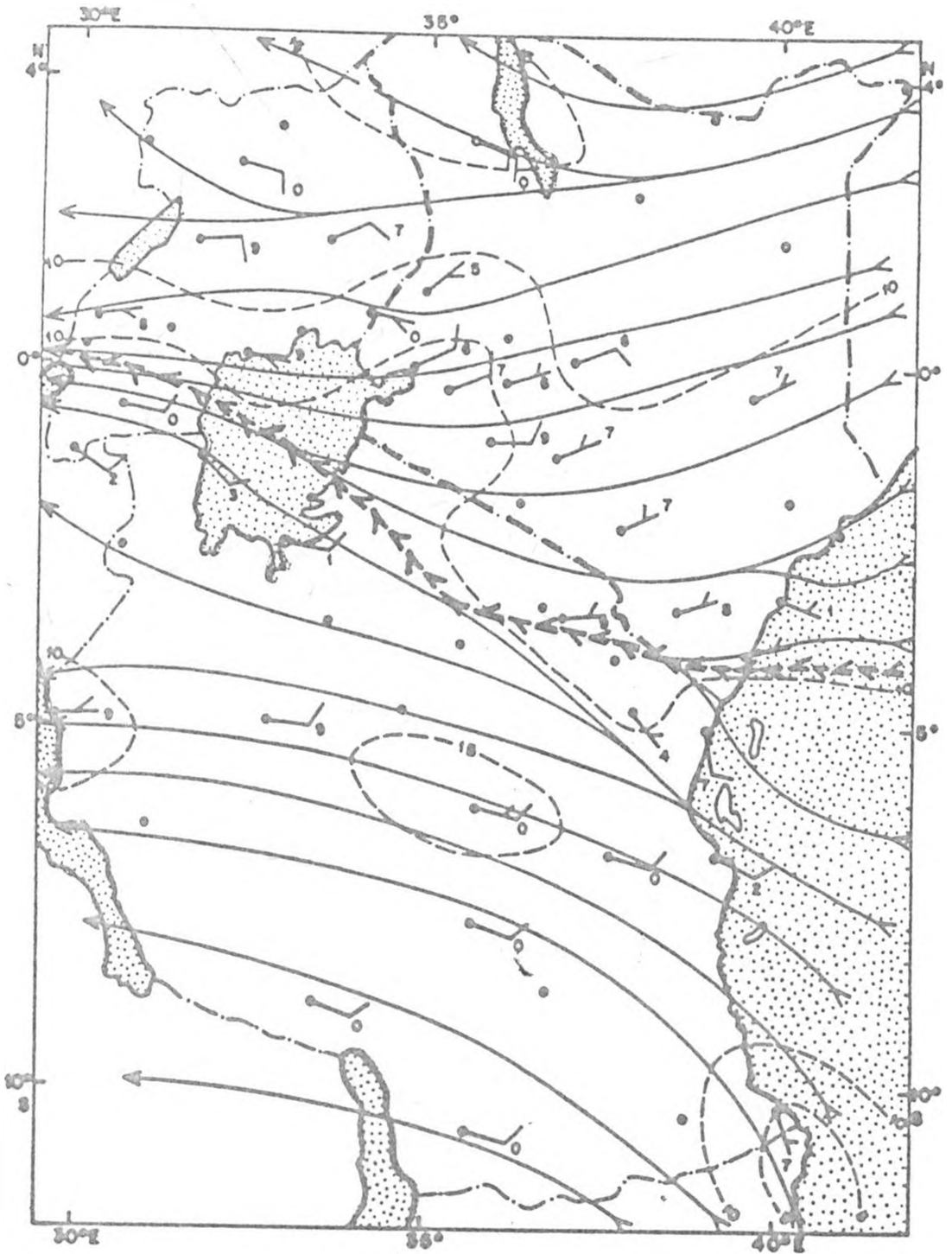
Figure 4: The resultant mean wind vectors (speed in knots) at 700 mb during April (from Kiangi et al., 1981).
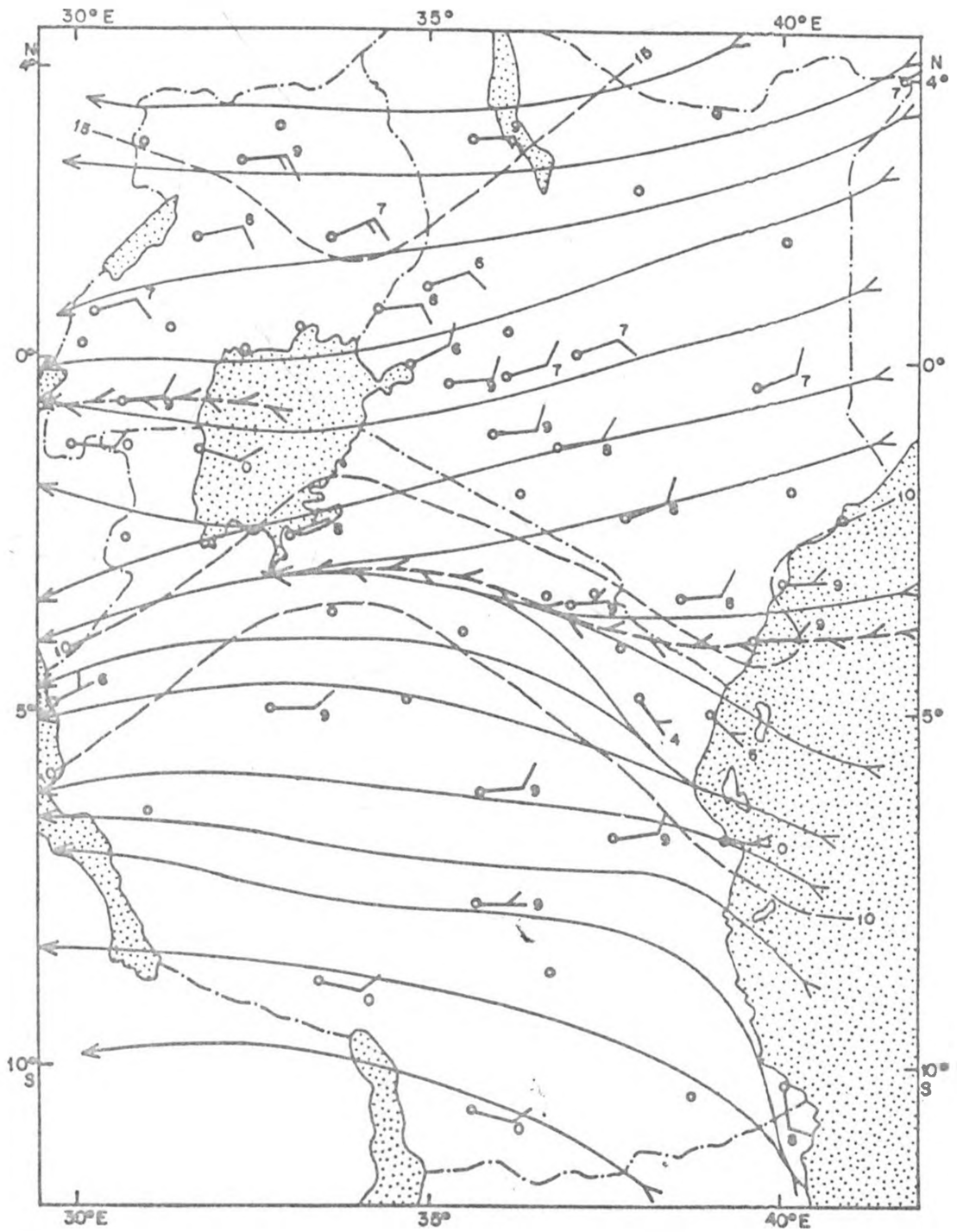
Figure 5: The resultant mean wind vectors (speed in knots) at 600 mb during April (from Kiangi et al., 1981).
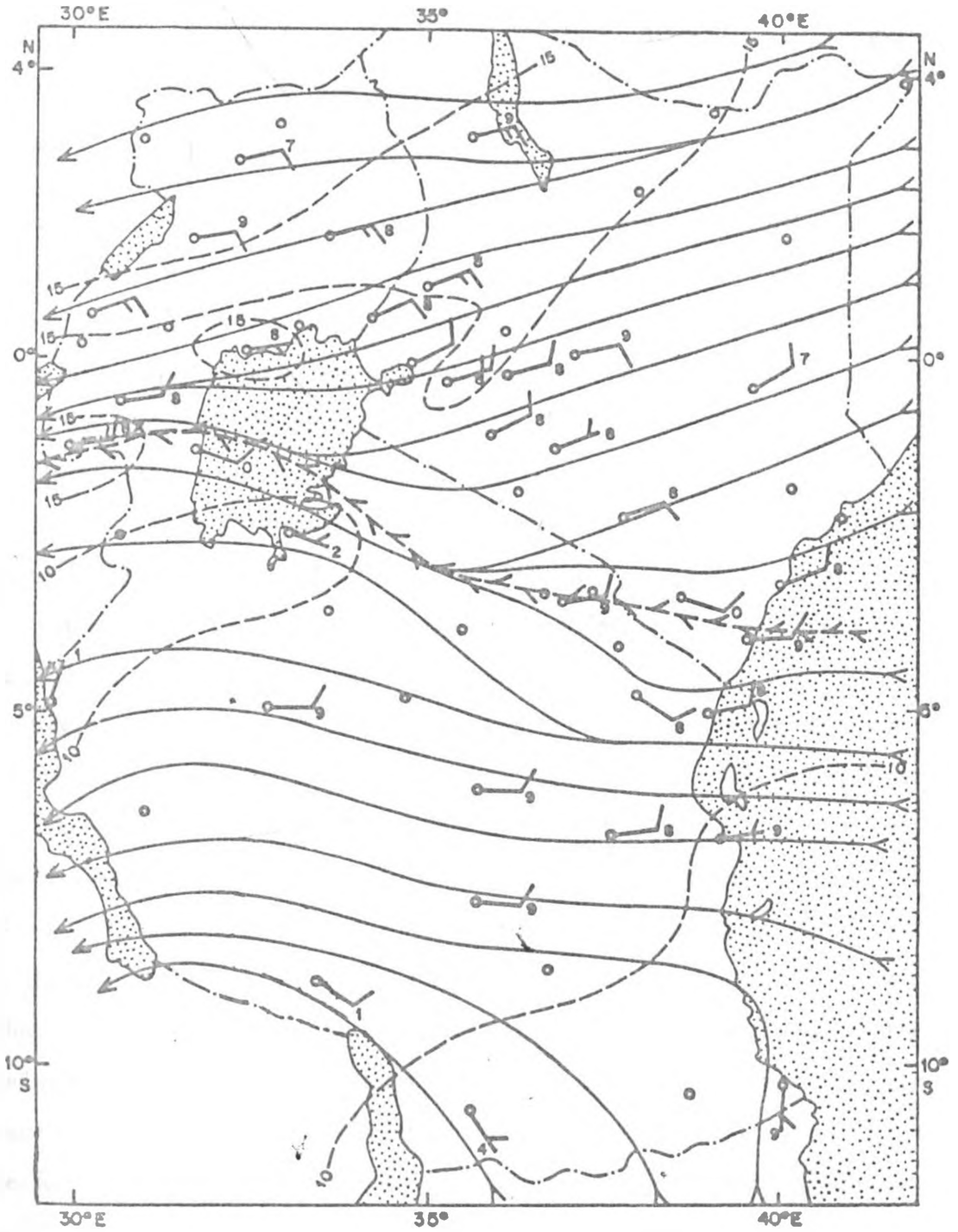
Figure 6: The resultant mean wind vectors (speed in knots) at 500 mb during April (from Kiangi et al., 1981).

aspects of the Kenyan rainfall are found in, for instance, Glover et al. (1954), Thompson (1957), Griffiths (1959), Johnson (1972), Nieuwolt (1974), Alusa and Gwage (1980), Otengi (1980), and Ogallo (1980) [see Figure 7].

1.2.2 Theoretical Studies

Few studies in numerical weather prediction exist for Kenya and a large part of the tropics. The only research in numerical weather prediction experiments over this region were carried out by Fraederick (1972), Semazzi (1979, 1983), and Okeyo (1982, 1987). Fraederick (1972) used a simple climatological model to study the dynamics and energetics of the nocturnal circulation at Lake Victoria. Using a three-dimensional model, Semazzi (1979) simulated the quasi-permanent trough over Lake Victoria enhanced by an orographic circulation that is created by an easterly wind regime and the north-south orientation of the high ground over central Africa. Semazzi (1983) used a linearized, primitive equation barotropic and baroclinic model based on the NCAR GCM to examine various aspects of the bounded derivative initialization model suitable for use in the equatorial region. He worked on the suppression of the gravitational oscillations during the forecast and employed the initialization procedure to further investigate the orographic dynamic trough phenomenon over equatorial Africa using an idealized mountain.

Okeyo (1982) used a two-dimensional model (which was one of the predecessors to RAMS – Regional Atmospheric Modeling System) to study the mesoscale circulation over Kenya. He examined the model-predicted convergence patterns that develop in response to the boundary layer fluxes of heat and momentum and compared the patterns against the observed precipitation. The degree of agreement between the model forecast convergence zones and observed showers indicated the intensity of convergence by the lake with the land/sea and lake/land breezes convergence, especially over the Nandi–Kericho highlands. Okeyo (1982), however, assumed the level of Lake Victoria to be at mean sea level. This assumption would not give results comparable with the observations on the western side of the model domain. However, Okeyo (1982) was only interested in the thermally-induced mesoscale systems which are strong in the tropics. Therefore, he did not consider the large-scale synoptic flows and the latent heat released from cumulus clouds, both of which
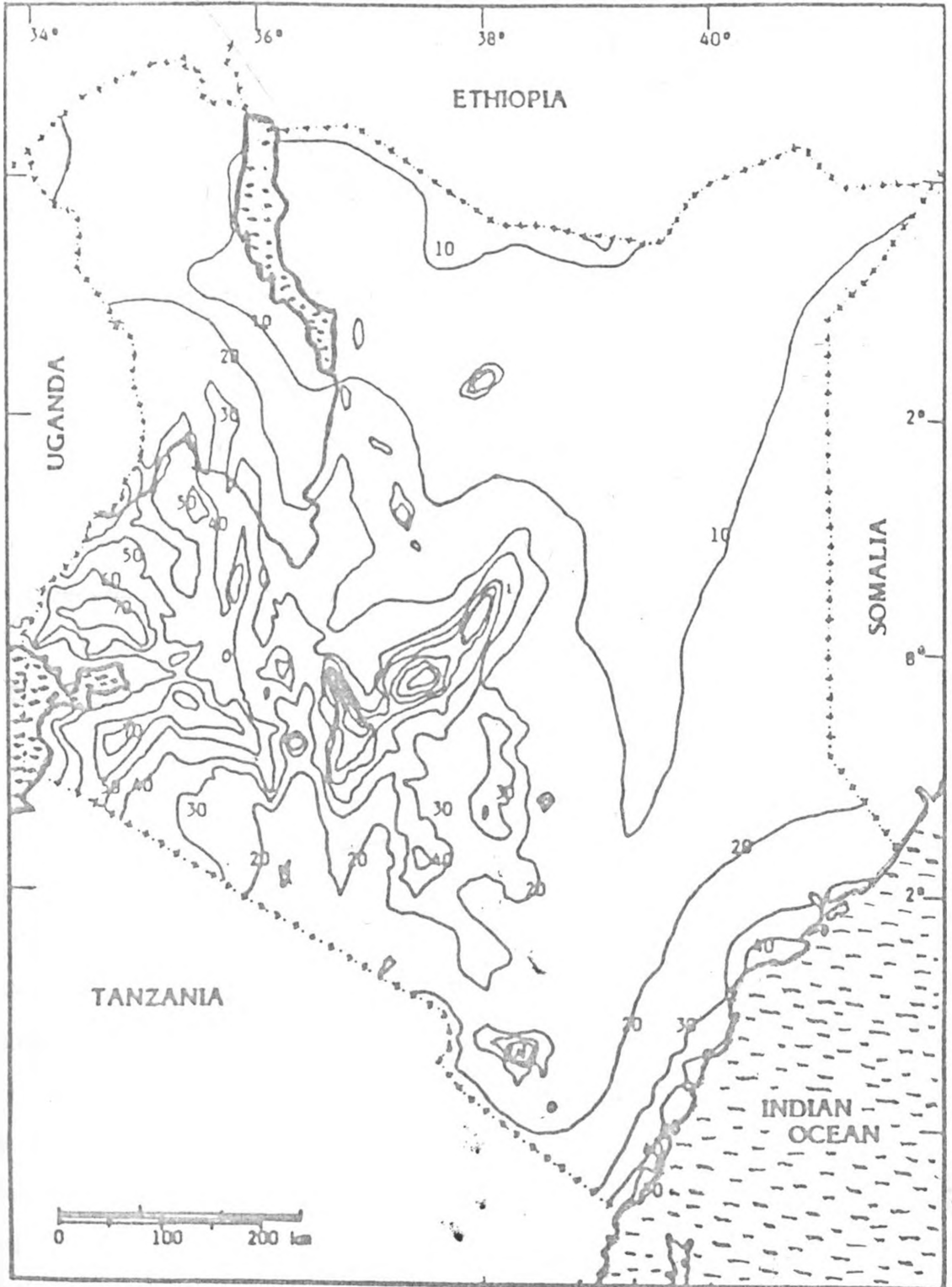
Figure 7: Mean annual rainfall in Kenya (in inches) (from Ojany and Ogendo, 1985).

are important in enhancing or modifying mesoscale flows. He commenced his integrations from an atmosphere at rest to exclude any influence of the large-scale synoptic forcing.

Pyuzza (1982) performed a study of the mean upper tropospheric horizontal motion field in the near-equatorial region. He extracted a 300 mb mean wind speeds and directions at east-west and north-south intervals of 5° in the region bounded by 30°N and 30°S latitudes for January, July, and October. He computed horizontal velocity divergence, relative vorticity, and absolute vorticity, among other terms, to get rotational and divergent components of wind vectors and compared various terms in the divergent and vorticity equations. One of Pyuzza's (1982) findings was that for the wind field, the magnitude for the zonal component (u) was larger than for the meridional component (v) in the near-equatorial region. Also, the horizontal velocity divergence was larger and positive near the equator above the surface position of the ITCZ with larger negative values occurring in the sub-tropics.

Okeyo (1987) used the three-dimensional Penn State/NCAR Mesoscale Model (MM4) (with a coarse grid of 120 km and a fine grid of 40 km horizontal increments) to perform several experiments to test the contribution of different forcing functions on the development of convective systems and mesoscale systems over Kenya. The forcing functions he used in the model were terrain heights, Lake Victoria, latent heating, and the contribution of a large-scale increased moisture. He started his model at 0300 UTC from a homogeneously initialized data and conducted experiments to find the impact of the hailstone/thunderstorm intensity over the Nandi-Kericho highlands, if there was no lake and the terrain was flat. Okeyo (1987) found that when Lake Victoria was removed the wind field over the lake region was weak, temperatures were high, and moisture and precipitation were less. Similarly, Okeyo (1987) found that high ground causes the moisture transport, both horizontally and vertically, to greater distances inland and greater depths aloft than over a flat terrain.

Okeyo (1987) concluded from the experiments that the strong convective activities over the Kenya highlands owe their existence to the lake breeze circulation generated by Lake Victoria with upslope flows from the highlands of the Nandi and Kericho areas. The

sea-breeze had negligible influence on the convective activities over the highlands because of the greater distance between the Indian Ocean and the inland highlands. Okeyo (1987) did not, however, include the large-scale synoptic flow in the model simulations since he was only interested in the influence of the mesoscale and convective scale systems on the weather over Kenya.

The work of Okeyo (1987) added substantially towards the understanding of the local mesoscale circulation complexes that occur between the Indian Ocean and Lake Victoria with hailstone and thunderstorm activity over the Nandi-Kericho highlands. However, various researchers in observational studies have shown that most of the weather in East Africa is caused by the convergence between the local factors such as lake-breezes, sea-breezes, upslope/downslope flows, and the synoptic scale monsoon winds (Flohn and Fraederick, 1966; Samson and Gichuiya, 1971; Chaggar, 1977; and Asnani and Kinuthia, 1979). These investigators assert that the large-scale monsoon circulations interact with local features to effect a convergence zone. Large-scale synoptic winds control the intensity, movement, and locations of the convergence complexes and shower activity. Inclusion of the synoptic scale monsoon winds in the numerical model, therefore, gives a more complete picture of the real atmosphere where different scale-systems interact, each contributing to the resultant weather patterns over this region.

Elsewhere, mesoscale numerical models have been used by Pielke (1974) to simulate sea/land breezes over southern Florida. The major objective was to examine the predicted convergence patterns that develop in response to the boundary layer fluxes of heat and momentum and that interact with the large-scale flows. Consequently, the model results were compared against the observed distribution of cumulonimbus clouds. The degree of agreement between the predicted convergence zones and the observed showers indicated the extent of the sea-breeze control over the cumulus convection and the thunderstorm activity (see the recent summary of the Florida work presented in Pielke et al., 1986). Other mesoscale numerical models have been used successfully by Estoque et al. (1976), McPherson (1970), Pielke and Mahrer (1975), etc.

This study will investigate the influence of the monsoonal winds on the weather patterns over Kenya through the interaction between the large-scale and mesoscale systems together with the associated impacts on the weather over the country.

Details of the study site are discussed in the next section.

1.3 The Study Site

1.3.1 Location of the Study Site

Kenya is located between 34°E and 42°E longitude and $4\frac{1}{2}$°N to about 5°S latitude. The region is bounded on the east by the Indian Ocean, on the west by Uganda, and Sudan to the northwest; to the north lies Ethiopia and Somalia to the northeast and Tanzania to the south. Kenya has an area of 582,600 km^2 (see Figure 8).

1.3.2 Physical Features of the Study Site

The Kenyan landscape bares the scars of previous volcanism and of the slow tectonic plates that formed the great Rift Valley, a deep trough with a chain of beautiful lakes. The eastern arm of the Rift Valley runs through Kenya from south to north and in it are Lakes Natron, Nakuru, Naivasha, Bogoria, and Turkana.

Most of Kenya lies over 1200 m above Mean Sea Level (AMSL). The land rises gradually from the bright coral beaches of the eastern coastline of the Indian Ocean through the remnants of the rain forest and through the dry bush country of the Nyika Plateau (400 – 1000 m); to the forest-covered East African highlands, which occupy a large part of central Kenya, parts of northern and southwestern Tanzania and southwestern Uganda. The highest mountains in Africa are found in this region with Mt. Kilimanjaro, in Tanzania, being the highest (5895 m) followed by Mt. Kenya (5199 m), Mt. Elgon (4321 m) on the Kenya/Uganda border, and Mt. Ruwenzori (5109 m) in Uganda (see Figure 8).

From the central highlands the land drops gradually to the west to Lake Victoria at 1132 m above MSL. To the north it falls again to Lake Turkana and to the Ethiopian border in Kenya. Most of Uganda and Tanzania lie in the so-called "Plateau Proper" (1000–2000 m), a country with undulating landscape. Lake Victoria lies in this plateau and is the second largest fresh water lake in the world (after Lake Superior in North
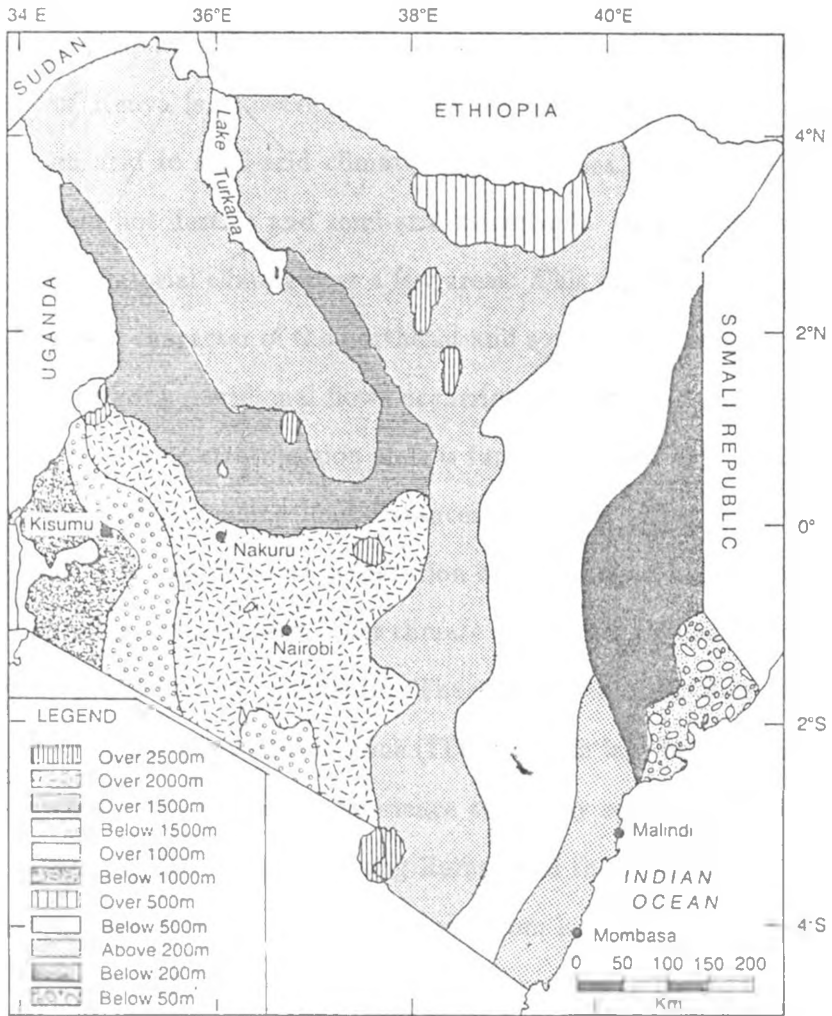
Figure 8: Relief map of Kenya (after Philips, 1967).

America) and has a remarkable influence on the weather of the region. The Lake covers an area of 68,400 km^2. It is the source of the River Nile and is fed by Rivers like Nzoia, Yala, Mara, Kuja, and Miriu, among many other smaller ones. The Lake also touches the three East African states of Kenya, Uganda, and Tanzania.

1.3.3 The Climate of the Study Site

Kenya lies on both sides of the equator, hence the region should exhibit an equatorial type of climate. An equatorial climate does have a lot of rainfall throughout the year. The climate of Kenya is, however, far from the equatorial type since over 80% of the country has an arid to semi-arid climate. Kenya does have a large variation in climate ranging from hot deserts and semi-arid rangelands to a polar climate on top of mountains and an equatorial climate over a few areas. This dryness has been explained to be due to the divergent character of the northeast and southeast monsoons as well as their shallow depth. The strong meridional flows occurring during the transition period of the rainy seasons and the stable stratification aloft is further marked by a decline in moisture content due to the winds travelling long distances over land (often relatively parallel to the coast line) and to the north-south orientation of the Kenyan highlands.

In Kenya rainfall is the most important climate or weather element since the country's economy is mostly dependent on agriculture. The rainfall seasons closely follow the movement of the Inter-Tropical Convergence Zone (ITCZ) which lags behind the overhead sun by a few weeks. Most parts of Kenya experience two rainy seasons and two dry seasons. The former is commonly known as the "Long Rains" and the latter as the "Short Rains". The two wet seasons last from March to May and from late October to early December. These rainy seasons coincide with the periods of the year when the ITCZ is passing over this part of the continent. The two dry periods, over most parts of Kenya, run from mid-December to late February and June to late September. Parts of western Kenya and the coast are wet throughout the year since they are close to large water bodies. The western parts further experience incursions of a warm, shallow, westerly, moist air mass from the Atlantic Ocean and the Zaire/Congo Basin which is locally known as the "Congo Airmass".

During the dry months the region is under the influence of the northeast or southeasterly winds of the west Indian Ocean. From December to February Kenya has northeast monsoons during which time the rainfall belts are concentrated far to the south of Kenya over southern Tanzania. From June through August the southeast/southwest monsoons prevail.

Generally, weather in Kenya is controlled by both synoptic and local factors. Some of the synoptic factors are: (i) ITCZ; (ii) subtropical anticyclones; (iii) tropical cyclones; (iv) the African Jetstreams; (v) easterly waves; and (vi) extratropical frontal weather incursions and upper air troughs. The mesoscale systems which affect weather over Kenya are: (i) the Lake Victoria trough; (ii) orographic influence; (iii) sea/land breezes; (iv) the Marsabit (or Turkana) Jetstream; and (v) the Near Equatorial Trough (N.E.T.). Weather over Kenya is also influenced by other global teleconnections brought about by hemispheric anomalies in the general circulation, like those associated with El Niño – Southern Oscillation (ENSO), the 30–60 day oscillation, the Quasi-Biennial Oscillation (QBO), etc.

Details pertaining to some of the synoptic and mesoscale features mentioned above will be highlighted when discussing results of the model simulations.

1.3.4 Vegetation of the Study Site

Vegetation patterns in Kenya closely follow the rainfall patterns. Most of northern and northeastern areas are semi-arid rangelands where little, if any, agricultural activities take place. These regions are hot and dry most of the year with high albedo; vegetation is mostly thorny acacia bushes, and pasturalism is the main activity. There are many national parks and reserves for wildlife here. Some of the areas are close to rivers (e.g. Turkwel and Tana) and are earmarked for reclamation through irrigation. The highlands in central and southwestern parts of Kenya experience a temperate (spring-like) climate. They are cool and wet most of the year with thick forests in unsettled areas along river banks and mountain slopes. The western parts of Kenya (the "Lake Victoria Region") experience equatorial climate with thick forests in uncultivated areas. The rest of Kenya is mostly Savanna with two dry and two wet seasons; lush vegetation with tall grass and scattered umbrella-shaped trees in unsettled areas.

Thus, although Kenya sits astride the equator and hence, receives more direct solar radiation, the temperatures are modified due to orographic features, water surfaces, and wind flow patterns. Since the region is mostly dependent on agriculture, improvement in weather forecasting is of great economic value to the entire area.

The following chapter describes the numerical model used in this study.

Chapter 2

THE NUMERICAL MODEL USED

This study used the three-dimensional Regional Atmospheric Modeling System (RAMS) developed at Colorado State University to examine the impact of the large-scale monsoon flows on the weather patterns over Kenya. RAMS has been developed at Colorado State University to provide a general and flexible framework for many scales of atmospheric flow simulations. For instance, it can be used for research of atmospheric scales ranging from large eddy simulations ($\Delta x \approx 100$ m) to mesoscale simulations of convective systems ($\Delta x = 1000$ m). RAMS is a product of the merging of one non-hydrostatic model developed by Cotton et al. (1982) and Tripoli and Cotton (1980, 1989a,b) and two hydrostatic models, one by Pielke (1974), Mahrer and Pielke (1977), McCumber and Pielke (1978), and the other by Tremback et al. (1985). This merging has given RAMS more flexibility and many options for the simulation of various scales of motions because many different numerical schemes and physical processes are incorporated into the model. Since RAMS has many options, only those options used in this study will be briefly described here. There are several current versions of RAMS, each configured to be more user-friendly with improvements in model code. The version used in this study was 2B. Tremback et al. (1986) and Cotton et al. (1988) give a full description of RAMS and the reader is referred to those detailed sources. However, the basic general equations will be presented here.

2.1 General Equations

The basic meteorological variables considered in the model are u, v, π, θ, and γ. Here u is the zonal wind component, v is the meridional wind component, and π is the total Exner function defined as: $\pi = \left(\frac{p}{p_o}\right)^{\frac{R}{c_p}}$. The variable θ is the potential temperature and γ

is the humidity mixing ratio. The above mentioned variables are presented in the following equations as grid-volume averaged quantities without the symbolic overbar. Also omitted for clarity are the horizontal and vertical grid coordinate transformed equations.

Equations of Motion

Zonal Motion:

$$\frac{\partial u}{\partial t} = -u\frac{\partial u}{\partial x} - v\frac{\partial u}{\partial y} - w\frac{\partial u}{\partial z} - \theta_0\frac{\partial \pi'}{\partial x} + fv + \frac{\partial}{\partial x}\left(K_m\frac{\partial u}{\partial x}\right) + \frac{\partial}{\partial y}\left(K_m\frac{\partial u}{\partial y}\right) + \frac{\partial}{\partial z}\left(K_m\frac{\partial u}{\partial z}\right) \quad (1)$$

Meridional Motion:

$$\frac{\partial v}{\partial t} = -u\frac{\partial v}{\partial x} - v\frac{\partial v}{\partial y} - w\frac{\partial v}{\partial z} - \theta\frac{\partial \pi'}{\partial y} - fu + \frac{\partial}{\partial x}\left(K_m\frac{\partial v}{\partial x}\right) + \frac{\partial}{\partial y}\left(K_m\frac{\partial v}{\partial y}\right) + \frac{\partial}{\partial z}\left(K_m\frac{\partial v}{\partial z}\right) \quad (2)$$

Thermodynamic Equation:

$$\frac{\partial \theta_{il}}{\partial t} = -u\frac{\partial \theta_{il}}{\partial x} - v\frac{\partial \theta_{il}}{\partial y} - w\frac{\partial \theta_{il}}{\partial z} + \frac{\partial}{\partial x}\left(K_h\frac{\partial \theta_{il}}{\partial x}\right) + \frac{\partial}{\partial y}\left(K_h\frac{\partial \theta_{il}}{\partial y}\right) + \frac{\partial}{\partial z}\left(K_h\frac{\partial \theta_{il}}{\partial z}\right)$$
$$+ \left(\frac{\partial \theta_{il}}{\partial t}\right)_{con} + \left(\frac{\partial \theta_{il}}{\partial t}\right)_{res} + \left(\frac{\partial \theta_{il}}{\partial t}\right)_{rad} \quad (3)$$

Moisture and condensate mixing ratio continuity equation:

$$\frac{\partial \gamma_n}{\partial t} = -u\frac{\partial \gamma_n}{\partial x} - v\frac{\partial \gamma_n}{\partial y} - w\frac{\partial \gamma_n}{\partial z} + \frac{\partial}{\partial x}\left(K_h\frac{\partial \gamma_n}{\partial x}\right) + \frac{\partial}{\partial y}\left(K_h\frac{\partial \gamma_n}{\partial y}\right) + \frac{\partial}{\partial z}\left(K_h\frac{\partial \gamma_n}{\partial z}\right)$$
$$+ \left(\frac{\partial \gamma_n}{\partial t}\right)_{con} + \left(\frac{\partial \gamma_n}{\partial t}\right)_{res} \quad n = 1, 2... \quad (4)$$

Mass Continuity Equation:

$$\frac{\partial \rho u}{\partial x} + \frac{\partial \rho v}{\partial y} + \frac{\partial \rho w}{\partial z} = 0 \quad (5)$$

Hydrostatic Equation:

$$\frac{\partial \pi}{\partial z} = -\frac{g}{\theta_v} \quad (6)$$

2.2 Grid Structure

The grid structure used in RAMS is the Arakawa-C grid stagger (Arakawa and Lamb, 1981; Mesinger and Arakawa, 1976). The grid is staggered both in the horizontal and vertical directions. All thermodynamic (θ) and moisture (q) variables are defined at the same point (x, y, z). The velocity components (u, v, w) are staggered between points, that is $\frac{1}{2\Delta x}$, $\frac{1}{2\Delta y}$, and $\frac{1}{2\Delta z}$, respectively.

For the purpose of weather analysis and viewing, weather parameters observed in the Earth's atmosphere are often depicted on flat charts. This is accomplished by representing or projecting the Earth's spherical surface on a plane surface. This projection tries as much as possible to preserve, with minimum distortion, such features as distance, direction, area, shape, etc. Map projections which preserve distance are called ISOMETRIC and those which preserve the angle between two intersecting curves are termed CONFORMAL. These two perspectives, isometric and conformal, are vital for a projection to have little distortion. The commonly used maps are the Polar Stereographic plan projection which is used at higher latitudes; a plane is placed tangent at latitudes 90°N or S, that is, at the Poles. Mercator cylindrical projection is true for the equatorial regions whereas the Lambert conical projection holds true for the mid-latitudes (i.e., 30°–60°N or S).

Although Polar Stereographic coordinates are suitable for higher latitudes and Mercator coordinates give less distortion at low latitudes (40°N–40°S), the former can be applied over any specified region on the globe by simply placing the tangent plane of projection at the center of the domain of interest (Tremback, 1990; personal communication). This application minimizes distortion due to projection over the domain of study specified and therefore, renders the use of other forms of projection, in this case Mercator coordinates, unnecessary.

The horizontal coordinates used in version 2B of RAMS is a Polar Stereographic coordinate system where the center of the domain is specified in degrees (latitude-longitude). The vertical structure of the grid uses the terrain-following sigma-z (σ_z) coordinate system defined as:

$$\sigma_z = \frac{s(z - z_{D(x,y)})}{(s - z_{D(x,y)})} \tag{7}$$

where s is the model top height, $z_{D(x,y)}$ is the surface terrain height, and z is any specified height. The coordinate transform for σ_z is described in Gal-Chen and Somerville (1975a,b) and Clark (1977).

2.3 Turbulence Closure (Diffusion)

As outlined in Tremback (1990), the diffusion parameters in RAMS are based on a local exchange coefficient (K) that is a function of deformation and stability. That is,

$$K_m = \frac{0.25}{\sqrt{2}} l^2 \sqrt{1 - \frac{K_h}{K_m} R_i} \sqrt{D^2 + MAX(-N, 0)^2} \tag{8}$$

where $K_h = 3 K_m$ and is the exchange coefficient for heat, K_m is the exchange coefficient for momentum, D is deformation, N is the Brunt Vaisala frequency, R_i is the Richardson Number and l is the turbulence scale length. For this study the turbulence scale length, l, was taken as Δz in the vertical and as the square root of the sum of Δx^2 and Δy^2 in the horizontal. Three-dimensional deformation (horizontal and vertical) was used to calculate the exchange coefficients in the vertical direction. However, only the horizontal components of deformation were used to calculate the horizontal exchange coefficients.

2.4 Finite Differencing (Or Advection) Scheme

RAMS has 2nd, 4th, and 6th order flux conservative forward-backward advection schemes and leap-frog schemes. This study used the 2nd order time-differencing forward-backward advection scheme. This scheme is computationally less expensive and has shown to give as good results as the more computationally expensive 4th and 6th order advection schemes (Cram, 1990). This 2nd order forward-backward operator is discussed by Crowley (1968) and described in detail by Tremback et al. (1987). The horizontal grid is usually held constant, but in the vertical grid, a geometric stretch ratio is used to provide a higher resolution close to the ground. In this study a stretch ratio of 1.1 was used on the initial

vertical interval of 250 m. A maximum stretch of 1000 m was allowed near the top of the model. This put the model top at 23 km in the tropical tropopause or the lower stratosphere.

The diffusion terms were computed using the Smagorinsky–Lilly deformation scheme. The mixing coefficients are computed and used to diffuse the prognostic fields. Calculations that are performed include computation of horizontal and vertical gradients, computing divergences, relative vorticity and local spatial averaging to obtain a value at a location in the grid stagger where it is not defined.

2.5 Hydrostatic and Nonhydrostatic Models

RAMS has both hydrostatic and non-hydrostatic model options. Tremback (1990) discusses the numerics of the hydrostatic model. A hydrostatic model is one where the equation for hydrostatic balance is used i.e the vertical pressure gradient term balances gravity in the absence of the vertical acceleration(see equation 6). In the non-hydrostatic model the vertical acceleration term is considered. The numerics of the non-hydrostatic model are discussed in detail by Tripoli and Cotton (1982).

For the first set of experiments, with ECMWF data, this study used a coarse grid spacing of 100 km and a fine grid mesh of 25 km. The grid motions simulated in this domain were hydrostatic, and hence, a hydrostatic version of the model was used. For the second sets of experiments, under horizontally homogeneous initialization, a non-hydrostatic version of the model was used since the hydrostatic version proved unstable for the experiments.

2.6 Grid Nesting

The use of grid nesting allows a wider range of motion scales to be modeled simultaneously and interactively. Nesting greatly eases the limitations imposed by unnested simulations where a compromise must be reached between covering an adequately large spatial domain and obtaining sufficient resolution of a particular local phenomenon. With nesting in RAMS, mesoscale circulations can be feasibly modeled in a large domain where low resolution is used, and at the same time resolve the large eddy structure within a cumulus cloud in a sub-domain of the simulation. RAMS adopted the two-way interactive nesting procedure documented in Clark and Farley (1979). This method is the means by which the different nested grid communicate with each other. The process of advancing a coarse grid mesh (G1) and a fine grid mesh (G2) forward in time, one step begins with

the advancing of grid G1 alone as if it had no nest within. The calculated fields from the coarse grid mesh (G1) are then interpolated tri-quadrically to the boundary points of the fine grid mesh (G2). The interior of G2 is then updated under the influence of its interpolated boundary values. Finally, the values of G1 in the region where G2 exists are replaced by local averages from the fields of G2. An increase in efficiency over the Clark and Farley method was implemented by allowing a coarse grid to be run at a longer timestep (60 seconds in this study) for the coarse grid mesh and a shorter timestep (15 seconds in this study) for the fine grid mesh.

2.7 Coriolis Force

In the tropics, and specifically the near-equatorial region, the balance between the pressure gradient force and the Coriolis force is not uniform and the wind flow pattern is cross-isobaric. The Coriolis force is small and near the equator the geostrophic approximation is not valid.

Therefore, no Coriolis force terms were included in this study as the Coriolis parameter $f = 2\Omega \sin\theta$ (where Ω is the Earth's angular velocity and θ is the latitude in degrees) is almost zero in the equatorial region.

2.8 Convective Parameterization

A simplified version of Kuo's (1965, 1974) cumulus parameterization scheme was used to compute convective heating and moistening by a cloud ensemble. This simplified version was used by Molinari (1985) then modified and discussed by Tremback (1990). The scheme uses a one-dimensional cloud model to calculate the convective heating and moistening in a unit column of the atmosphere. Air parcels are forced to rise dry-adiabatically (through thermal forcing, frictional convergence due to terrain, or large-scale air convergence) to the Lifting Condensation Level (LCL). Moisture in the air parcels condense at the LCL releasing latent heat of condensation which increases buoyancy in the unit atmospheric column so that the air parcels rise to greater heights.

For convection to be activated there must be vertical motion (usually 0.01 m s^{-1}) at the LCL. The updraft region of the air parcel has a constant equivalent potential

temperature (θ_e) and is saturated with respect to water. The latent heat due to ice formation is not considered in the simplified Kuo (1974) scheme. The convective air starts at the LCL and cloud tops for the large tropical cumulus "towers" are calculated on the basis of the grid-scale moisture convergence and vertical motion. The cloud top (CT) is one level above the Equilibrium Temperature Level (ETL) of air. There will be no convection if the cloud top is under 500 mb. The updraft region in the model is defined as positive. The scheme has also a simple downdraft model in which the area is defined as negative. A requirement is imposed that the positive area be 50% greater than the negative area of the unit atmospheric column below the level of free convection. The positive area should also be 5% greater than the negative area in total. If there is more negative area than positive area convection will not be activated.

The downdraft starts at the level of minimum θ_e. The downdraft is set to be 2°C colder than the environment at the cloud base (LCL) and 5°C colder than the environment at the ground. The downdraft is also weighted against the updraft to ensure vertical motion. A fraction (b) of the total moisture that converges in the unit atmospheric column is assumed to moisten the column and the remaining fraction ($1-b$) precipitates out. The term b is referred to as the moisture partitioning factor or as the "infamous" b parameter by Tremback (1990). The next step is to compute the vertical profiles of heating and moistening in the atmospheric unit column of the ensemble cloud. The heating profile is defined as the difference between convective θ and environmental θ. The moisture profile is the difference between mixing ratio of updraft and environment air in the cloud layer. Below the cloud base air is dried. Downdrafts are assumed to have no effect on this drying. Consequently, the heating rates and moistening rates are computed using $1-b$ and b, respectively. As one can readily note, the parameterization is somewhat ad hoc as many arbitrary parameters are tuned and many assumptions made. However, previous simulations with this type of parameterization (Cram, 1990; Tremback, 1990) do produce realistic rainfall rates, vertical heating, and moistening profiles.

2.9 Explicit Microphysics Parameterization

RAMS uses the bulk microphysical parameterization scheme developed by Flatau (1989) that is related to that of Cotton et al. (1982, 1987). This scheme deals with the grid-scale resolved condensation and precipitation processes of pristine ice crystals, snow,

graupel, aggregates, and rain. The scheme has options for the distribution of the above types of precipitation. In the present study the type of precipitation considered was rain, pristine ice crystals, and graupel (or hailstones).

2.9.1 Radiation Parameterization

RAMS uses the radiation parameterization schemes developed by Pielke and Mahrer (1977), and the other by   Chen and Cotton (1983). The Mahrer and Pielke (1977) parameterization scheme includes   calculation of both longware and shortware radiation fluxes as a function of the vertical temperature and water vapour. The Chen and Cotton (1983) scheme includes additional radiative effects of condensate, water vapour, ozone and carbon dioxide.   Therefore , this latter scheme is computationally more expensive than the former, but gives more accurate results. The Chen and Cotton (1983) scheme was chosen for these simulations to compute the   longwave and shortwave radiation tendencies.

2.9.2 Lower Boundary Conditions

For the lower boundary conditions the surface layer and soil model parameterization by Tremback and Kessler (1985) were used. The model is a modified version of McCumber and Pielke (1981). The two models were shown to give similar results for a moist soil but the latter model does not converge for a dry soil, whereas the former gives more accurate results for both dry and moist soils. The model calculates a surface energy budget which includes shortwave and longwave radiative fluxes, sensible and latent heat fluxes, and conduction to and from the soil.

2.9.3 Lateral Boundary Conditions

For "variable initialization" in RAMS, one has the option of using either of two schemes; the "Sponge" model developed by Perkey and Kreitzberg (1976) or the Davies (1976) relaxation model. Both models use data at the two given times of 0 Z and 12 Z to force the boundary values of the meteorological variable tendencies. The Davie's nudging (or relaxation) scheme was used because it had been shown to result in less computational noise (Cram, 1990). The nudging zone used was 5 grid points wide and the weights (towards the model center from outside the boundary) were 0.75, 0.45, 0.25, 0.10, and 0.05.

2.9.4 Top Boundary Conditions

"Pressure at the model top", computed by hydrostatic integration from prognostic surface pressure was used for the ECMWF data. This condition uses an open model top and allows vertical velocity to exist at the model top. This boundary condition also depends on what happens at the surface. For the thermally-induced mesoscale simulations, however, the "Wall on Top" boundary condition, with Rayleigh Friction (10 layers from the model top) to diffuse gravity waves in the model, was used.

The acquisition, analyses, and initialization of the data used in the experiments for this study are discussed in the next chapter.

Chapter 3

DATA USED IN THE STUDY

Initially, this study intended to use the global ECMWF monthly-averaged gridded data sets of April, representing the "long-rains" season over Kenya, which runs from March to May with maximum rainfall usually occurring during the month of April. The year 1985 had a normal rainfall distribution over the country.   Although the ECMWF data archived at NCAR had monthly-mean gridded data, there was no corresponding monthly-mean gridded data sets for the NMC rawinsonde and surface observations needed for the model initialization. Therefore, in order to use the available archived daily gridded data, a method (based on daily rainfall at 23 synoptic stations in Kenya) was devised to pick a day that best represented the average conditions in April, 1985. This date was 14 April 1985. This date had a fairly widespread rainfall over the whole country and displayed the average synoptic climatology reminiscent of a typical April weather situation over Kenya.

The data set from the global ECMWF records used in this study to set the initial conditions were processed with a Mesoscale Isentropic Data Analysis and Assimilation Package (now called ISentropic ANalysis package, ISAN) for observed data developed by Tremback (1990). The analysis package was initially developed to read data for the Northern Hemisphere. However, for this study, the package was modified to also read data for the Southern Hemisphere, since Kenya sits astride the equator. This analysis package is organized in five distinct stages. A brief review of the data used in the experiments shall therefore be discussed in the following sections based on the stages of analysis. However, the reader is referred to Tremback (1990) for a detailed review of the data assimilation technique.

3.1 Stage 1 Data Analysis

This stage dealt with access of the ECMWF pressure data in the horizontal (x, y) at grid spacing (degrees) of 2.5° by 2.5°. There were seven mandatory pressure levels given:

1000 mb, 850 mb, 700 mb, 500 mb, 300 mb, 200 mb, and 100 mb.

The data access and analysis domain was bounded by the area from 5°E to 65°E longitude and 25°N to 25°S latitude (see Fig. 9). The number of grid points in the x-direction were 25 and 21 grid points in the y-direction. The ECMWF data together with the NMC (National Meteorological Center) mandatory pressure levels 2.5° global analysis, plus the NMC rawinsonde and surface observations data set are archived at NCAR (National Center for Atmospheric Research). Rawinsonde reports provided winds (u, v), temperature $(T$ or $\theta)$, and moisture (RH) at various levels (z). These reports were for 0 Z and 12 Z (see Figures 10, 11, 12, 13, and 14).

3.2 Stage 2 Data Analysis

This stage considered the isentropic conversion of pressure data accessed in stage 1 over the same latitude and longitude bounds. The weather parameters $(u, v, \theta,$ and RH) were interpolated vertically to isentropic levels of 5 K intervals from the surface to 360 K and at intervals of 10 K from 370 K to 400 K. The minimum θ at 1000 mb was 289.7 K and the maximum θ at 100 mb was 401.72 K. There were 19 isentropic levels generated between 1000 mb (or 289.7 K) and 100 mb (401.72 K). These levels are listed below (in K):

290, 295, 300, 305, 310, 315, 320, 325, 330, 335, 340, 345, 350, 360, 370, 380, 390, 400

The terrain height and sea surface temperature data sets were used at this stage and the Barnes (1973) objective analysis scheme was applied to smooth out results by removing the delta two $(2\Delta s)$ waves that generate "noise" in the model output. The Montgomery function $(C_p T + gz)$ was objectively analyzed at level 360 K as the boundary condition for hydrostatic integration (see Figures 15 and 16).
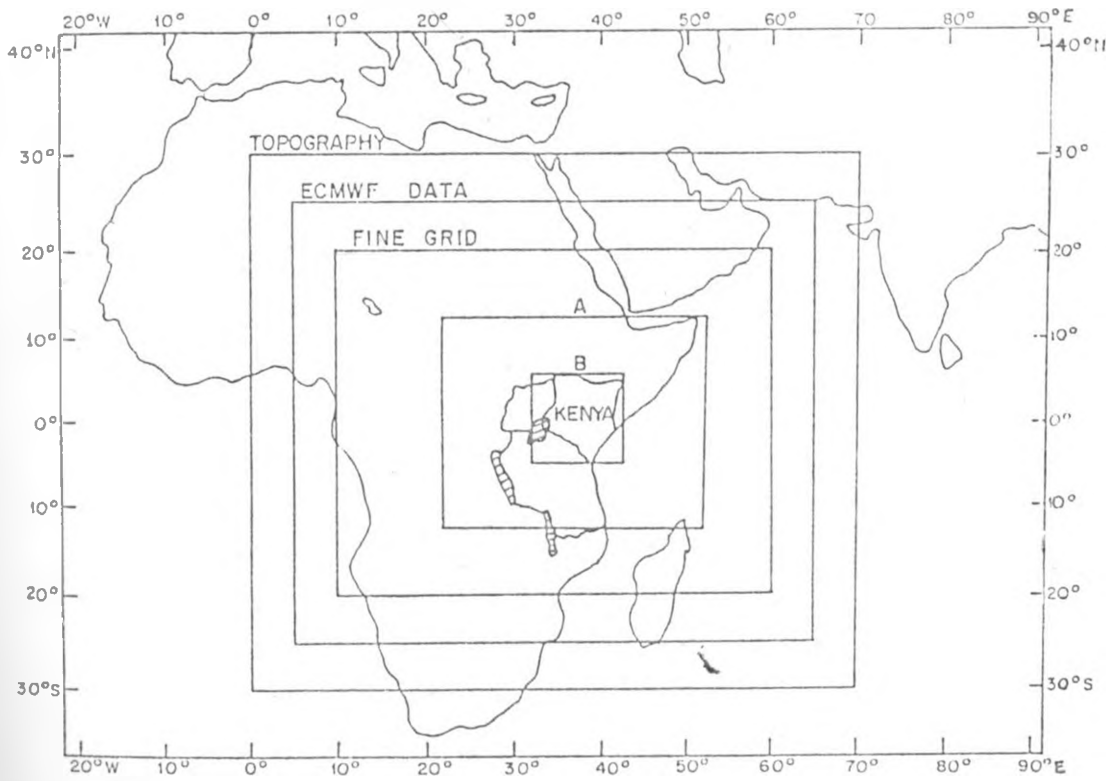
Figure 9: The model domain.
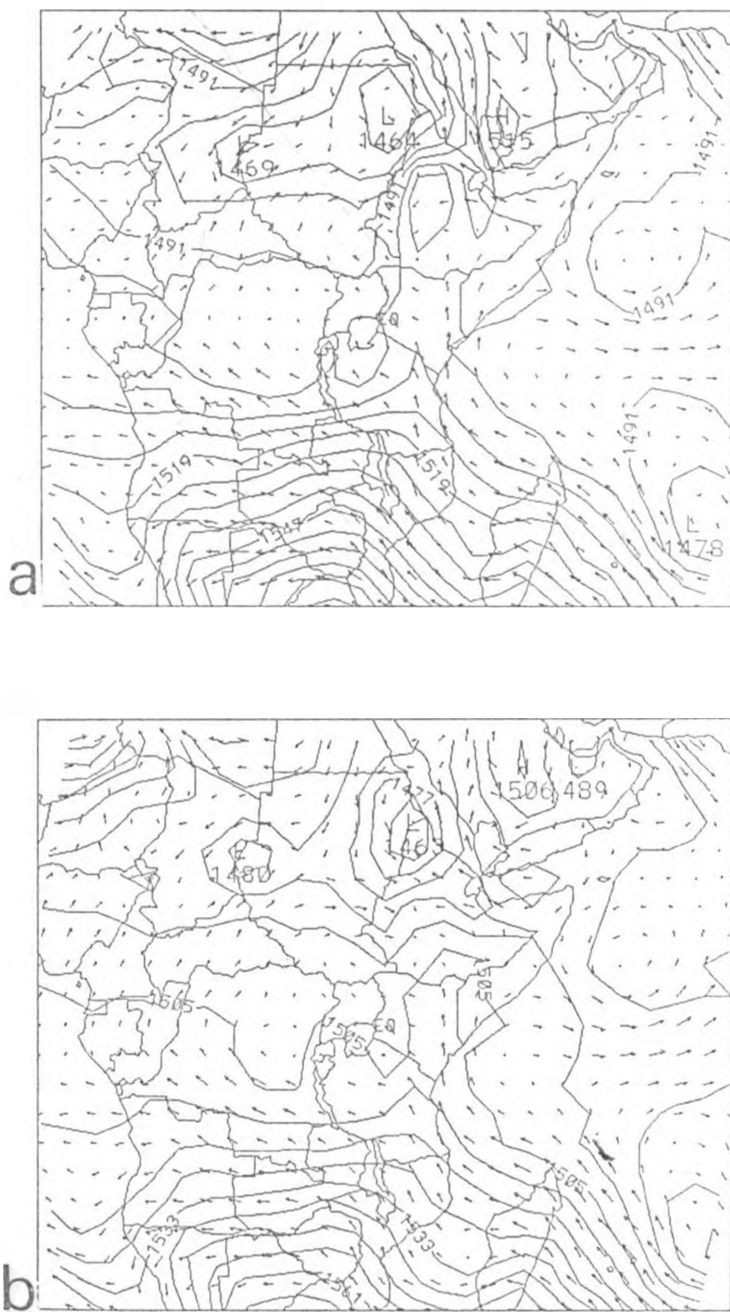
Figure 10: Geopotential on the 850 mb isobaric surface at (a) 0 Z, and (b) 12 Z on 14 April 1985 (Stage 1). Contour intervals are 7.0 m² s⁻². The maximum wind vector is 12.9 m s⁻¹.
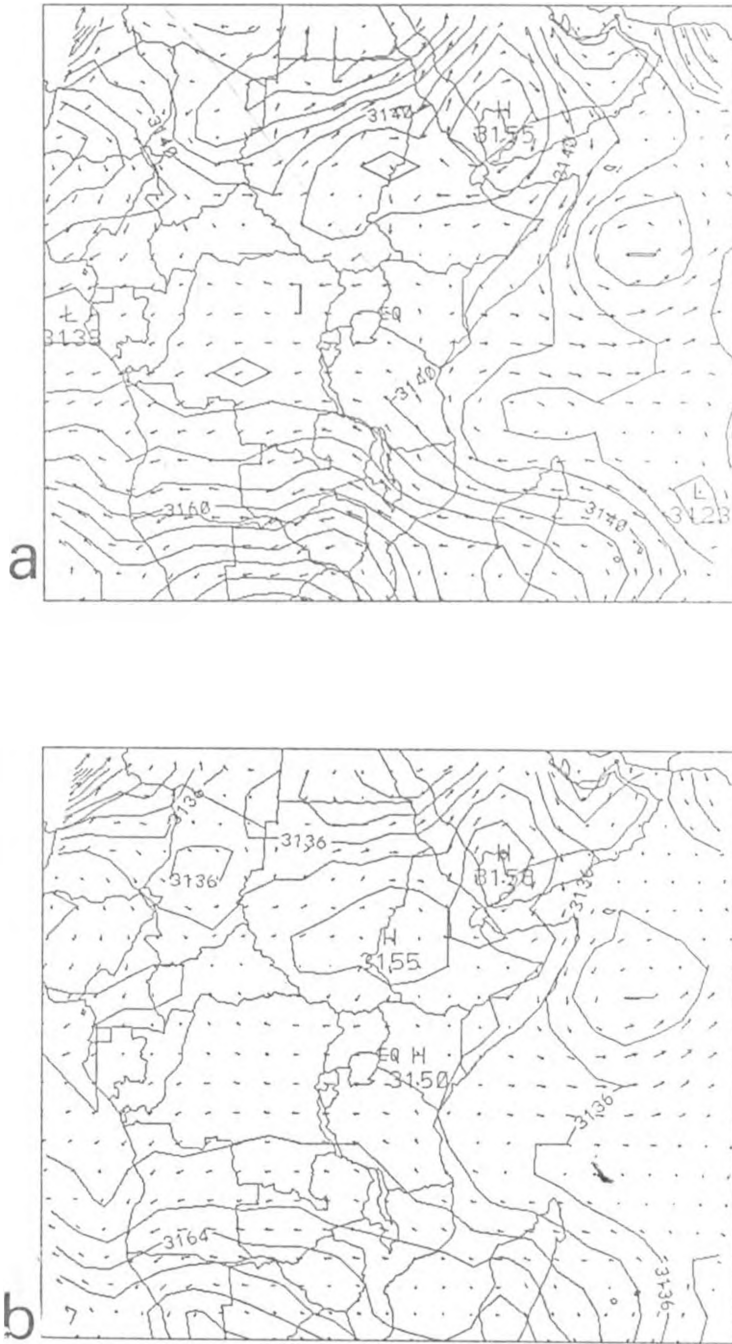
Figure 11: Geopotential on the 700 mb isobaric surface at (a) 0 Z, and (b) 12 Z on 14 April 1985 (Stage 1). Contour intervals are 5.0 m² s⁻². The maximum wind vector is 14.0 m s⁻¹ at 0 Z and 20 m s⁻¹ at 12 Z.
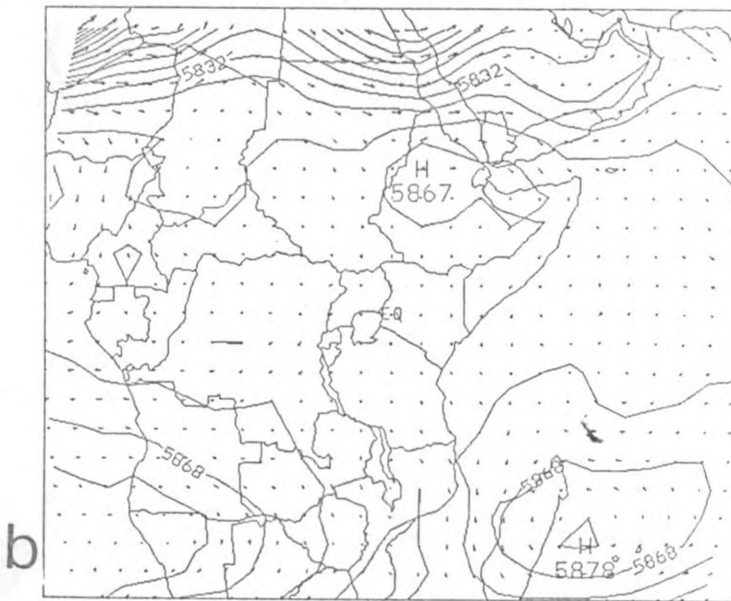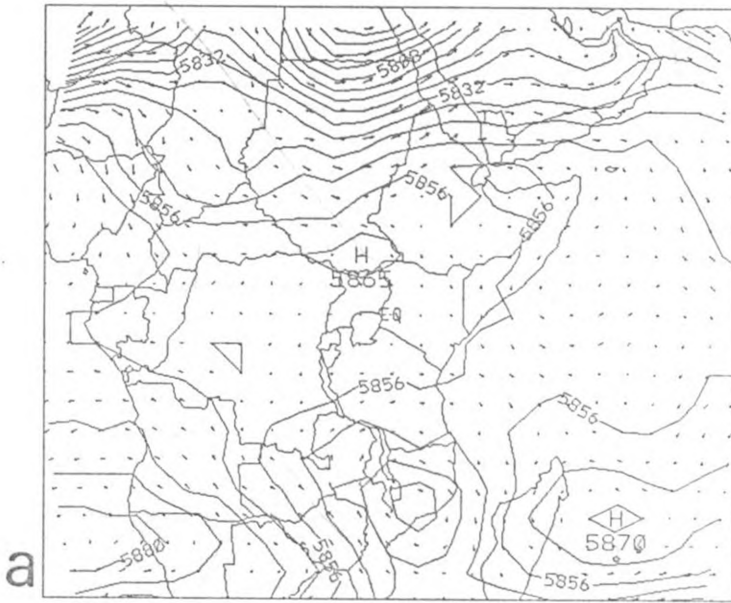
Figure 12: Geopotential on the 500 mb isobaric surface at (a) 0 Z, and (b) 12 Z on 14 April 1985 (Stage 1). Contour intervals are 6.0 m^2 s^{-2}. The maximum wind vector is 23.9 m s^{-1} at 0 Z and 31.5 m s^{-1} at 12 Z.
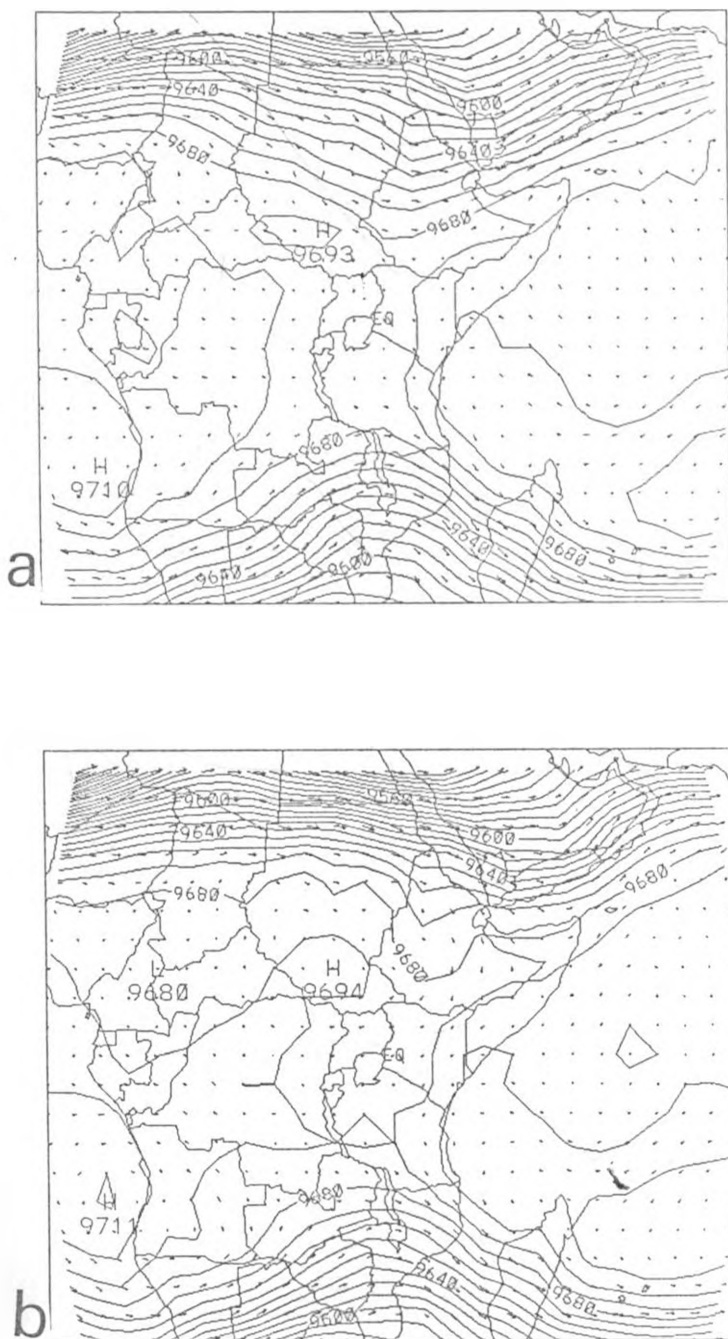
Figure 13: Geopotential on the 300 mb isobaric surface at (a) 0 Z, and (b) 12 Z on 14 April 1985 (Stage 1). Contour intervals are 10.0 m^2 s^{-2}. The maximum wind vector is 42.3 m s^{-1} at 0 Z and 50 m s^{-1} at 12 Z.
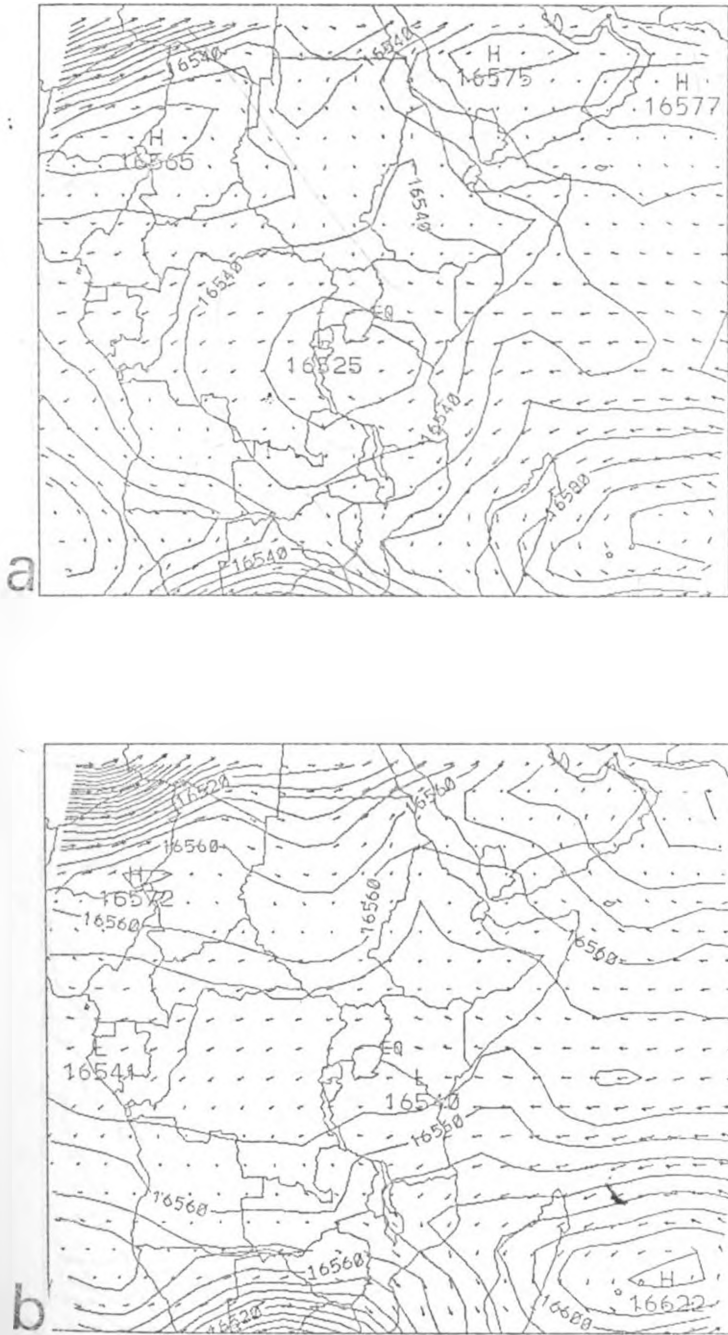
Figure 14: Geopotential on the 100 mb isobaric surface at (a) 0 Z, and (b) 12 Z on 14 April 1985 (Stage 1). Contour intervals are 10.0 m s^{-1}. The maximum wind vector is 29.5 m s^{-1} at 0 Z and 31.4 m s^{-1} at 12 Z.
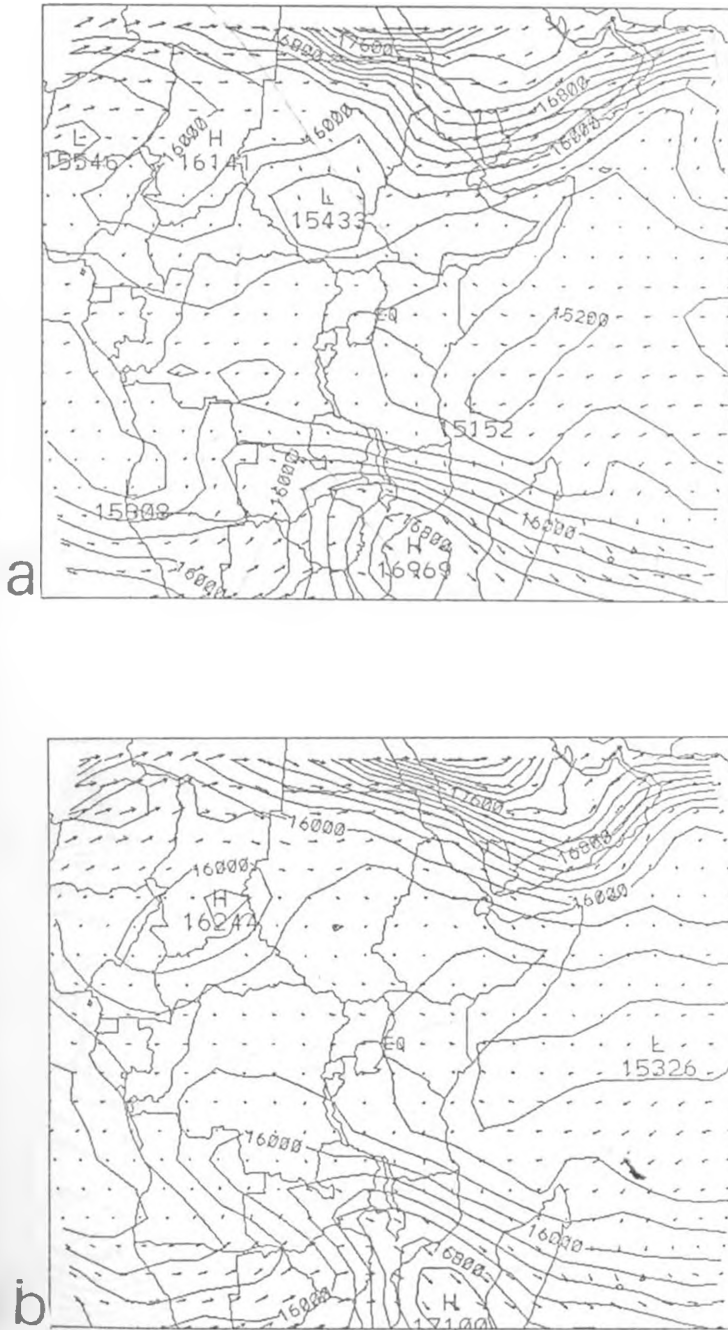
Figure 15: Pressure fields on the 360 K isentropic surface at (a) 0 Z, and (b) 12 Z on 14 April 1985 (Stage 2). Contour intervals are 0.2 kPa. The maximum wind vector is 43.8 m s^{-1}.
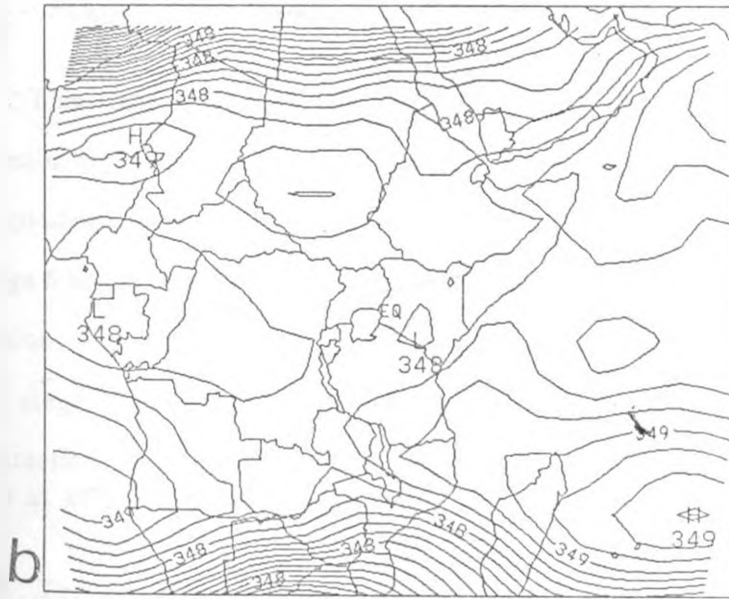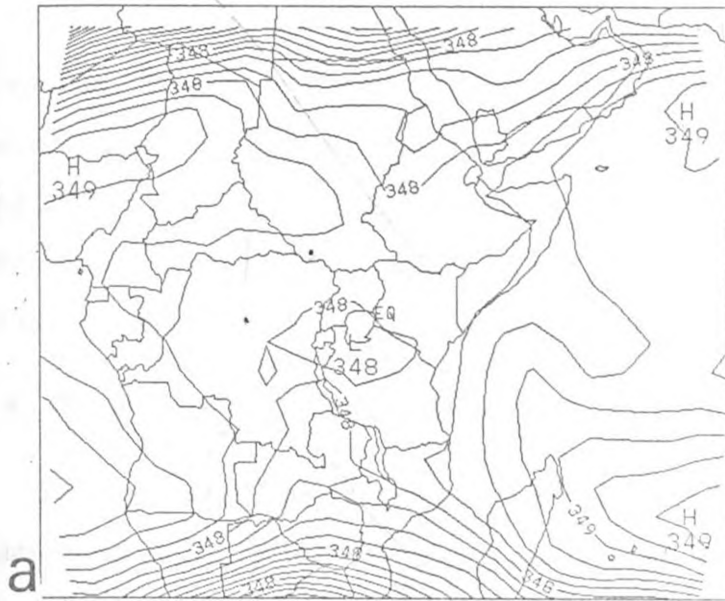
Figure 16: Montgomery streamfunction fields on the 360 K isentropic surface at (a) 0 Z, and (b) 12 Z on 14 April 1985 (Stage 2). Contour intervals are 100.0 m^2 s^{-2}.

3.3   Stage 3 Data Analysis

This stage performed the objective analysis of the isentropic data from Stage 2 to a prescribed "fine grid" with rawinsonde data, terrain heights data, and sea surface temperature data sets. The 'fine grid' used in this study was bounded by 10°E to 60°E longitude and 20°N to 20°S latitude. It had a grid spacing (degrees) of 1.25° by 1.25°. The number of grid points in the x-direction was 41 with 33 grid points in the y-direction (see Figures 17 to 31 displaying various weather parameters at different levels).

3.4   Stage 4 Data Analysis and Plotting

This stage dealt with the plotting and analysis of Stages 1, 2, and 3 fields. The fields that could be plotted were temperature (T or θ), winds (u, v, $|\vec{v}|$), humidity (RH), pressure (mb), Montgomery stream function ($C_p T + gz$), geopotential, topography, etc. Winds could be plotted either as vectors, contours, or streamlines.

3.5   Stage 5 Data Analysis and RAMS Model Initialization

This stage dealt with the RAMS model initialization of Stage 3 data to the model domain. This was done by interpolating Cartesian (x, y) and sigma-z grids from isentropic longitude-latitude grids. In version 2B of RAMS, the center of the domain is specified in Stage 5 in degrees latitude-longitude. A Polar Stereographic coordinate was used in this version. The number of x, y, and z grid points of the model domain were specified at this stage. Thus, for this study, the model domain (coarse grid) had 34 grid points in the x-direction, 29 in the y-direction, and 34 in the z-direction. The domain center for this study was at 37°E longitude, 0° latitude.

3.3   Terrain Height Data

This data was used in Stages 2 and 3. The topography package was run on the CRAY X-MP/48 computer to access a 10-minute (0.1666666°) global averaged data set archived at NCAR. The analysis domain was bounded by 0°E to 70°E longitude and 30°N to 30°S latitude (see Figure 9). The number of grid points in the x-direction (longitude) was 421 with 361 grid points in the y-direction (latitude).

41
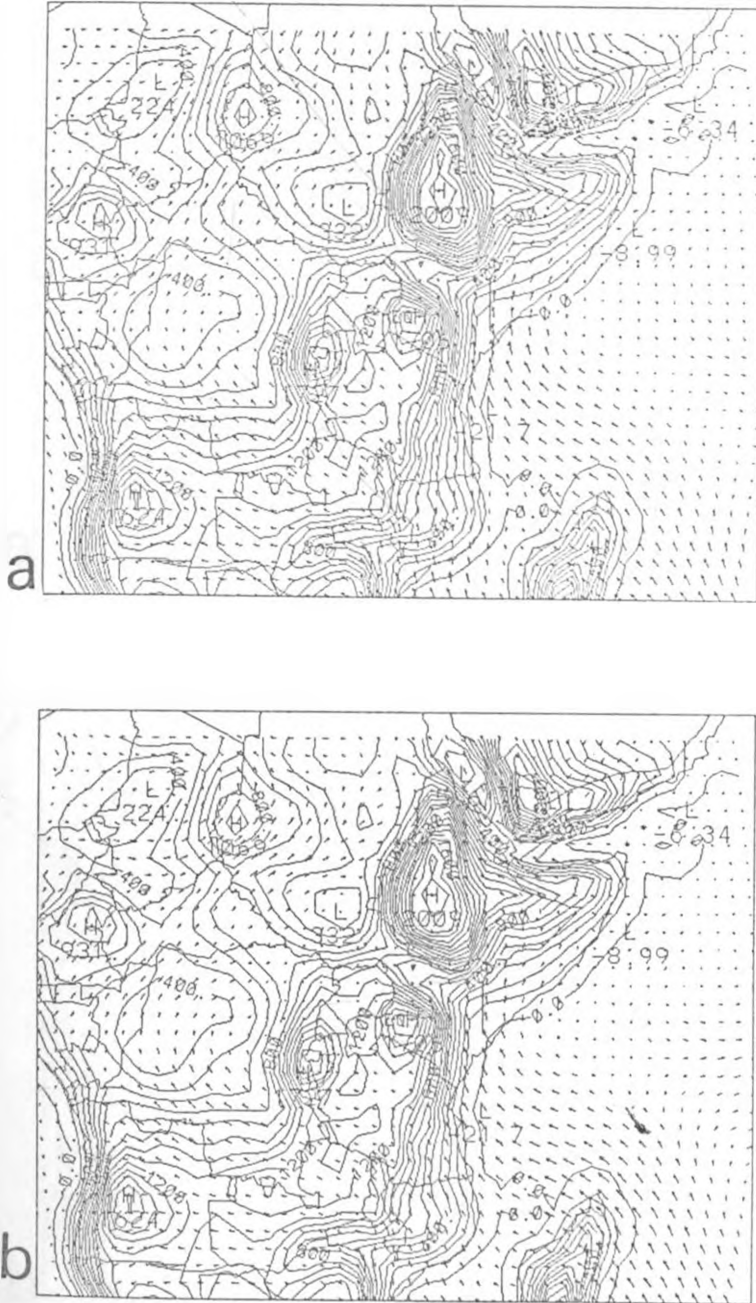
Figure 17: 1.25° topography field interpolated from a 10 minute data set (Stage 3). Contour intervals are 100 m. The surface wind vectors shown are for (a) 0 Z, and (b) 12 Z. Maximum wind vectors are 14 m s^{-1} at 0 Z and 16.6 m s^{-1} at 12 Z.
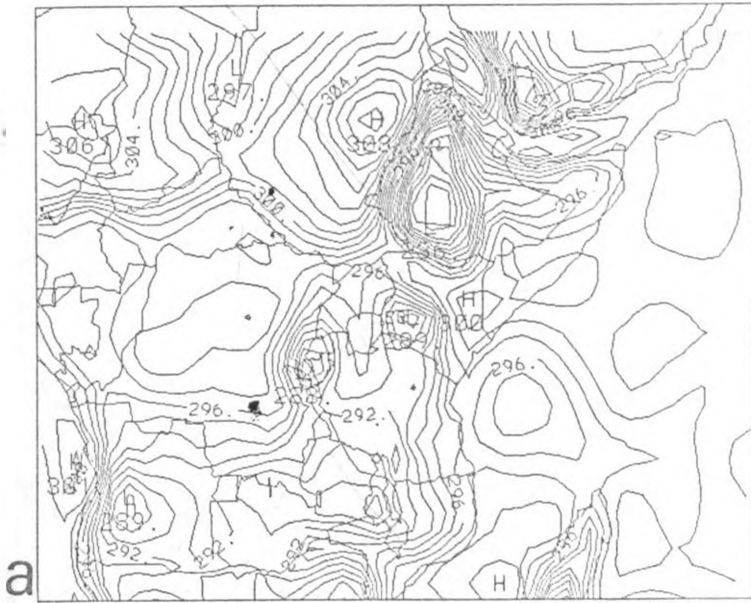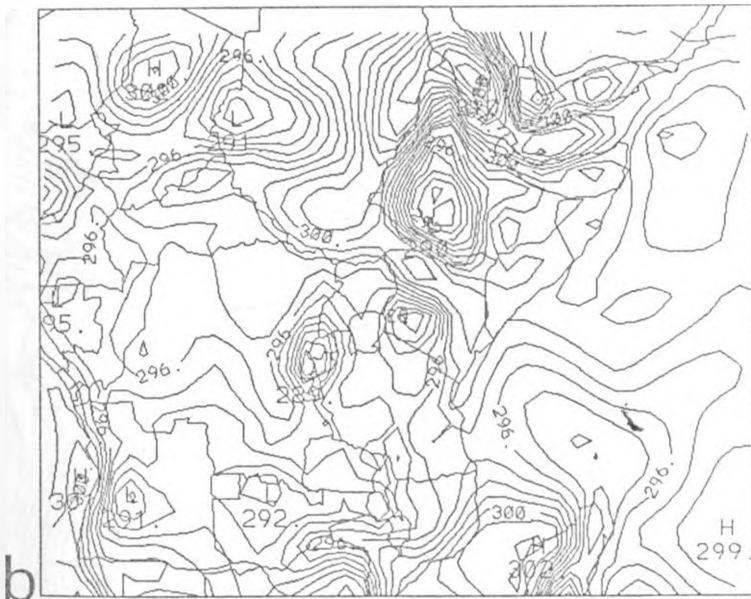
Figure 18: Surface temperature at (a) 0 Z, and (b) 12 Z on 14 April 1985 (Stage 3). Contour intervals are 1 K. Temperature ranges from 286 K to 308 K.
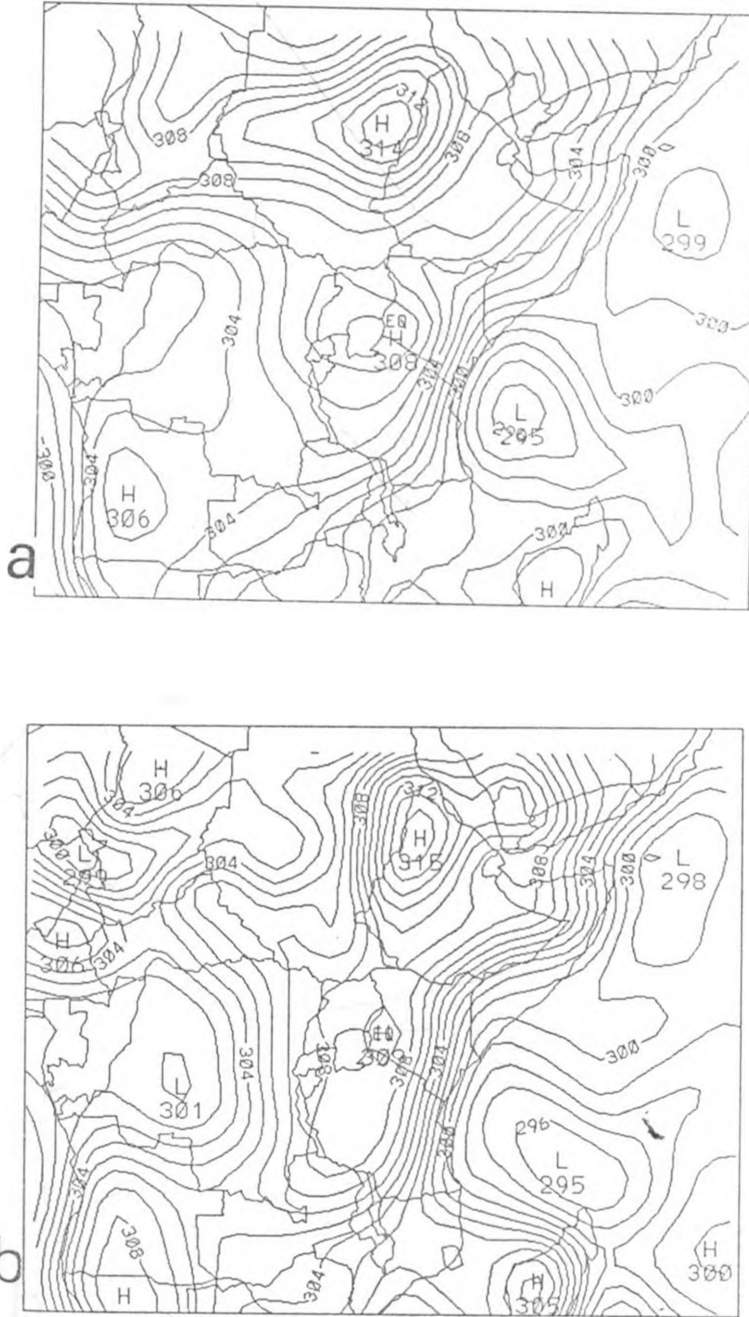
Figure 19: Surface Montgomery streamfunction at (a) 0 Z, and (b) 12 Z on 14 April 1985 (Stage 3). Contour intervals are 1000 m^2 s^{-2}. The ranges are from 29,500 to 31,300 m^2 s^{-2}. Labels were multiplied by 0.01.
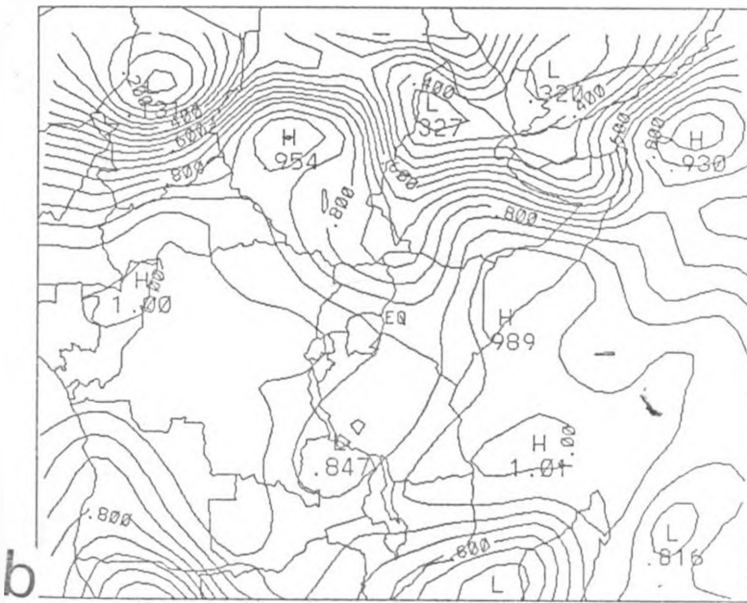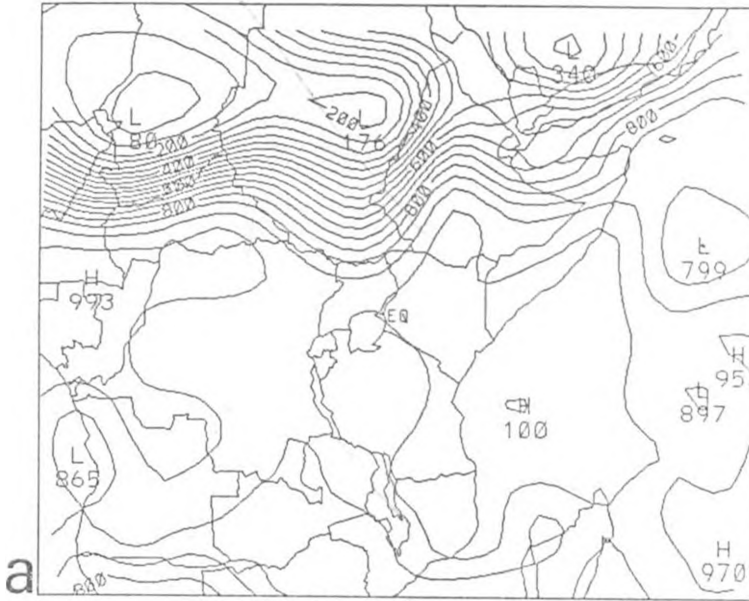
Figure 20: Surface relative humidity at (a) 0 Z, and (b) 12 Z on 14 April 1985 (Stage 3). Contour intervals are 0.05 (or 5%).

Figure 21: Surface mixing ratio at (a) 0 Z, and (b) 12 Z on 14 April 1985 (Stage 3). Contour intervals are 0.001 g kg^{-1} or 1 g kg^{-1}. The mixing ratio ranges from 2.0 g kg^{-1} to 21 g kg^{-1}.

Figure 22: Surface speed at (a) 0 Z, and (b) 12 Z on 14 April 1985 (Stage 3). Contour Intervals are 0.8 m s^{-1} at 0 Z and 1.0 m s^{-1} at 12 Z. The wind speeds range from 0.0 m s^{-1} to 13.6 m s^{-1} at 0 Z and from 0.0 m s^{-1} to 17.0 m s^{-1} at 12 Z.

Figure 23: Pressure on the 320 K isentropic surface at (a) 0 Z, and (b) 12 Z on 14 April 1985 (Stage 3). Contour intervals are 0.6 kPa at 0 Z and 0.8 kPa at 12 Z.
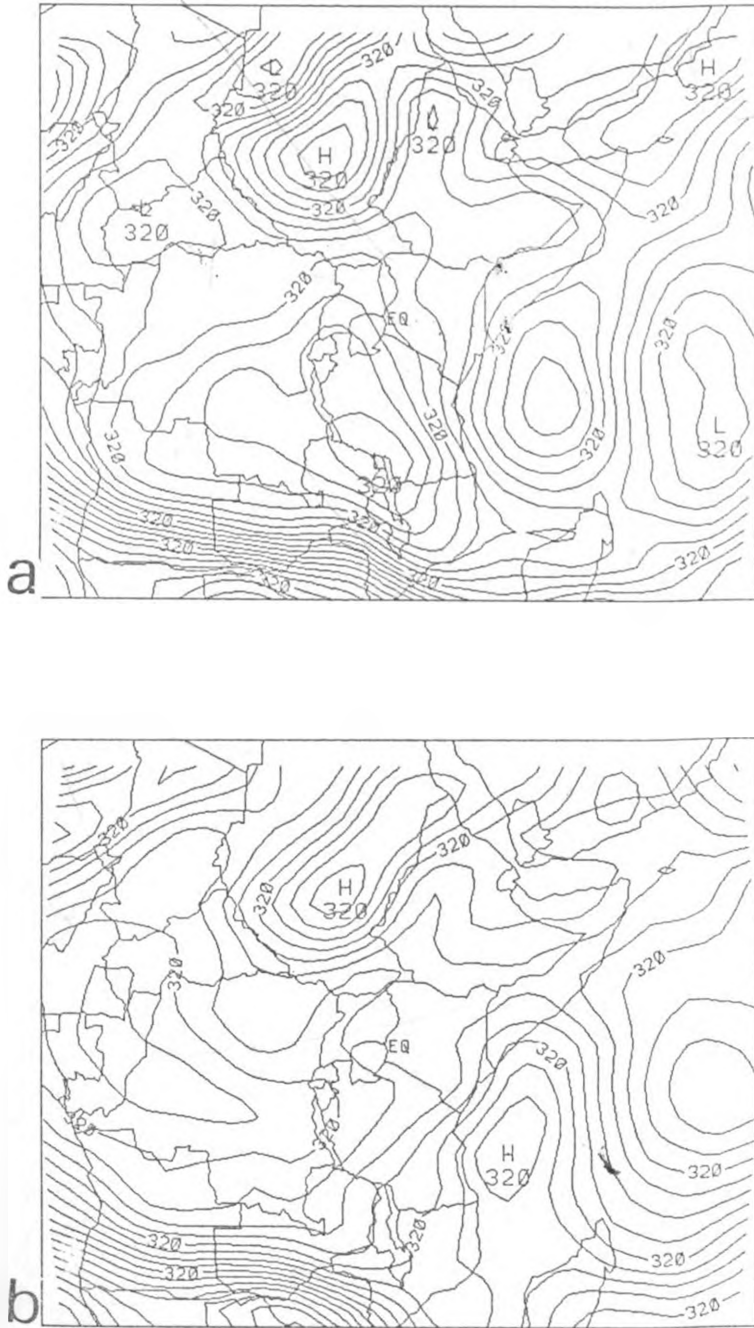
Figure 24: Montgomery streamfunction on the 320 K isentropic surface at 0 (a) Z, and (b) 12 Z on 14 April 1985 (Stage 3). Contour intervals are 40 m^2 s^{-2} at 0 Z and 50 m^2 s^{-2} at 12 Z. The labels are $* 0.1 \times 10^{-2}$.

Figure 25: Wind speed on the 320 K isentropic surface at (a) 0 Z, and (b) 12 Z on 14 April 1985 (Stage 3). Contour intervals are 0.7 m s^{-1} Wind speeds range from 0.0 m s^{-1} to 11.2 m s^{-1}.
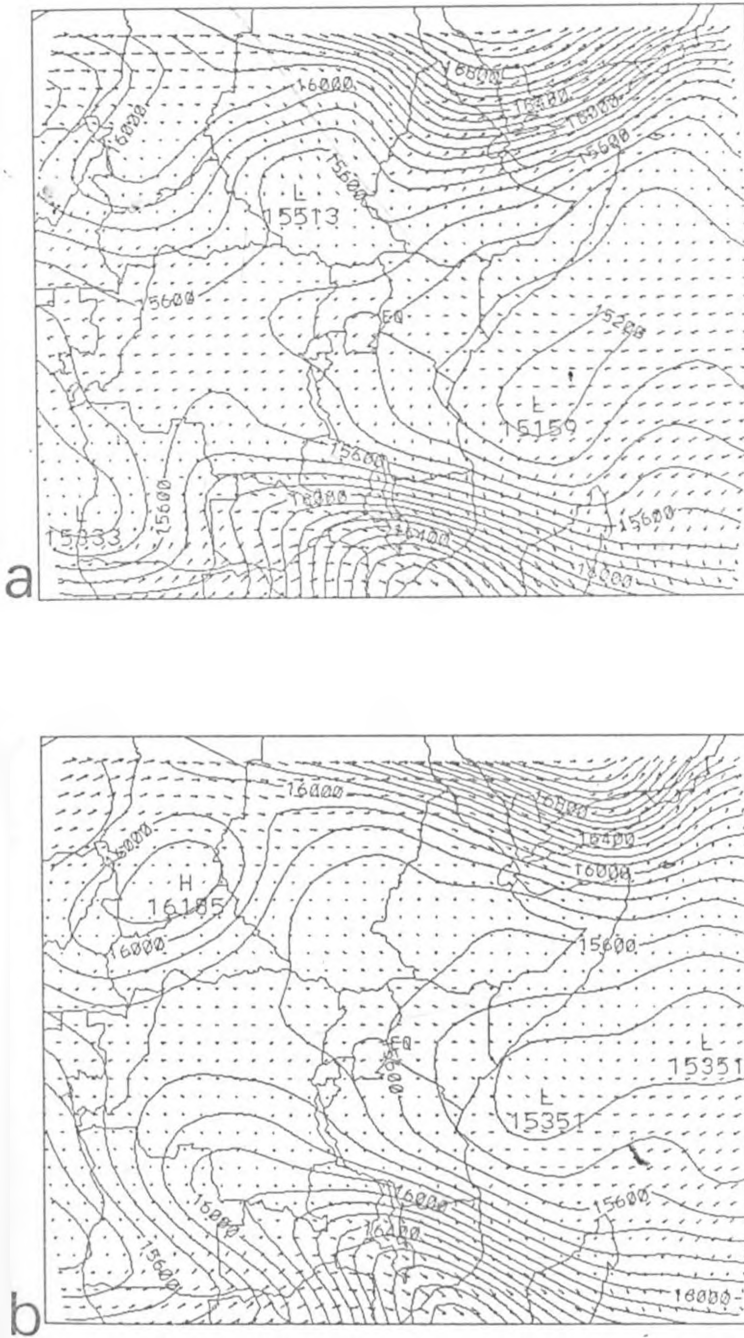
Figure 26: Pressure on the 360 K isentropic surface at (a) 0 Z, and (b) 12 Z on 14 April 1985 (Stage 3). Contour intervals are 0.1 kPa.
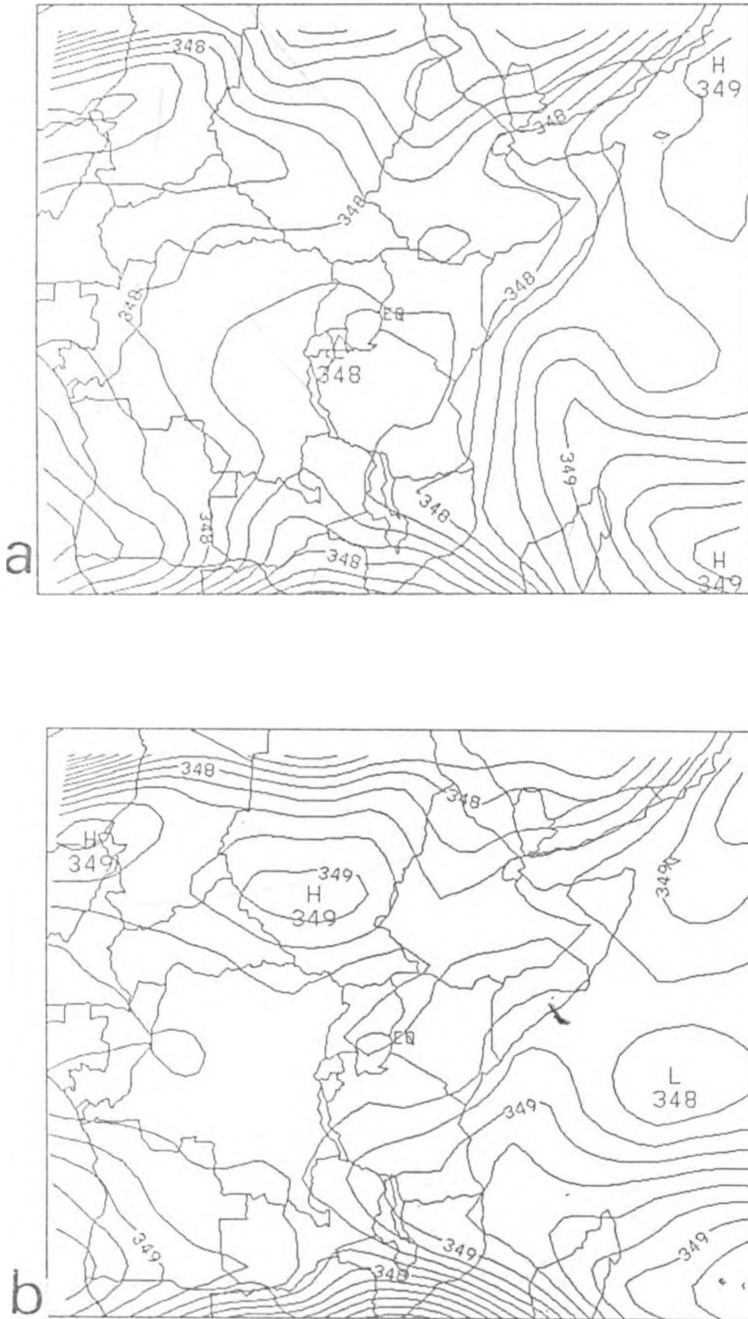
Figure 27: Montgomery streamfunction on the 360 K isentropic surface at (a) 0 Z, and (b) 12 Z on 14 April 1985 (Stage 3). Contour intervals are 600 m^2 s^{-2} at 0 Z and 700 m^2 s^{-2} at 12 Z. The labels are $* \, 0.1 \times 10^{-2}$. ↘
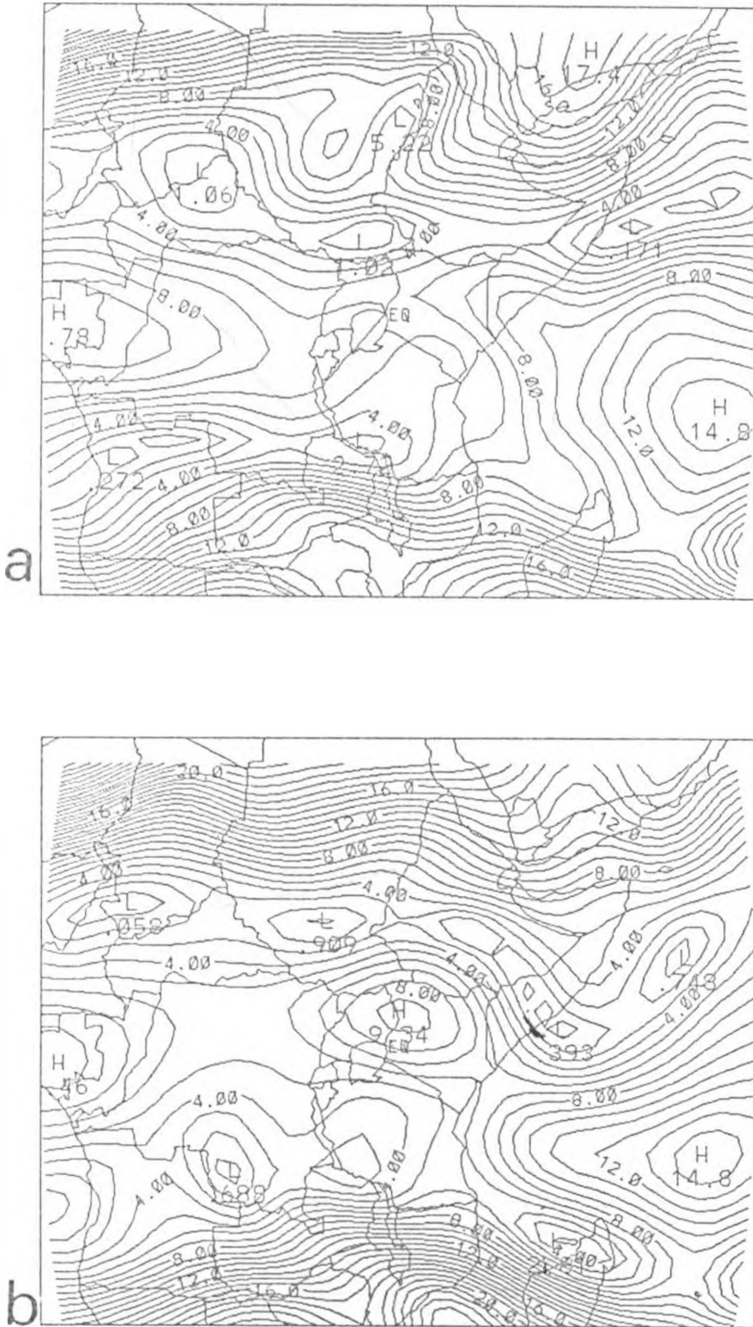
Figure 28: Wind speed on the 360 K isentropic surface at (a) 0 Z, and (b) 12 Z on 14 April 1985 (Stage 3). Contour intervals are 1.0 m s⁻¹. Wind speeds range from 0.0 m s⁻¹ to 25.0 m s⁻¹ at 0 Z and 0.0 m s⁻¹ to 30.0 m s⁻¹ at 12 Z.
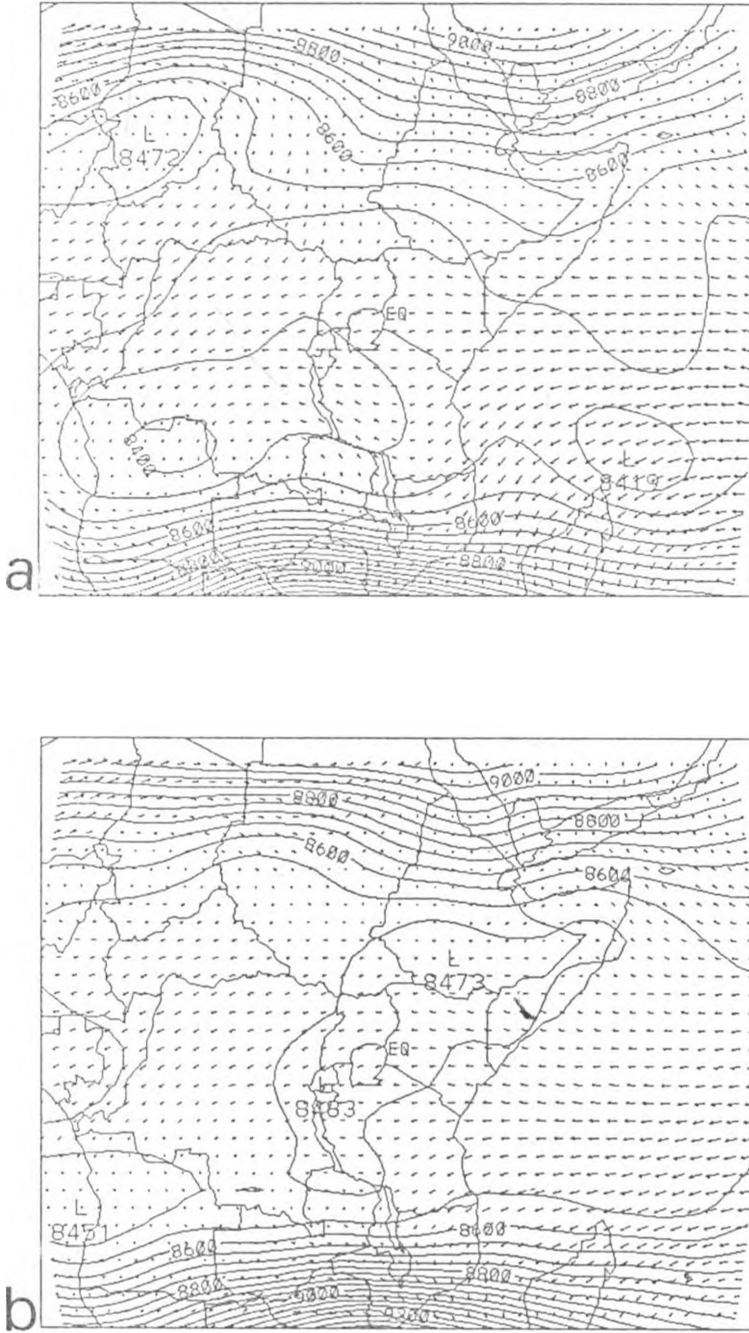
Figure 29: Pressure on the 400 K isentropic surface at (a) 0 Z, and (b) 12 Z on 14 April 1985 (Stage 3). Contour intervals are 0.05 kPa. The maximum wind vector is 18.0 m s^{-1}.
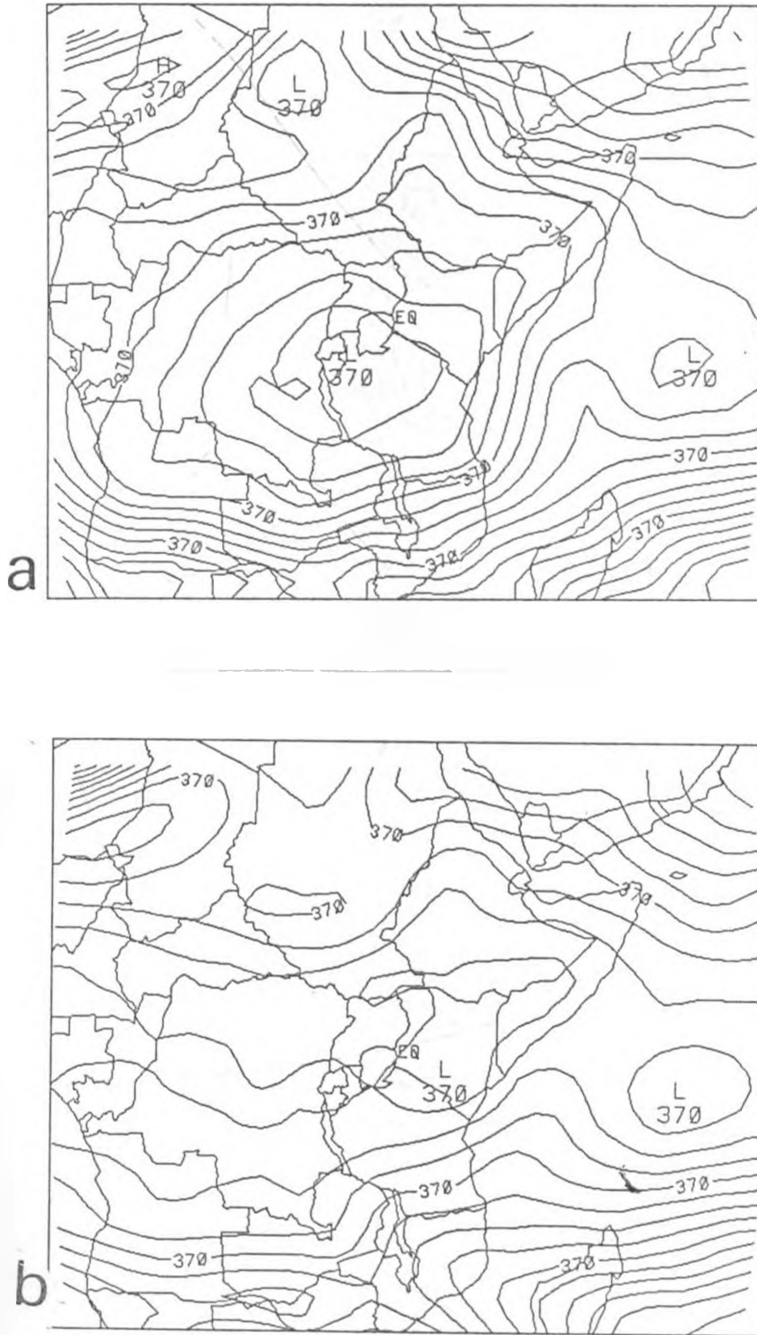
Figure 30: Montgomery streamfunction on the 400 K ($\approx$100 mb) isentropic surface on 14 April 1985 (Stage 3). Contour intervals are 500 m^2 s^{-2}. The labels are $*$ 0.001. The values range from 3.697 $\times$ 10^5 to 3.705 $\times$ 10^5 m^2 s^{-2}. (a) 0 Z, and (b) 12 Z.
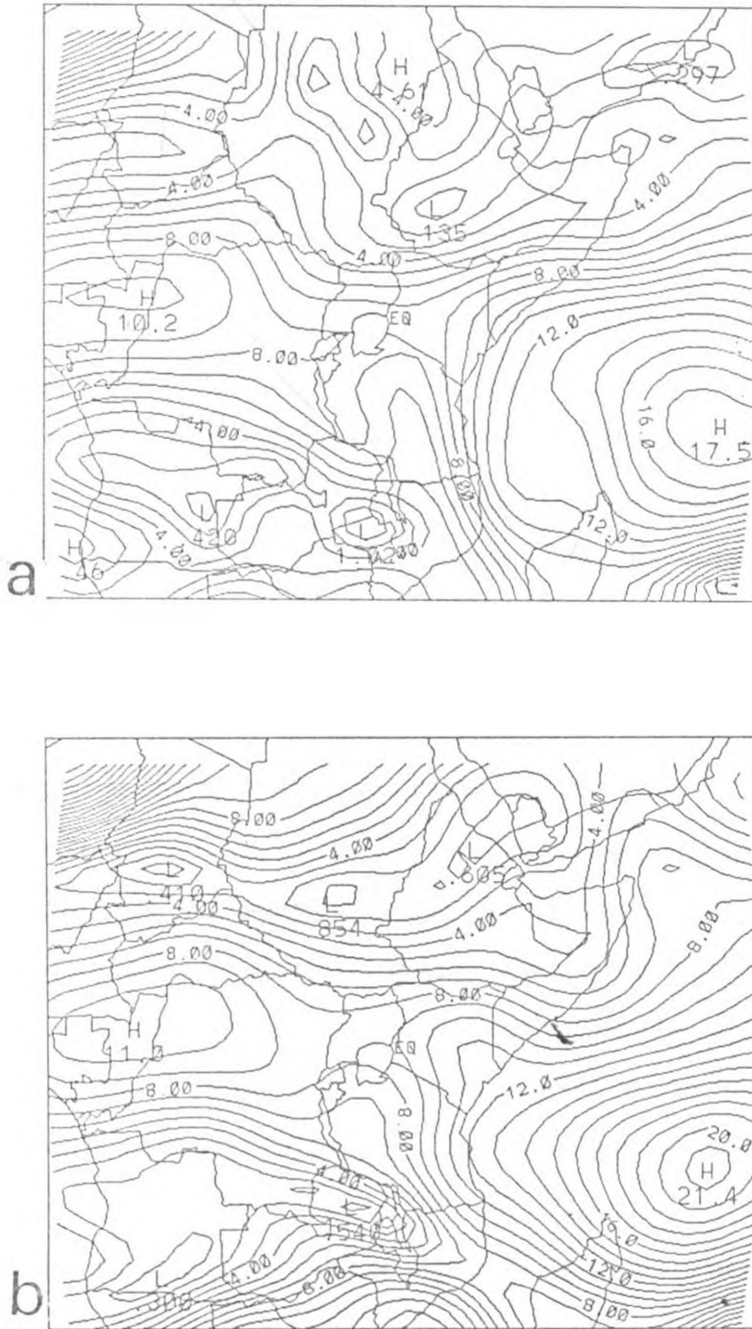
Figure 31: Wind speed on the 400 K isentropic surface on 14 April 1985 (Stage 3). Contour intervals are 1.0 m s^{-1}. The wind speeds range from 0.0 m s^{-1} to 17.0 m s^{-1} at (a) 0 Z, and from 0.0 m s^{-1} to 23.0 m s^{-1} at (b) 12 Z

3.7   Sea Surface Temperature Data

This data was similarly used in Stages 2 and 3. The global sea surface temperature data set archived on the Mass Storage System of the supercomputer at NCAR was accessed. This data had a grid spacing (degrees) of 1° in the x-direction and 1° in the y-direction. The number of grid points were 360 in the x-direction and 181 in the y-direction.

Thus, to use the "variable initialization" procedure in RAMS, two Stage 5 data fields were required; one for 0 Z and the other for 12 Z.

One may have course to argue that the ECMWF data used for initialization in this study may not perform well for the equatorial region citing as reasons, the facts that the unavailability of observed data from many areas of the equatorial latitudes to the Global Teleconnection Systems (GTS) and the subsequent inadequate representation of the meteorology of the equatorial regions in the Global Circulation Models (GCMs), due to insufficient observational studies in the area, may result in outputs that may not replicate the observed weather phenomenon of the equatorial regime.

However, the limited-area model (in this case RAMS) that use the ECMWF data for initialization has more built-in physics and is capable of finer resolutions due to grid nesting. By using a ten-minute global topography, global sea surface temperature, soil moisture and temperature, roughness parameter, land-percentage, albedo of the study domain with the assimilated data set from the global ECMWF records subjected to certain constraints, a more accurate prediction of weather parameters on the study domain is envisaged.

The subsequent chapter deals with the numerical experiments and how they were performed during this investigation.

Chapter 4

NUMERICAL EXPERIMENTS PERFORMED

In order to fulfill the objectives which were outlined in Section 1.1, three major sets of simulations were carried out. These are briefly discussed below.

4.1 EXPERIMENT 1: Dry Simulations of the Large-Scale Monsoonal Flow

The first set of model simulations were dry and included a background synoptic wind using a data set from the global ECMWF records of 14 April 1985. The data was accessed from NCAR using a five-stage Data Analysis and Assimilation Package as described in Chapter 3. A "variable initialization" procedure was performed to create the model initial fields. The model integration was started at 0 Z (0 GMT which is equivalent to 0 UTC) and nudged with data at 12 Z. The model was integrated forward-in-time for 24 hours.

Low level, middle level, and upper level flows were displayed on an hourly basis in the course of the simulation to show the dynamics of the region. Vertical east-west cross sections of the selected weather parameters were displayed to show the vertical structure of the atmosphere over the study domain. Low-level moisture fields were displayed to establish the moisture incursion into the region by the large-scale forcing. Perturbation Exner function was used to show the low-level pressure cells over the domain which were indicative of likely areas of active convection. The potential temperature fields and the vertical velocity fields were generated to further determine the thermal structure (both lateral and vertical) and the rising/sinking motion over the study domain.

4.2 EXPERIMENT 2: Dry Simulations of the Mesoscale Flows

The second set of model simulations were also dry and were started with an atmosphere at rest (that is, $u = 0$, $v = 0$, $w = 0$) in order to suppress the influence of the

large-scale monsoon flow. The inputs of these latter simulations were a one-station sounding data (pressure, dry bulb temperature, and mixing ratio) of the same date as in Section 4.1 above from Dagoretti Weather Station in Nairobi. Topography, sea-surface temperature, and land-percentage data were read into the model and a "horizontally-homogeneous initialization" procedure was used to procure the initial fields for the model. The model simulations were also commenced at 0 Z and integrated forward in time for 24 hours. The low level flow (u, v, w) were displayed to reveal the mesoscale circulations over the country. The vertical east-west cross sections were displayed to determine the vertical extent of these mesoscale circulations. Pressure perturbation fields, thermal structure, and moisture fields created by the mesoscale circulations were likewise displayed over the study domain.

4.2.1 Determination of the Interaction Between the Large-Scale and the Local Mesoscale Flows

Experiments 1 and 2 are dry simulations, as stated above, and are termed as, "level-2 supersaturation condensed"; that is, clouds are allowed to occur in the model but precipitation is not generated.

The model-generated mesoscale circulations (Experiment 2) were "superimposed" on the prevailing large-scale synoptic flows (Experiment 1) at low levels to determine possible areas of low level convergence/divergence which are likely areas of active convection. The magnitudes of the opposing motions were also noted as a way of establishing the intensity or strength of the convergence/divergence. Convergence zones were taken as areas where the mesoscale circulations were in direct opposition to the prevailing large-scale winds, whereas the divergence zones were areas where the mesoscale flows and the large-scale winds were in the same direction.

The moisture incursion into the study domain firstly, by the large-scale synoptic winds, and secondly, by the mesoscale circulations, were separately generated over the domain and the contribution due to the large-scale flows was determined by establishing the difference in magnitudes between the large-scale moisture fields and the moisture fields accruing from the mesoscale circulations.

4.3 EXPERIMENT 3: Simulations of the Moist Convection

The third set of experiments constituted moist simulations using the data set from the global ECMWF records (as in Experiment 1). The aim or purpose of Experiment 3 was to determine:

(i) Whether the low level convergence zones established through "superimposition" of the flow fields of Experiments 1 and 2 were indeed active weather zones by generating precipitation over the domain;

(ii) The control of the large-scale monsoon flow on the movement and locations with time (diurnal pattern) of the precipitating zones over the country.

In order to fulfill the above-mentioned aims, cumulus parameterization and explicit microphysics modules were turned on to generate, among other parameters, convective precipitation rate. This parameter was used as an indicator of locations of precipitation over the country. Accumulated precipitation was likewise generated and compared with the actual 24-hours observed rainfall to determine the skill of the model using the ECMWF data over the equatorial region. The computational methods used in the numerical experiments are highlighted in the next section.

4.4 Computational Methodology Used in the Numerical Experiments

The computational procedure used for the large-scale flow fields (with the ECMWF data) was as follows:

(i) Two nested grid networks were used. The outer coarse grid domain extended from 22°E to 52°E longitude and 12.5°N to 12.5°S latitude.

It had a grid interval of 100 km in both the x- and y-directions with a timestep of 60 seconds. The number of grid points used were 34 in the x-direction, 29 in the y-direction and 34 σ_z levels. The inner fine grid domain extended from 31°E to 43°E longitude and from 5°N to 5°S latitude and covered the whole of Kenya. The horizontal fine grid spacing was 25 km in both the east-west and north-south

directions. There were 58 grid points in the x-direction and 46 grid points in the y-direction with 34 σ_z levels in the vertical. The vertical spacing used for both grids was 250 m with a geometric stretch ratio of 1.1 and the maximum stretch of 1000 m at the model top layers. This put the model top at about the 23 km level. The time step for the fine grid-mesh was 15 seconds (see Figure 9 where the coarse grid is marked A and and the fine grid B).

(ii) For the thermally-induced mesoscale simulations, the domain bounds, and the time steps remained the same as for the ECMWF data experiment above. However, the coarse grid spacing was reduced to 75 km in both the x- and y-directions. The vertical spacing was 150 m with a geometric ratio of 1.15 and a maximum stretch at the model top of 1000 m. The model top was at the 17 mb height level.

Two-dimensional model simulations were first completed in order to check the model performance over the study domain. Most of the simulations, data analysis, and computer graphics were completed on the NCAR supercomputing facilities; the CRAY X-MP/48 and the CRAY Y-MP8/864 (or "Shavano") and the Ardent Titan (or "Triton") superworksta- tion which was available to this project. The next chapter will discuss the observational analyses of the synoptic conditions prevailing during the study period in order to help examine the skill of the model in replicating observed results.

directions. There were 58 grid points in the x-direction and 46 grid points in the y-direction with 34 σ_z levels in the vertical. The vertical spacing used for both grids was 250 m with a geometric stretch ratio of 1.1 and the maximum stretch of 1000 m at the model top layers. This put the model top at about the 23 km level. The time step for the fine grid-mesh was 15 seconds (see Figure 9 where the coarse grid is marked A and and the fine grid B).

(ii) For the thermally-induced mesoscale simulations, the domain bounds, and the time steps remained the same as for the ECMWF data experiment above. However, the coarse grid spacing was reduced to 75 km in both the x- and y-directions. The vertical spacing was 150 m with a geometric ratio of 1.15 and a maximum stretch at the model top of 1000 m. The model top was at the 17 mb height level.

Two-dimensional model simulations were first completed in order to check the model performance over the study domain. Most of the simulations, data analysis, and computer graphics were completed on the NCAR supercomputing facilities; the CRAY X-MP/48 and the CRAY Y-MP8/864 (or "Shavano") and the Ardent Titan (or "Triton") superworkstation which was available to this project. The next chapter will discuss the observational analyses of the synoptic conditions prevailing during the study period in order to help examine the skill of the model in replicating observed results.

Chapter 5

THE OBSERVATIONAL ANALYSES

The importance of observational data in numerical weather prediction experiments cannot be overstressed. Surface and upper air data are needed both for the initialization of the model and for the validation of the model-generated results. Real-time upper air data helps determine the vertical structure of the atmosphere and improve the capability to perform short-range forecasts with more accuracy in models. However, there is generally insufficient upper air data and observational studies in the equatorial regions including Kenya.

Data for observational analyses were collected from the Data Processing Section (DPS) of the Kenya Meteorological Department at Dagoretti in Nairobi. These dataset included the surface winds, surface mixing ratios, relative humidity plus radiosonde soundings, and the rainfall of 14 April 1985. An attempt to acquire the pilot balloon winds and the satellite photographs was unsuccessful because of the unavailability of these records. All the observations which were available have been used here in an attempt to validate the results of the model. Figure 32 shows the distribution and location of the stations used in Kenya for observational analysis, including the Lake Victoria region.

5.1 Synoptic Climatology of the Case Study

5.1.1 The Observed Cloud Cover

Most of the synoptic stations in the country reported a monthly-averaged cloud cover for April, 1985 of at least 6 oktas (i.e., $\frac{6}{8}$) both at 06 Z and at 12 Z as shown in Table 1. From these records, it can be inferred that there was a fairly widespread cloud cover during the month of April, 1985; and hence, on the case study day as supported by other information discussed in the subsequent section below.
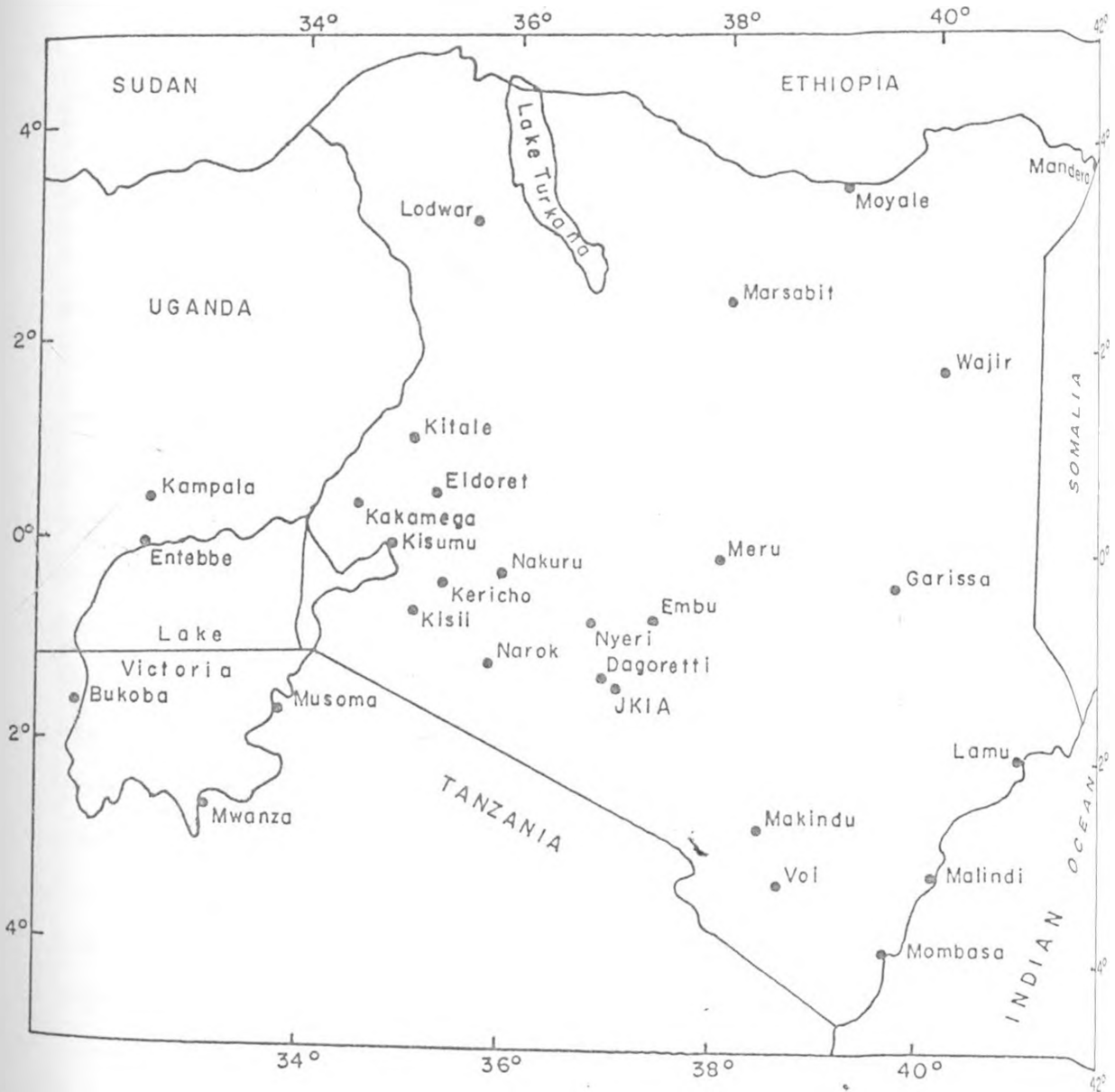
Figure 32: The distribution and location of the stations used for observational analysis in Kenya, including the Lake Victoria region.

Table 1: Observed monthly-averaged cloud cover and surface relative humidity of April, 1985.

		06Z		12Z	
Station Number	Station Name	Cloud Cover (Oktas)	Relative Humidity (%)	Cloud Cover (Oktas)	Relative Humidity (%)
612	Lodwar	6	69	7	51
619	Moyale	8	93	6	74
624	Mandera	6	72	6	53
641	Marsabit	7	97	6	77
661	Kitale	5	86	7	72
671	Wajir	7	75	6	48
686	Eldoret	5	73	6	58
708	Kisumu	6	78	6	61
710	Kericho	6	81	7	82
714	Nakuru	6	84	6	62
717	Nyeri	7	89	7	66
720	Embu	7	84	6	65
737	Narok	7	89	6	62
741	Dagoretti	7	86	6	60
766	Makindu	–	–	–	–
687	Kakamega	6	84	7	66
695	Meru	6	84	6	73
709	Kisii	6	77	*7	74
723	Garissa	6	72	6	43
740	Jkia*	6	86	6	57

* Jomo Kenyatta International Airport.

5.1.2 The Observed Radiosonde Soundings

Inspection of the radiosonde ascents for 0 Z (Figure 33) reveals that there was a calm surface wind at Dagoretti Weather Station in Nairobi; although at the Jomo Kenyatta International Airport (JKIA), about 16 km away, the surface winds were easterly with a strength of 7 knots. However, the westerlies were quite low at 0 Z and occupied a thicker layer (from 700 mb to 400 mb) as compared to the situation in the afternoon. The winds at 300 mb level were northerly at 0 Z showing a general veer of the winds to become easterlies above 300 mb (9.2 km). There was a weak temperature inversion (a stable layer) at the surface (821 mb to 770 mb) and another in the layer bounded by 700 mb and 600 mb isobaric surfaces. These inversion layers were absent in the ascent at 12 Z; the time at which solar insolation and subsequent vertical air overturning or mixing breaks up the inversion layer.

The relative humidity profile at 0 Z showed a substantial amount of moisture in the atmospheric column (over 85% in the lower and middle levels).

The radiosonde ascent at 12 Z (Figure 34) was characterized by the presence of the easterlies at low levels (surface to 650 mb, or 3.6 km), westerlies at mid-levels (600 mb to 500 mb) and easterlies aloft (from 400 mb upwards). The existence of a strong westerly current at mid-levels of the atmosphere over Kenya has been observed to occur during the rainy period (e.g., Kagenyi, 1990). The tropopause winds were registered at 94 mb level (17 km height) and had a strength of 35 knots.

The relative humidity profile at 12 Z showed that the atmosphere was quite humid from the surface to 500 mb ($\approx$5.6 km) although the amount of moisture in the atmospheric column was less than at 0 Z. The amount of relative humidity close to the surface (66%) was less than that of the immediate layer above (84%). This condition may be attributed to the fact that the dry bulb temperature profile (Figure 34) showed a near-adiabatic lapse rate from the surface (821 mb) to 750 mb level.

In the absence of the pilot balloon winds of the case study day over the country, the radiosonde soundings at 0 Z and 12 Z, as discussed above, may be taken to represent the general configuration and structure of the winds, moisture and temperature at different height levels of the atmosphere over the country.

Figure 33: The Nairobi radiosonde sounding at 0 Z.

✕━✕━✕ Dry Bulb Temperature (°C)

●━●━● Dew Point Temperature (°C)

Figure 34: The Nairobi radiosonde sounding at 12 Z.

×—×—× Dry Bulb Temperature (°C)

o—•—o Dew Point Temperature (°C)

5.1.3 The Observed Surface Mixing Ratio

The surface mixing ratio analyses over the country are illustrated in Figure 35 (at 06 Z) and 36 (at 12 Z). It can be seen that the magnitudes of the surface mixing ratios (or
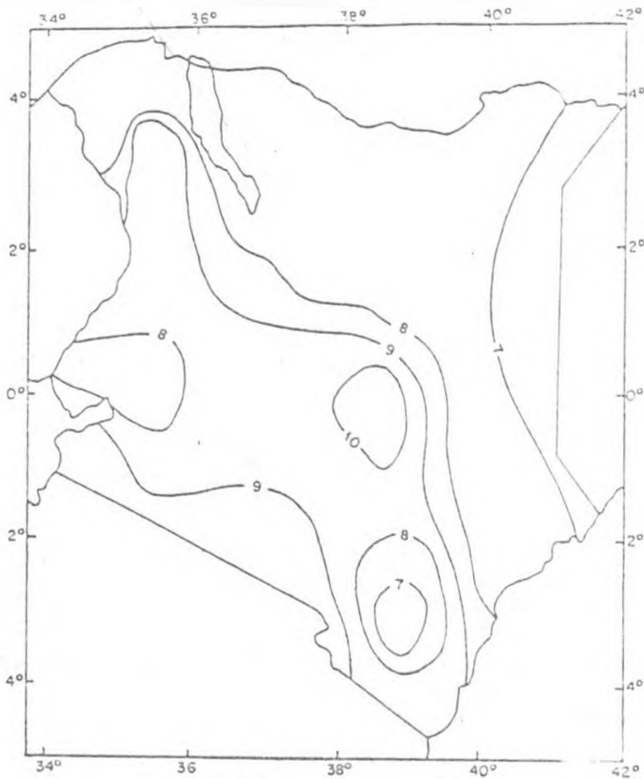
Figure 35: Surface mixing ratio for 14 April 1985 at 06 Z.

moisture) were generally more in the morning at 06 Z (9:00 a.m. local time) than at 12 Z (3:00 p.m. local time). This is because there was more solar insolation at 12 Z than at 06 Z. This insolation triggered off vertical eddy flux of water vapour to enrich the upper layers above the surface with humidity. The coastal region, the Kenya highlands and the Lake Victoria region registered more surface mixing ratios than other parts of the country; most notably the northeastern region which is generally rangeland.

5.1.4 The Observed Surface Winds

As was discussed above under Section 5.1.2, the synoptic conditions of the case study day were characterized by low level easterlies, middle level westerlies, and upper level easterlies. In this section, illustrations will be made of the available surface wind flow (about 10 m, or 33 feet, above the ground) patterns processed by subjecting the surface wind data to streamline and isotach analysis procedure. This was done in an attempt
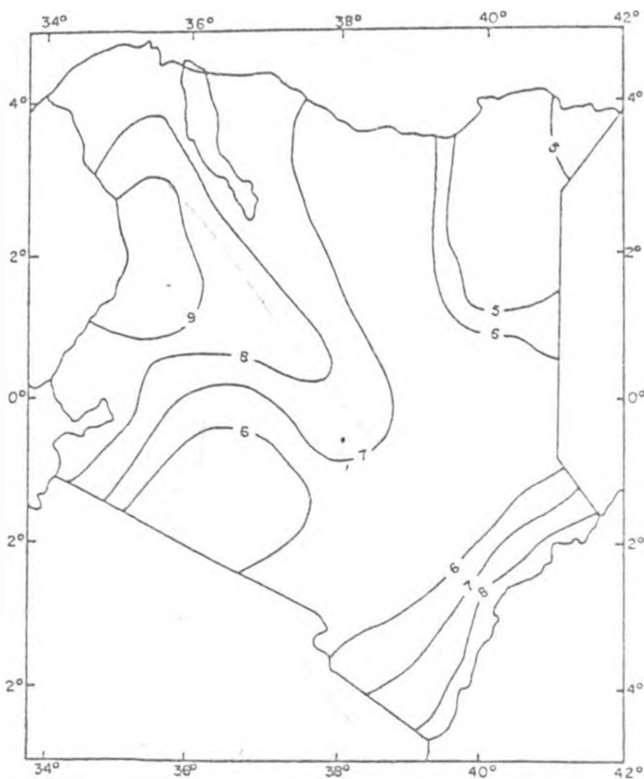
Figure 36: Surface mixing ratio for 14 April 1985 at 12 Z. Contour intervals are in units of g kg^{-1}.

to understand the low level flow field of the large-scale winds and their interaction with the local mesoscale and convective scale features. The low level flow fields will further be used to verify the low level output of the model simulations; the low level layers in the model are taken at 72 m and 122 m from the ground (or sea level) on a terrain-following coordinate surface. It may be noted that the free flow of the large-scale winds at the surface is altered by the existing roughness features (like terrain undulations, vegetation, etc.) in such a way that the measured large-scale surface wind field has a strong reflection of the local conditions prevailing in the area.

The streamline isotach analyses of the observed surface winds were performed at an interval of 3 hours, starting at 0 Z to 21 Z. Figures 37, 38, and 39 display the surface wind flow patterns at 0 Z, 03 Z, and 06 Z, respectively (that is 3:00 a.m., 6:00 a.m., and 9:00 a.m. local times, respectively). There was generally a southerly flow parallel to the coast over the eastern sector of the country at these times; the southerly flow converged with a southwesterly current along the coastal region. This southwesterly current seemed to be partly composed of the downslope winds from the eastern slopes of the Kenyan highlands coupled with the land-breeze circulation along the coast which occurred at these late

Figure 37: Surface streamline isotach analysis for 14 April 1985 at 0 Z. Wind speeds and directions are plotted in the usual international symbolic codes.
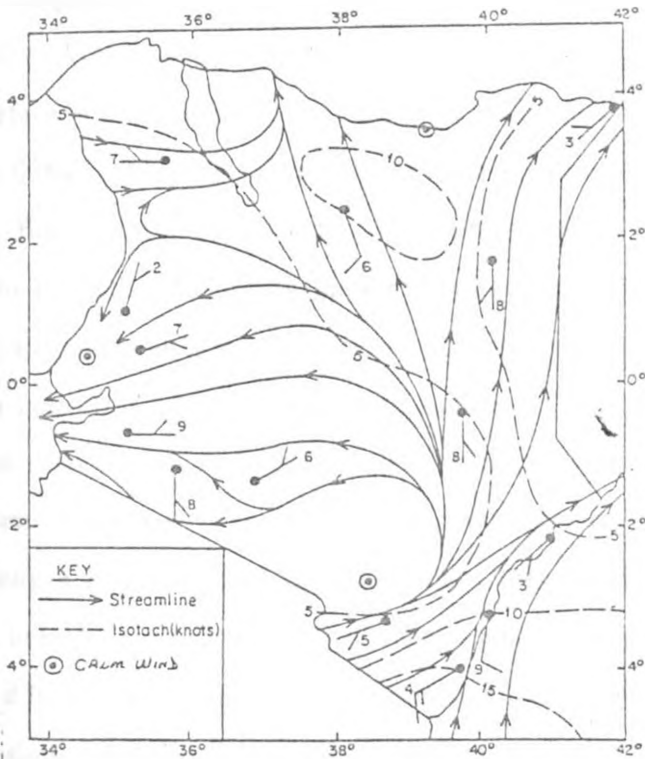
Figure 38: Surface streamline isotach analysis for 14 April 1985 at 03 Z. Wind speeds and directions are plotted in the usual international symbolic codes.
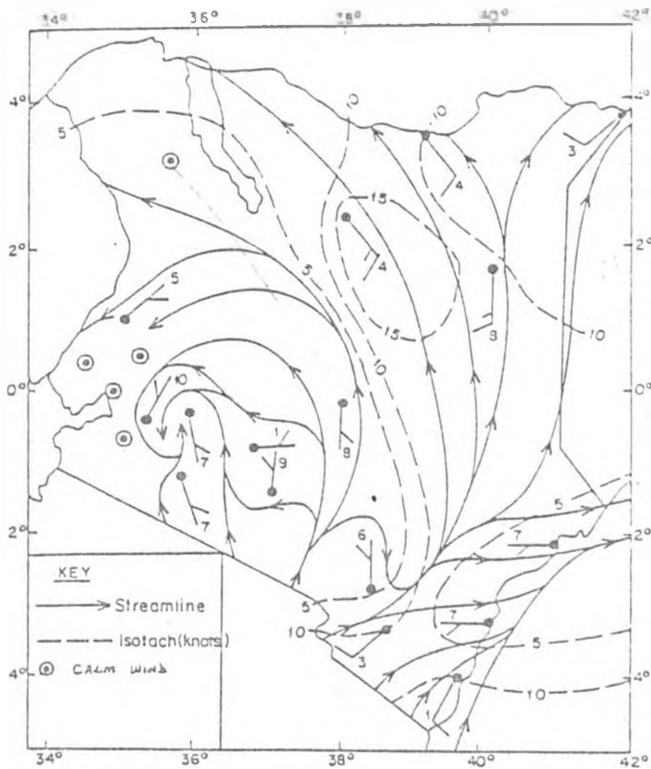
Figure 39: Surface streamline isotach analysis for 14 April 1985 at 06 Z. Wind speeds and direction are plotted in the usual international symbolic codes.

night-to-morning hours. The low level convergence at the coastal region is most evident in Figures 38 and 39.

The surface winds veered in the middle of the country to become southeasterly to easterly and flowed over the highlands to the Lake Victoria Basin on the western sector of the country. However, the winds over the western region close to Lake Victoria were seen to decrease in strength with time; being strongly easterly at 0 Z to almost calm conditions at 06 Z with a subsequent change in direction to a westerly current at 09 Z (see Figure 40). This was an indication of the influence of Lake Victoria on the local circulation pattern of the region since at 0 Z and 03 Z the large-scale synoptic easterly winds flowing into the Lake Victoria Basin were coupled with and accelerated by both the downslope winds from the Kenyan highlands and the land-to-lake breeze circulation. However, by 09 Z (Figure 40) henceforward (during the afternoon and evening hours) solar insolation and subsequent differential heating produced a strong lake-breeze circulation which coupled with the upslope winds to flow towards the Kenyan highlands to counteract the large-scale easterlies, thereby producing a convergence zone. In the surface analysis at 09 Z, the large-scale surface easterlies seemed to have been overcome by the opposing flows of
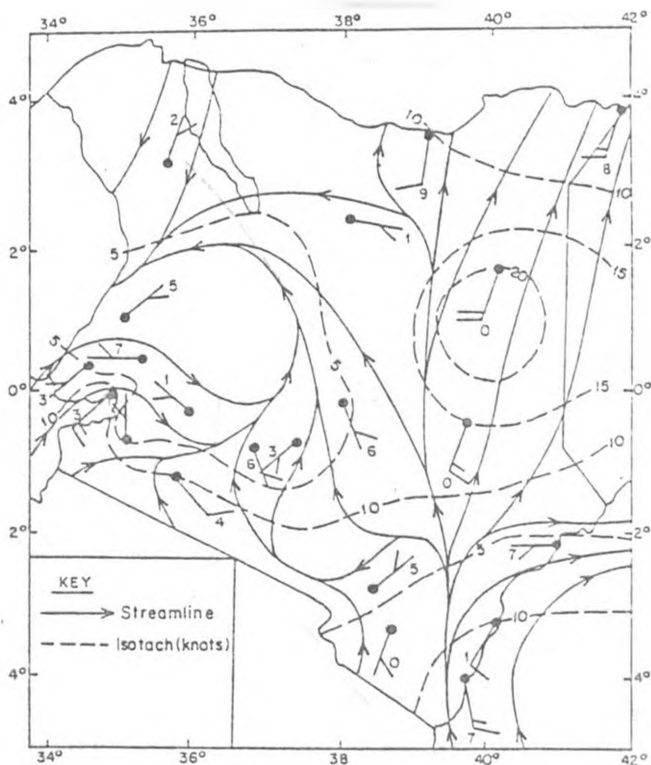
Figure 40: Surface streamline isotach analysis for 14 April 1985 at 09 Z. Wind speeds and directions are plotted in the usual international symbolic codes.

the coupled lake-breeze/upslope circulations; although one would expect the large-scale synoptic flow to be stronger than the local circulations above this surface layer and to maintain the general easterly flow pattern.

The wind flow over the northern half of the country was characterized by low level divergence in the northeastern part of the country from 0 Z, 03 Z, 06 Z, and 09 Z (see Figures 37, 38, 39, and 40) with a general confluence over the northwestern part (over the Turkana district). The diffluent flow over the northeastern part of the country decreased with time and a general confluence set in during the afternoon and early evening (Figures 41, 42, and 43) up to 18 Z with a diffluent flow setting in again over the area at 21 Z (Figure 44).

The surface winds flow patterns at 09 Z, 12 Z, and 15 Z (Figures 40, 41, and 42) depicted a fairly strong confluence zone over the Kenyan highlands. The flow patterns were indicative of the influence of orography on the low level wind circulation over the country. During the afternoon periods mentioned above, there was more solar insolation which triggered off a pressure drop over the Kenyan highlands (as compared to the low lands and large water bodies) and the subsequent temperature gradients generated upslope
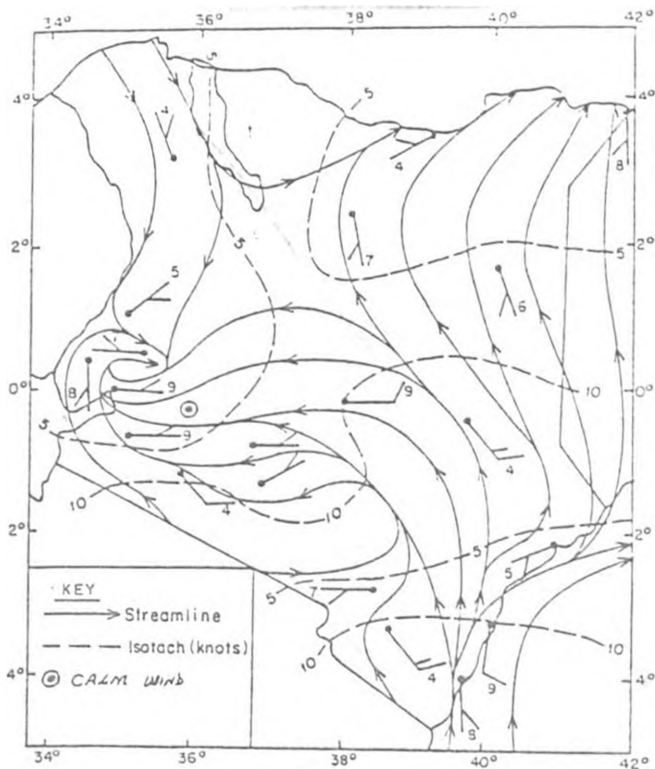
Figure 41: Surface streamline isotach analysis for 14 April 1985 at 12 Z. Wind speeds and directions are plotted in the usual international symbolic codes.
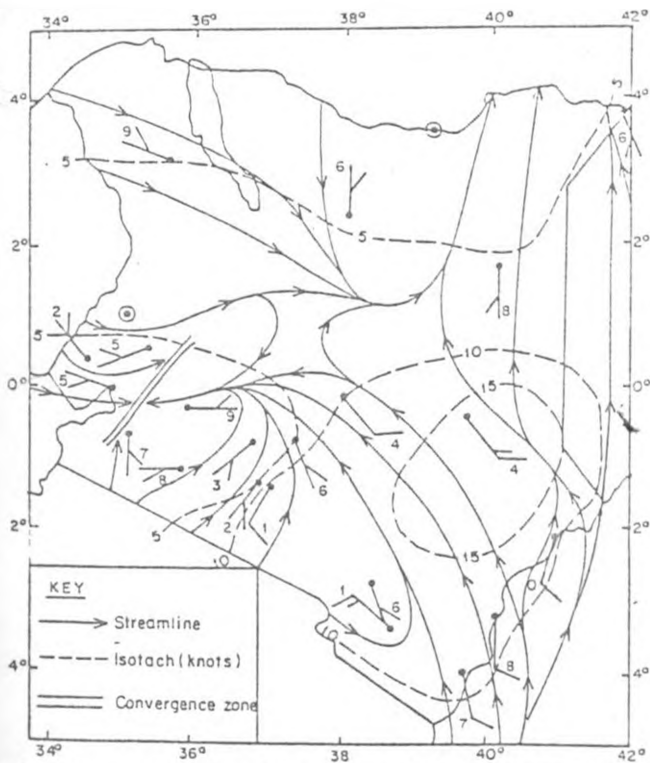
Figure 42: Surface streamline isotach analysis for 14 April 1985 at 15 Z. Wind speeds and directions are plotted in the usual international symbolic codes.

73
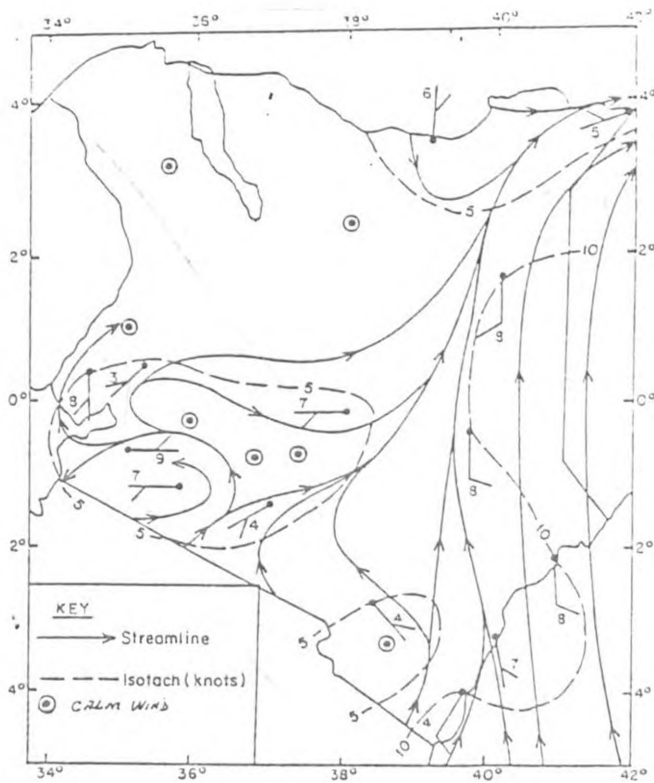
Figure 43: Surface streamline isotach analysis for 14 April 1985 at 18 Z. Wind speeds and directions are plotted in the usual international symbolic codes.
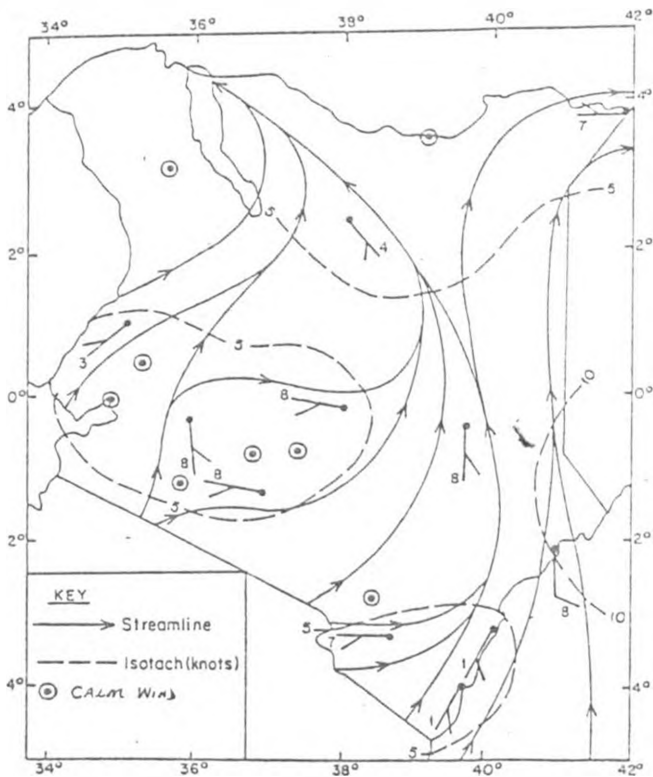
Figure 44: Surface streamline isotach analysis for 14 April 1985 at 21 Z. Wind speeds and directions are plotted in the usual international symbolic codes.

winds which coupled, on the western sector, with the lake-breeze circulation. This scenario is especially well illustrated in Figure 42 at 15 Z (6:00 p.m. local time).

Inspection of the surface wind strength showed that the winds remained generally stronger over the ocean than over the land. Nevertheless, at 0 Z wind maxima of 15 knots was experienced at the coast (see Figures 37 and 38). The situation changed at 06 Z and 09 Z when wind maximas were experienced further inland; with a wind maxima of 20 knots being experienced at 09 Z over the eastern part of the country and another maxima of 15 knots occurring during the afternoon at 15 Z inland over the northern coast (Figure 42). One generally observes that in the region of confluence there were weaker winds as compared to zones of diffluent motions.

Figures 45 and 46 show the monthly mean surface winds for April, 1985 at 06 Z and 12 Z. respectively. At 06 Z (Figure 45) there was a convergence between a southwesterly flow
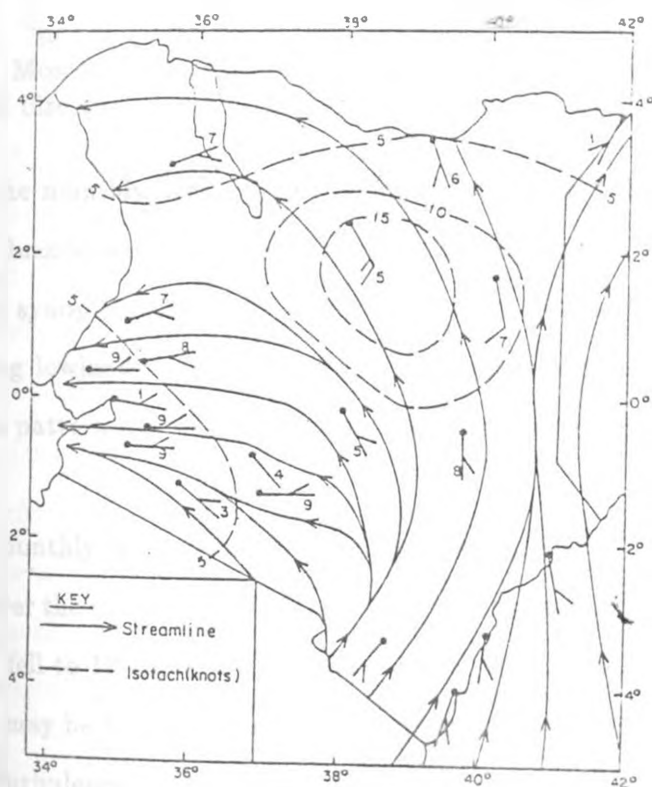
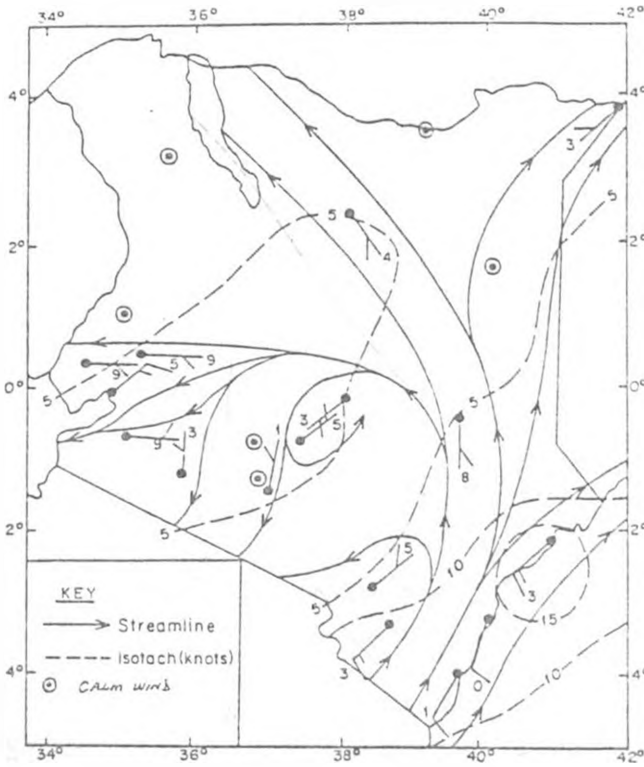Figure 45: Monthly mean surface streamline isotach analysis for April, 1985 at 06 Z. Wind speeds and directions are plotted in the usual international symbolic codes.

and a southeasterly wind current at the coast; with a diffluent flow over the northeastern part of the country. Winds flowed westwards over the Kenyan highlands and into the Lake Victoria trough region without much confluence on the eastern side of the Lake.
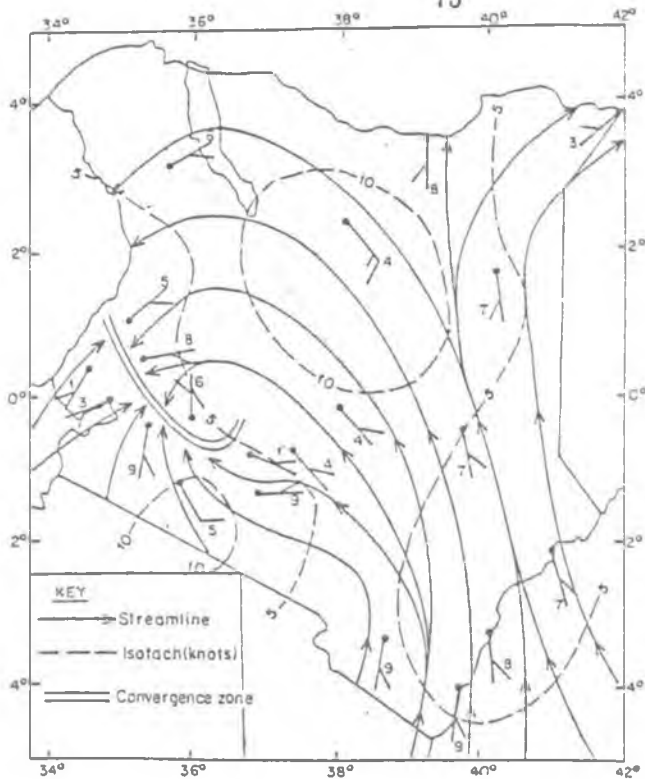
Figure 46: Monthly mean surface streamline isotach analysis for April, 1985 at 12 Z. Wind speeds and directions are plotted in the usual internation symbolic codes.

At 12 Z, the monthly-averaged winds flowed into the country from the southeast. There was a confluence zone over the Kenyan highlands; being a resultant contribution of the large-scale synoptic winds, the lake-breeze circulation and the upslope winds from the surrounding lowlands. Again, the influence of Lake Victoria and orography on the local circulation pattern was well depicted in these surface flow fields of the large-scale monsoon current.

The monthly mean wind strength for April, 1985 showed that there was an average maxima over the northern half of the country with a magnitude of 15 knots at 06 Z (Figure 45) which fell to 10 knots at 12 Z (Figure 46). This decrease in wind strength during the afternoon may be attributed to the vertical transfer of momentum (vertical mixing) which increases turbulence in the planetary boundary layer (PBL) and, together with the surface frictional drag, impedes the free flow of air in the frictional layer.

The Observed Rainfall Distribution

Figure 47 shows the 24-hour rainfall in tenths of mm which occurred over the country on the case study day. The rainfall distribution may be described as fairly widespread
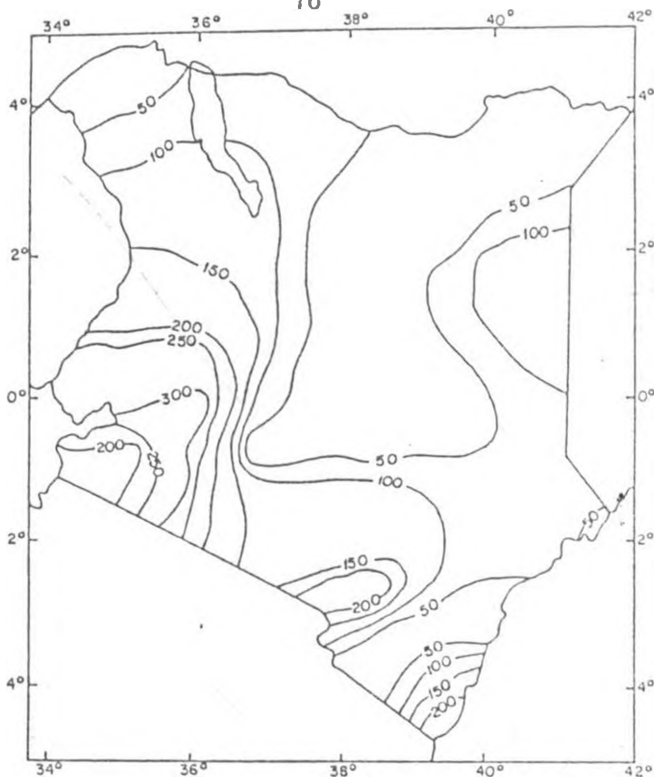
Figure 47: Rainfall over Kenya in tenths of mm for 14 April 1985.

over the whole country. As expected, the coastal region, the Kenyan highlands, and the Lake Victoria region received more rainfall than other areas over the country. It is worthy noting that on this particular day the northeastern region of the country (around Wajir) and the northwestern region of the country (around Lodwar) which are generally dry semi-arid rangelands received over 13.0 mm and over 10.0 mm of rainfall, respectively. The maximum amount of rainfall over the country was 30.0 mm experienced over the highlands and areas close to the Lake Victoria region.

Details of the results generated by the model will be discussed in the next chapter. While discussing the model-generated results, an attempt will be made to verify the model forecast products using the available observational analyses as presented and discussed above.

Chapter 6

RESULTS AND THEIR DISCUSSION

In this chapter the results from the three experiments are presented. The results from Experiments 1 and 2 involving the large-scale and the thermally-induced mesoscale simulations are discussed independently under two separate sections. Discussions of the scale-interactions between the mesoscale circulations and the prevailing large-scale monsoonal winds are also presented under a separate section. Finally, the results of the moist convection are discussed in relation to the generation of precipitation in the established convergence zones and the control of the large-scale monsoon flow on the movement and locations of these precipitating zones/convergence zones over the domain in order to generate specific diurnal patterns of weather over the country.

8.1 Results from Experiment 1: The Large-Scale Flow Fields

The output from a three-dimensional model forecast with "variable initialization" using the ECMWF data shall be discussed.

The results discussed here are for field outputs at 1600 UTC (7:00 p.m. Kenya Local Time). The model integration is started at 0 Z (00 UTC or 3:00 a.m. Kenya Local Time) and nudged with data at 12 Z. However, important features from outputs other than 1600 UTC will be discussed to clarify certain points. This is a dry simulation (Level 2, super saturation condensed; where clouds form but no precipitation occurs).

Results from the coarse grid will also be presented in this chapter (although the area of interest is Kenya); firstly, for the purpose of comparison with the more detailed fields of the finer grid mesh and secondly, for the sake of viewing and noting some features around the domain of interest (Kenya) since the coarse grid represents a bigger area. The following subsections will discuss various outputs of the model forecast from the large-scale

synoptic flow fields, namely: the wind field, the pressure field, the temperature (θ), and moisture fields. Topography of the region of study is illustrated in Figures 48 and 49.
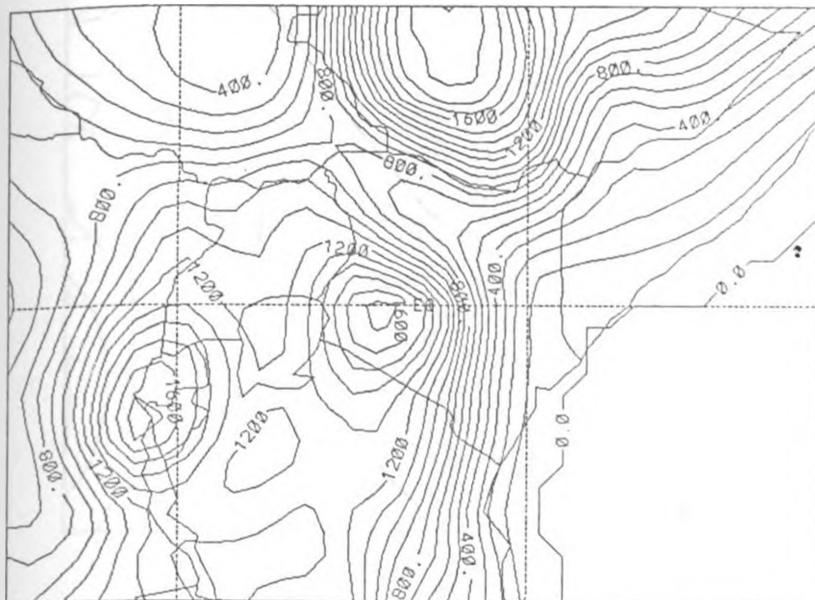
Figure 48: Topography fields interpolated from a 10-minute data set with Barnes (1973) objective analysis (coarse grid). Contour interval is 100 m.

6.1.1   The Large-Scale Wind Field

The synoptic climatology for this day (representing the "Long Rains" season of March–May with a peak in April) showed a strong southeast monsoon current at low levels ($\sigma_z = 122$ m) in Figures 50 and 51. There was a convergence of winds towards the western part of the country where winds were easterly. There was a low-level diffluent motion to the northwestern part of the country. The monsoon winds are known to emanate from the subtropical anticyclones – the "Arabian Anticyclone" in the northern hemisphere and the "Mascarene Anticyclone" in the southern hemisphere. The two anticyclones intensify and relax seasonally, thus producing a profound influence on the weather over Kenya.   They are characterized by a counter clockwise circulation (in the southern hemisphere). These circulations give rise to subsidence and low-level divergence of air masses. The Hadley circulation produces semi-permanent warm core anticyclones both on the oceans and over continents.
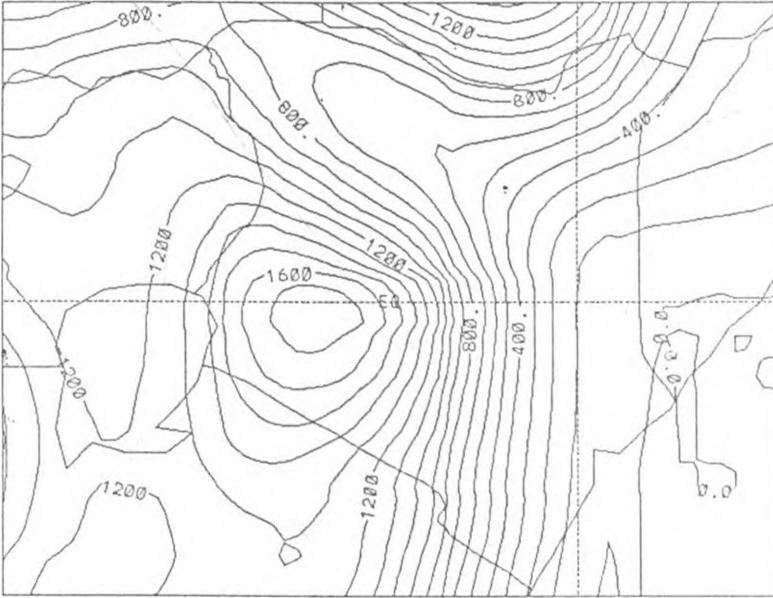
Figure 49: Topography fields interpolated from a 10-minute data set with Barnes (1973) objective analysis (fine grid). Contour interval is 100 m.
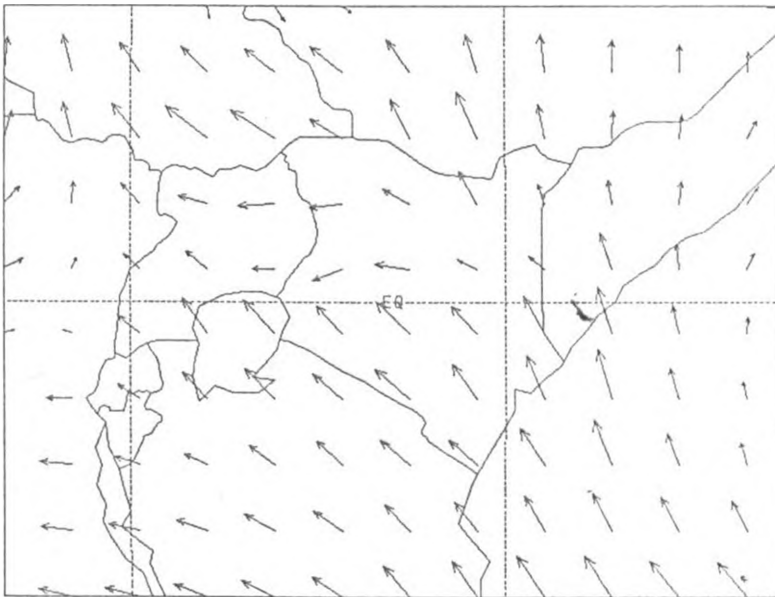
Figure 50: Wind vectors on terrain following coordinate 122 m above surface at 1600 UTC (coarse grid). Case with synoptic wind.

0 938E+01
MAXIMUM VECTOR

Figure 51: Wind vectors on terrain following coordinate 122 m above surface at 1600 UTC (fine grid). Case with synoptic wind.

During the northern hemisphere summer (July–August) the Mascarene Anticyclone intensifies while the Arabian Anticyclone weakens. The ITCZ is pushed northwards and so is the low-level convergence zone. During the equinoxes (March and September) the ITCZ is passing over this part of the continent. During the southern hemisphere summer (December–January–February) the Arabian Anticyclone intensifies while the Mascarene Anticyclone relaxes. The ITCZ moves southwards with the rainbelt. However, not all parts of central Africa exhibit this pattern.

Intensification of the "St. Helena Anticyclone" over the southern Atlantic Ocean reactivates the Congo Air Boundary (CAB) pushing it eastwards to couple with the Lake Victoria Trough to give active weather over the western parts of Kenya. This is the incursion of the Congo Airmass which causes a third peak of rainfall within a year over the western zone, especially during July–August.

In Figures 52 and 53 a convergence in the simulation occurs over Kenya between two hemispheric air masses, the northeast monsoon current (from the Arabian Anticyclone), and the southeast monsoon flow (from the Mascarene Anticyclone). This is the Inter-Tropical Convergence Zone (ITCZ). The ITCZ is a relatively narrow, low latitude zone
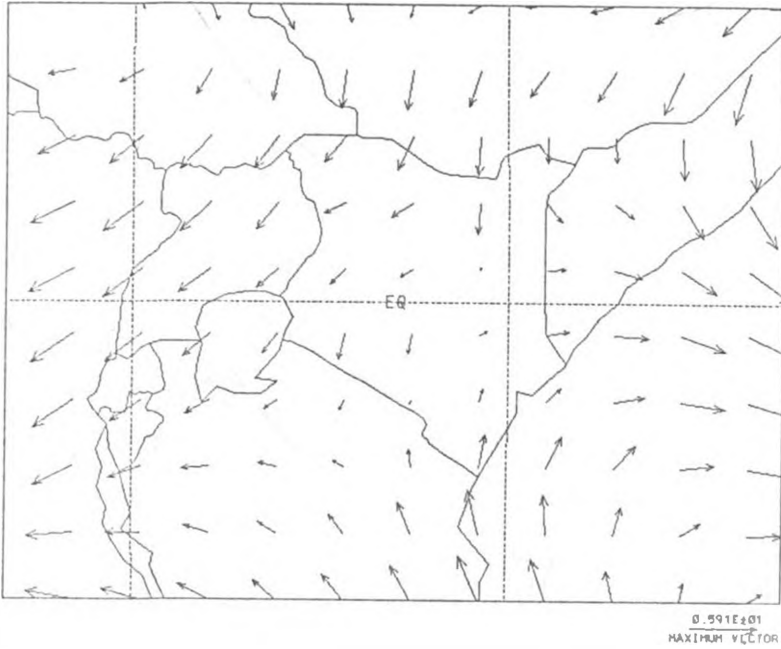
Figure 52: Wind vectors on terrain following coordinate 2.609 km above surface at 1600 UTC (coarse grid). Case with synoptic wind.
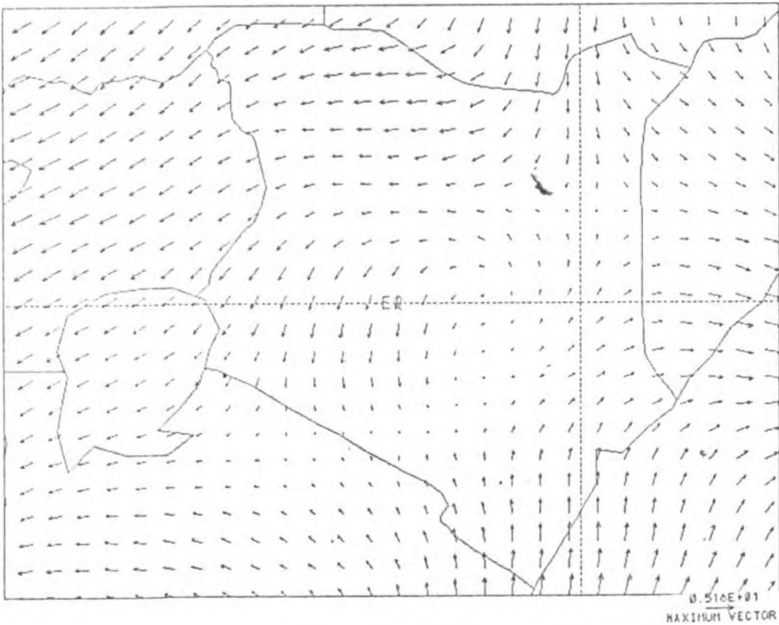
Figure 53: Wind vectors on terrain following coordinate 2.609 km above surface at 1600 UTC (fine grid). Case with synoptic wind.

in which the air originating from the two hemispheres converges at low levels. It follows the overhead sun with a time lag of two to three weeks. The essential part of the ITCZ is the instability induced by the convergence and the resultant cloud formations (as seen from infrared satellite cloud imagery) are distinctly convective and frequently in clusters, especially over land. Over central Africa the ITCZ is known to exhibit two components: the meridional and the zonal components. The meridional component forms over the Congo Air Boundary on the western part of East Africa and oscillates roughly between 25°E to 36°E longitude. It sometimes couples with the Lake Victoria Trough to produce active weather over much of western Kenya throughout the year. The zonal component of the ITCZ, on the other hand (depicted as a convergence zone of winds in Figures 52 and 53), has a diffuse front at the surface over Kenya because the high mountains in the region break up the ITCZ pattern by superimposing their own influence on this diffuse belt of convergence. The mountains together with the influence of Lake Victoria bring such modification into the flow that the seasons do not follow a classical ITCZ pattern. During this time of the year (April) the ITCZ is on its migration to the northern hemisphere and rainfall occurs as this zone of convergence traverses this region. Thus, the ITCZ is very diffuse near the surface over much of its extent in Kenya (it is absent in Figures 50 and 51 and 54 and 55 grid which are closer to the surface). However, the ITCZ appears explicitly at 2.609 km ($\approx$ 741.3 mb) above the ground. This finding is consistent with many aspects of observations, for instance, Kiangi et al. (1981).

The horizontal zonal wind (u) at 1.339 km ($\approx$ 861.2 mb) Above Mean Sea Level (AMSL) decreases over the Indian Ocean during the early hours of model integration and increases towards the northwestern part of Kenya (see Figures 56 and 57 at 0300 UTC). The zonal wind in the northwestern part of the country was seen to increase in intensity to a peak at 0800 UTC (11:00 a.m. Kenya Local Time). This can be seen in Figures 58 and 59. The zonal wind started to decrease in intensity after 1000 UTC (or 1:00 p.m. Kenya Local Time) as depicted in Figures 60 and 61. By 1600 UTC the easterly zonal wind component (dotted lines) had lost much of its strength (see Figures 62 and 63). A westerly zonal wind component now dominated over the eastern and southeastern parts of

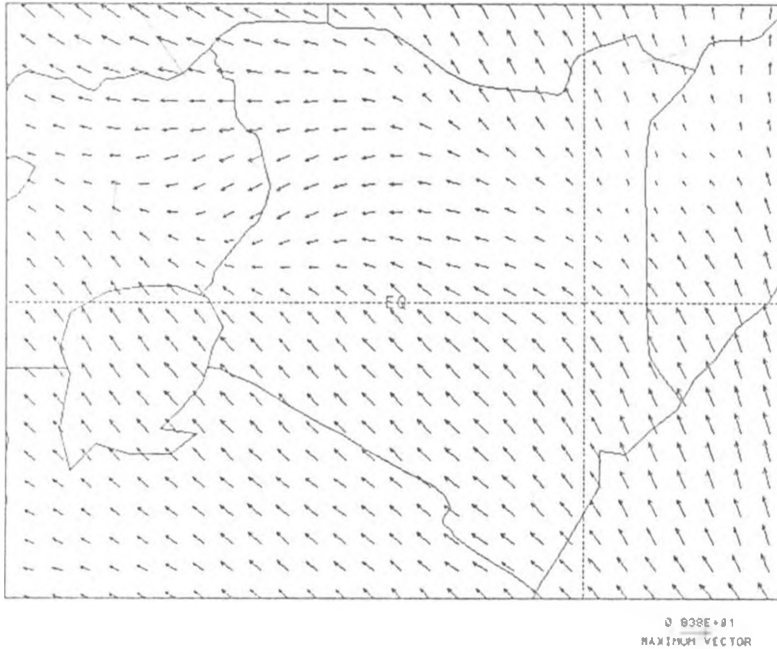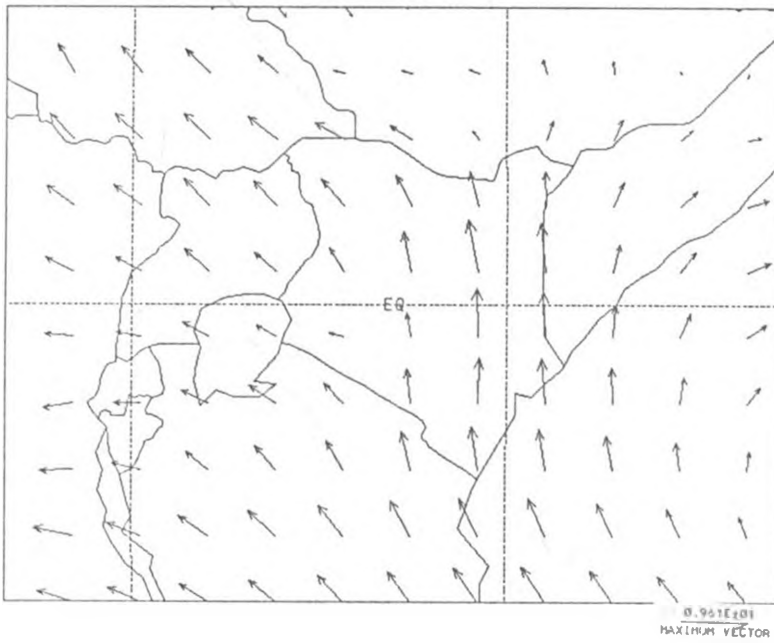Figure 54: Wind vectors on terrain following coordinate 1.339 km above surface at 1600 UTC (coarse grid). Case with synoptic wind.
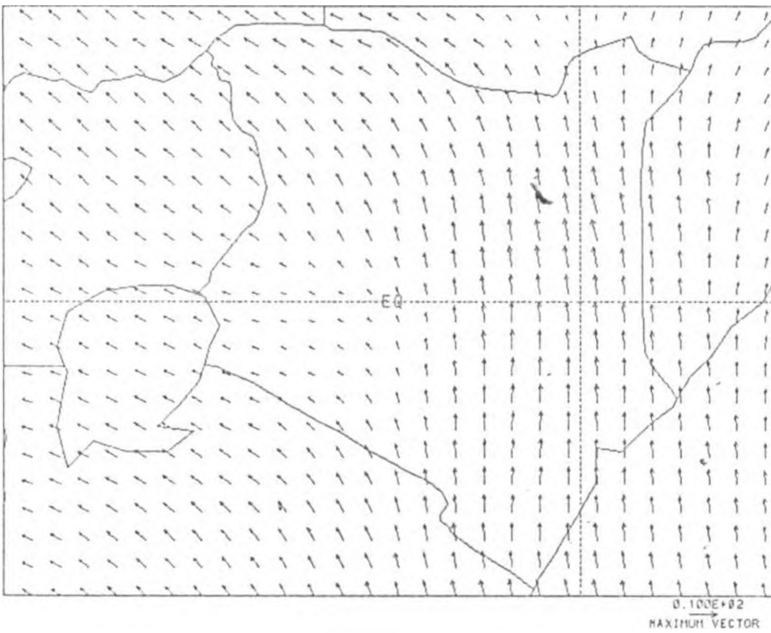
Figure 55: Wind vectors on terrain following coordinate 1.339 km above surface at 1600 UTC (fine grid). Case with synoptic wind.

Figure 56: The zonal wind field (u) on terrain following coordinate 1.339 km above surface at 0300 UTC (coarse grid). Contour interval is 0.6 m s^{-1}. Case with synoptic wind.

Figure 57: The zonal wind field (u) on terrain following coordinate 1.339 km above surface at 0300 UTC (fine grid). Contour interval is 0.3 m s^{-1}. Case with synoptic wind.

Figure 58: The zonal wind field (u) on terrain following coordinate 1.339 km above surface at 0800 UTC (coarse grid). Contour interval is 0.7 m s^{-1}. Case with synoptic wind.

Figure 59: The zonal wind field (u) on terrain following coordinate 1.339 km above surface at 0800 UTC (fine grid). Contour interval is 0.5 m s^{-1}. Case with synoptic wind.
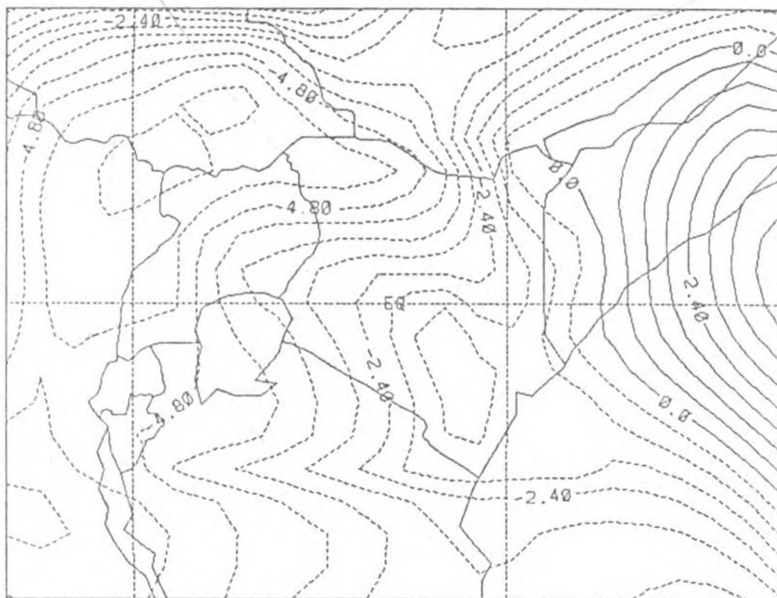
Figure 60: The zonal wind field (u) on terrain following coordinate 1.339 km above surface at 1000 UTC (coarse grid). Contour interval is 0.6 m s^{-1}. Case with synoptic wind.
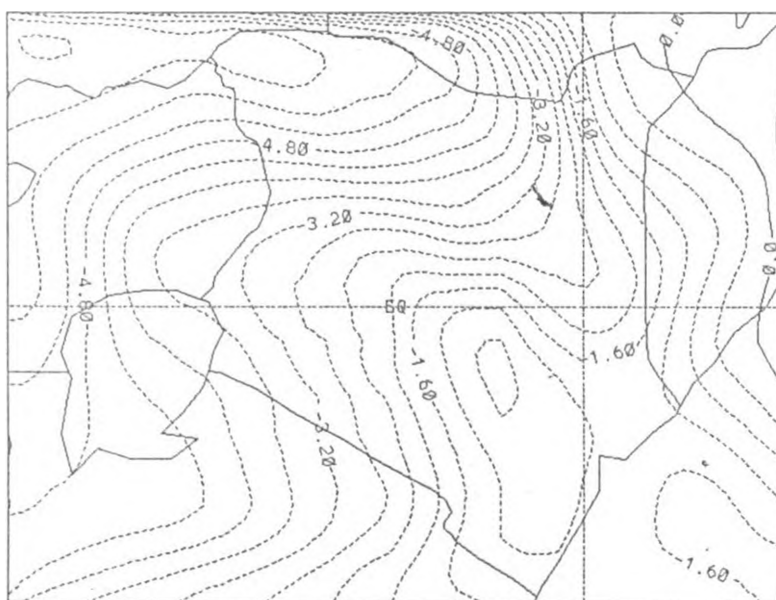
Figure 61: The zonal wind field (u) on terrain following coordinate 1.339 km above surface at 1000 UTC (fine grid). Contour interval is 0.4 m s^{-1}. Case with synoptic wind.
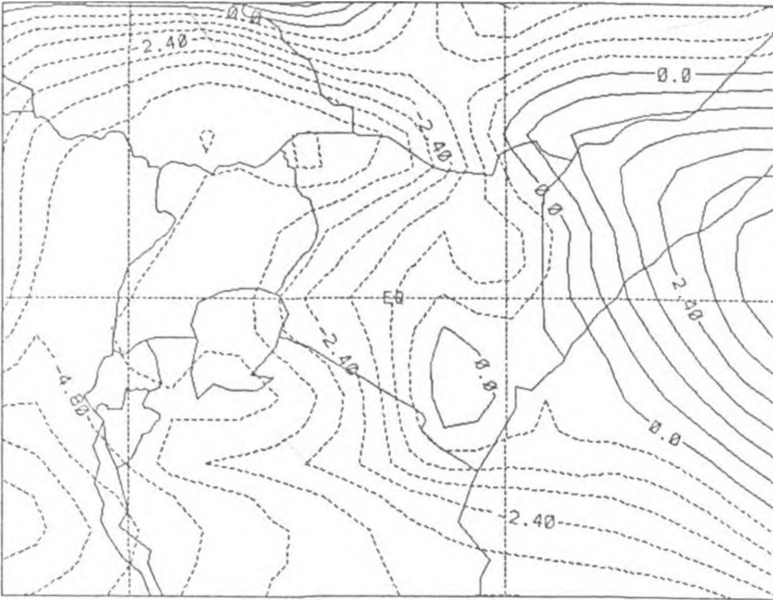
Figure 62: The zonal wind field (u) on terrain following coordinate 1.339 km above surface at 1600 UTC (coarse grid). Contour interval is 0.6 m s^{-1}. Case with synoptic wind.
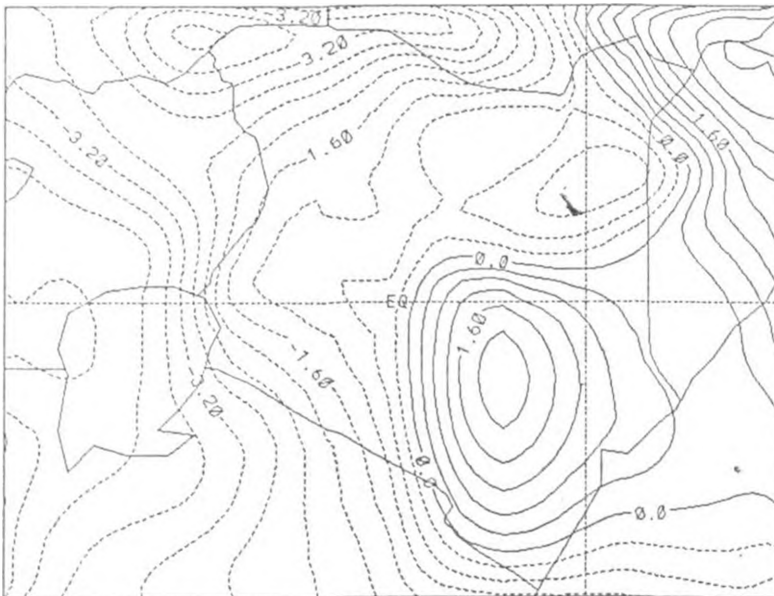
Figure 63: The zonal wind field (u) on terrain following coordinate 1.339 km above surface at 1600 UTC (fine grid). Contour interval is 0.4 m s^{-1}. Case with synoptic wind.

the domain. The decrease in the intensity of the low level wind maxima was attributed to an increase in static instability of the atmosphere (more vertical mixing) brought about by increased insolation during the afternoon hours. Thus, an eddy at the surface forced up by the surface roughness or insolation to regions of faster moving wind and momentum, upon mixing, imparts a net decrease in velocity at the upper level.

The maximum wind in the northwestern part of the country could constitute the so-called Turkana (or Marsabit) Jetstream which occurs all year round with a core at about 1.5 km AMSL. This jetstream has been studied by Asnani and Kinuthia (1979, 1980). A jetstream is a strong wind which blows at high levels, middle levels, or sometimes at lower levels of the atmosphere. The wind above, below, and on either side of the maxima are weaker. A jetstream is usually an ordinary thermal wind and is produced by the strong horizontal temperature gradients such as at fronts. Jetstreams also form through the channeling effect in narrow gaps between mountain chains or highlands. The Turkana Jetstream is due to the channeling effect triggered off by the orientation of the terrain which forms a corridor in this locality between the Kenyan Highlands to the south and the Ethiopian Highlands to the north (see the topography in Figures 48 and 49).

The meridional flow (v) becomes stronger over the Indian Ocean than over land during the initial hours of the model simulation. The wind component decreases in intensity during the afternoon more over land than over the ocean. This decrease over land may be due to a combination of turbulence brought about by more frictional stress offered by the terrain roughness as compared to the ocean and also by enhanced vertical mixing which develop during the day and is more over land than over water. A jet core appears ($\approx$ 16.8 m s^{-1}) over the southern coast of Kenya (see Figures 64 and 65) in the first hour of model integration. The core moved northwards with time, first along the coast and then inland over the eastern part of Kenya and, also decreases in speed during the day, probably due to the convective mixing (see maximum speeds in Figures 66 and 67). The decrease in speed was seen to begin at 10:00 a.m. Kenyan Local Time. In Figures 68 and 69 the meridional wind maxima is evident over the eastern part of Kenya (over Garissa) where it remained stationary for a long time in the course of the simulation. The meridional
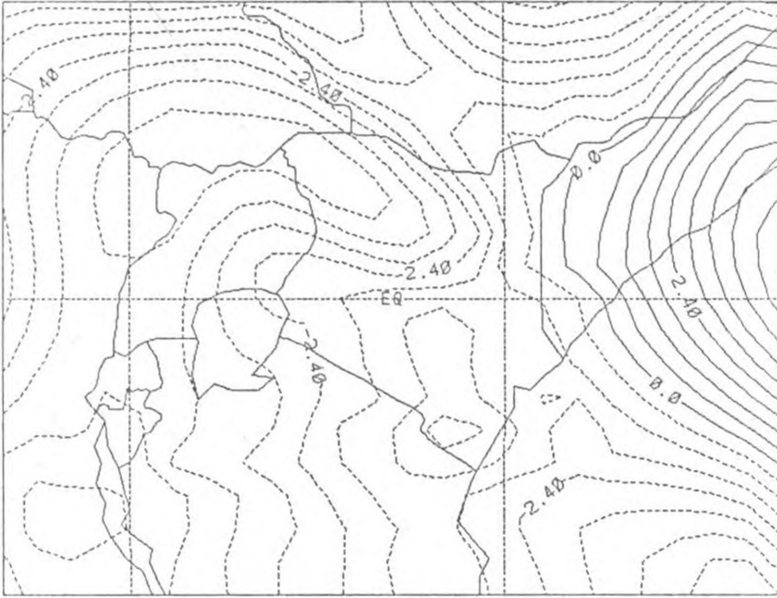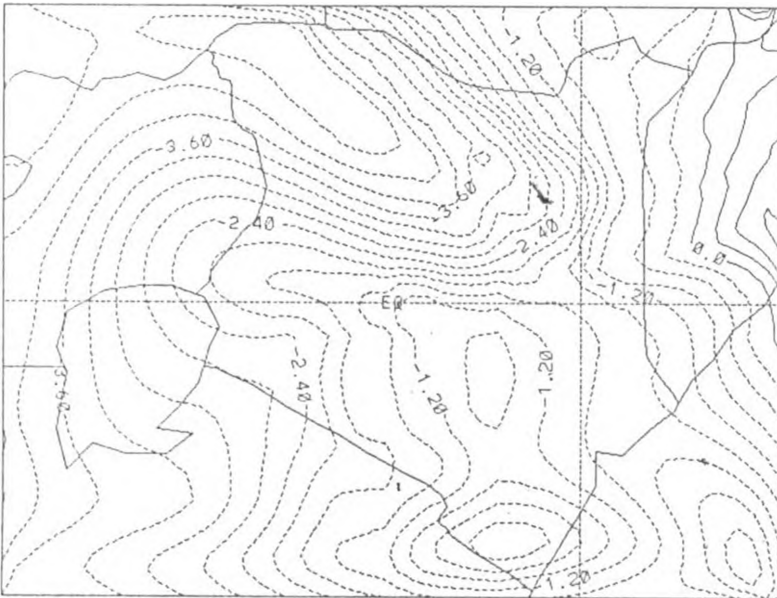
Figure 64: The meridional wind field (v) on terrain following coordinate 1.339 km above surface at 0100 UTC. Contour interval is 0.60 m s^{-1}. Case with synoptic wind.
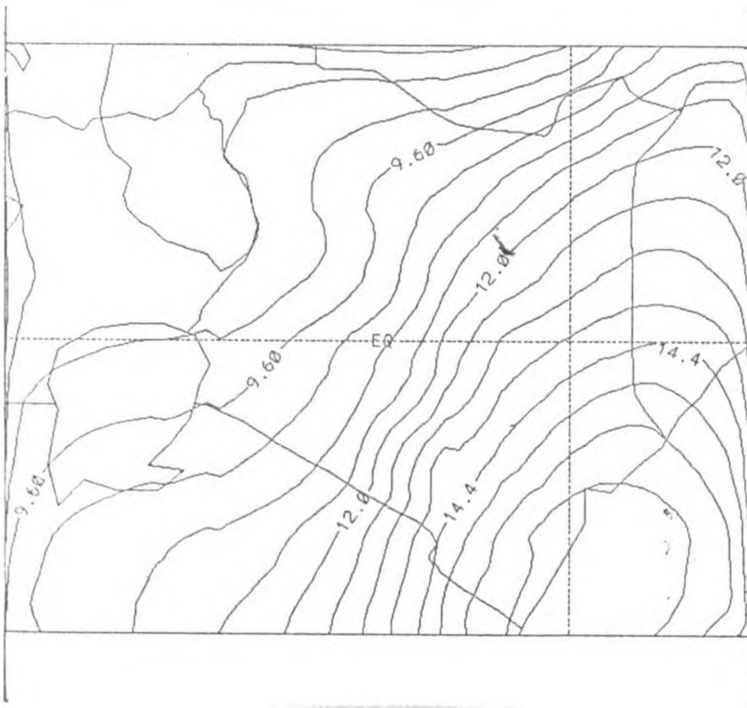
Figure 65: The meridional wind field (v) on terrain following coordinate 1.339 km above surface at 0100 UTC. Contour interval is 0.60 m s^{-1}. Case with synoptic wind.
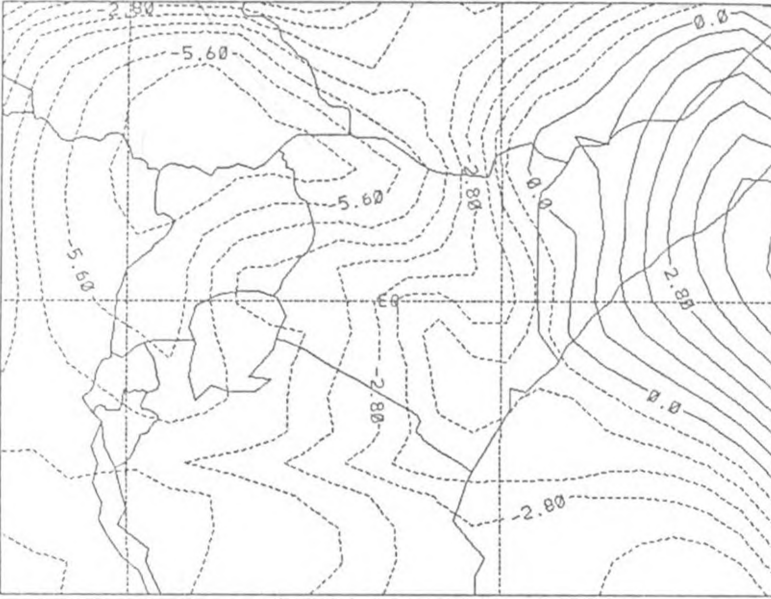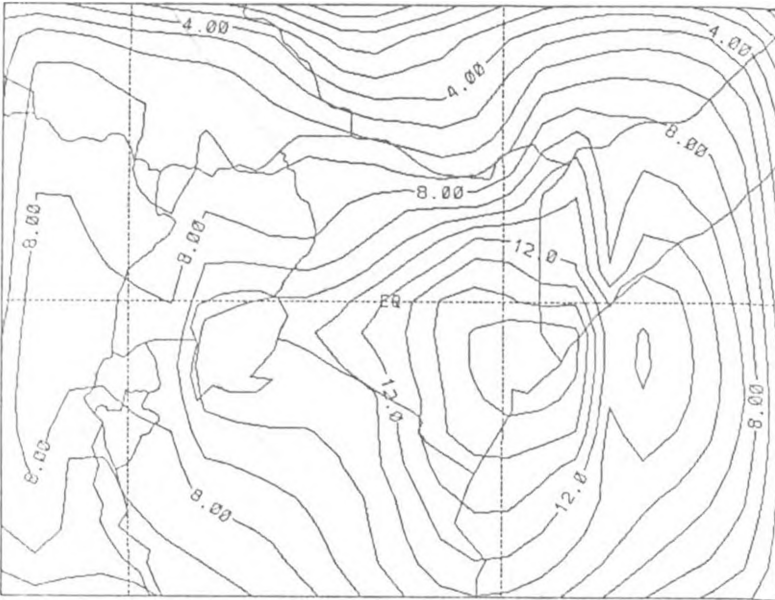
Figure 66: Meridional wind field (v) at 0300 UTC on terrain following coordinate 1.339 km above surface (coarse grid). Contour interval is 1.0 m s^{-1}. Case with synoptic wind.
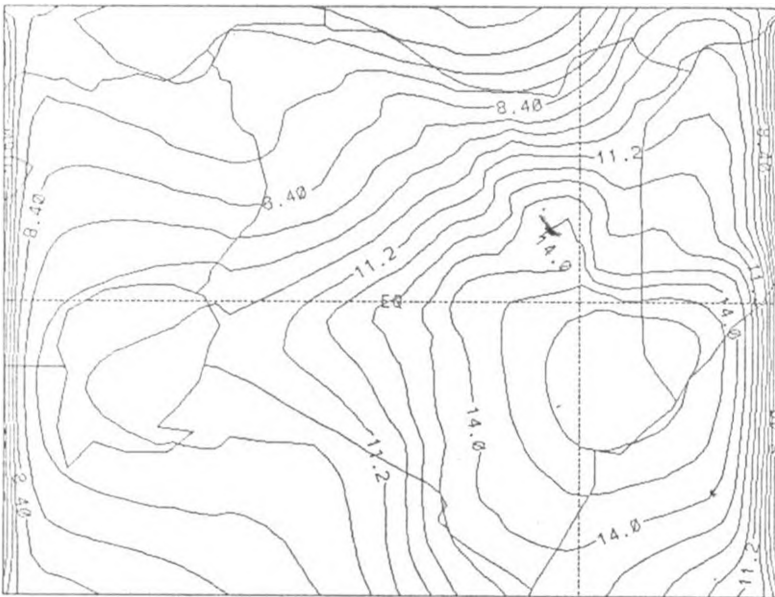
Figure 67: Meridional wind field (v) at 0300 UTC on terrain following coordinate 1.339 km above surface (fine grid). Contour interval is 0.7 m s^{-1}. Case with synoptic wind.
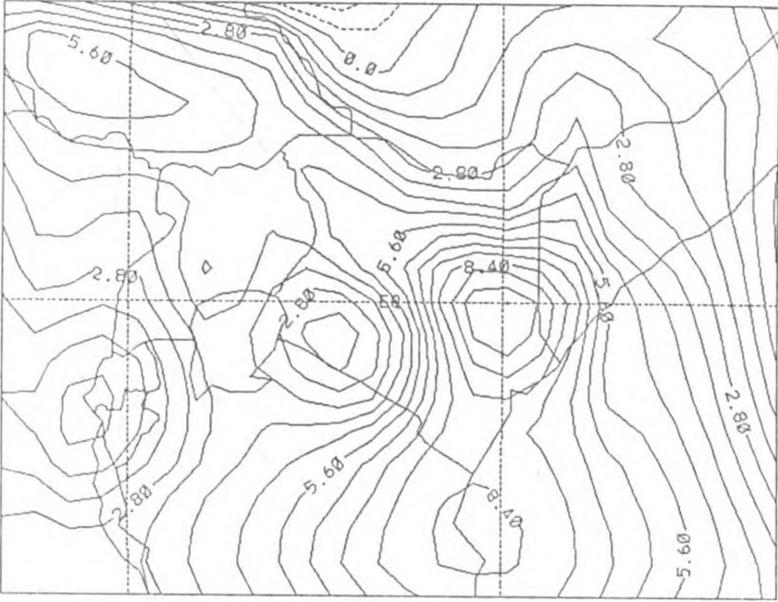
Figure 68: Meridional wind field (v) on terrain following coordinate 1.339 km above surface at 1000 UTC (coarse grid). Contour interval is 0.7 m s^{-1}. Case with synoptic wind.
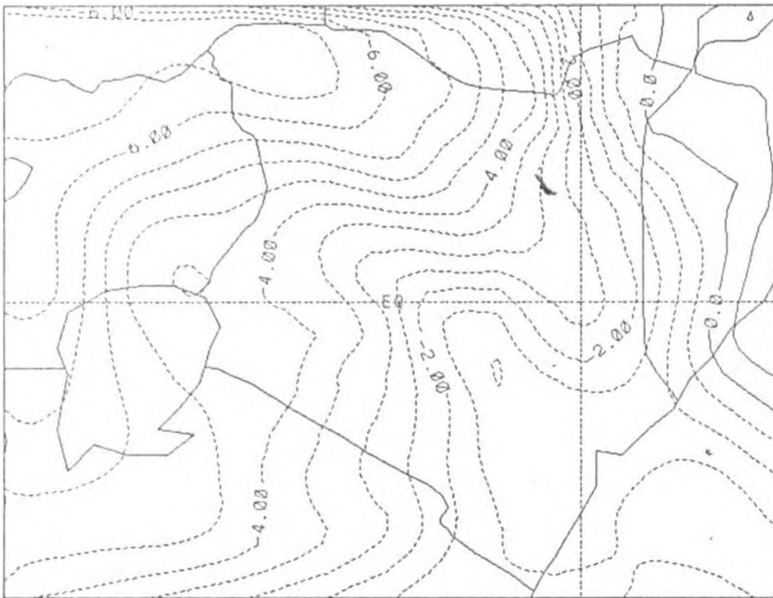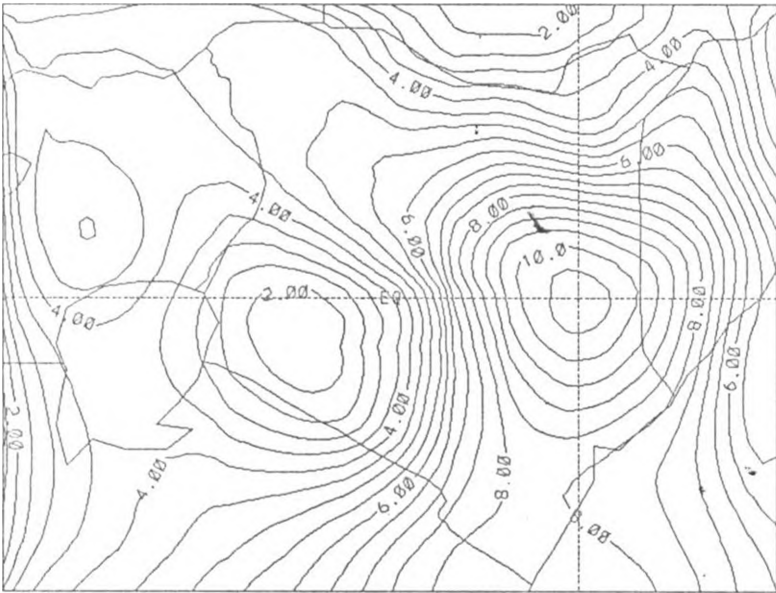

Figure 69: Meridional wind field (v) on terrain following coordinate 1.339 km above surface at 1000 UTC (fine grid). Contour interval is 0.5 m s^{-1}. Case with synoptic wind.

wind maxima was still present in Figures 70 and 71 at 1600 UTC (7:00 p.m. Kenya Local Time).
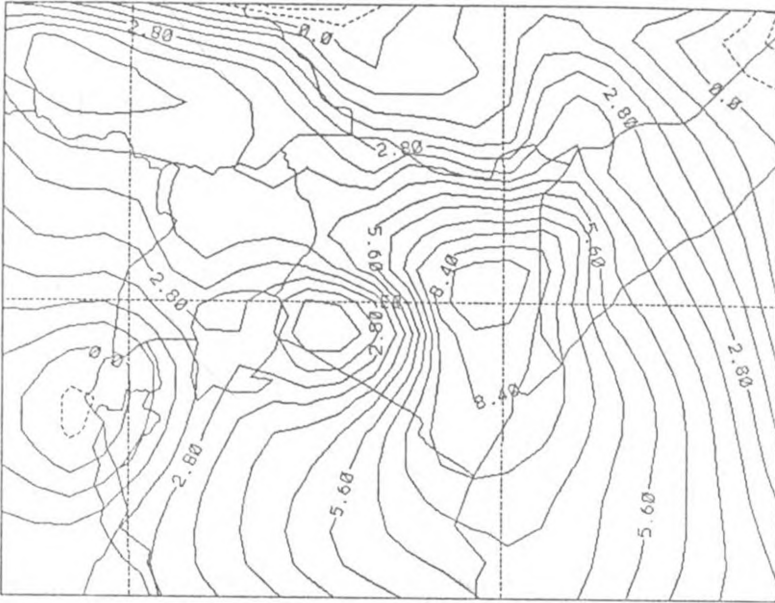
Figure 70: Meridional wind field (v) on terrain following coordinate 1.339 km above surface at 1600 UTC (coarse grid). Contour interval is 0.7 m s^{-1}. Case with synoptic wind.
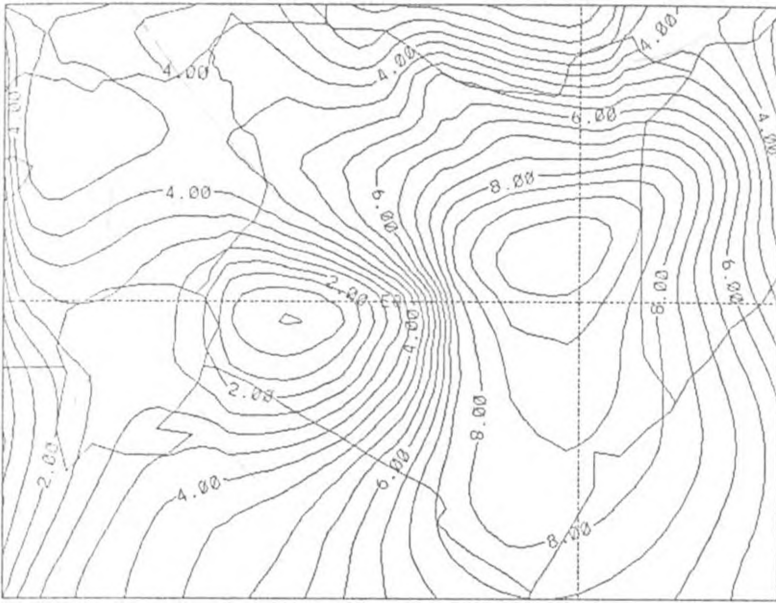
Figure 71: Meridional wind field (v) on terrain following coordinate 1.339 km above surface at 1600 UTC (fine grid). Contour interval is 0.5 m s^{-1}. Case with synoptic wind.

At 2000 UTC the wind maxima has shifted northwards and displaced slightly inland to the west (see Figure 72).

The meridional wind maxima could be the East African Low-Level Jetstream (EALLJ) which flows at about 1.5 km AMSL at the Kenyan coast and is reputed to have a core over the town of Garissa. It has been studied by Findlater (1966, 1967, 1968, 1969), Ngara (1978), Asnani and Ngara (1978), among others. It produces a secondary peak of rainfall at the coast in July–August when its intensity is at a maximum. It starts building up in the months of April and May, acquires a maximum intensity in July–August and breaks down in October. The jet has strong instabilities due to its horizontal and vertical wind shears which alter weather at the coast during the period when its intensity is high. This cross-equatorial jetstream also transfers moisture and momentum from the southern hemisphere to the northern hemisphere. The jet occurs only during the northern hemisphere summer.

There were dramatic features in the wind field from the surface to the model top (at 23 km AMSL). In Figures 50, 51, 54, and 55 at 122 m and 1.34 km AMSL, respectively,
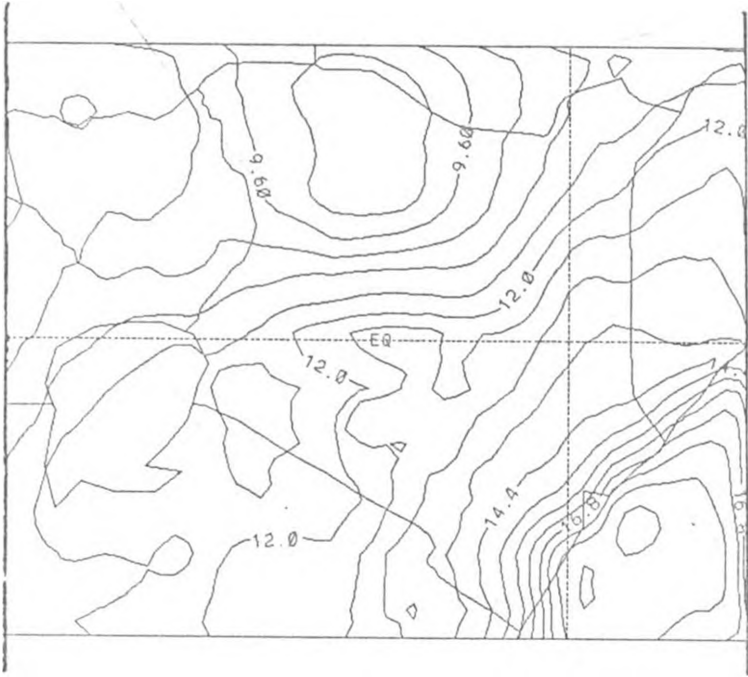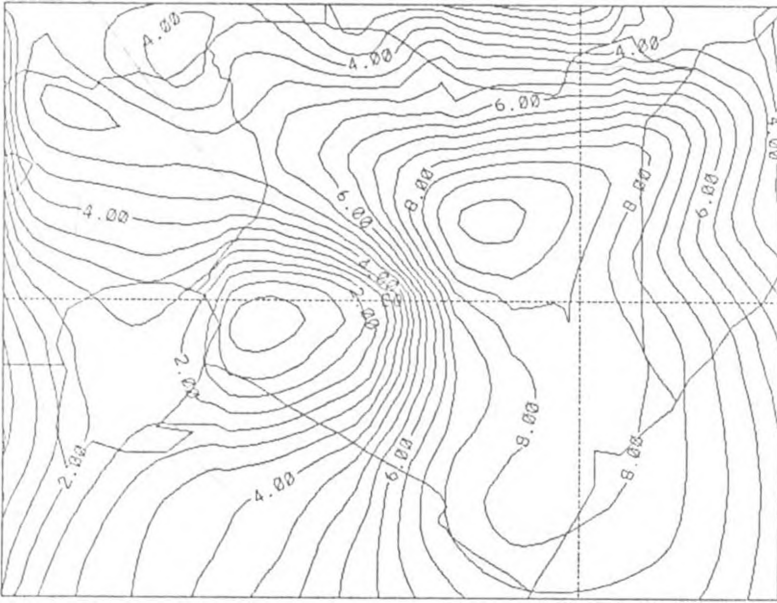
Figure 72: Meridional wind field (v) on terrain following coordinate 1.339 km above surface at 2000 UTC. Contour interval is 0.5 m s^{-1}. Case with synoptic wind.

strong southeasterly winds were depicted. At 5.729 km ($\approx$505 mb) AMSL there was a complete reversal of winds. That is, during the early hours of the model integration, winds were almost westerly (see Figures 73 and 74 at 0300 UTC). These winds reversed in direction to become northwesterly (see Figures 75 and 76) six hours into the simulation. At 1600 UTC (see Figures 77 and 78) the winds had a strong northerly component over Kenya; this direction was maintained in the subsequent hours of the model simulation.

At 10.4 km ($\approx$267 mb) AMSL the strong southeasterly winds, over most parts of Kenya, converged with an almost equally strong northwesterly current. This confluence occurred over the northwestern and northern part of the model domain, creating a "neutral" area over this region with the two air masses merging to give rise to northerly and southwesterly currents over the study domain (see Figures 79 and 80 at 0600 UTC). At 0900 UTC, the easterlies pushed the westerly winds out of Kenya towards the west (see Figures 81 and 82 representing the coarse and fine grids, respectively). By 1600 UTC the contest is won by the easterly wind regime which then dominated most parts of the model domain (see Figures 83 and 84). At 17.44 km ($\approx$86.3 mb) AMSL the winds were strong easterlies (see Figures 85 and 86 at 1600 UTC).
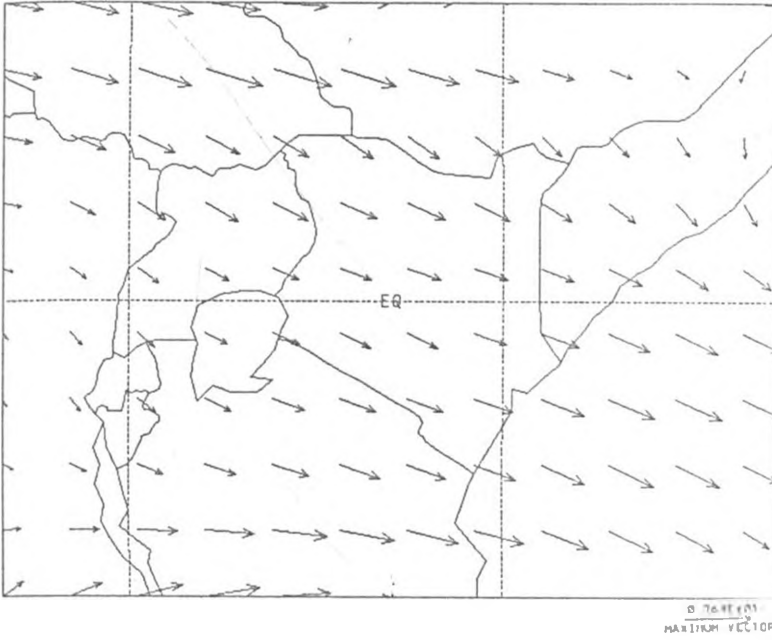
Figure 73: The wind vectors on terrain following coordinate 5.73 km above surface at 0300 UTC (coarse grid). Case with synoptic wind.
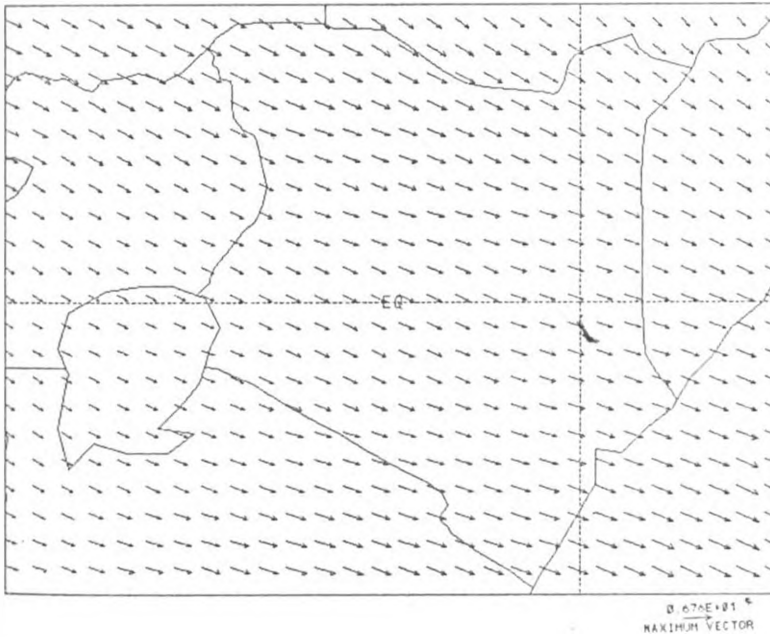
Figure 74: The wind vectors on terrain following coordinate 5.73 km above surface at 0300 UTC (fine grid). Case with synoptic wind.
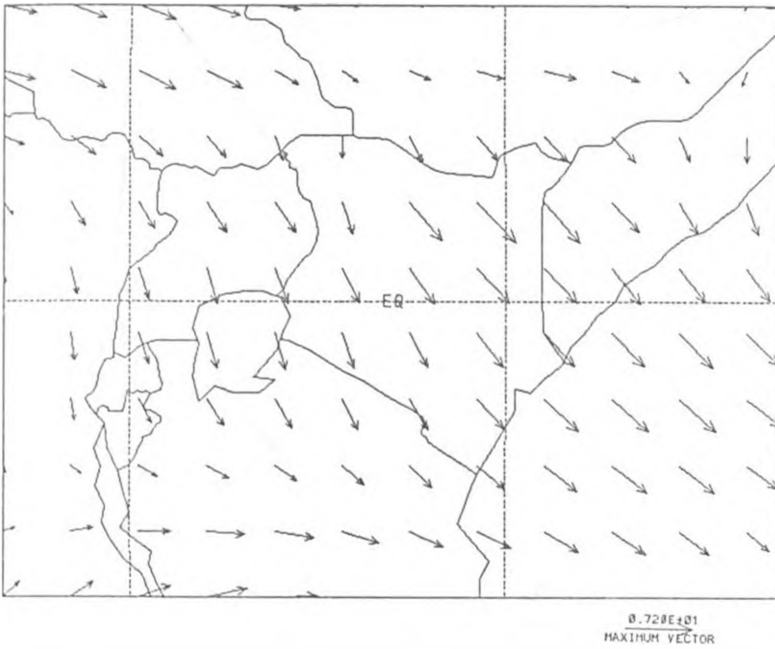
Figure 75: The wind vectors on terrain following coordinate 5.73 km above surface at 0600 UTC (coarse grid). Case with synoptic wind.
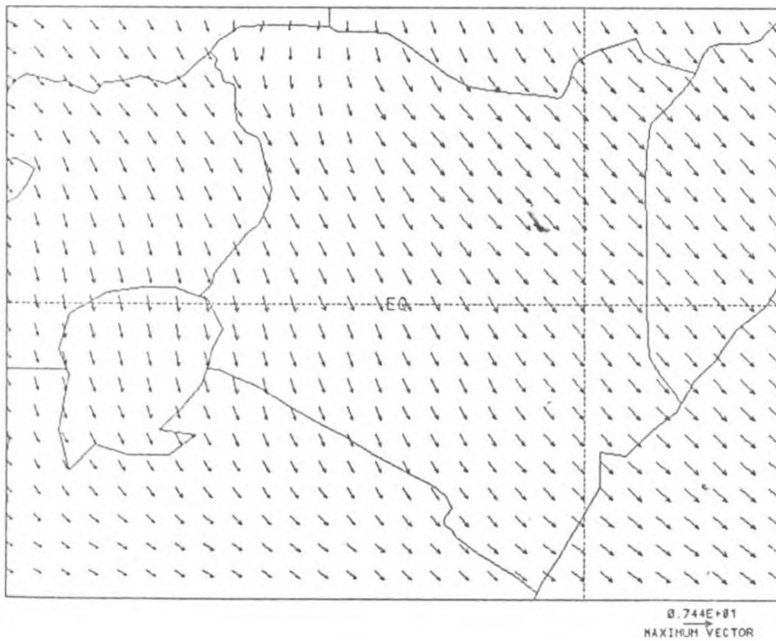
Figure 76: The wind vectors on terrain following coordinate 5.73 km above surface at 0600 UTC (fine grid). Case with synoptic wind.
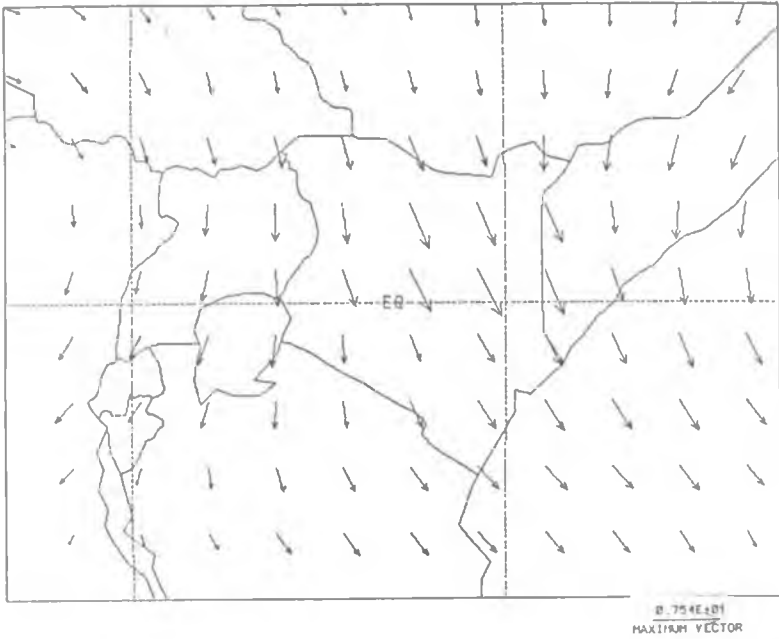
Figure 77: The wind vectors on terrain following coordinate 5.73 km above surface at 1600 UTC (coarse grid). Case with synoptic wind.
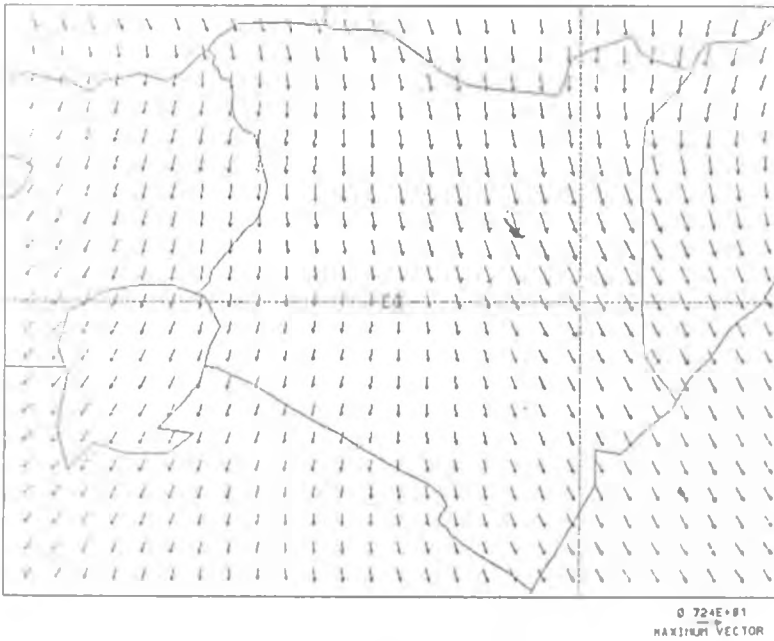
Figure 78: The wind vectors on terrain following coordinate 5.73 km above surface at 1600 UTC (fine grid). Case with synoptic wind.
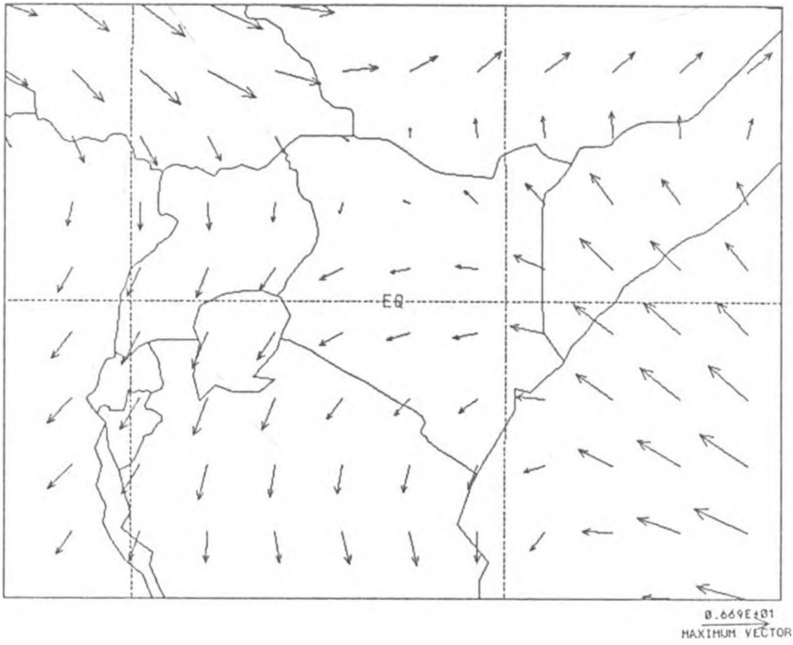
Figure 79: The wind vectors on terrain following coordinate 10.44 km above surface at 0600 UTC (coarse grid). Case with synoptic wind.
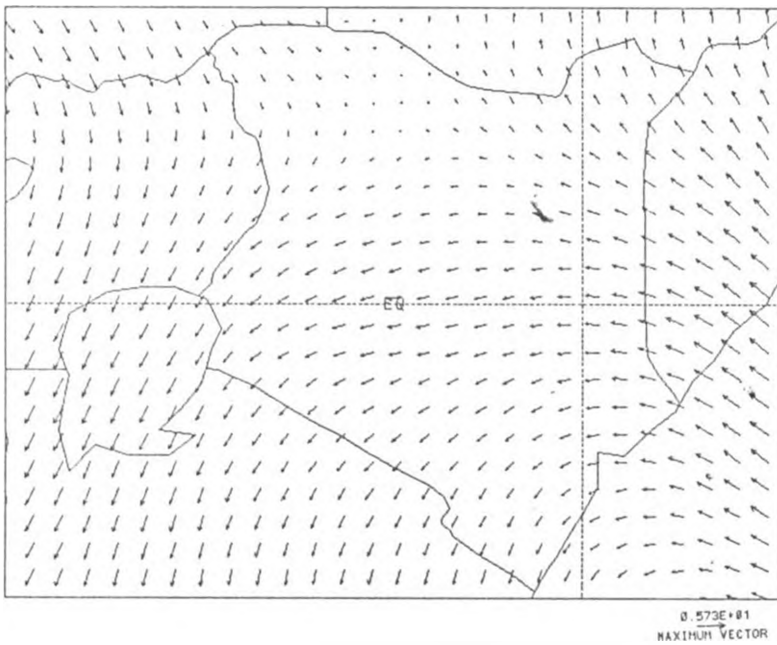
Figure 80: The wind vectors on terrain following coordinate 10.44 km above surface at 0600 UTC (fine grid). Case with synoptic wind.

0.733E+01
MAXIMUM VECTOR
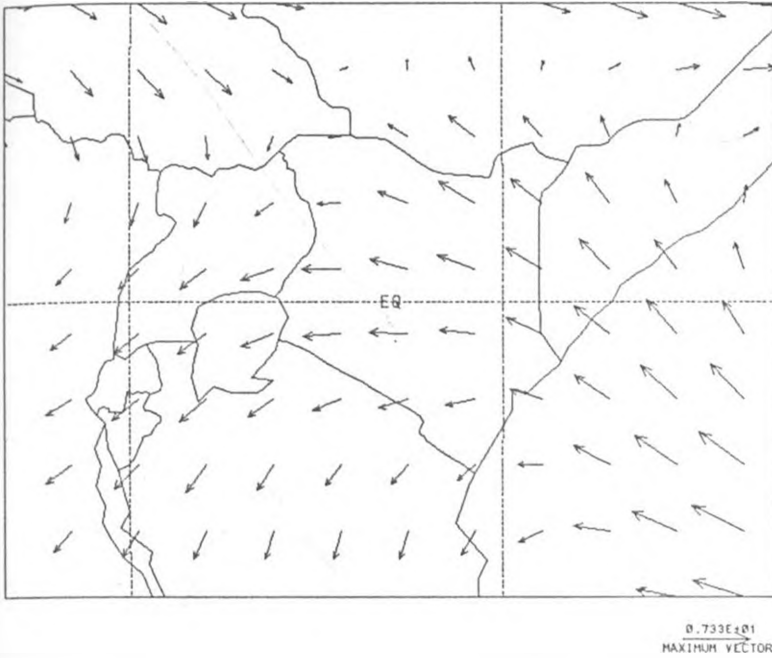
Figure 81: The wind vectors on terrain following coordinate 10.44 km above surface at 0900 UTC (coarse grid). Case with synoptic wind.

0.591E+01
MAXIMUM VECTOR
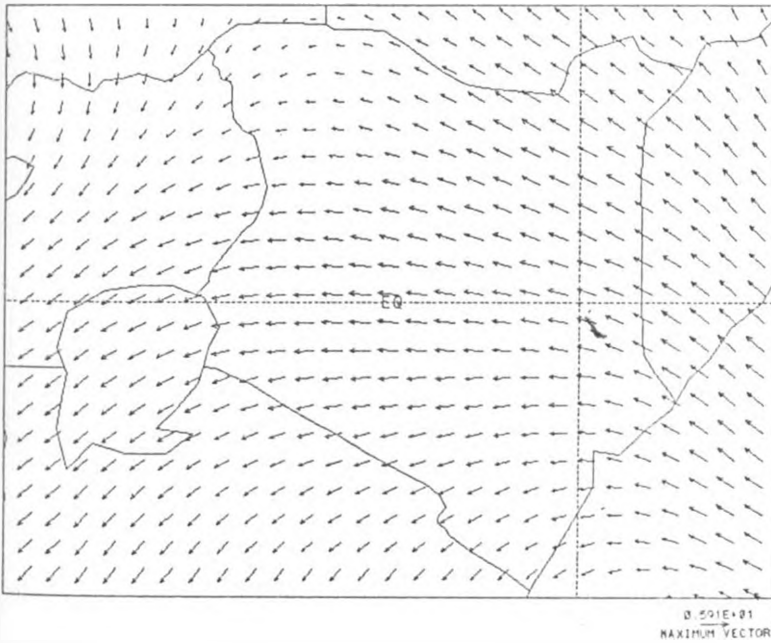
Figure 82: The wind vectors on terrain following coordinate 10.44 km above surface at 0900 UTC (fine grid). Case with synoptic wind.

0.122E+02
MAXIMUM VECTOR
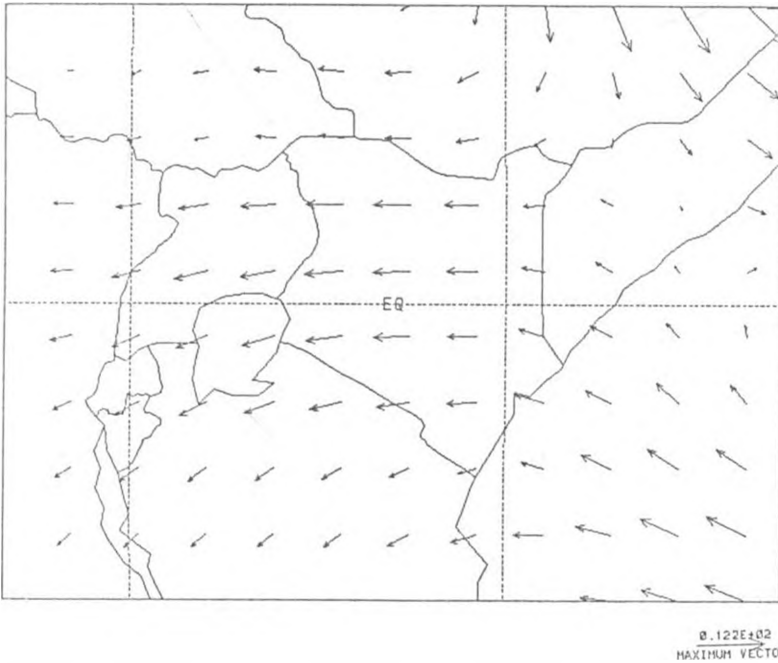
Figure 83: The wind vectors on terrain following coordinate 10.44 km above surface at 1600 UTC (coarse grid). Case with synoptic wind.

0.782E+01
MAXIMUM VECTOR
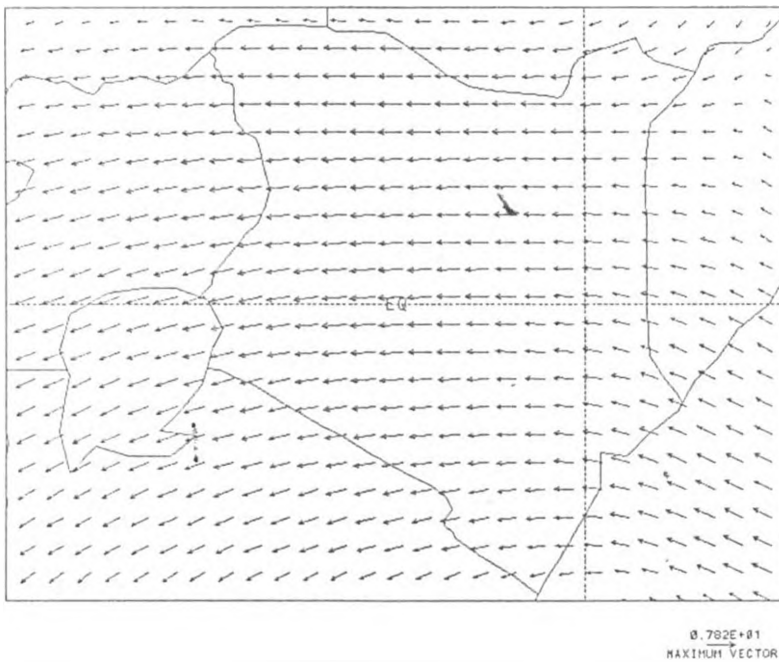
Figure 84: The wind vectors on terrain following coordinate 10.44 km above surface at 1600 UTC (fine grid). Case with synoptic wind.
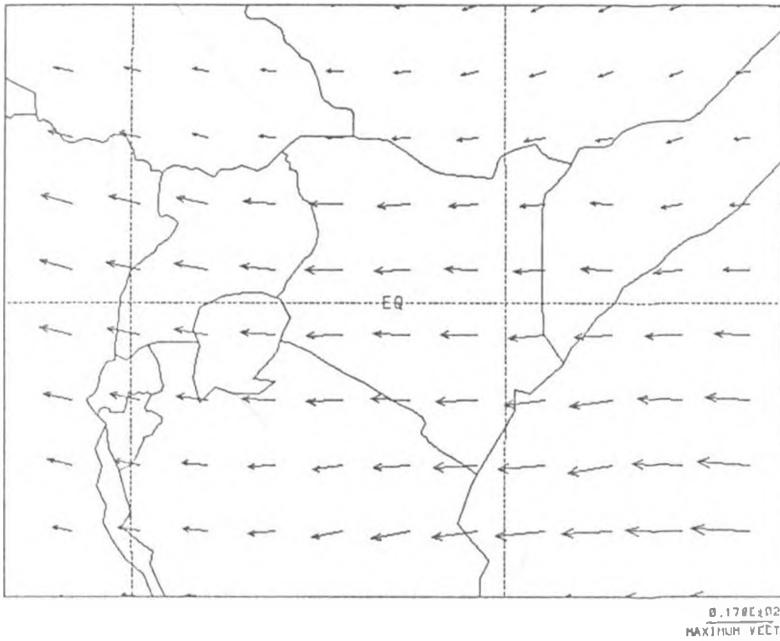
Figure 85: The wind vectors on terrain following coordinate 17.44 km above surface at 1600 UTC (coarse grid). Case with synoptic wind.
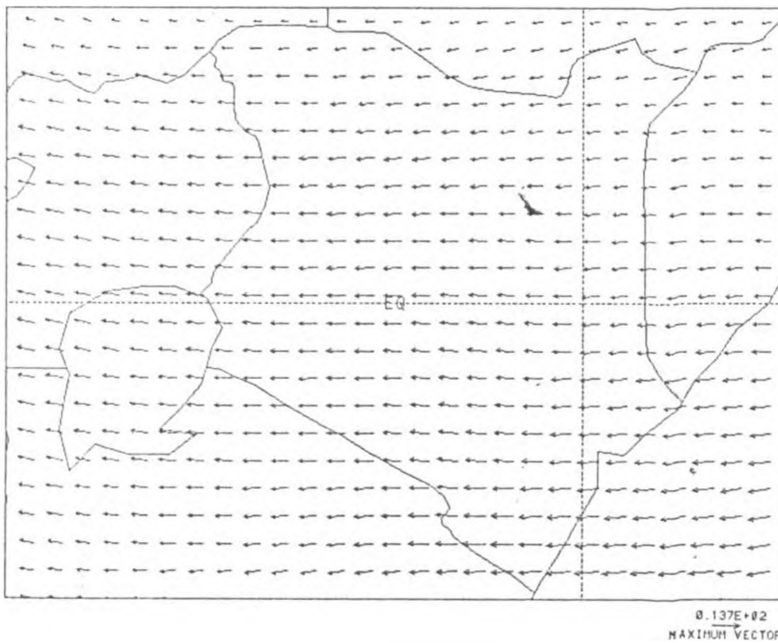
Figure 86: The wind vectors on terrain following coordinate 17.44 km above surface at 1600 UTC (fine grid). Case with synoptic wind.

In Figure 87 which is a vertical east-west cross-section (50 km south of the equator) linking Lake Victoria and the Indian Ocean, one can easily observe that the monsoon winds (low-level easterlies) were very shallow in depth over Kenya; about 4 km in depth across the domain on average – and deeper on the west side of the domain than to the east and over the ocean. Westerly winds occupied the middle levels of the atmosphere over the
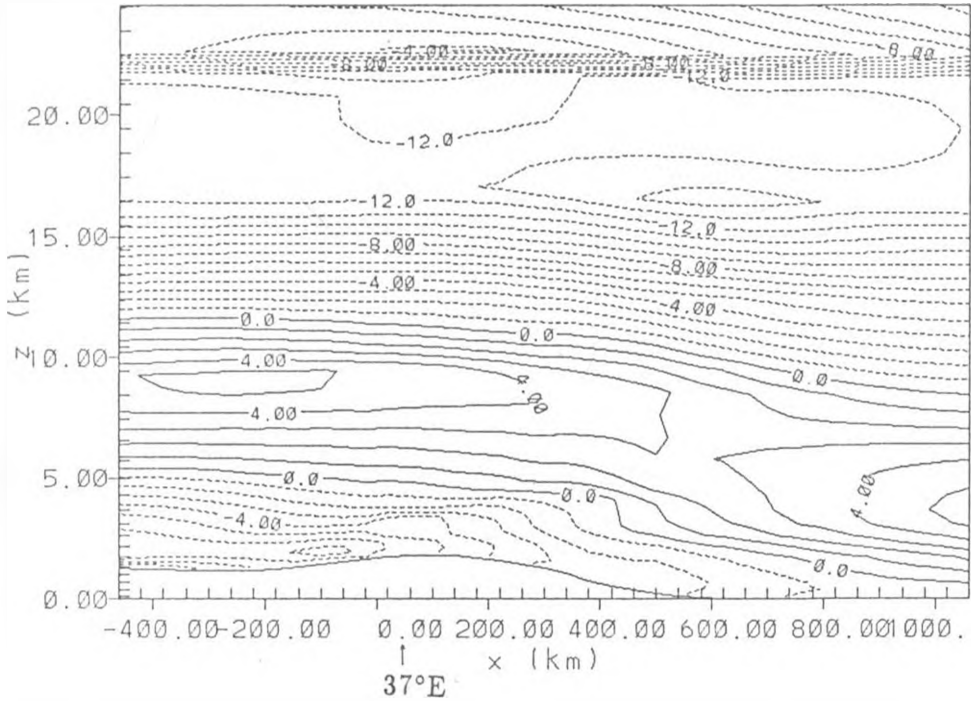
Figure 87: Vertical east-west cross-section of zonal wind (u) at 0.5°S for 0600 UTC. Contour interval is 1.0 m s^{-1}. Case with synoptic wind.

study domain (from about 6.0 km height level to 11.0 km height level on average over land) and easterly winds were aloft. In the course of the model simulation, one observes the mid-level westerlies receding eastwards to the ocean and being replaced by the easterlies. In Figures 88 and 89 one observes that the westerlies become thinner, especially over land. The low-level easterlies and upper-level easterlies seemed to expand from down and above "compressing" the mid-level westerlies and pushing them to the eastern part of the domain. By 1600 UTC (see Figure 90) the mid-level westerlies over land had receded considerably eastwards. There was an easterly wind maxima between 16.0 km and 21.0 km heights. A coupling of the lower-level and upper-level easterlies occurred on the western half of the domain. The presence of this maxima conformed to the observational analysis (see
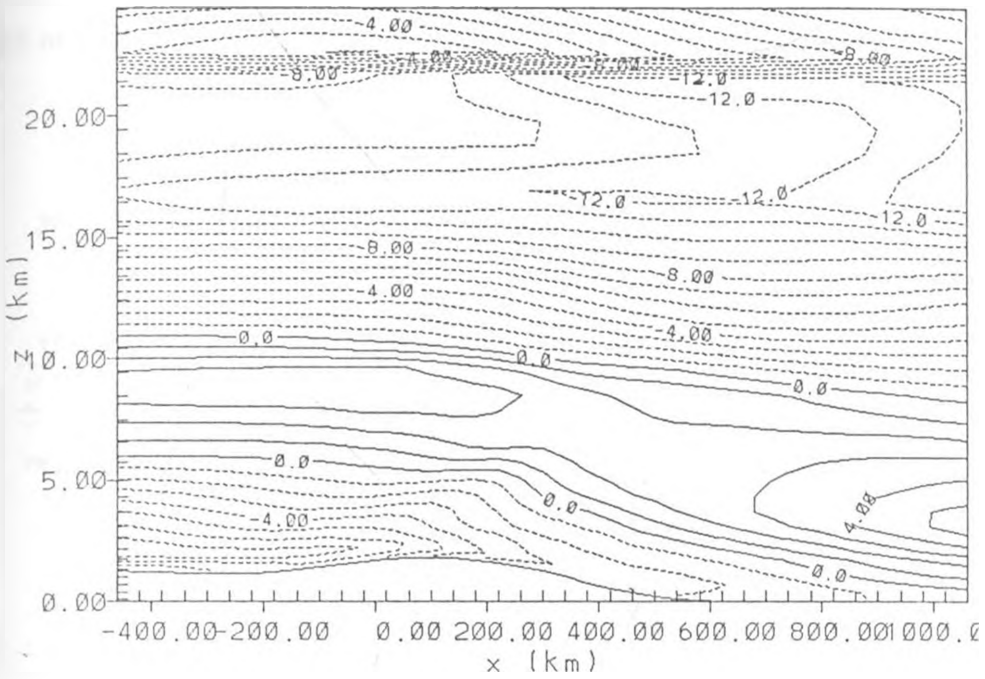
Figure 88: Vertical east-west cross-section of zonal wind (u) at 0.5°S for 0900 UTC. Contour interval is 1.0 m s^{-1}. Case with synoptic wind.
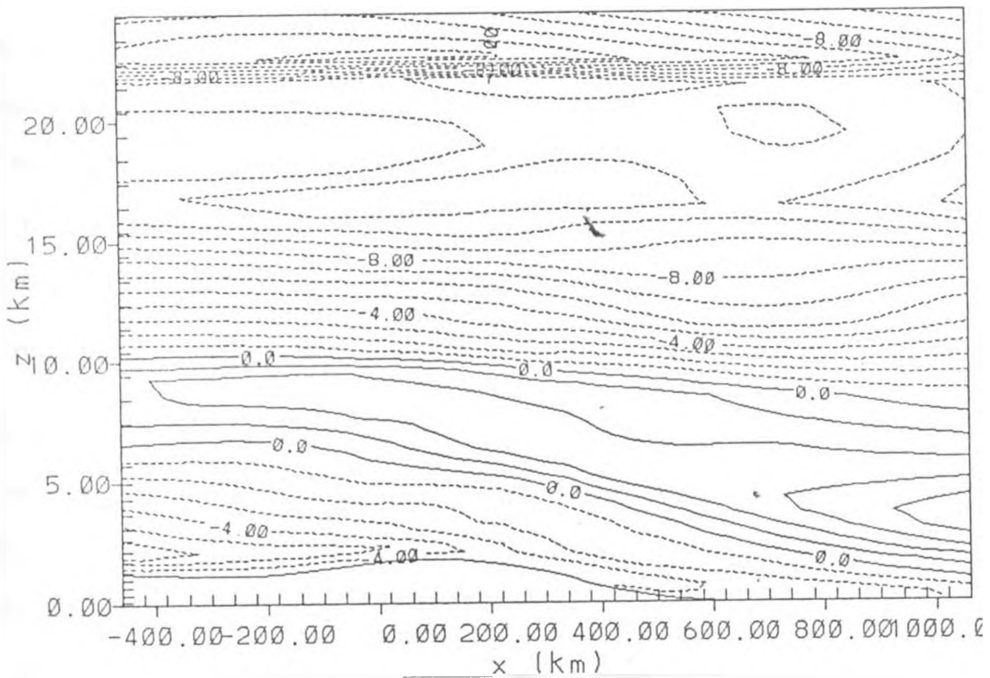
Figure 89: Vertical east-west cross-section of zonal wind (u) at 0.5°S for 1200 UTC. Contour interval is 1.0 m s^{-1}. Case with synoptic wind.

Figure 34) which registered the tropopause winds at 17 km height ($\approx$94 mb) with a wind strength of 35 knots.
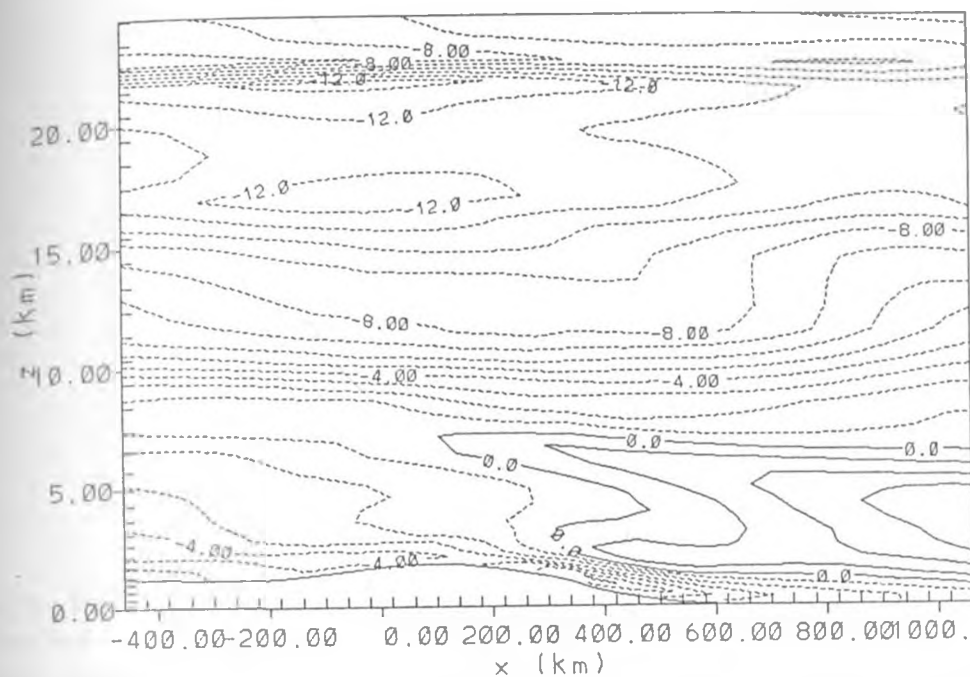
Figure 90: Vertical east-west cross-section of zonal wind (u) at 0.5°S for 1600 UTC. Contour interval is 1.0 m s^{-1}. Case with synoptic wind.

The replacement of the mid-level westerlies by the easterlies in the course of the model simulation over this equatorial domain could be attributed to the vertical transfer of easterly momentum by convergence associated with the low-level easterlies. Also, during the day, the air close to the ground heats up and warms the boundary layer, creating thermal eddies which transfer easterly momentum aloft.

6.1.2 The Large-Scale Pressure Field

The perturbation pressure Exner function showed a low pressure zone over Kenya with more negative pressure cells over the eastern and southwestern part of the country. There was high pressure close to the northern border over southern Ethiopia (see Figures 91 and 92 at 0600 UTC).

By 1200 UTC two low pressure cells appeared over the country; one to the east and another to the south (see Figures 93 and 94). These low pressure cells were observed to shift from south to north during the model integration. The position of the ITCZ at 2.609

Figure 91: Perturbation Exner function on terrain following coordinate 122 m above surface at 0600 UTC (coarse grid). Contour values are in units of J K^{-1} kg^{-1}. Case with synoptic wind.

Figure 92: Perturbation Exner function on terrain following coordinate 122 m above surface at 0600 UTC (fine grid). Contour values are in units of J K^{-1} kg^{-1}. Case with synoptic wind.

Figure 93: Perturbation Exner function on terrain following coordinate 122 m above surface at 1200 UTC (coarse grid). Contour values are in units of J K^{-1} kg^{-1}. Case with synoptic wind.

Figure 94: Perturbation Exner function on terrain following coordinate 122 m above surface at 1200 UTC (fine grid). Contour values are in units of J K^{-1} kg^{-1}. Case with synoptic wind.

km ($\approx$741 mb) is depicted in Figures 95 and 96 as a zone of low pressure (more negative

perturbation pressure Exner Function) at 1200 UTC. The orientation of the isobars in

Figure 95: Perturbation pressure Exner function on terrain following coordinate 2.61 km above surface at 1200 UTC (coarse grid). Contour values are in units of J K^{-1} kg^{-1}. Case with synoptic wind.

Figure 97 at 1800 UTC was an additional indication of an intense ITCZ over Kenya on this day and at this time.

By 1600 UTC at lower levels the two prominent pressure cells have moved northwards and intensified more; one sat to the east and another to the west (or southwest) of the country. These cells can be seen in Figures 98 and 99. These pressure cells induced by the general flow pattern and the ITCZ position must have been responsible for the wide spread convective activity that occurred on this particular day of the "Long Rains" season. At 2400 UTC one of the low pressure cells to the east has moved to the northeastern part of the country, relaxed a bit and aligned itself in a northeast-southwest orientation (see Figures 100 and 101). A striking feature at this time was the presence of another more intense low pressure cell just to the north of Lake Victoria in Uganda (in addition to the one in western Kenya) which was also well organized.
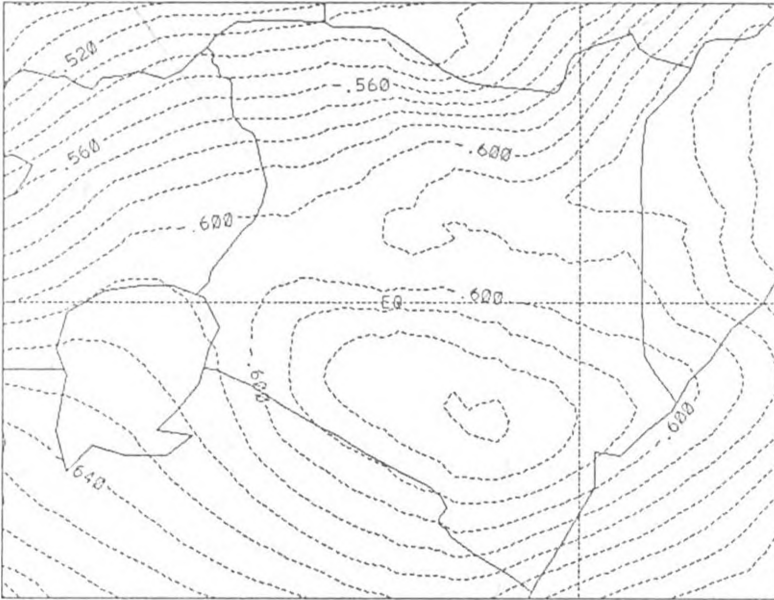
Figure 96: Perturbation pressure Exner function on terrain following coordinate 2.61 km above surface at 1200 UTC (fine grid). Contour values are in units of J K^{-1} kg^{-1}. Case with synoptic wind.
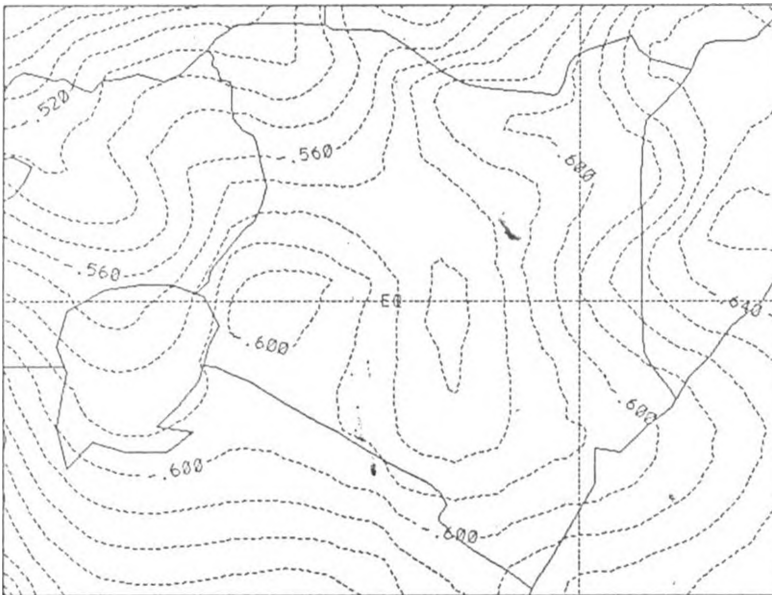
Figure 97: Perturbation pressure Exner on terrain following coordinate 2.61 km above surface at 1800 UTC. Contour values are in units of J K^{-1} kg^{-1}. Case with synoptic wind.
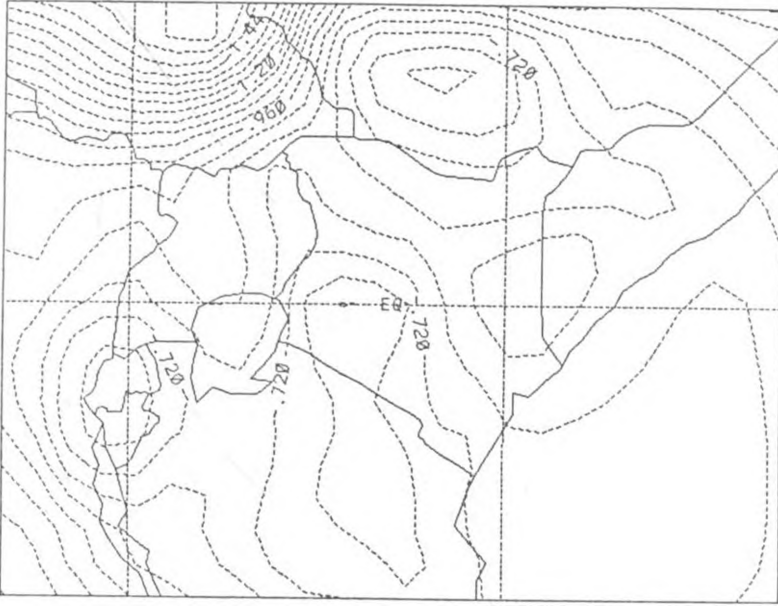
Figure 98: Perturbation Exner function on terrain following coordinate 122 m above surface at 1600 UTC (coarse grid). Contour values are in units of J K^{-1} kg^{-1}. Case with synoptic wind.
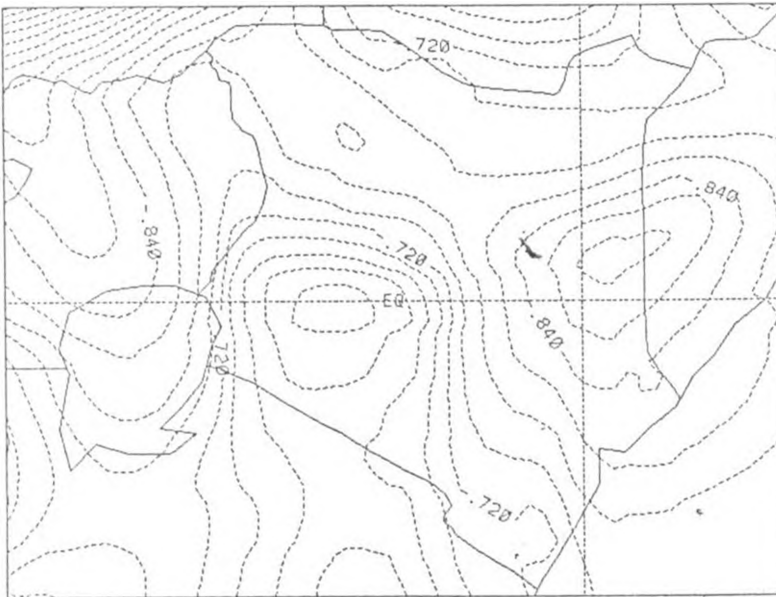
Figure 99: Perturbation Exner function on terrain following coordinate 122 m above surface at 1600 UTC (fine grid). Contour values are in units of J K^{-1} kg^{-1}. Case with synoptic wind.
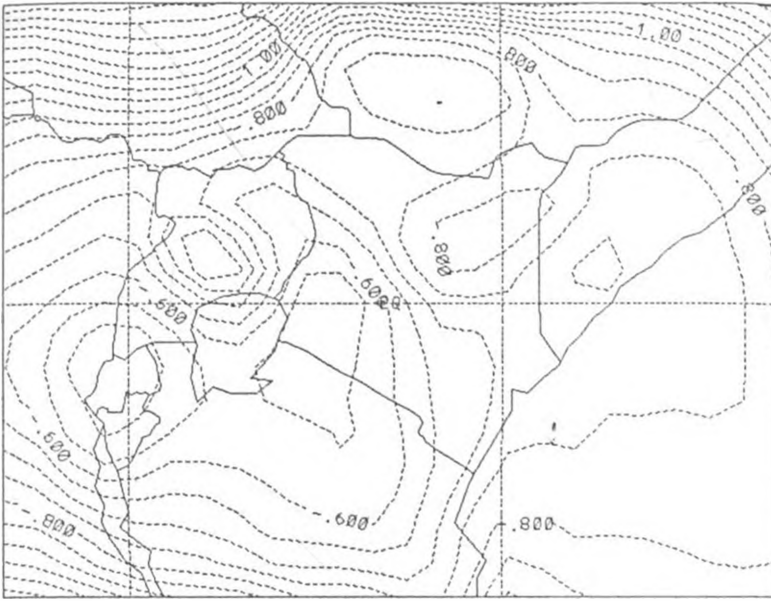
Figure 100: Perturbation Exner function on terrain following coordinate 122 m above surface at 2400 UTC (coarse grid). Contour interval is 0.05 J K^{-1} kg^{-1}. Case with synoptic wind.
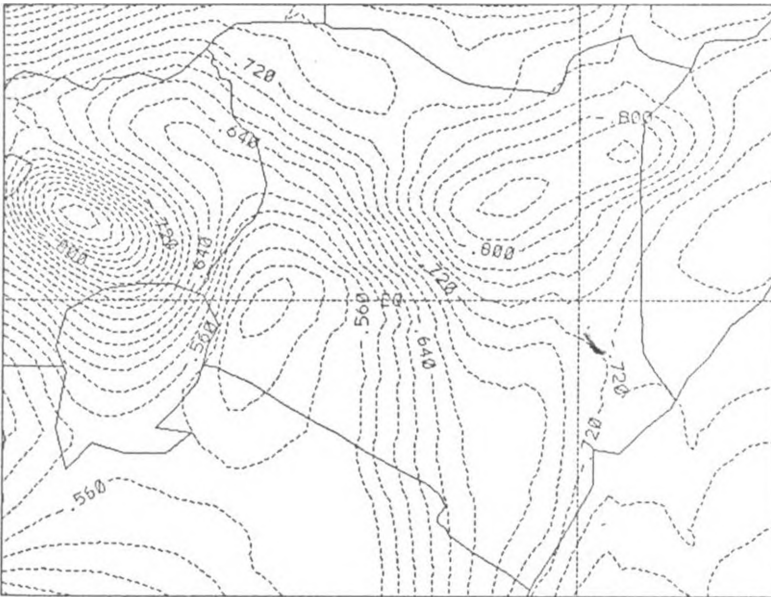
Figure 101: Perturbation Exner function on terrain following coordinate 122 m above surface at 2400 UTC (fine grid). Contour interval is 0.02 J K^{-1} kg^{-1}. Case with synoptic wind.

Perturbations pressure Exner function fields at 1.33 km AMSL are shown in Figures 102 and 103. Pressure cells were still evident at this level although displaced to the south,

Figure 102: Perturbation Exner function on terrain following coordinate 1.339 km above surface at 1600 UTC (coarse grid). Contour values are in units of J K^{-1} kg^{-1}. Case with synoptic wind.

one on the northern-most coast over Kenya and another to the south on the border with Tanzania. To the west another pressure cell spread from central Uganda into Kenya. Figure 104 displays the isobars at 5.729 km height where the wind was seen to be almost northerly (see Figure 78) flowing almost parallel to the isobars especially to the western half of the domain. Figure 105 depicts the isobars at 10.443 km height where the winds from the northwest converged with winds from the southeast over the northwestern part of Kenya (see Figures 79 and 80). Negative pressure perturbation was significant even at this level. Figures 106 at 1600 UTC and 107 at 1800 UTC show the isobars at 17.443 km height and 19.443 km height, respectively, at levels where the winds were strongly easterly. At 19.443 km height it could be observed that most parts of Kenya were under a high pressure zone.

The vertical east-west cross-sectional displays of the pressure perturbation Exner function are illustrated in Figures 108 to 112 which depict isobars at various times in the
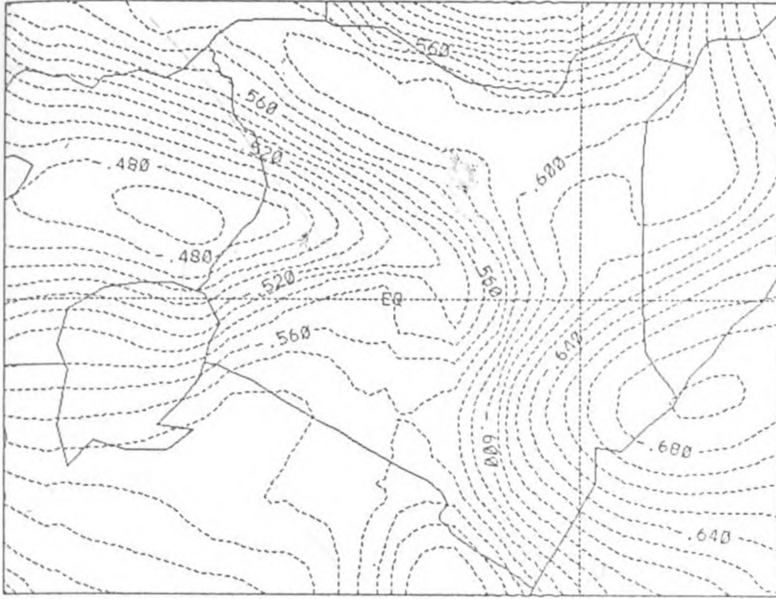
Figure 103: Perturbation Exner function on terrain following coordinate 1.339 km above surface at 1600 UTC (fine grid). Contour values are in units of J K^{-1} kg^{-1}. Case with synoptic wind.
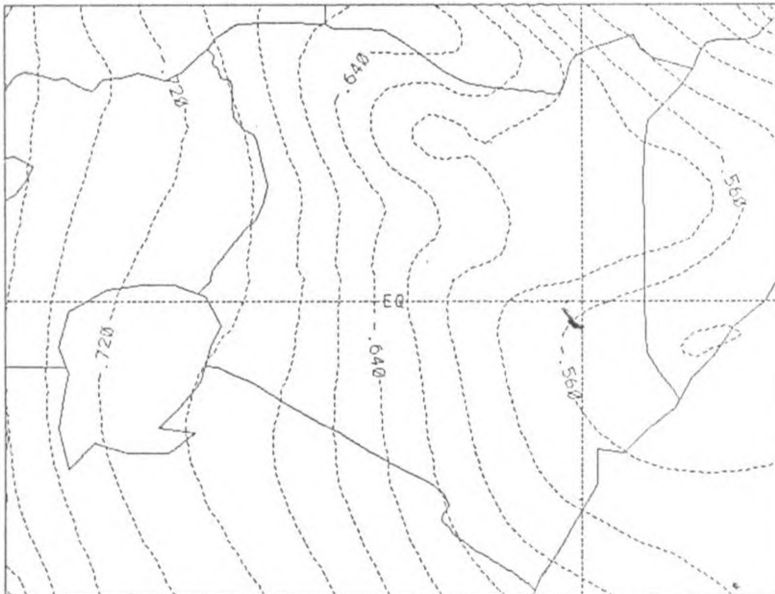
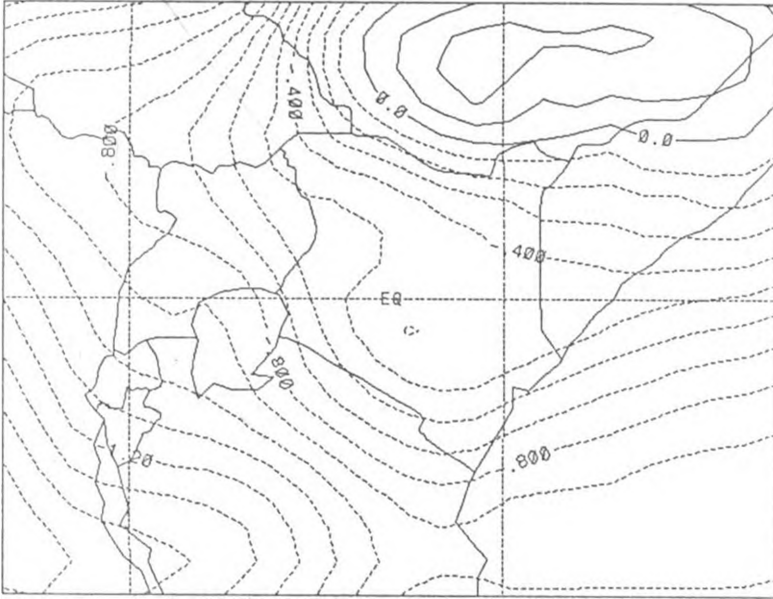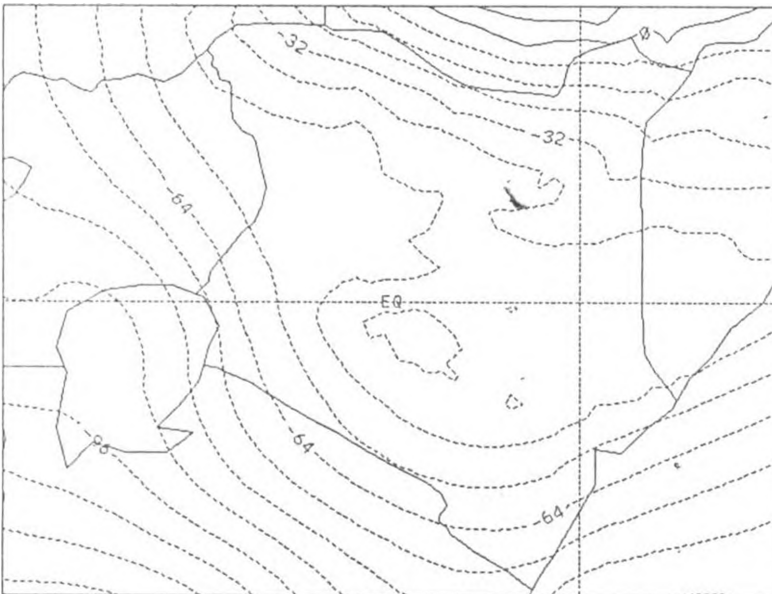Figure 104: Perturbation Exner function on terrain following coordinate at 5.73 km above surface at 1600 UTC. Contour values are in units of J K^{-1} kg^{-1}. Case with synoptic wind.
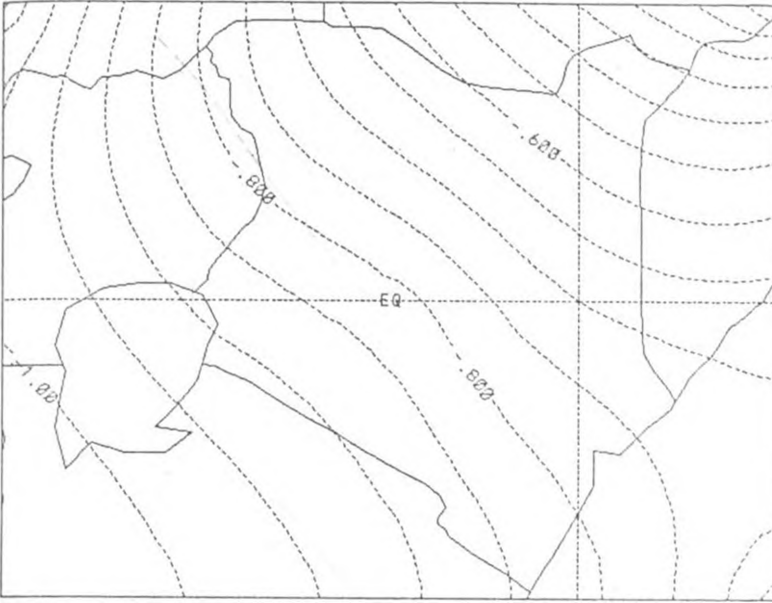
Figure 105: Perturbation Exner function on terrain following coordinate at 10.44 km above surface at 1600 UTC. Contour values are in units of J K^{-1} kg^{-1}. Case with synoptic wind.
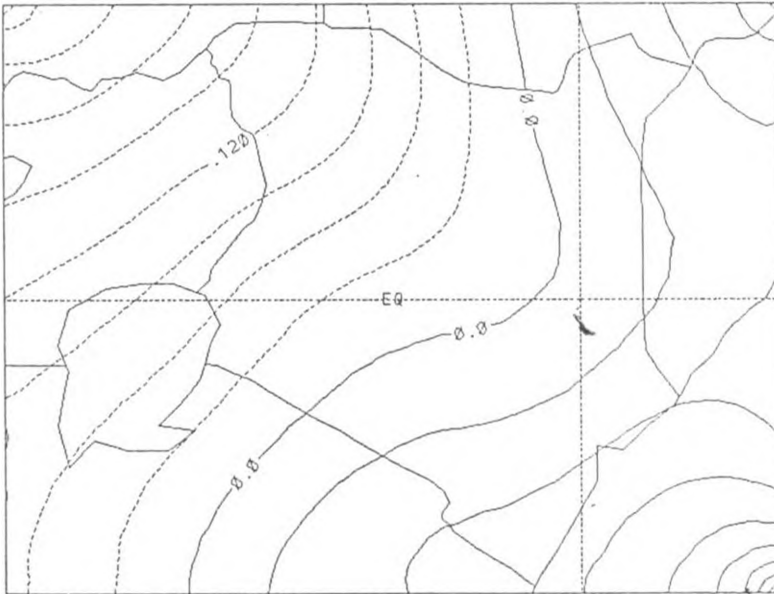
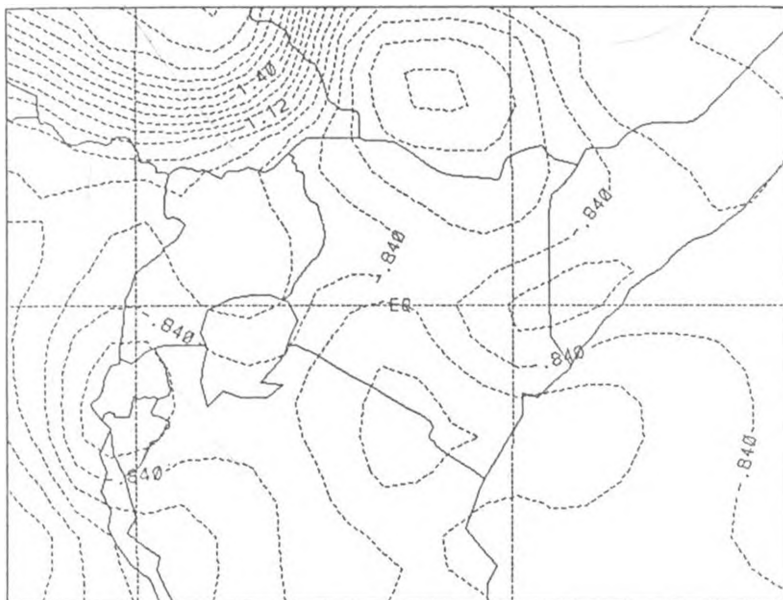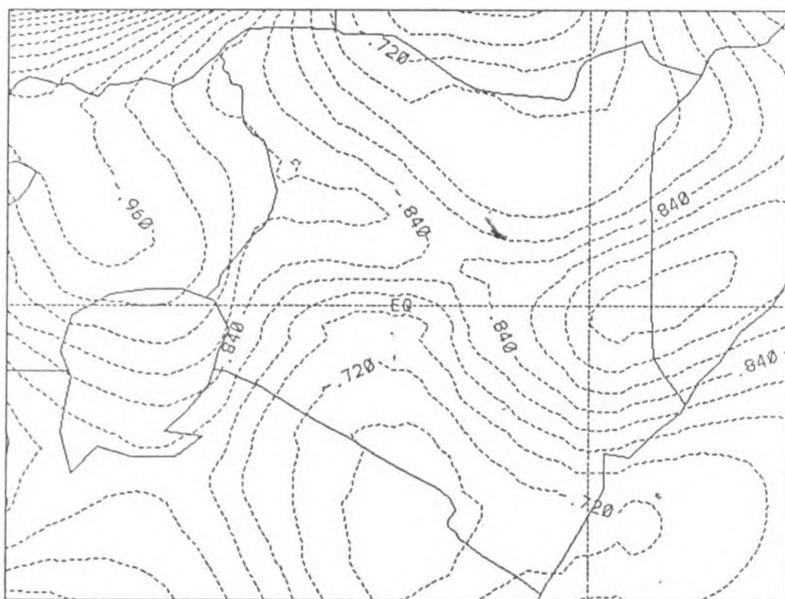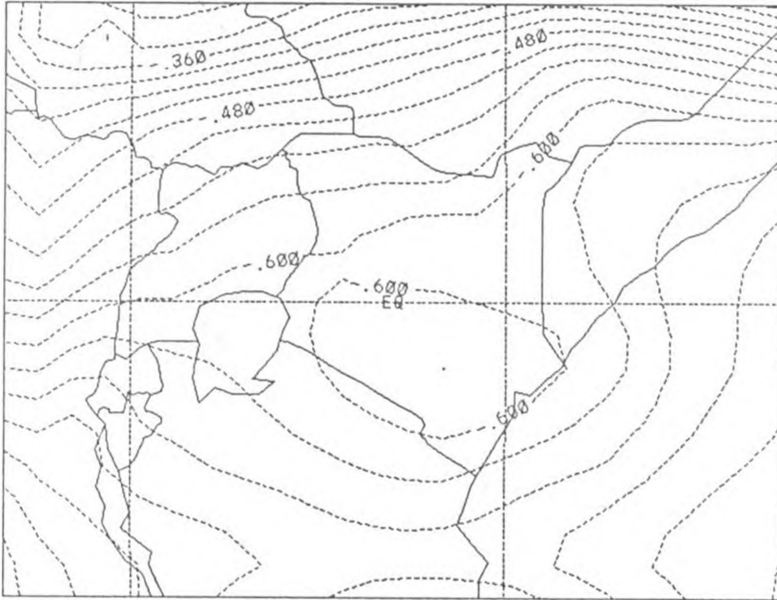

Figure 106: Perturbation Exner function on terrain following coordinate 17.44 km above surface at 1600 UTC. Contour values are in units of J K^{-1} kg^{-1}. Case with synoptic wind.
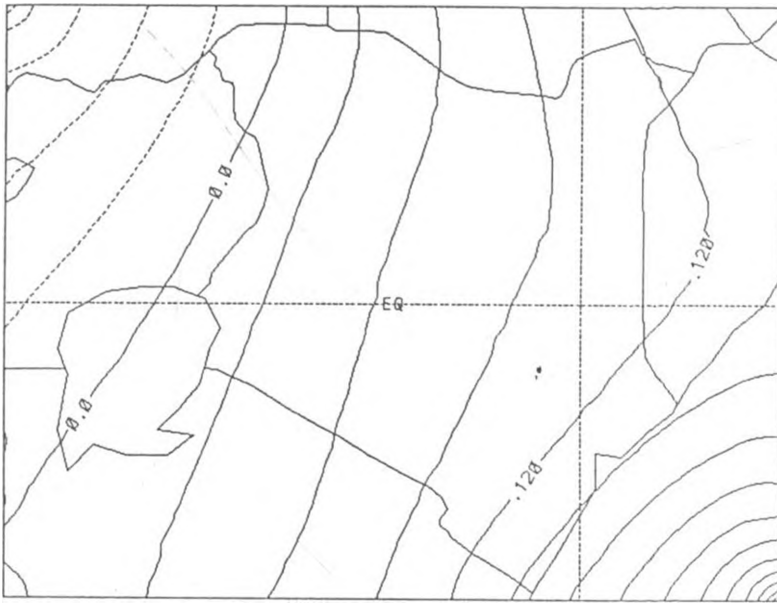
Figure 107: Perturbation Exner function on terrain following coordinate 19.44 km above surface at 1800 UTC. Contour values are in units of J K^{-1} kg^{-1}. Case with synoptic wind.

course of the simulations. Generally, pressure fell more at lower levels and middle levels but increased at upper levels during the model integration. In Figure 108 the high pressure was at a height of about 20.0 km and confined to the western part of the domain. Figures 109 to 112 show that this high pressure layer moved eastwards across the model domain in the course of the day (as did the mid-level westerlies) and also became thicker and thus, it was displaced lower in height to about 17.0 km height level on average. A maximum negative pressure perturbation at lower and middle levels was registered at 1600 UTC as depicted in Figure 111 and remained the same even at 1800 UTC (see Figure 112).

6.1.3 The Large-scale Vertical Wind Field

The vertical wind field over the study domain increased with time especially during the day and decreased towards the end of the model simulation. In Figures 113 and 114 six hours after the start of the model, the maximum vertical velocity registered over Kenya was 3.2 cm s^{-1} (with a maximum subsidence motion of -2.0 cm s^{-1}). There was rising motion over most parts of the country except on the eastern side of the Lake Victoria
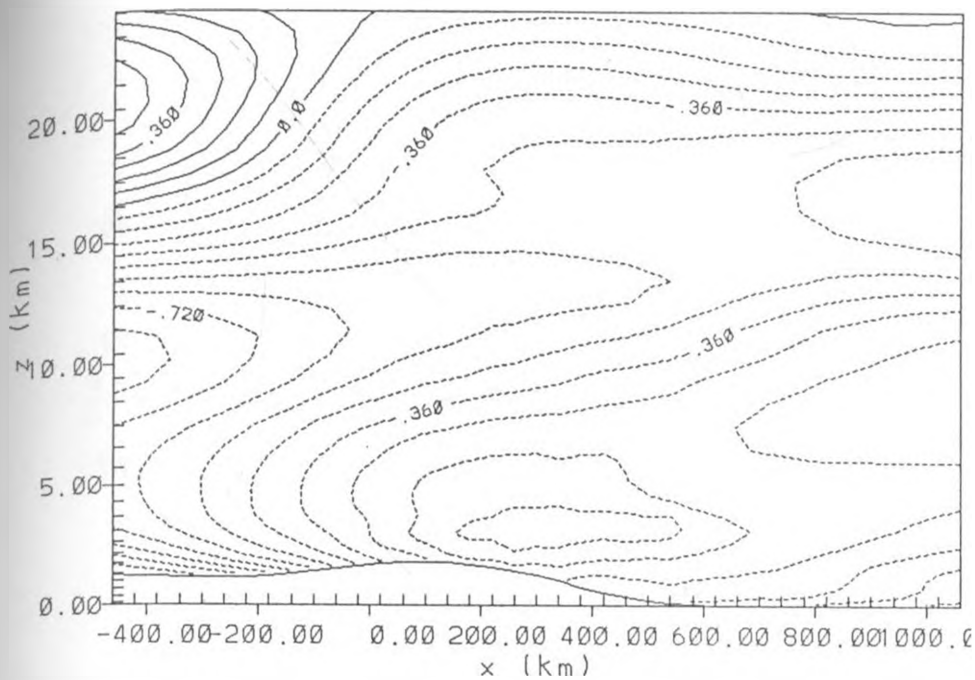
Figure 108: Vertical east-west cross-section of the perturbation Exner function at 0.5°S for 0600 UTC. Contour values are in units of J K^{-1} kg^{-1}. Case with synoptic wind.
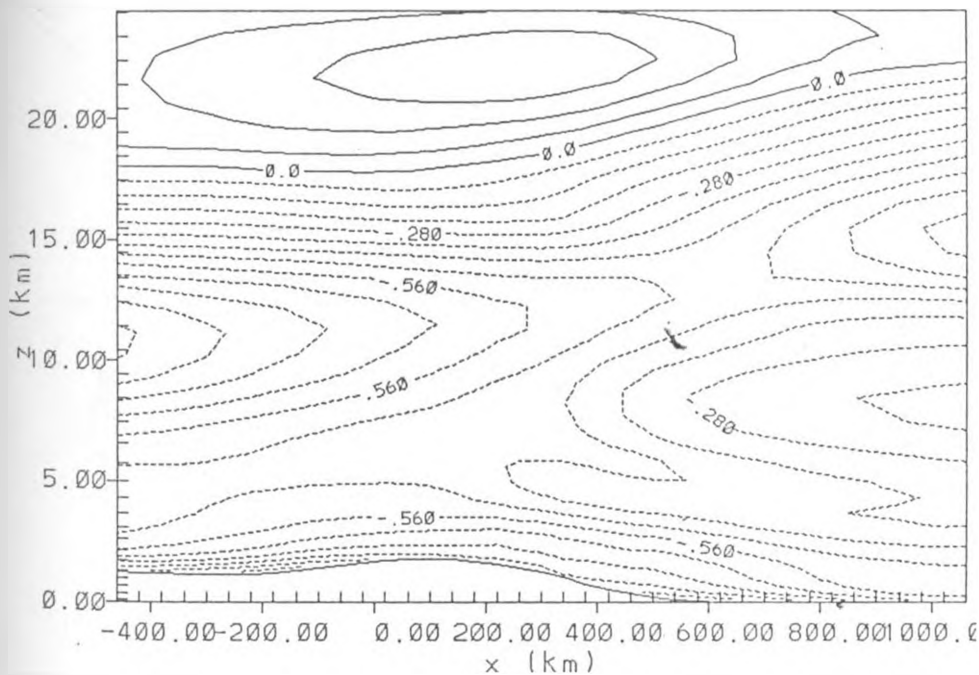
Figure 109: Vertical east-west cross-section of the perturbation Exner function at 0.5°S for 0900 UTC. Contour values are in units of J K^{-1} kg^{-1}. Case with synoptic wind.
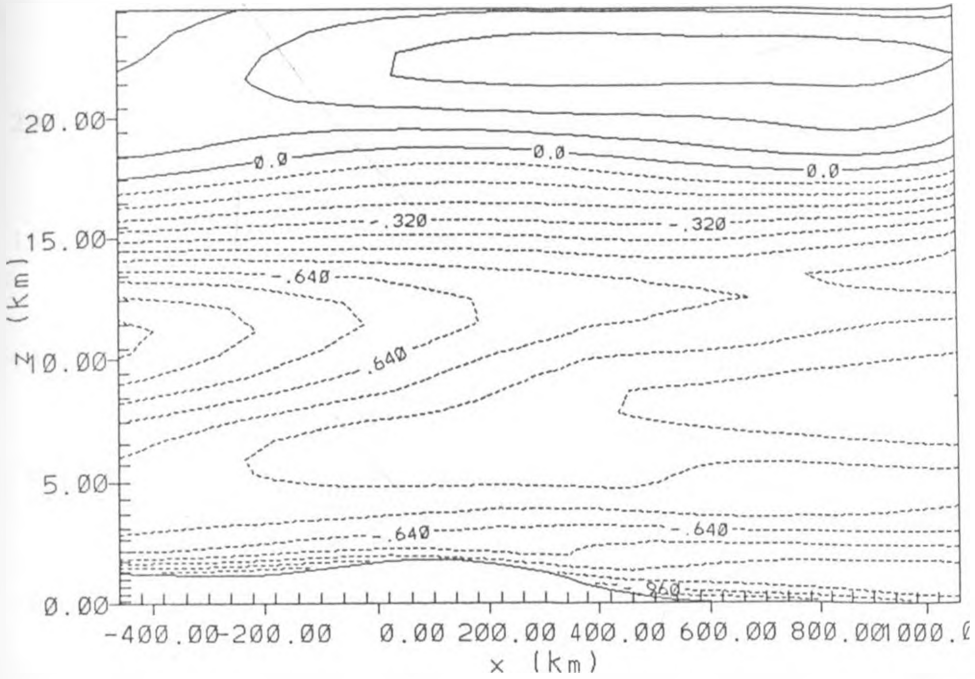
Figure 110: Vertical east-west cross-section of the perturbation Exner function at $0.5^\circ S$ for 1200 UTC. Contour values are in units of $J\ K^{-1}\ kg^{-1}$. Case with synoptic wind.
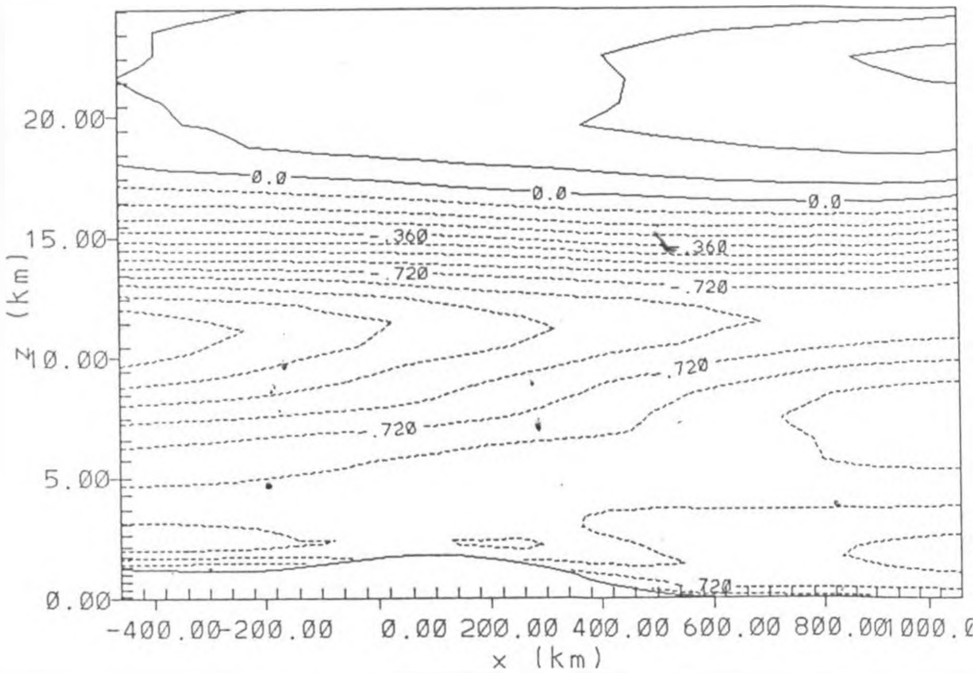
Figure 111: Vertical east-west cross-section of the perturbation Exner function at $0.5^\circ S$ for 1600 UTC. Contour values are in units of $J\ K^{-1}\ kg^{-1}$. Case with synoptic wind.
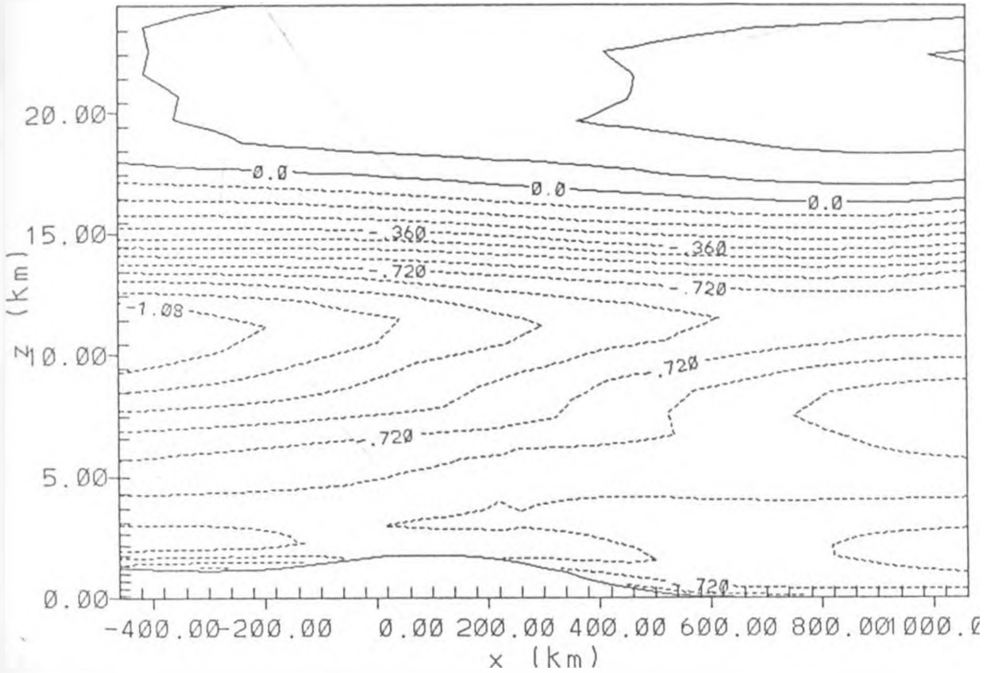
Figure 112: Vertical east-west cross-section of the perturbation Exner function at 0.5°S for 1800 UTC. Contour values are in units of J K^{-1} kg^{-1}. Case with synoptic wind.
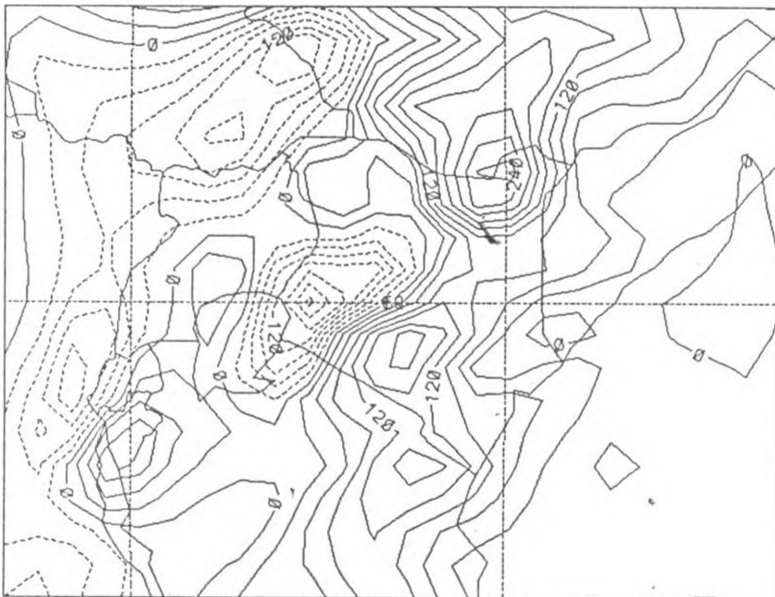
Figure 113: Vertical velocity field on terrain following coordinate surface 122 m above sea level at 0600 UTC (coarse grid). Contour values are in units of m s^{-1}. Labels *1.0×10^{-4}. Case with synoptic wind.
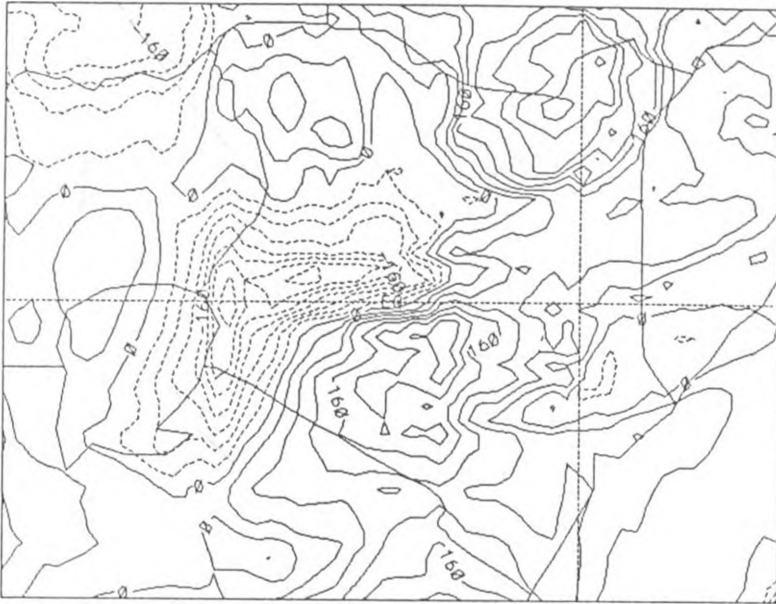
Figure 114: Vertical velocity field on terrain following coordinate 122 m above surface at 0600 UTC (fine grid). Contour values are in units of m s^{-1}. Labels *1.0×10^{-4}. Case with synoptic wind.

Trough and northern sloping side of the Kenyan Highlands. The subsiding air over the study site was part of the down-currents of the southeasterly monsoon as they flowed over the north-south oriented mountains into the Lake Victoria Basin. Figures 115 and 116 at 1600 UTC showed that the vertical wind field had increased in strength to a maximum of 4.2 cm s^{-1} over Kenya with a maximum subsidence of −1.0 cm s^{-1}. The region of subsidence had diminished as compared to the scenario at 0600 UTC since the land at 1600 UTC was warmer and contributed more to rising motion. The regions associated with low pressure cells in the previous section have significant rising motions.

Figures 117 and 118 show a region (2.609 km height or 741.2 mb) where the ITCZ was evident as a zone of convergence for the two hemispheric air masses; the northeasterly and southeasterly monsoon currents. Although the zone of convergence was evident in the wind field (Figures 52 and 53) and in the pressure perturbation field (Figures 95 and 96) the vertical wind field also showed subsidence close to the belt of the ITCZ, with a maximum vertical motion of 3.2 cm s^{-1}. Figures 119 and 120 at 2400 UTC show strong
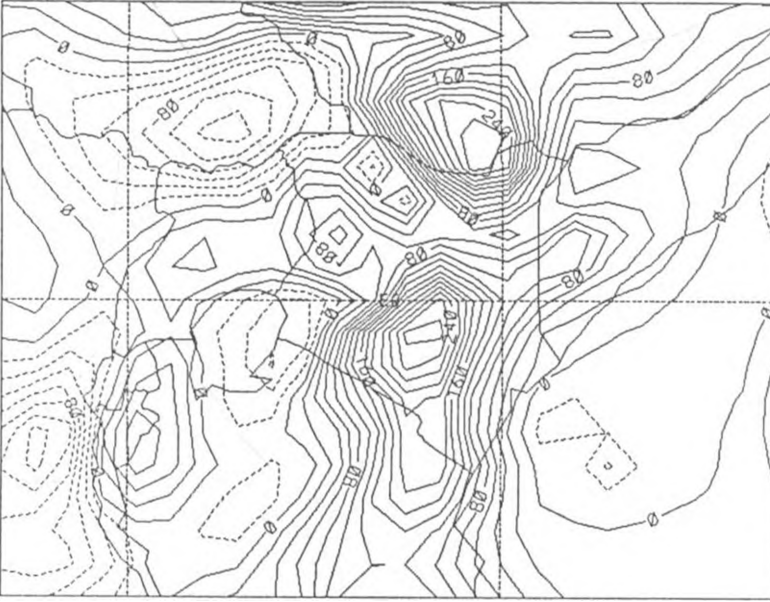
Figure 115: Vertical velocity field on terrain following coordinate 122 m above surface at 1600 UTC (coarse grid). Contour values are in units of m s^{-1}. Labels *1.0×10^{-4}. Case with synoptic wind.
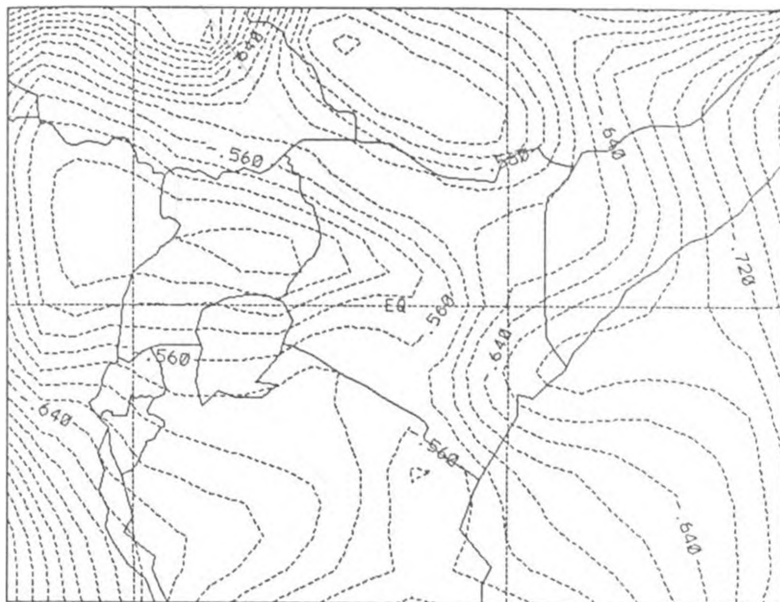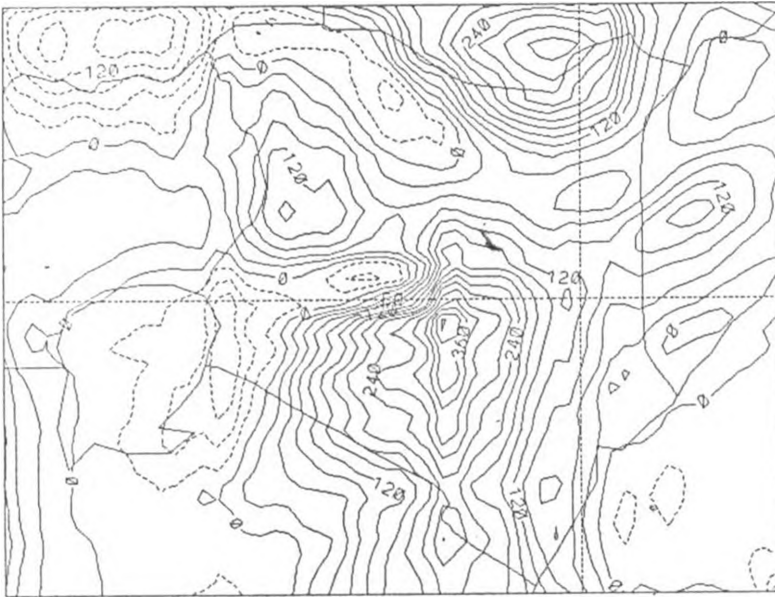

Figure 116: Vertical velocity field on terrain following coordinate 122 m above surface at 1600 UTC (fine grid). Contour values are in units of m s^{-1}. Labels *1.0×10^{-4}. Case with synoptic wind.
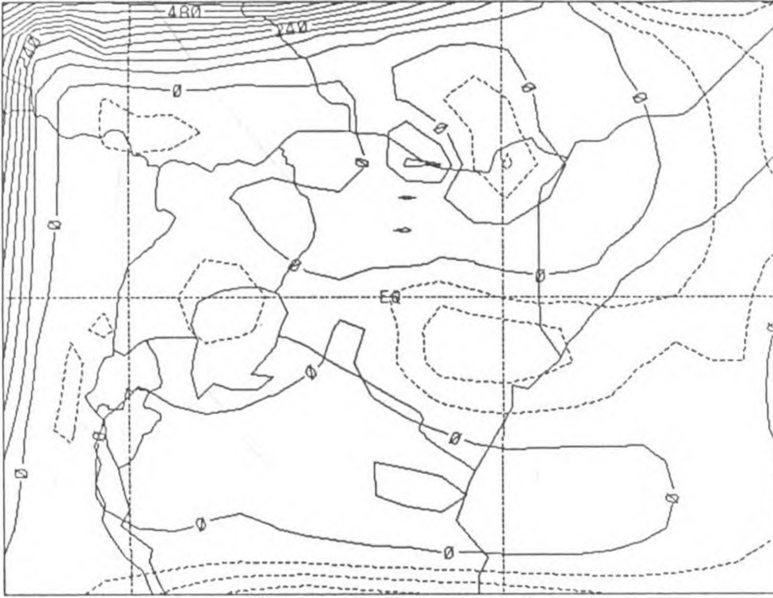
Figure 117: Vertical velocity field on terrain following coordinate 2.61 km above surface at 1200 UTC (coarse grid). Contour values are in units of m s^{-1}. Labels *1.0×10^{-4}. Case with synoptic wind.

Figure 118: Vertical velocity field on terrain following coordinate 2.61 km above surface 1200 UTC (fine grid). Contour values are in units of m s^{-1}. Labels *1.0×10^{-4}. Case with synoptic wind.

vertical motion in the region where low pressure cells were registered with a maximum vertical motion of 3.9 cm s^{-1} and maximum subsidence of 2.1 cm s^{-1}.
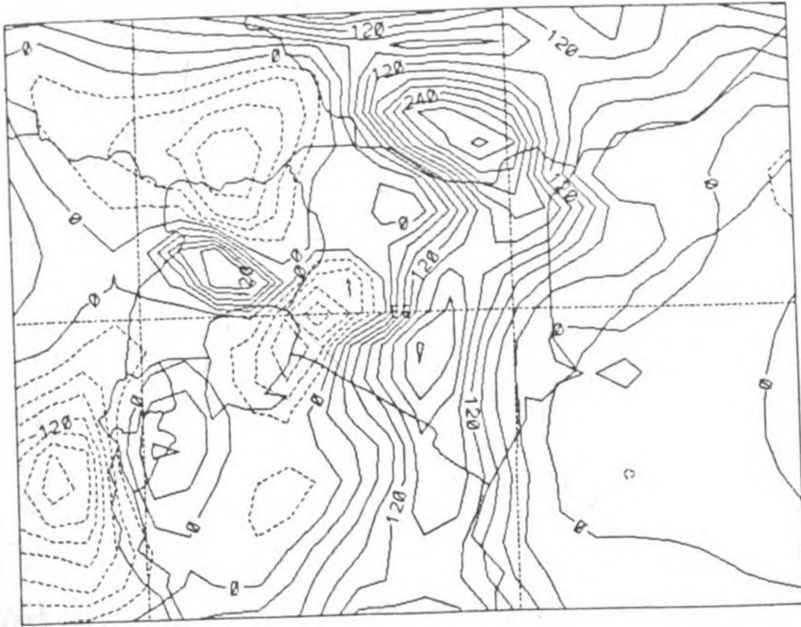
Figure 119: Vertical velocity field on terrain following coordinate 122 m above surface at 2400 UTC (coarse grid). Contour values are in units of m s^{-1}. Labels $*1.0 \times 10^{-4}$. Case with synoptic wind.

At upper levels the vertical wind fields are illustrated in Figure 121 at 5.729 km height where the maximum value registered over the domain was 4.2 cm s^{-1} with a maximum subsidence value of -6.0 cm s^{-1}. It should be recalled that there was a confluence between a northwesterly current and a southeasterly current at 10.443 km height (see Figures 79 and 80). The vertical wind field at the 10.443 km height level showed a subsidence motion with a maximum of -11.2 cm s^{-1} and maximum vertical motion of 0.7 cm s^{-1} over the whole domain. These features are illustrated in Figures 122 and 123. Figure 124 shows vertical motion at 17.443 km height AMSL. The maximum value registered was 3.2 cm s^{-1} with minimal subsidence. Figure 125 shows vertical motion field at 19.443 km height AMSL at 1800 UTC. The maxima vertical motion at this level was 2.4 cm s^{-1} with a maximum subsidence value of -1.0 cm s^{-1} over the southern boundary of Kenya and Tanzania.
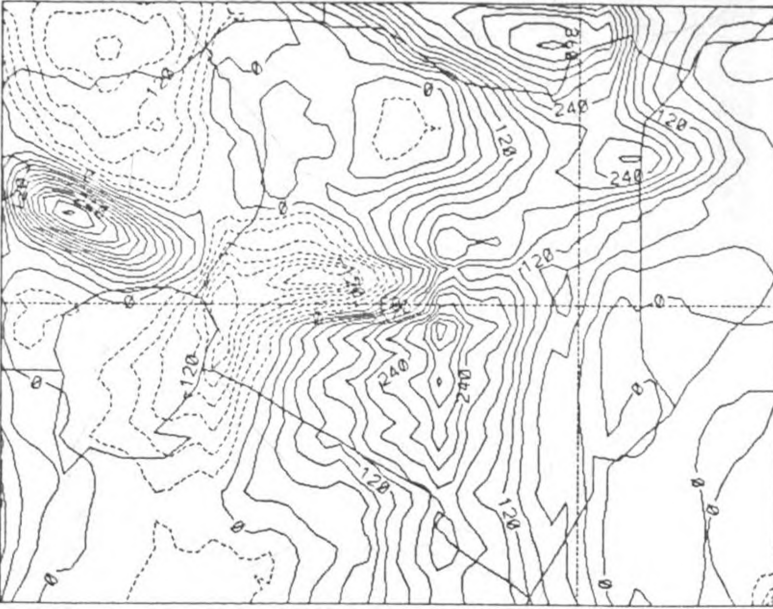
Figure 120: Vertical velocity field on terrain following coordinate 122 m above surface 2400 UTC (fine grid). Contour values are in units of m s^{-1}. Labels *1.0×10^{-4}. Case with synoptic wind.
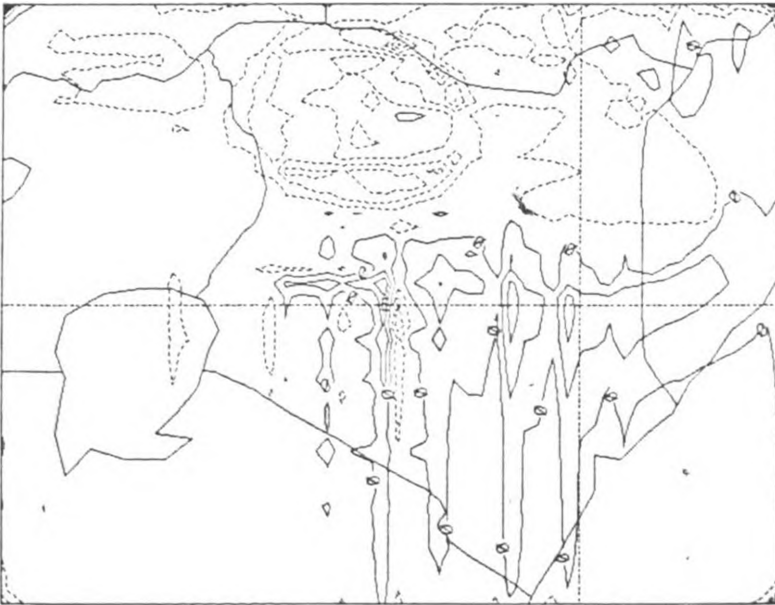
Figure 121: Vertical velocity field on terrain following coordinate 5.73 km above surface at 1600 UTC. Contour values are in units of m s^{-1}. Labels *1.0×10^{-4}. Case with synoptic wind.

123
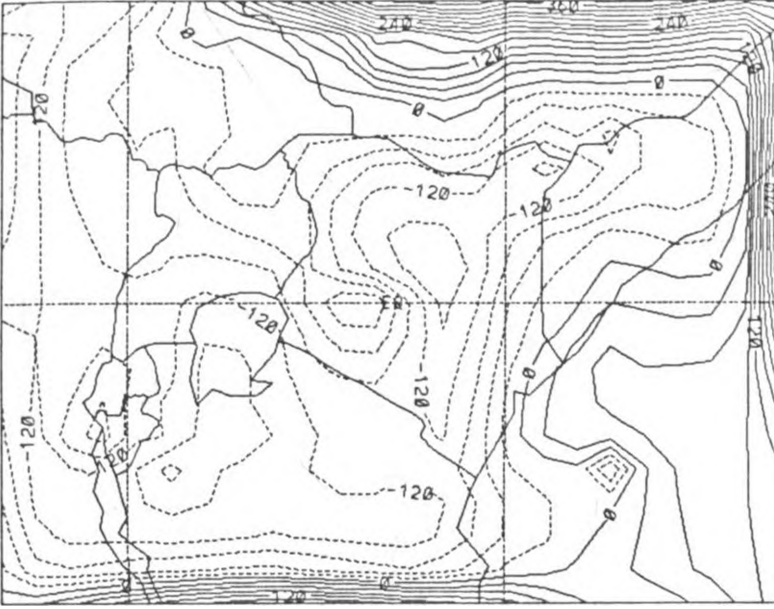
Figure 122: Vertical velocity field on terrain following coordinate 10.44 km above surface at 1600 UTC (coarse grid). Contour values are in units of m s^{-1}. Labels *1.0×10^{-4}. Case with synoptic wind.
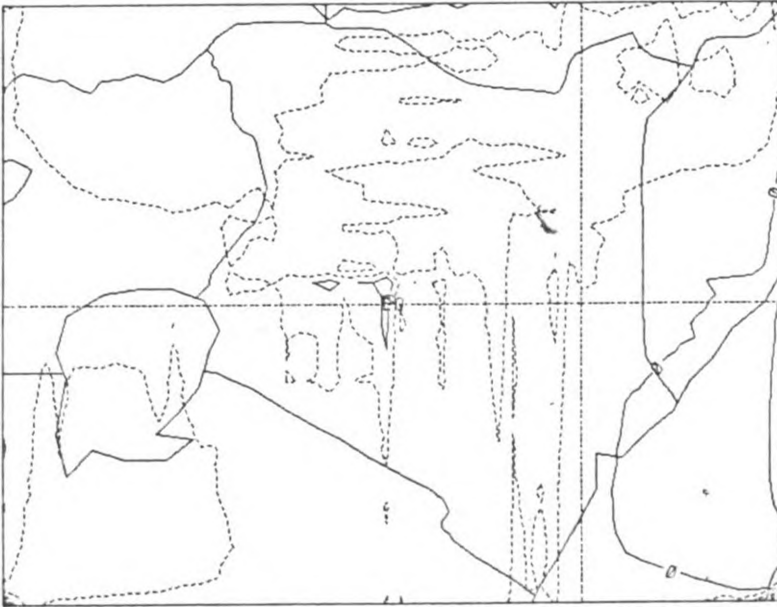
Figure 123: Vertical velocity field on terrain following coordinate 10.44 km above surface at 1600 UTC (fine grid). Contour values are in units of m s^{-1}. Labels *1.0×10^{-4}. Case with synoptic wind.
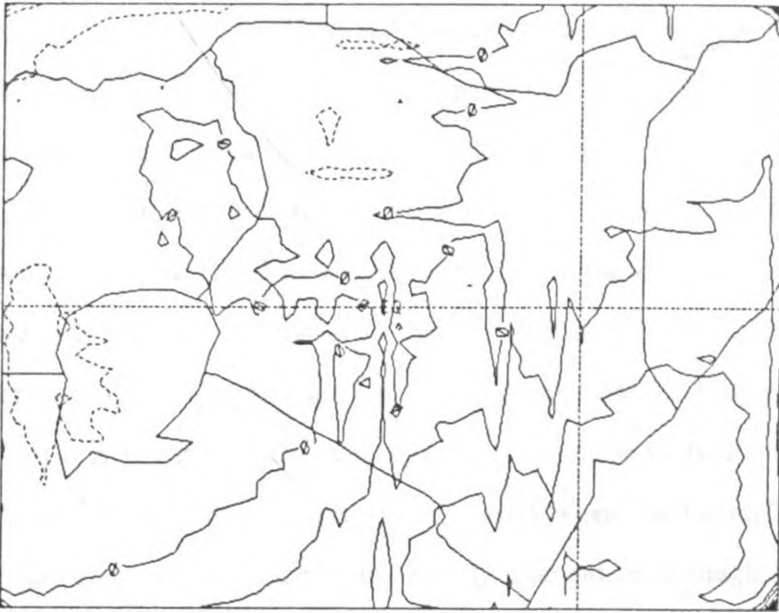
Figure 124: Vertical velocity field on terrain following coordinate 17.44 km above surface at 1600 UTC. Contour values are in units of m s^{-1}. Labels *1.0×10^{-4}. Case with synoptic wind.
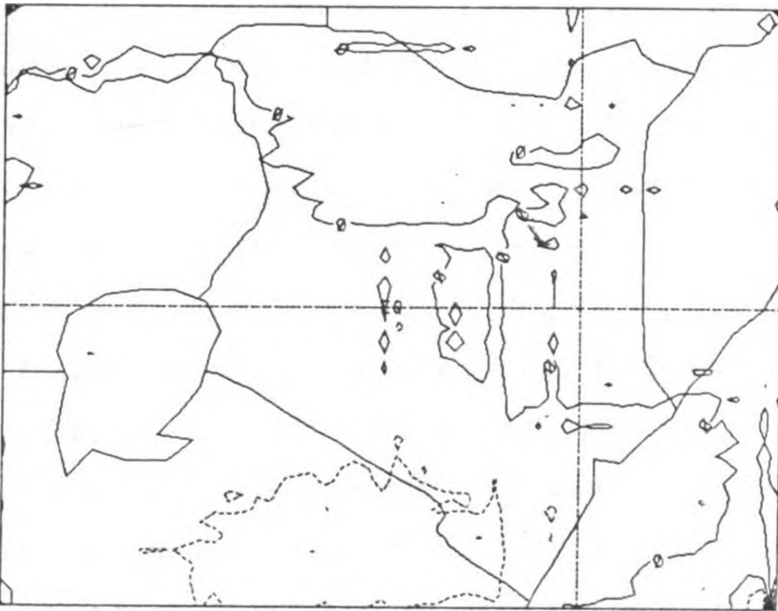
Figure 125: Vertical velocity field on terrain following coordinate 19.44 km above surface at 1800 UTC. Contour values are in units of m s^{-1}. Labels *1.0×10^{-4}. Case with synoptic wind.

The vertical east-west cross-sections of the vertical wind field 50 km south of the equator showed rising motion in a shallow layer at lower levels where we have southeasterly monsoon winds. There was subsidence in some parts of the middle levels where we had westerly winds and rising motion in the upper level easterlies. The subsidence in some parts of the middle layers is therefore indicative of a cold surge of an unstable westerly current of air which has been found to occur over Kenya during the rainy season (Kagenyi, 1990). This westerly current at mid-levels can be seen in Figures 73 to 78 where the middle layers are represented by 5.73 km ($\approx$505 mb) height AMSL. Cold air at mid-levels may increase static instability of the atmosphere and induce vertical overturning over the region. The shallow easterlies present at low levels when mechanically lifted by the Kenyan highlands or by vertical transfer of easterly momentum through insolation, may likewise interact with these westerly currents to generate active weather conditions over the highlands. The rising motion in the easterlies was evidence of the vertical transfer aloft of easterly momentum from lower levels. Figure 126 at 0600 UTC registered a maximum vertical motion of 1.5 cm s^{-1} with a strong subsidence of -6.5 cm s^{-1}, especially over the ocean on the eastern side of the model domain. Figure 126 further shows two locations in the mid-level westerlies that experienced maximum subsidence motions. At 0900 UTC in Figure 127 rising motion increased to a maximum of 2.5 cm s^{-1} with a maximum subsidence of -5.5 cm s^{-1}. There was also increased vertical motion in the middle layers as compared to the situation at 0600 UTC. Figure 128 at 1200 UTC illustrates low-level vertical motion over most parts of the land area including a large part of the ocean in the study domain. The maximum vertical motion registered at this time was 2.7 cm s^{-1} with a maximum subsidence of -2.1 cm s^{-1}. It may also be noted that rising motion at lower levels was occurring over a deeper layer at 1200 UTC than at any other time during the simulation. Moreover, there was sinking motion over Lake Victoria and over the Indian Ocean during daytime hours. At 1600 UTC (see Figure 129) the situation lapses back to look similar to the scenario after a few hours of model integration (e.g., at 0600 UTC); that is, rising motion in a shallow layer at lower layers and at upper levels with subsidence in parts of the middle layers, but the maximum value of the vertical motion registered
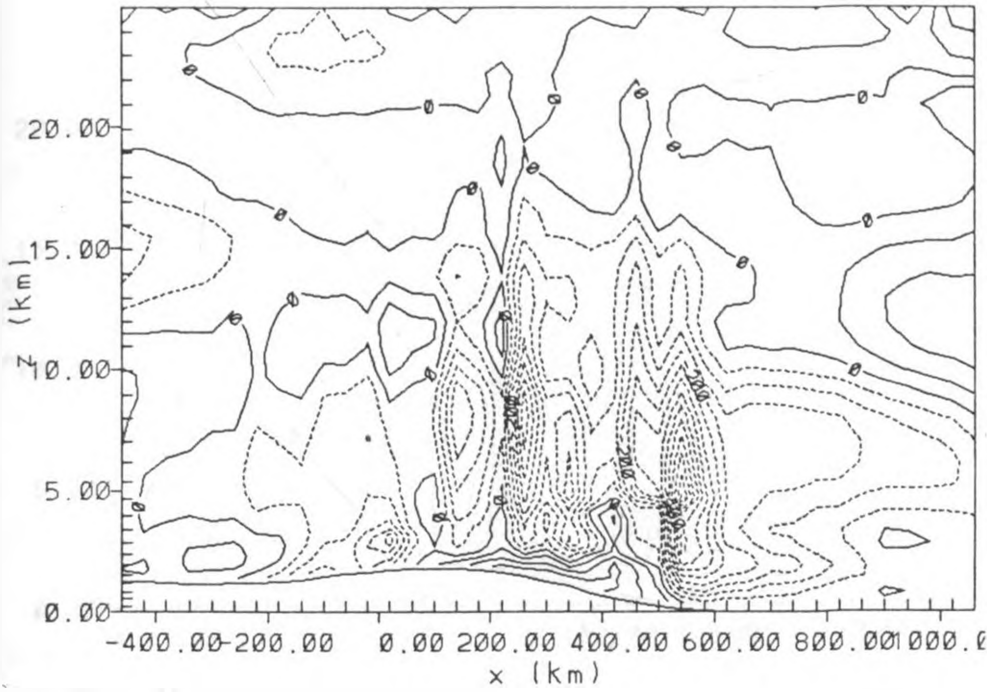
Figure 126: Vertical east-west cross-section of vertical velocity at 0.5°S for 0600 UTC. Contour values are in units of m s^{-1}. Labels *1.0×10^{-4}. Case with synoptic wind.
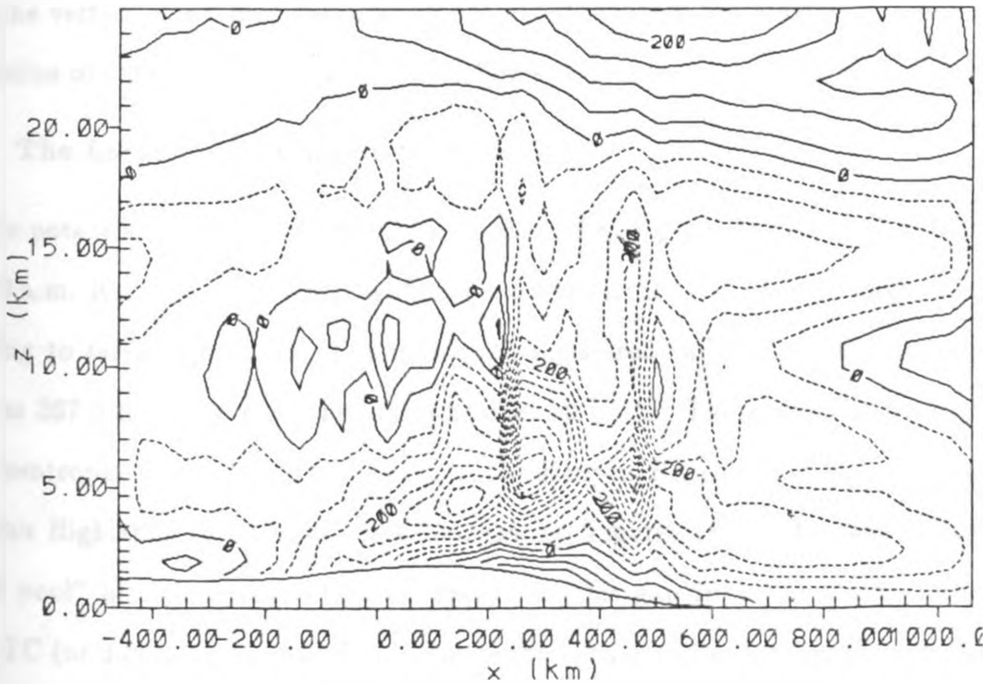

Figure 127: Vertical east-west cross-section of vertical velocity at 0.5°S for 0900 UTC. Contour values are in units of m s^{-1}. Labels *1.0×10^{-4}. Case with synoptic wind.
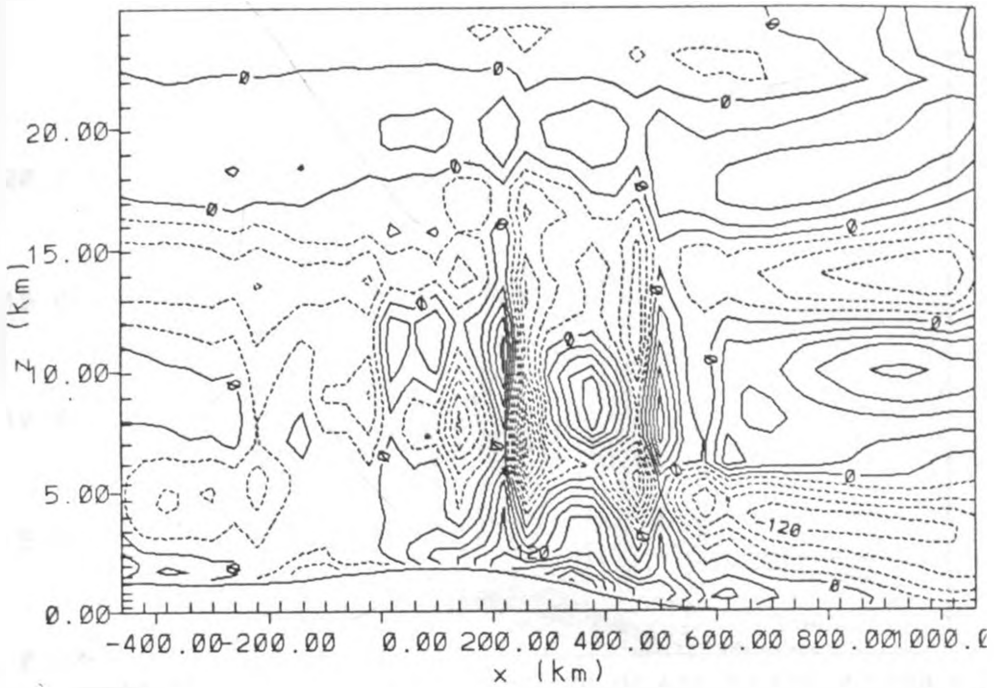
Figure 128: Vertical east-west cross-section of vertical velocity at 0.5°S for 1200 UTC. Contour values are in units of m s^{-1}. Labels *1.0×10^{-4}. Case with synoptic wind.

was 4.0 cm s^{-1} with corresponding subsidence of −2.0 cm s^{-1}. Figure 130 at 1600 UTC shows the vertical wind field taken along the equator where the maximum rising motion had a value of 3.0 cm s^{-1} with a corresponding subsidence value of −2.4 cm s^{-1}.

6.1.4   The Large-Scale Temperature Field

The potential temperature (θ) field is illustrated in Figures 131 and 132 at 0600 UTC (or 9:00 a.m. Kenya Local Time). At first glance the isentropes seem to align themselves according to terrain contours. The maximum registered value of θ over Kenya at this time was 307.0 K (same as in the initial field at 00 UTC). The alignment or orientation of the isentropes in the "corridor" between the Kenyan Highlands to the south and the Ethiopian Highlands to the north (see topography, Figures 48 and 49) was indicative of a "cold pool" of air currents being channelled in this gap from the Indian Ocean. At 1200 UTC (or 3:00 p.m. Kenyan Local Time) the temperature over Kenya increased to a maximum of 308.5 K (see Figures 133 and 134). This was an increase of 1.5 K from the temperature at 0600 UTC. The maximum θ value at 1200 UTC was the highest recorded throughout the simulation at a height of 122 m AMSL. This seemingly slight increase in
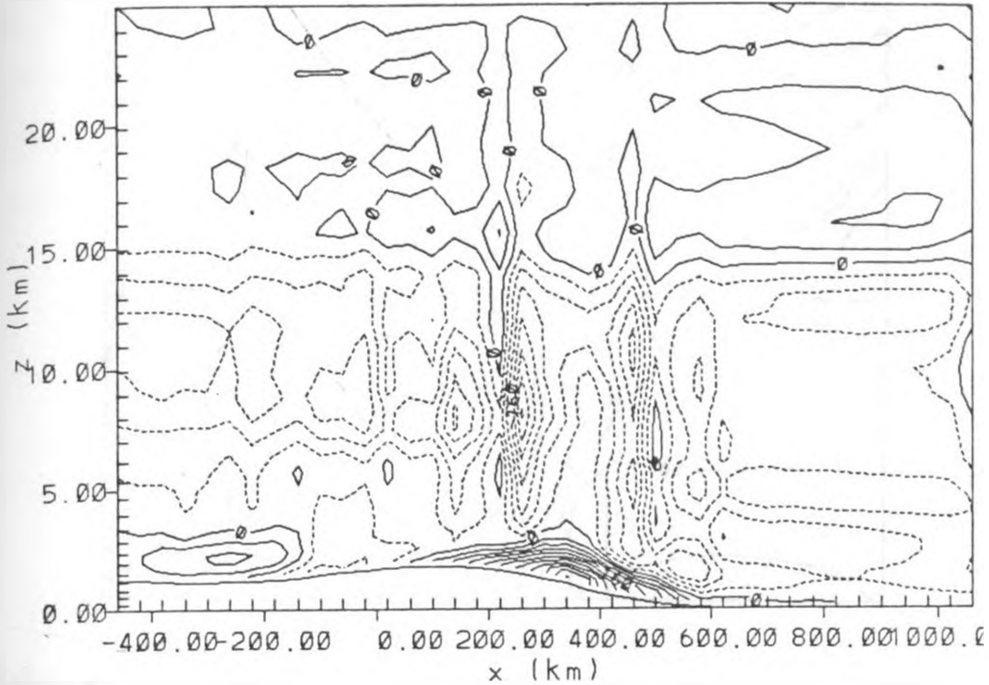
Figure 129: Vertical east-west cross-section of vertical velocity at 0.5°S for 1600 UTC. Contour values are in units of m s^{-1}. Labels *1.0×10^{-4}. Case with synoptic wind.
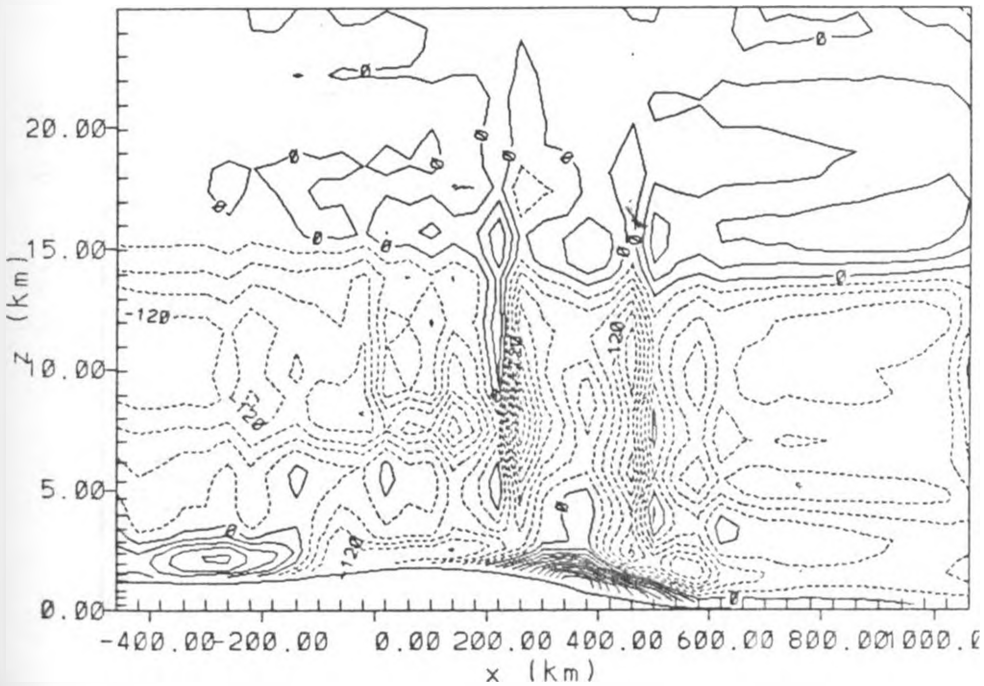
Figure 130: Vertical east-west cross-section of vertical velocity at 0.0° for 1600 UTC. Contour values are in units of m s^{-1}. Labels *1.0×10^{-4}. Case with synoptic wind.
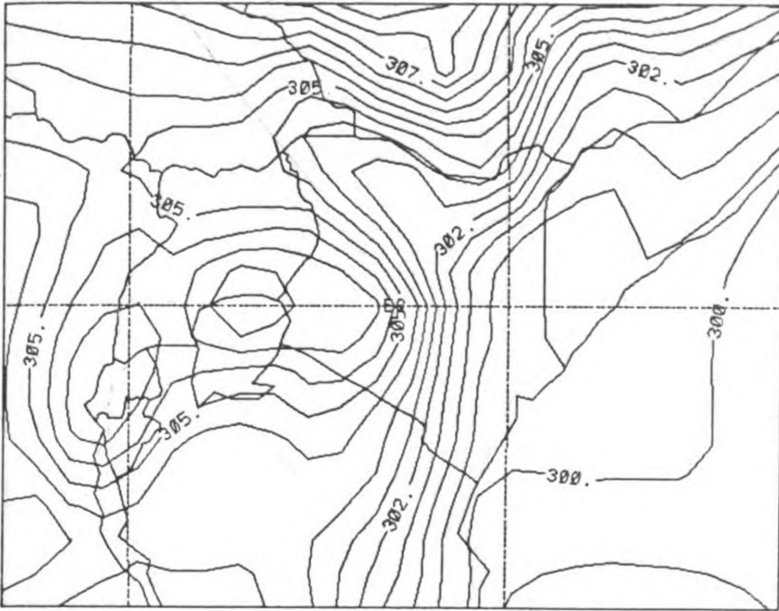
Figure 131: Potential temperature field on terrain following coordinate 122 m above surface at 0600 UTC (coarse grid). Contour intervals are in units of K. Case with synoptic wind.
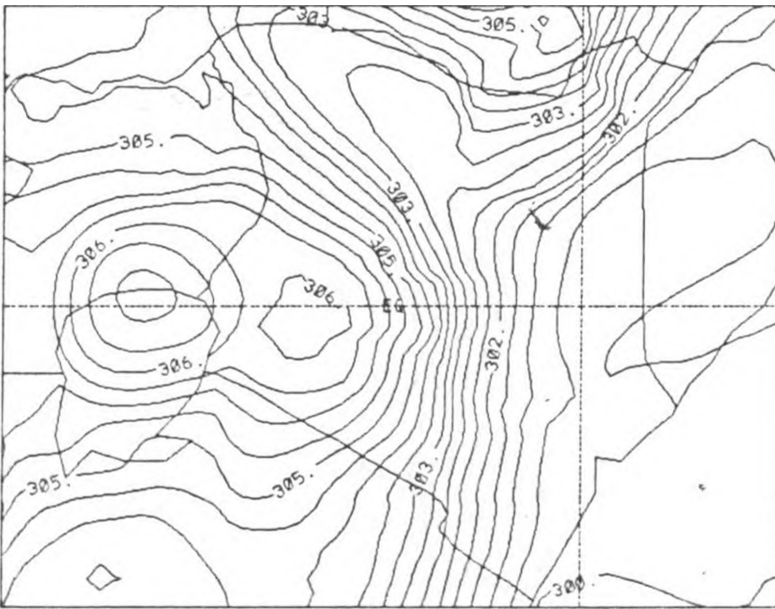
Figure 132: Potential temperature field on terrain following coordinate 122 m above surface at 0600 UTC (fine grid). Contour intervals are in units of K. Case with synoptic wind.

130
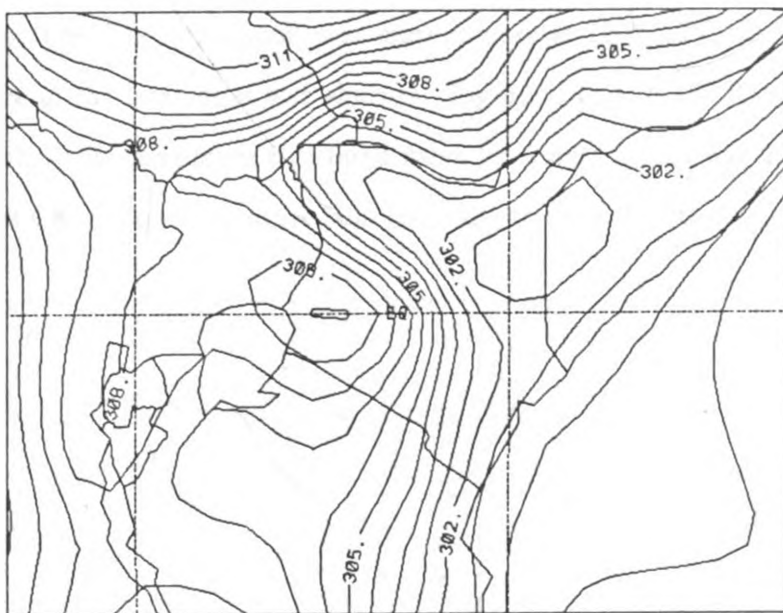
Figure 133: Potential temperature field on terrain following coordinate 122 m
above surface at 1200 UTC (coarse grid). Contour intervals are in units of K. Case with
synoptic wind.

Figure 134: Potential temperature field on terrain following coordinate 122 m
above surface at 1200 UTC (fine grid). Contour intervals are in units of K. Case with
synoptic wind.

the lower-level large-scale temperature (or moisture) field in the tropics has a profound effect on the weather. The "cold pool" was more intense at 1200 UTC than at 0600 UTC as the curvature of the isentropes was sharper. Figures 135 and 136 display the θ field at 1600 UTC where the maximum registered value for θ over Kenya was 308.4 K (with a minimum of 300.4 K). The temperature falls gradually to the end of the simulation. Figure

Figure 135: Potential temperature field on a terrain following coordinate 122 m above surface at 1600 UTC (coarse grid). Contour intervals are in units of K. Case with synoptic wind.

137 showed that the isentropes at 19.443 km height had the same general orientation as those close to the surface.

The vertical east-west cross-sections for the θ field are depicted in Figures 138 to 141 at 0600 UTC, 0900 UTC, 1200 UTC, and 1600 UTC, respectively. These fields were 50 km south of the equator. There was no dramatic change in the θ fields from 0600 UTC to 1600 UTC. However, the general configuration of the isentropes depicted a well-mixed layer in the lower levels and middle levels up to an average height of 12.0 km and an isothermal layer in the upper levels.

Figure 136: Potential temperature field on terrain following coordinate 122 m above surface l at 1600 UTC (fine grid). Contour intervals are in units of K. Case with synoptic wind.

Figure 137: Potential temperature field on terrain following coordinate 19.44 km above surface at 1800 UTC. Contour intervals are in units of K. Case with synoptic wind.

133
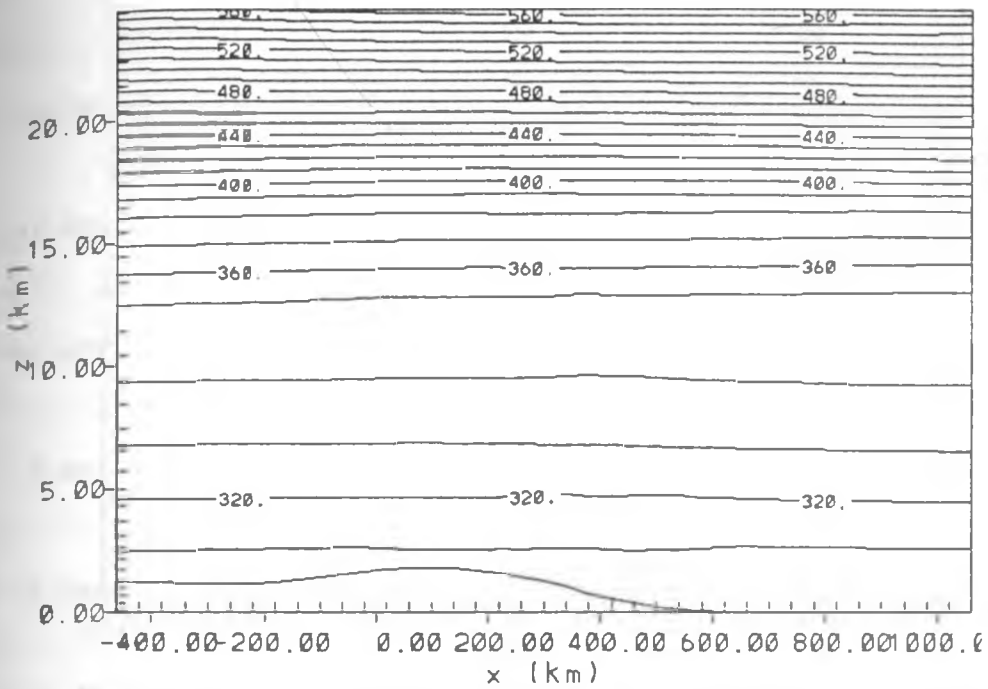
Figure 138: Vertical east-west cross-section of potential temperature at 0.5°S for 0600 UTC. Contour intervals are in units K. Case with synoptic wind.
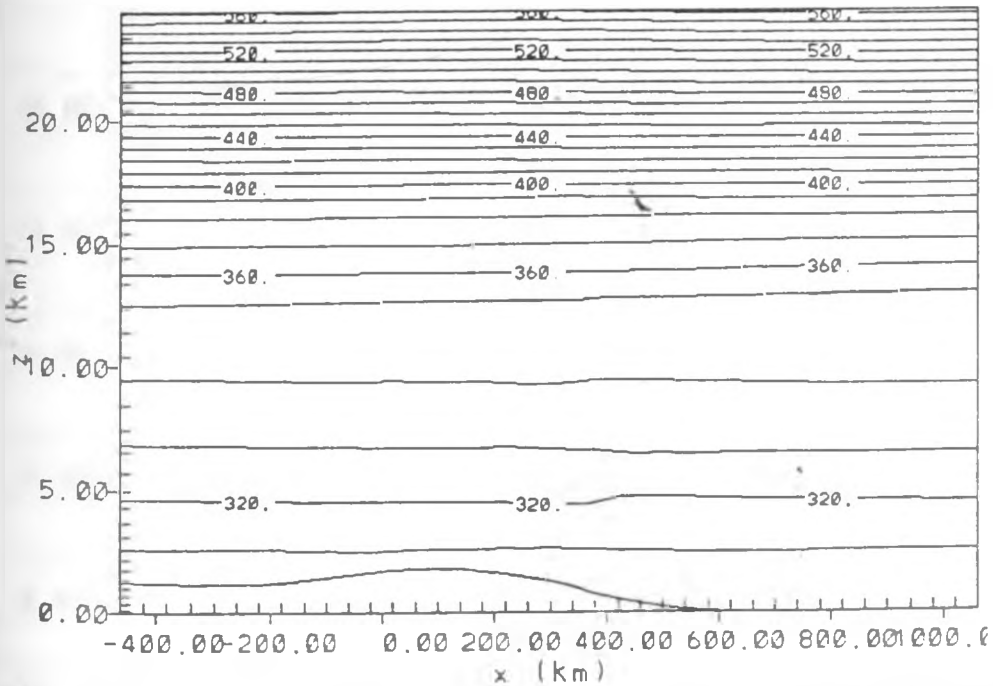
Figure 139: Vertical east-west cross-section of potential temperature at 0.5°S for 0900 UTC. Contour intervals are in units of K. Case with synoptic wind.
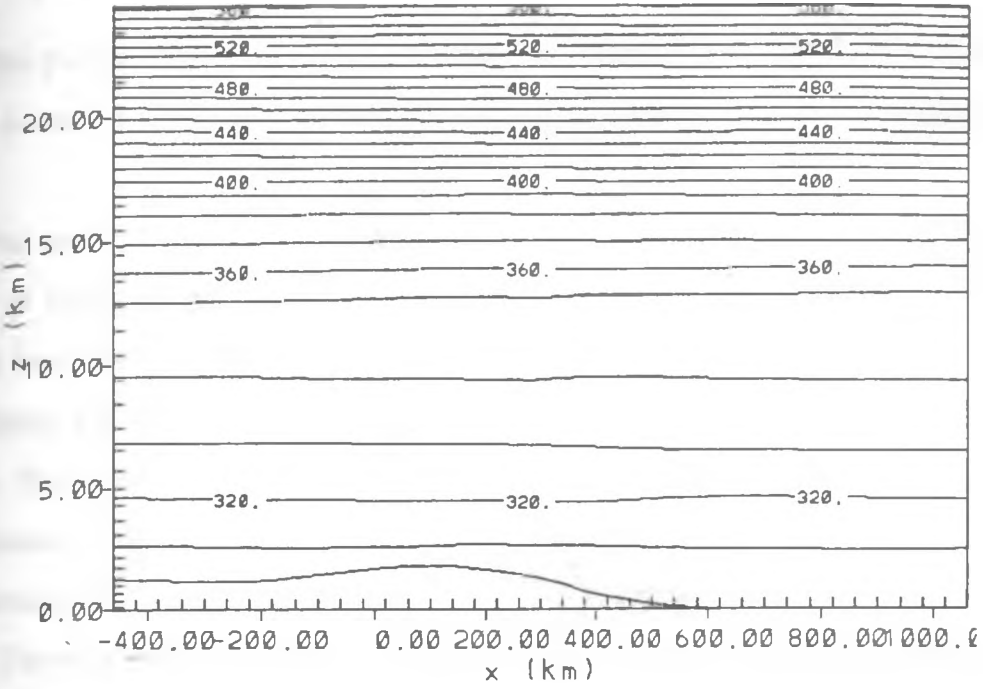
Figure 140: Vertical east-west cross-section of potential temperature at 0.5°S for 1200 UTC. Contour intervals are in units of K. Case with synoptic wind.
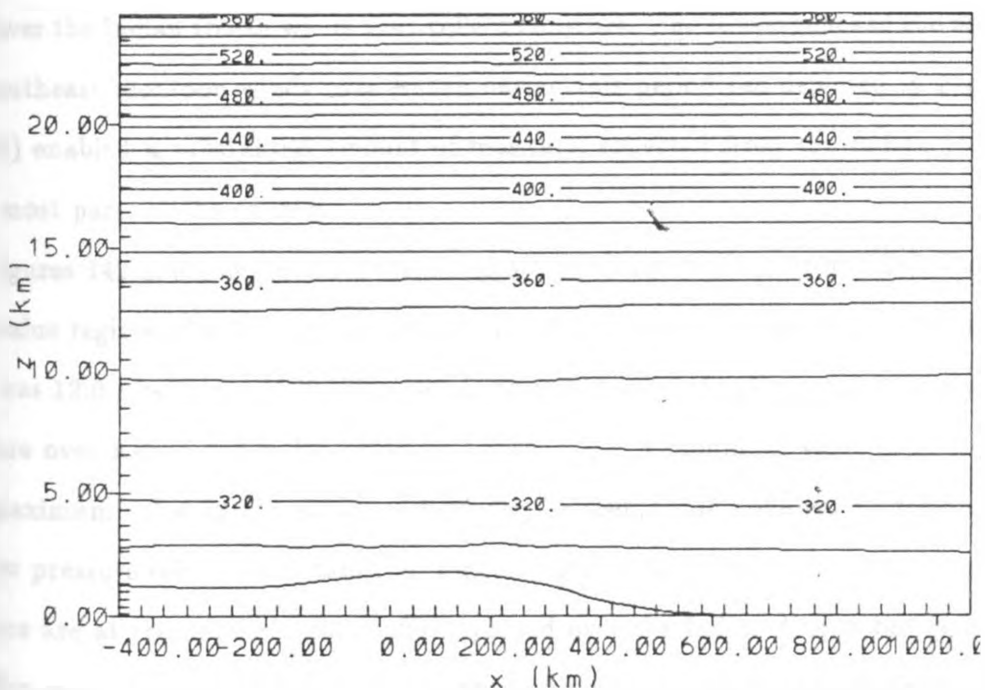
Figure 141: Vertical east-west cross-section of potential temperature at 0.5°S for 1600 UTC. Contour intervals are in units of K. Case with synoptic wind.

8.1.5 The Large-Scale Moisture Field

The parameter used to measure moisture in this study was the Total Water Mixing Ratio which is defined as the total amount of moisture (in grams) contained in one kilogram of air.

The moisture field at low levels ($\sigma_z = 122$ m) decreases with time during the initial hours of the afternoon. This decrease could probably be attributed to the fact that as the land heated up the air warmed up and expanded, causing an increase in static instability, and through vertical mixing, the moisture or vapour is transferred to upper layers. The moisture increased in the afternoon from a maximum value of 20.8 g kg^{-1} over the domain at the start of the simulation to a maximum of 22.4 g kg^{-1} at 12 hours into the simulation. This was an increase of 1.6 g kg^{-1} in the lower-level large-scale moisture field. The moisture decreased slightly during the last hours of the model simulation. This decrease could well be due to precipitation having taken place. The increase in moisture in the course of the simulation lent support to the assertion that the large-scale monsoon winds inject moisture into the region having had a long trajectory (especially the southeast flow) over the Indian Ocean where they collect moisture. The convergence of the northeast and southeast monsoon winds over Kenya during this period (as depicted in Figures 52 and 53) enabled a substantial amount of moisture, collected from the Indian Ocean, to reach most parts of the country.

Figures 142 and 143 illustrate the Total Mixing Ratio field at 0600 UTC. The maximum value registered over Kenya at this level and time was 21.0 g kg^{-1} and the minimum value was 12.0 g kg^{-1}. At 1200 UTC (see Figures 144 and 145) the maximum value of the moisture over Kenya had increased to 22.4 g kg^{-1} and a minimum value of 14.0 g kg^{-1}. The maximum value of the moisture field can be seen to be confined to regions which had low pressure cells. For instance, in Figure 143 at 0600 UTC, the maximum moisture contours are at the northern coast of Kenya and over the Indian Ocean but (see Figure 145) the maxima moved inland in a northward direction to the east of Kenya exactly where there was a low pressure cell (see Figures 94 and 99). Contour configuration in Figures 146 and 147 at 1600 UTC indicated that moisture was being pushed to the west
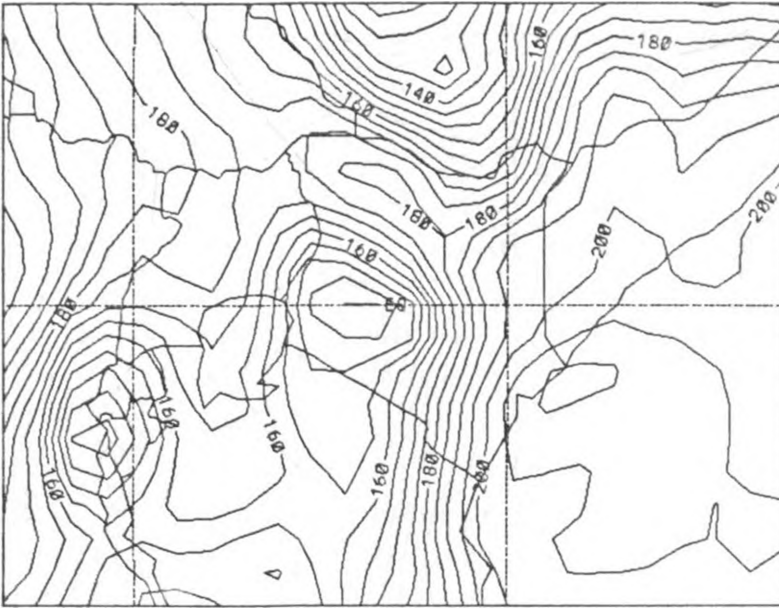
Figure 142: Total water mixing ratio field on terrain following 122 m above surface 0600 UTC (coarse grid). Contour intervals are in g kg^{-1}. Labels *1.0×10^{-1}. Case with synoptic wind.
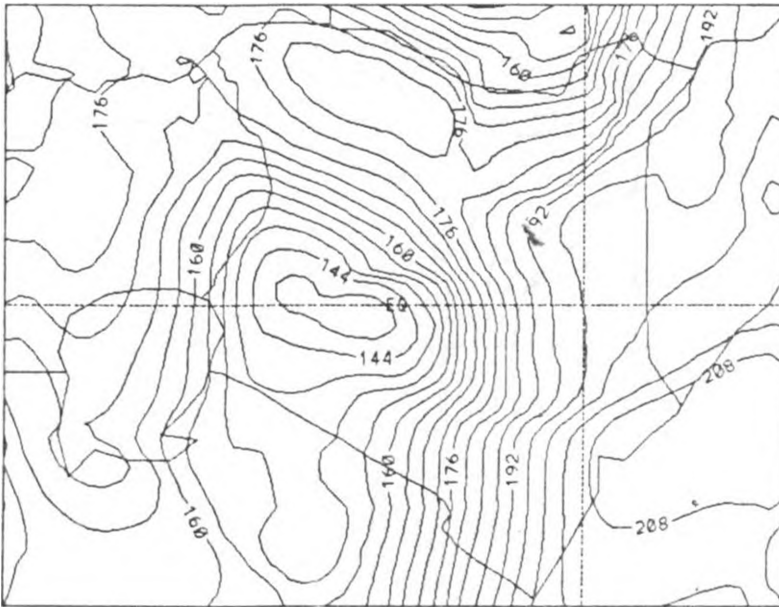
Figure 143: Total water mixing ratio field on terrain following coordinate 122 m above surface1 at 0600 UTC (fine grid). Contour intervals are in units of g kg^{-1}. Labels *1.0×10^{-1}. Case with synoptic wind.
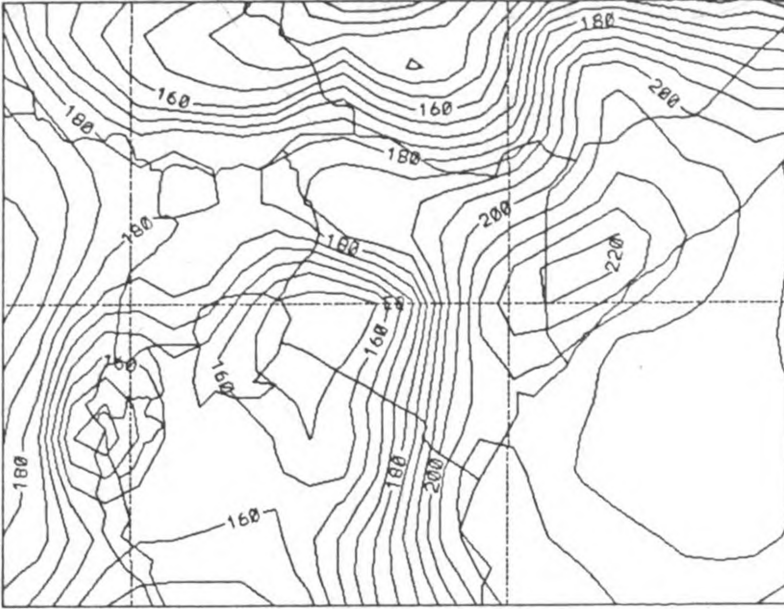
Figure 144: Total water mixing ratio field on terrain following coordinate 122 m above surface at 1200 UTC (coarse grid). Contour intervals are in units of g kg^{-1}. Labels *1.0×10^{-1}. Case with synoptic wind.
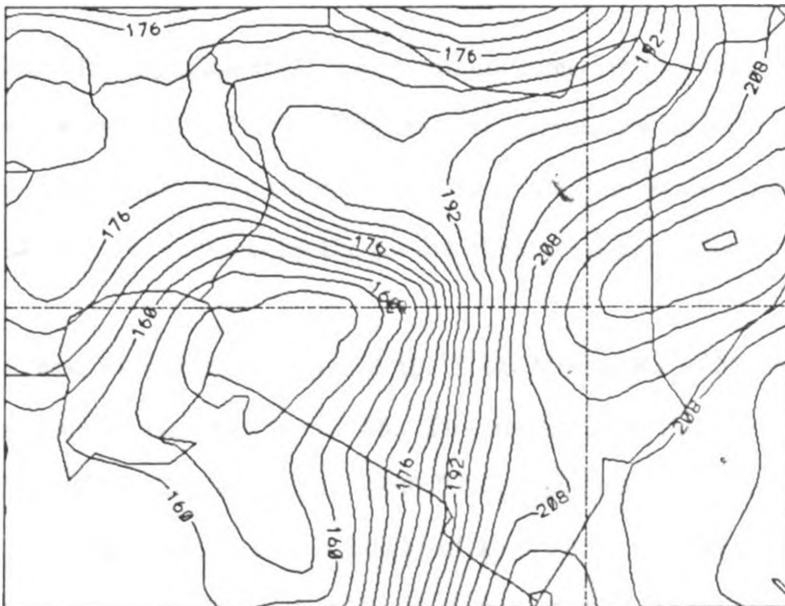
Figure 145: Total water mixing ratio field on terrain following coordinate 122 m above surface at 1200 UTC (fine grid). Contour intervals are in units of g kg^{-1}. Labels *1.0×10^{-1}. Case with synoptic wind.

138

and north of the study domain as compared to the situation at 0600 UTC and 1200 UTC. However, the maximum value of moisture registered on the domain at 1600 was still 22.4
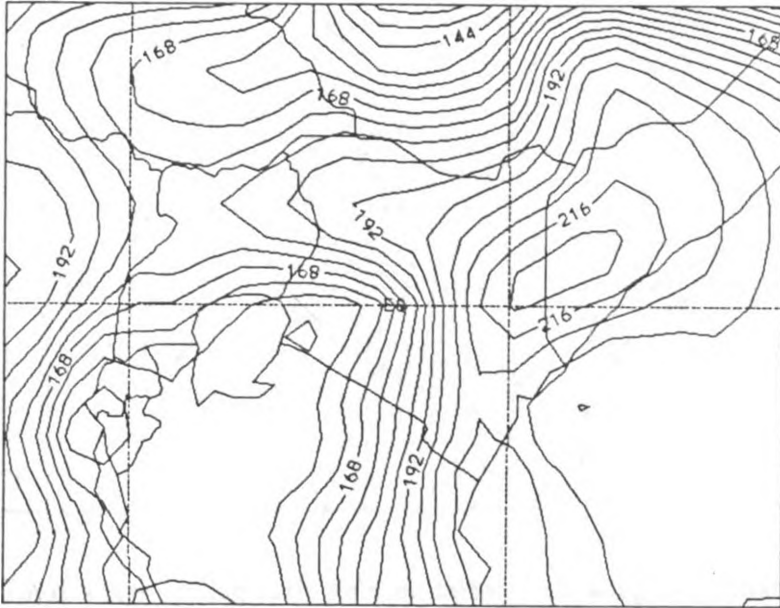
Figure 146: Total water mixing ratio field on terrain following coordinate 122 m above surface at 1600 UTC (coarse grid). Contour intervals are in units of g kg^{-1}. Labels *1.0×10^{-1}. Case with synoptic wind.

g kg^{-1} as at 1200 UTC. By 2400 UTC the maximum moisture had slightly decreased to 22.0 g kg^{-1} (see Figures 148 and 149). The transfer of moisture inland over Kenya may be attributed, in large measure, to the contribution of the large-scale winds at low levels as will be verified later when discussing the results of moisture generated by the mesoscale circulations.

The vertical east-west cross-sections for the Total Mixing Ratio 50 km south of the equator are displayed in Figures 150 to 155. The figures show moisture fields at 0600 UTC, 0900 UTC, 1200 UTC, 1600 UTC, 1800 UTC, and 2000 UTC, respectively. The fields show that moisture extended to a height of about 8.0 km from the surface. The vertical moisture profile indicates that moisture decreased with height from a maximum of about 21.0 g kg^{-1} at σ_z = 112 m from the surface diminishing to a negligible value at 8.0 km height. There was no appreciable increase or decrease of moisture across the domain with time although the model registered a maximum moisture value of 21.0 g kg^{-1}
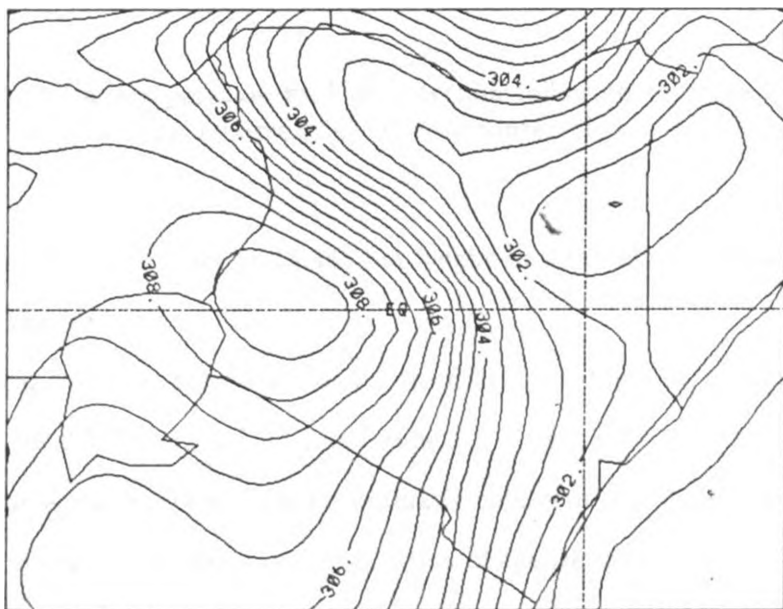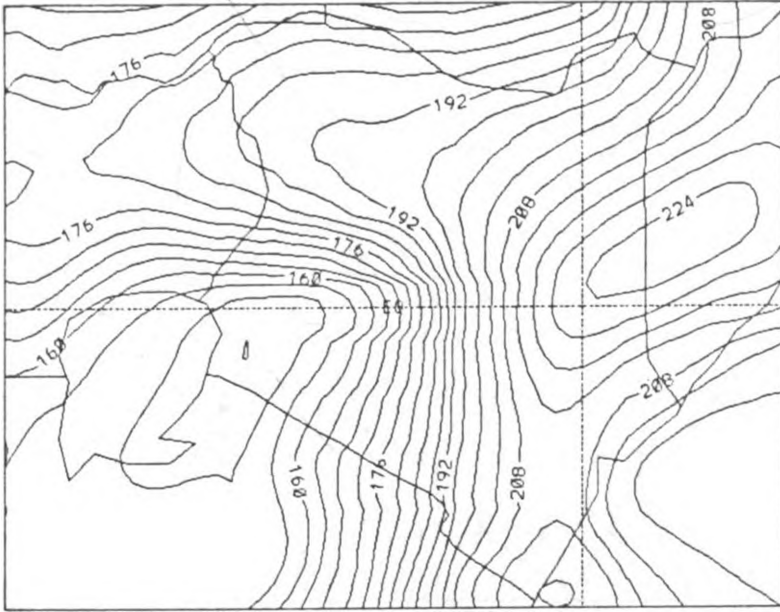
Figure 147: Total water mixing ratio field on terrain following coordinate 122 m above surface at 1600 UTC (fine grid). Contour intervals are in units of g kg^{-1}. Labels *1.0×10^{-1}. Case with synoptic wind.
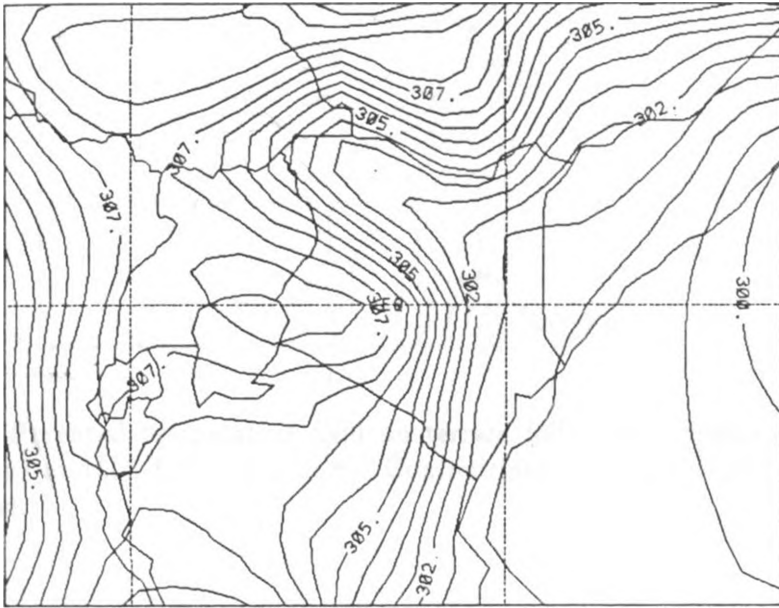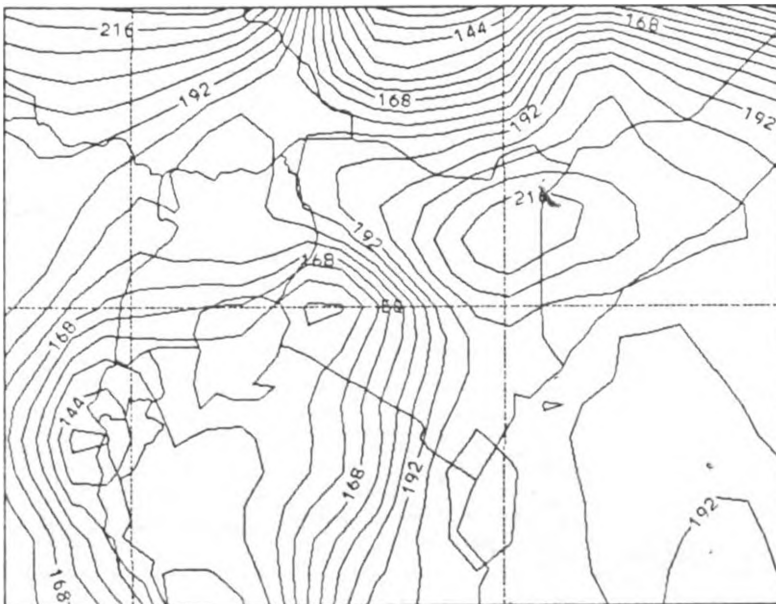

Figure 148: Total water mixing ratio field on terrain following coordinate 122 m above surface at 2400 UTC (coarse grid). Contour intervals are in units of g kg^{-1}. Labels *1.0×10^{-1}. Case with synoptic wind.
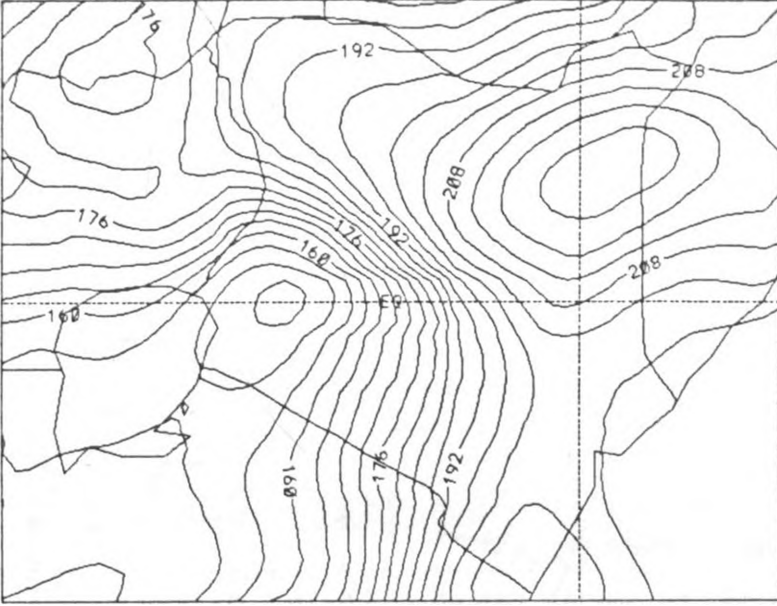
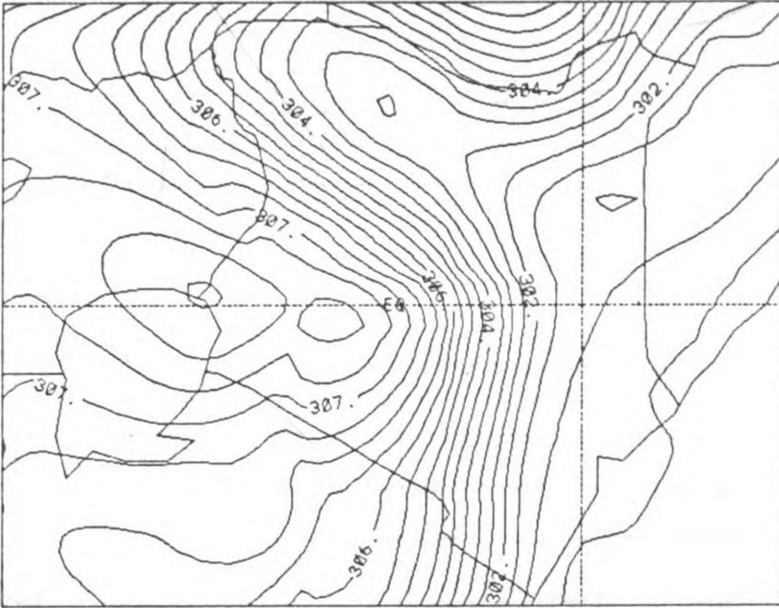Figure 149: Total water mixing ratio field on terrain following coordinate 122 m above surface at 2400 UTC (fine grid). Contour intervals are in units of g kg^{-1}. Labels *1.0×10^{-1}. Case with synoptic wind.
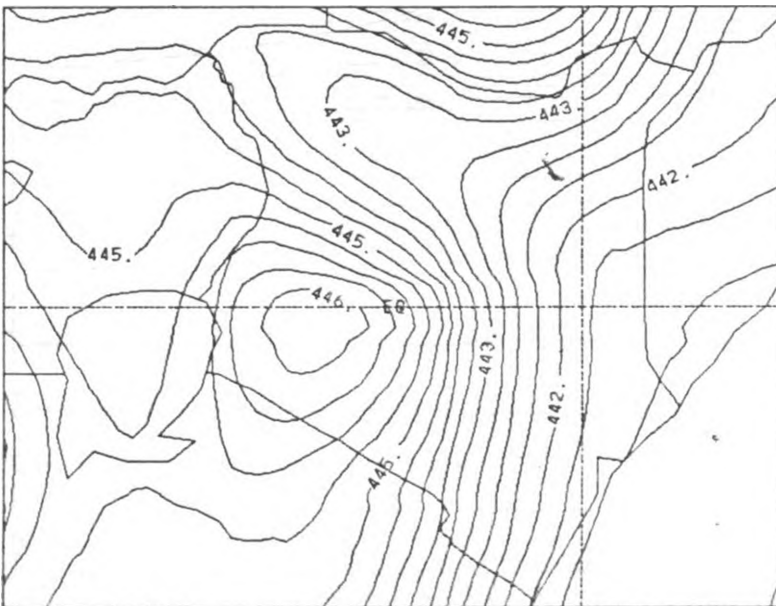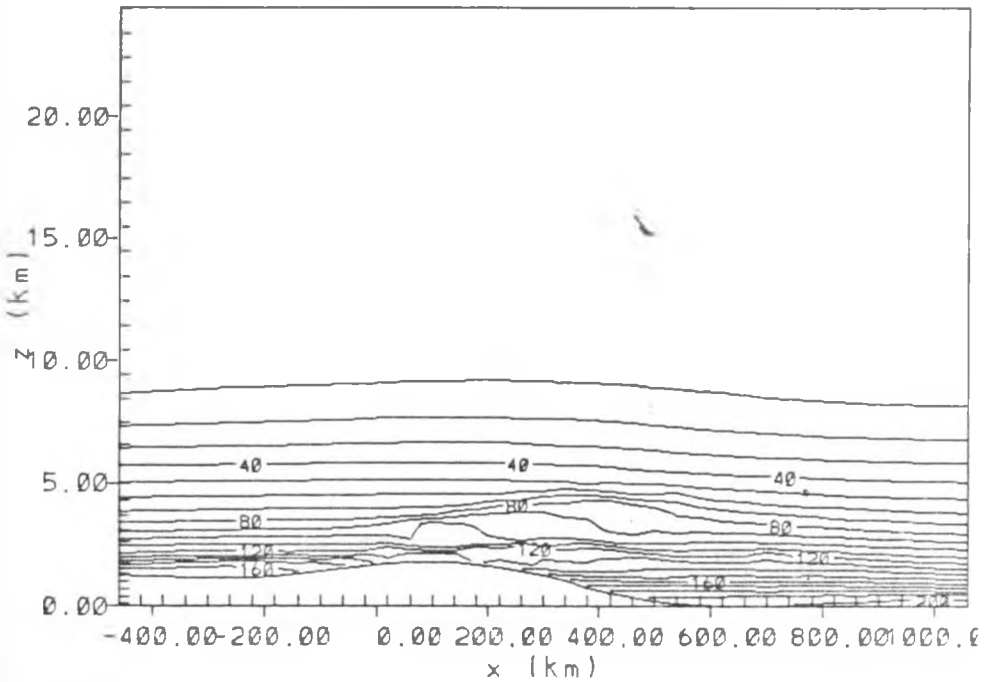

Figure 150: Vertical east-west cross-section of total water mixing ratio of 0.5°S for 0600 UTC. Contour intervals are in units of g kg^{-1}. Labels *1.0×10^{-1}. Case with synoptic wind.
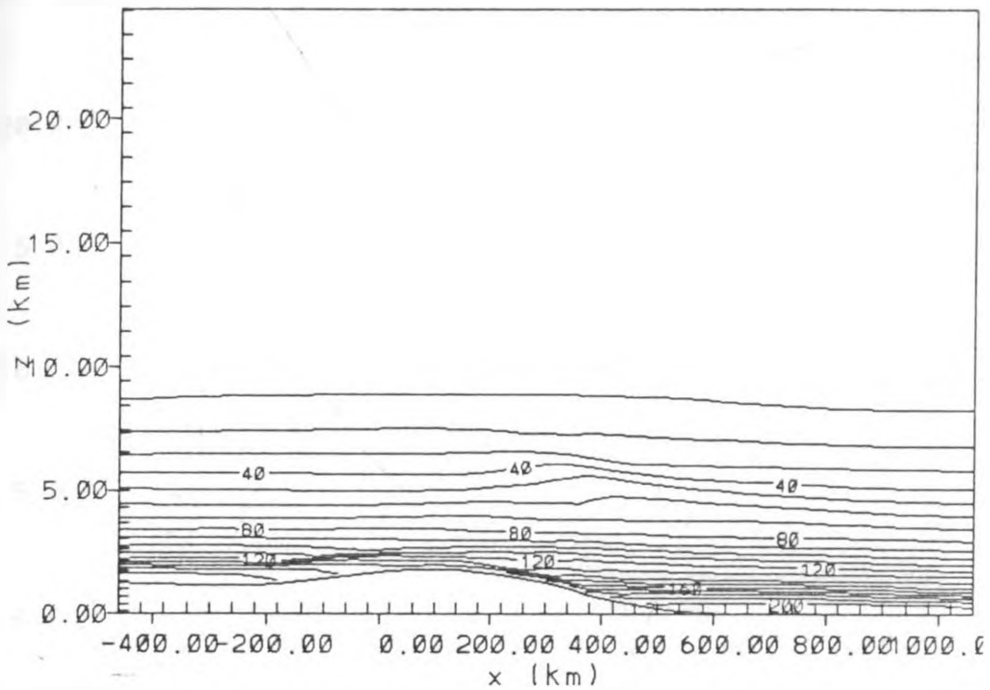
Figure 151: Vertical east-west cross-section of total water mixing ratio of 0.5°S for 0900 UTC. Contour intervals are in units of g kg^{-1}. Labels *1.0×10^{-1}. Case with synoptic wind.
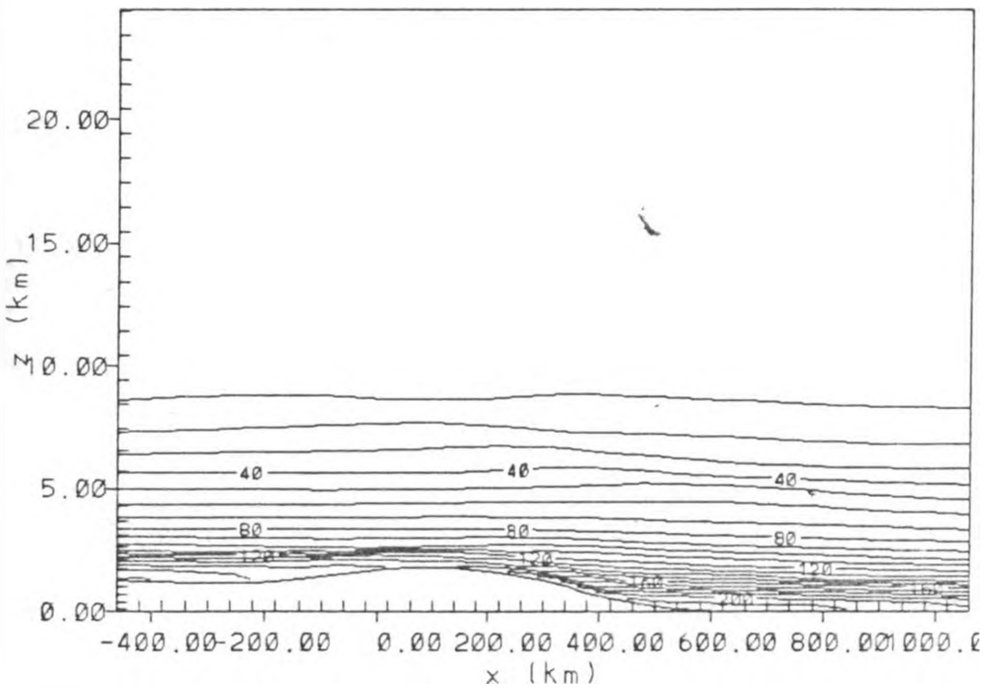
Figure 152: Vertical east-west cross-section of total water mixing ratio at 0.5°S for 1200 UTC. Contour intervals are in units of g kg^{-1}. Labels *1.0×10^{-1}. Case with synoptic wind.
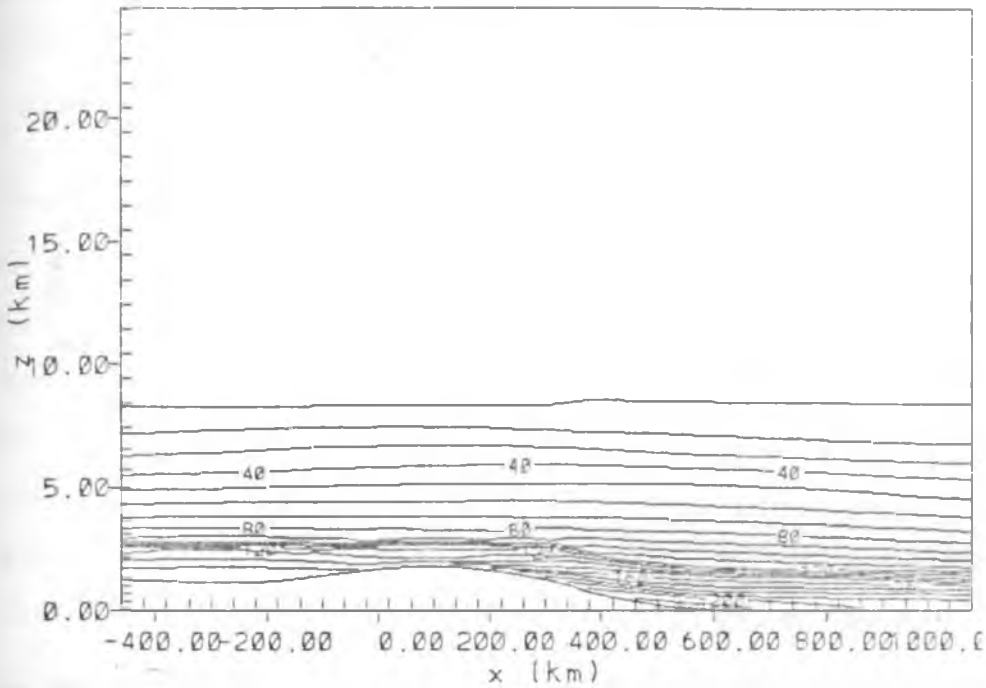
Figure 153: Vertical east-west cross-section of total water mixing ratio at 0.5°S for 1600 UTC. Contour intervals are in units of g kg^{-1}. Labels *1.0×10^{-1}. Case with synoptic wind.
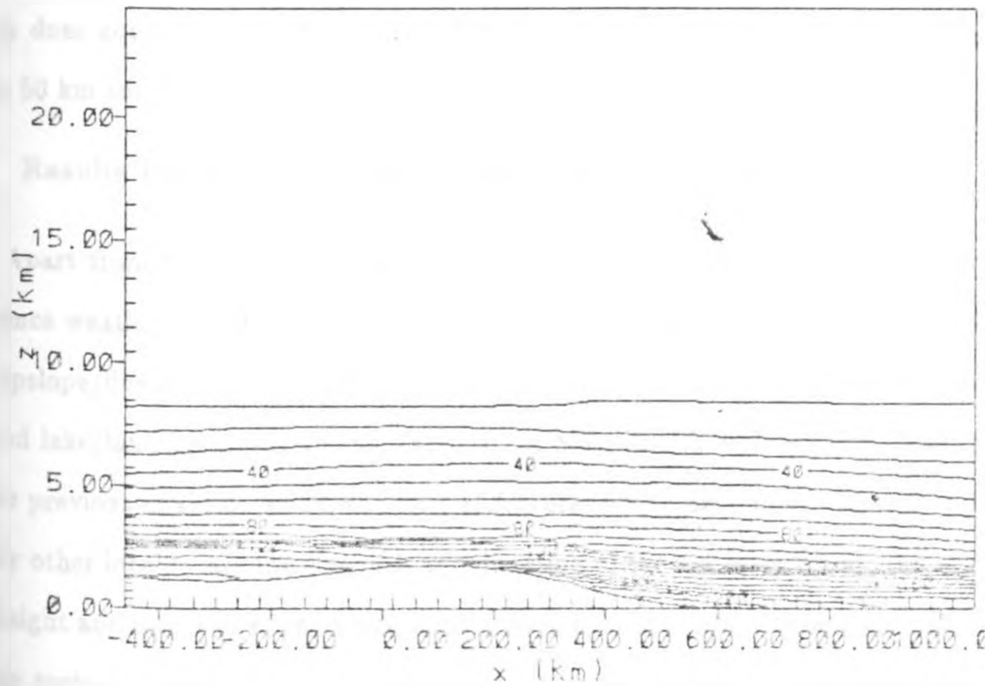
Figure 154: Vertical east-west cross-section of total water mixing ratio at 0.0°S for 1600 UTC. Contour intervals are in units of g kg^{-1}. Labels *1.0×10^{-1}. Case with synoptic wind.
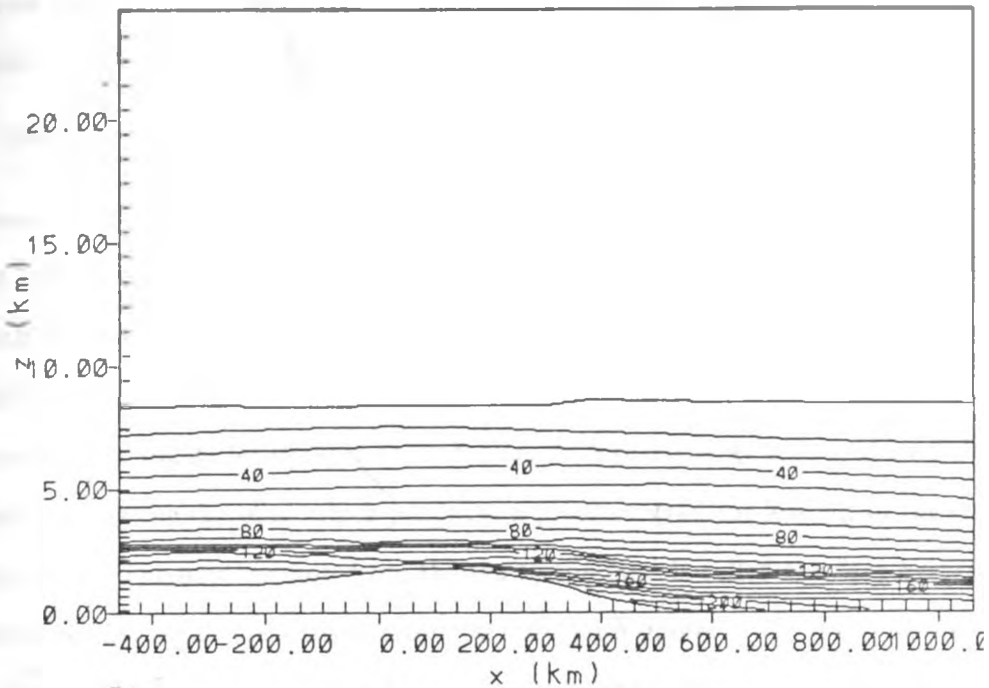
Figure 155: Vertical east-west cross-section of total water mixing ratio at 0.5°S for 2000 UTC. Contour intervals are in units of g kg^{-1}. Labels *1.0×10^{-1}. Case with synoptic wind.

(at lower levels) at 1200 UTC and 1600 UTC as compared to 20.5 g kg^{-1} at the equator, which does not show any significant difference in configuration from the other moisture fields 50 km south of the equator.

6.2   Results From Experiment 2: Mesoscale Flow Fields

Apart from the synoptic-scale systems, the convective and mesoscale systems also influence weather over Kenya. The systems include (i) sea/land breezes along the coast; (ii) upslope/downslope winds due to orography; (iii) the Lake Victoria Trough and the related lake/land breezes; (iv) the Turkana (or Marsabit) Low Level Jetstream discussed in the previous chapter. Thus, the critical features which determine weather in Kenya as in any other locality are the strength and direction of the low level winds, the topography, the height and intensity of the trade wind inversion, the land/sea breeze and the lake/land breeze regimes. These local influences are superimposed upon the synoptically-induced weather discussed in the previous section and are fairly strong in the tropics. There is also surface forcing through surface roughness, latent and sensible heating. In the following

sections of this chapter the above mentioned mesoscale features affecting weather over Kenya are discussed in light of the model output.

8.2.1 Breeze Circulations

Breeze circulations are local winds caused by the unequal heating and cooling of the adjacent land and water surfaces. The water surfaces as well as the air immediately above rarely exhibit any appreciable diurnal temperature change. On the other hand, the land frequently displays a large temperature range from day to night, particularly in the tropics and at middle and higher latitudes in the summer. As a result large temperature difference can develop along the shoreline which produces a pressure gradient leading to the creation of a circulation. The daytime flow from the sea to the land is called the "sea breeze" and the reverse flow at night and early morning as the "land breeze".

In Kenya, the breeze circulations are generated within the vicinity of Lake Victoria and along the coast. A weak land breeze can be seen in Figure 156 along the coast at 0300 UTC (6:00 a.m. Kenya Local Time). A relatively strong land to lake breeze is
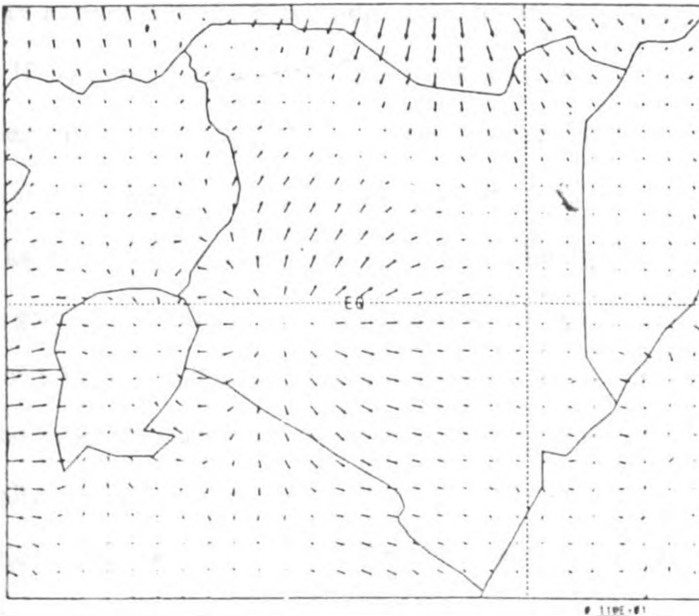
Figure 156: Wind vectors on terrain following coordinate 72.4 m (at 0300 UTC) above surface   Case with no synoptic wind.

depicted in Figure 157 at 0500 UTC (or 8:00 a.m. Kenya Local Time). The sea breeze in
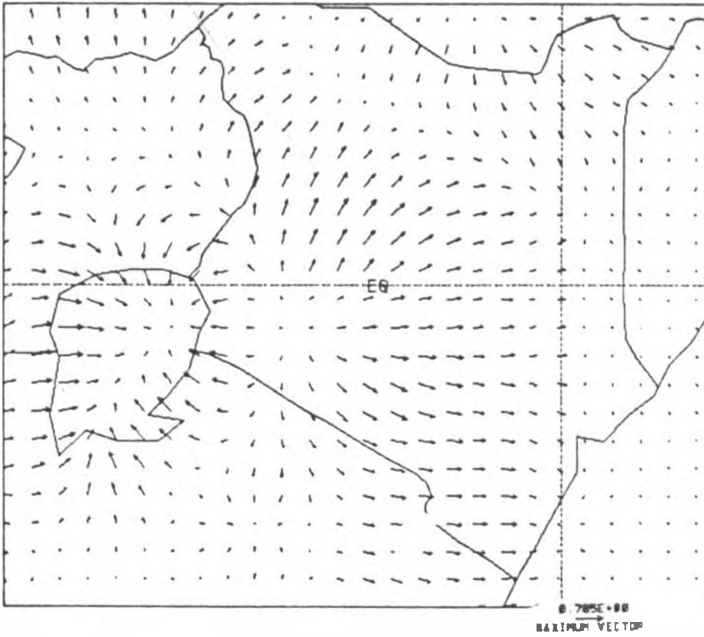
Figure 157: Wind vectors on terrain following coordinate 72.4 m above surface
at 0500 UTC. Case with no synoptic wind.

Figure 158 at 1600 UTC (7:00 p.m. Kenya Local Time) was seen to be stronger than the
land breeze; it coupled with the upslope wind along the coast and transported moisture
from the ocean surface inland. The modeled sea breeze was observed to start during the
forenoon (at 10:00 a.m. Kenya Local Time) and attained a maximum intensity at 1600
UTC. However, in order to adequately resolve a strong breeze circulation in RAMS, grid
intervals of about 10 km in the horizontal and 20 to 25 m intervals in the vertical are
necessary. The resolution used in this study (i.e., a horizontal grid increment of 75 km
in the coarse grid and 25 km in the fine grid with 150 m intervals in the vertical and a
stretch ratio of 1.15) was sufficient to generate a weak breeze. Nevertheless, the resolution
used was considered satisfactory for this study since a finer resolution would have been
computationally very expensive.

As mentioned above, the impact of this breeze circulation is firstly, to transport
moisture from the water surface inland; and secondly, the breeze circulation may couple
with upslope winds to converge with the prevailing large-scale winds at low levels (flowing
in the opposite direction) to effect some active weather (clouds and precipitation).
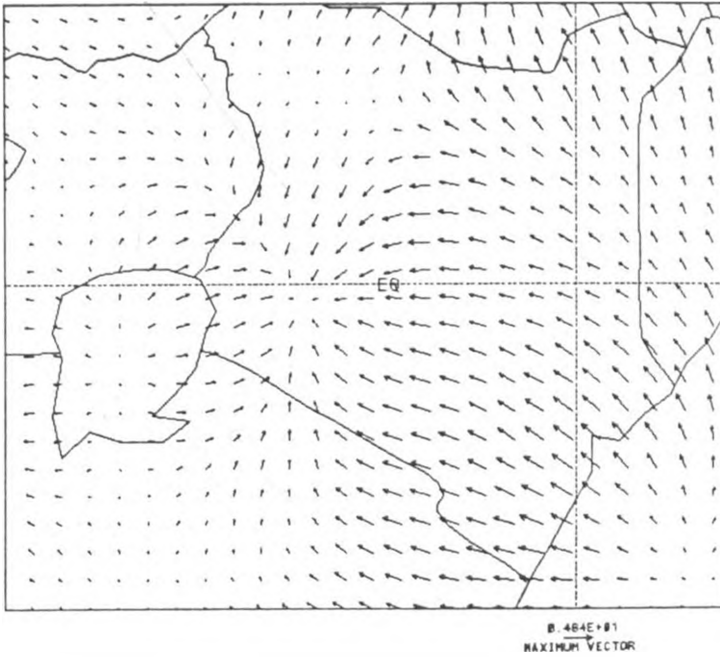
Figure 158: Wind vectors on terrain following coordinate 72.4 m above surface at 1600 UTC. Case with no synoptic wind.

6.2.2 Orographic Effects

Topography plays a major role in weather modification in Kenya in that the country is complicated with many mountains with the great Rift Valley running in the middle meridionally. Most of the country is high (over 1200 m above MSL) hence the general flow is very modified both laterally and vertically.

One of the local effects are the thermally-induced downslope (or katabatic) winds depicted in Figures 156 and 157 during the early morning when the highlands were colder (due to more radiational cooling) than the lowlands and water surfaces. The winds were seen to drain off downwards from the highest point in the model domain located in the southwestern part of Kenya, in the Kericho area. Some of the downslope winds moving north converged with other similar winds draining off downwards from the Ethiopian Highlands into the "Turkana-Marsabit corridor" and over Lake Turkana in the northwestern part of the country.

The reverse currents, the upslope (or anabatic) winds are depicted in Figure 158 in the late afternoon. The high grounds warmed up faster than the lowlands and the large water

bodies and so the temperature and pressure gradients developed to reverse the direction of the winds towards the highest point in the domain where the pressure was lowest. The winds were seen moving from all directions to the highest point in the southwest part of the country and up the Ethiopian Highlands to the north of Kenya. The town of Kericho is located within the zone of convergence and the surrounding area is reputed to have the highest frequency of thunderstorm/hailstorm days in the world (Alusa, 1986; Okeyo, 1987).

It should be noted that a strong confluence over the highlands was registered in the surface winds observed at 15 Z (see Figure 42) whose flow reflected influence from surface features. There was a divergence of air within the Turkana-Marsabit corridor with more divergence over Lake Turkana. Lake Turkana lies in the eastern arm of the great Rift Valley in Kenya and is the largest lake in the country. Thus, apart from modifying temperatures, orography in Kenya also assists in the raising of low level air thereby causing the release of instability with the resultant formation of clouds and precipitation.

6.2.3 The Lake Victoria Trough

The quasi-permanent Lake Victoria Trough has a strong influence on the weather of the "Lake Region". Lake Victoria has its own circulation pattern which causes rainfall all year round over the surrounding area.

Downslope winds from the highlands coupled with the land breeze during the early hours of the morning (see Figures 156 and 157). The upslope winds, on the other hand, coupled with the lake breeze to flow upslope towards the highest grounds in the model domain during the afternoon and early evening (Figure 158).

Some results from the coarse grid resolution simulated the flow features in the model domain and for that reason several were shown alongside the fine grid forecast products.

Figure 159 and 160 illustrate the zonal wind component (u) during the early morning at 0500 UTC (or 8:00 a.m. local time). The dotted lines for the zonal wind field denote the easterlies and the solid lines the westerlies. The maximum value for the easterlies was 0.48 m s^{-1} and 0.72 m s^{-1} for westerlies over Kenya. The westerlies and easterlies are seen to converge over Lake Victoria and to flow away from the high grounds. Westerly winds were depicted on the eastern side of the highlands and off-shore winds at the coast.

Figure 159: The zonal wind field (u) on terrain following coordinate 72.4 m above surface at 0500 UTC (coarse grid). Contour interval is 0.2 m s^{-1}. Case with no synoptic wind.

Figure 160: The zonal wind field (u) on terrain following coordinate 72.4 m above surface at 0500 UTC (fine grid). Contour interval is 0.08 m s^{-1}. Case with no synoptic wind.
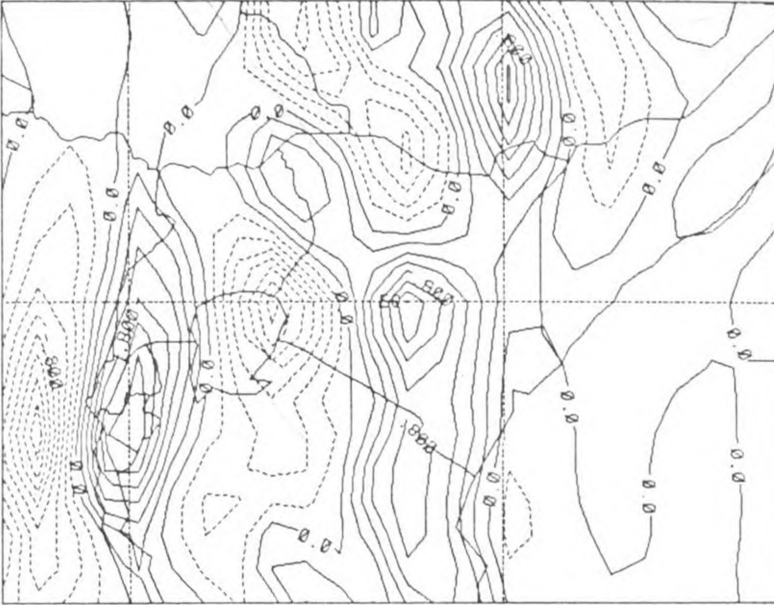
Figures 161 and 162 show the zonal wind (u) at 1600 UTC and illustrate a reverse flow of the morning winds. The maximum value of easterlies was -4.4 m s^{-1} with maximum

Figure 161: The zonal wind field on terrain following coordinate 72.4 m above surface at 1600 UTC (coarse grid). Contour interval is 0.5 m s^{-1}. Case with no synoptic wind.

westerlies of 2.4 m s^{-1}. There was divergence over Lake Victoria and convergence over the high grounds.

Figures 163 and 164 depict the meridional wind component (v) during the early morning at 0500 UTC. Here, the dotted lines denote a flow from north to south (northerlies) and solid lines denote a flow from south to north (southerlies). The winds are seen to converge over Lake Victoria (from north and south) and to drain off from the high grounds (towards north and south). The maximum value of the southerlies was 0.56 m s^{-1} and -0.49 m s^{-1} for the northerlies. The meridional flow field depicted in Figures 165 and 166 similarly showed a reverse scenario to the flow during the morning hours as northerlies and southerlies flowed out of Lake Victoria (low-level divergence) and towards the highest point over the highlands (low-level convergence). The maximum value of northerlies was -2.4 m s^{-1} and 3.6 m s^{-1} for the southerlies. The southerlies were relatively strong at the coast and over the northeastern part of the country.

Figure 162: The zonal wind field on terrain following coordinate 72.4 m above surface at 1600 UTC (fine grid). Contour interval is 0.4 m s^{-1}. Case with no synoptic wind.
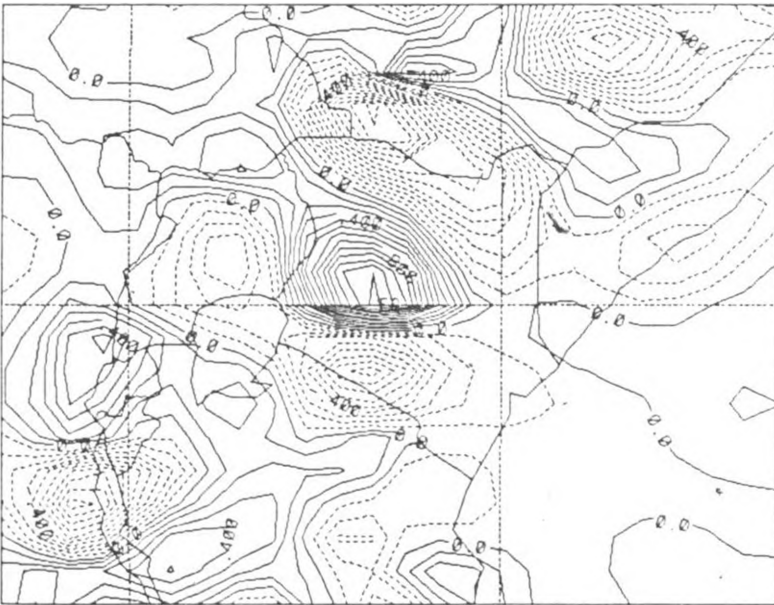
Figure 163: The meridional wind field (v) on terrain following coordinate 72.4 m above surface at 0500 UTC (coarse grid). Contour interval is 0.1 m s^{-1}. Case with no synoptic wind.
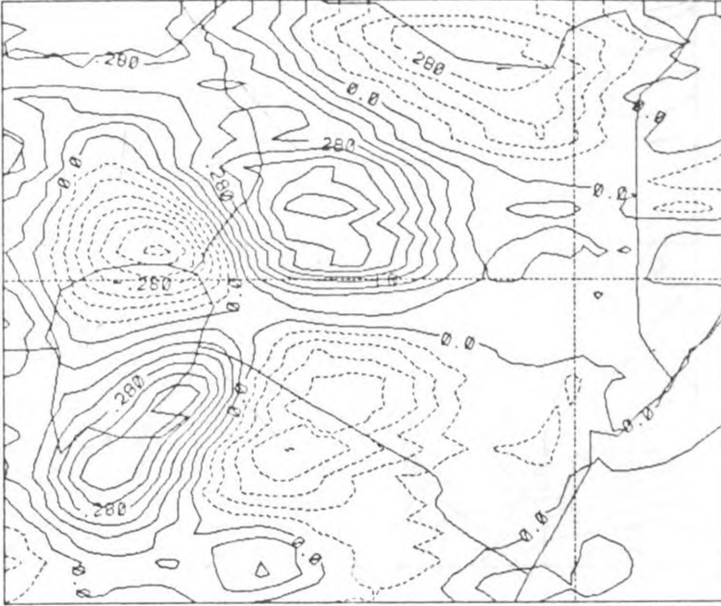
Figure 164: The meridional wind field (v) on terrain following coordinate 72.4 m above surface at 0500 UTC (fine grid). Contour interval is 0.07 m s^{-1}. Case with no synoptic wind.
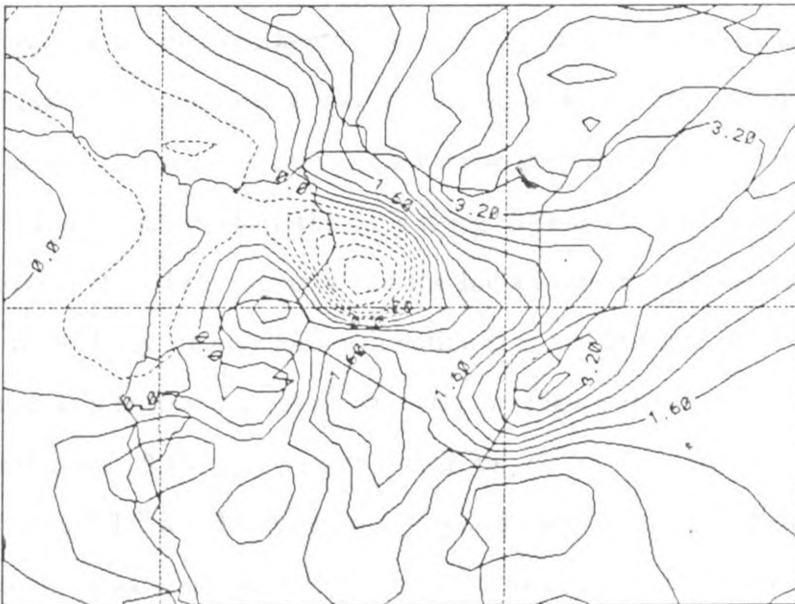
Figure 165: The meridional wind field (v) on terrain following coordinate 72.4 m above surface at 1600 UTC (coarse grid). Contour interval is 0.4 m s^{-1}. Case with no synoptic wind.
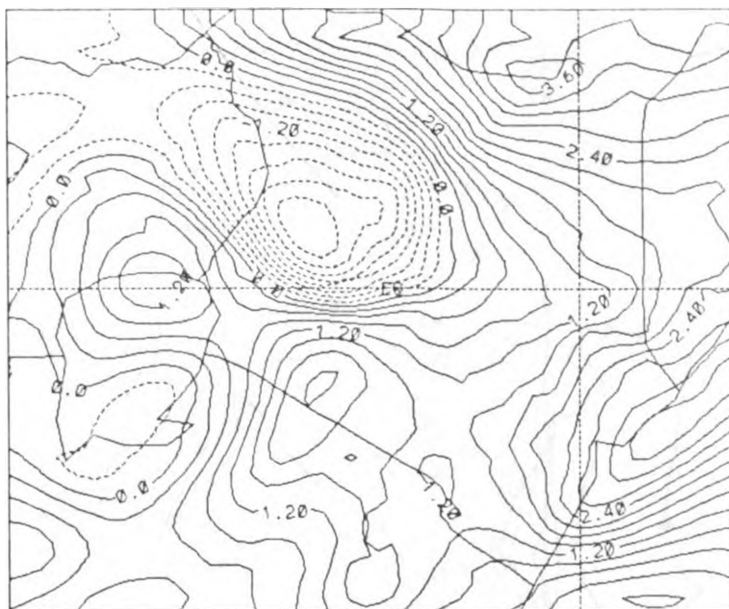
Figure 166: The meridional wind field (v) on terrain following coordinate 72.4 m above surface ₁ at 1600 UTC (fine grid). Contour interval is 0.3 m s^{-1}. Case with no synoptic wind.

The vertical motion field is displayed in Figures 167 and 168. The dotted lines denote subsidence or descending motion and the solid lines denote upward or ascending motion. It is evident that during the morning hours there was sinking motion over much of the land areas except the low-lying areas such as part of the Turkana-Marsabit corridor (and over Lake Turkana), along the northern coast and a narrow strip along the eastern portion of the country (and into Somalia) where the air is rising. There was also rising motion over large water bodies, that is, Lake Victoria and the Indian Ocean that were warmer than the land at this time of day. It may be worth noting that the Turkana-Marsabit corridor is very well defined as a narrow zone of rising motion in Figure 168. The maximum value of ascending motion was 0.15 cm s^{-1} with -0.42 cm s^{-1} of subsidence. The vertical motion fields at 1600 UTC are displayed in Figures 169 and 170. These fields displayed an ascending motion (maximum value of 3.0 cm s^{-1}) over most parts of the land surface except parts of the Turkana-Marsabit corridor, particularly over Lake Turkana, where there was subsidence (maximum value of -0.4 cm s^{-1}). It should be noted that Lake Turkana is the biggest lake within Kenya and might well be the cause of this sinking

Figure 167: The vertical wind motion field (w) on terrain following coordinate 72.4 m above surface at 0500 UTC (coarse grid). Contour interval is 0.6×10^{-3} m s^{-1}. Case with no synoptic wind.

Figure 168: The vertical wind motion field (w) on terrain following coordinate 72.4 m above surface at 0500 UTC (fine grid). Contour interval is 0.3×10^{-3} m s^{-1}. Case with no synoptic wind.
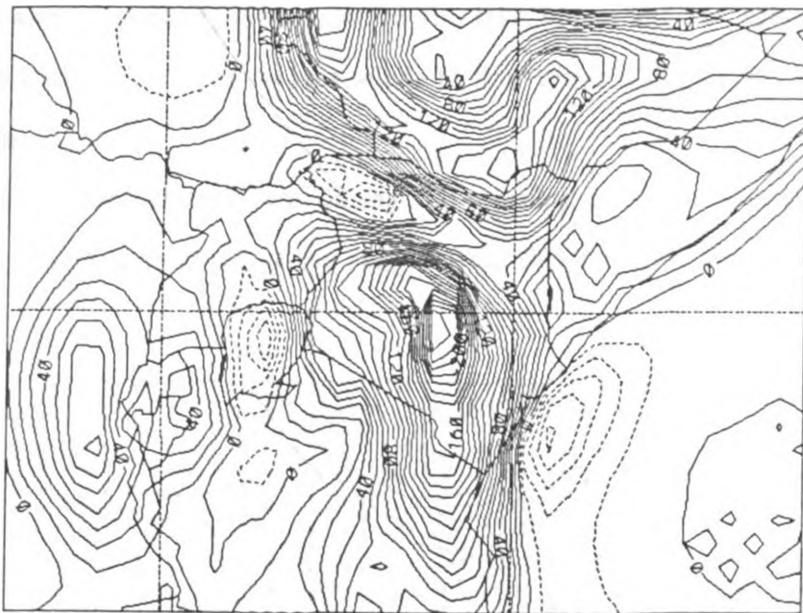
Figure 169: The vertical wind motion field (w) on terrain following coordinate 72.4 m above surface at 1600 UTC (coarse grid). Contour interval is 0.1×10^{-2} m^{-1}. Case with no synoptic wind.
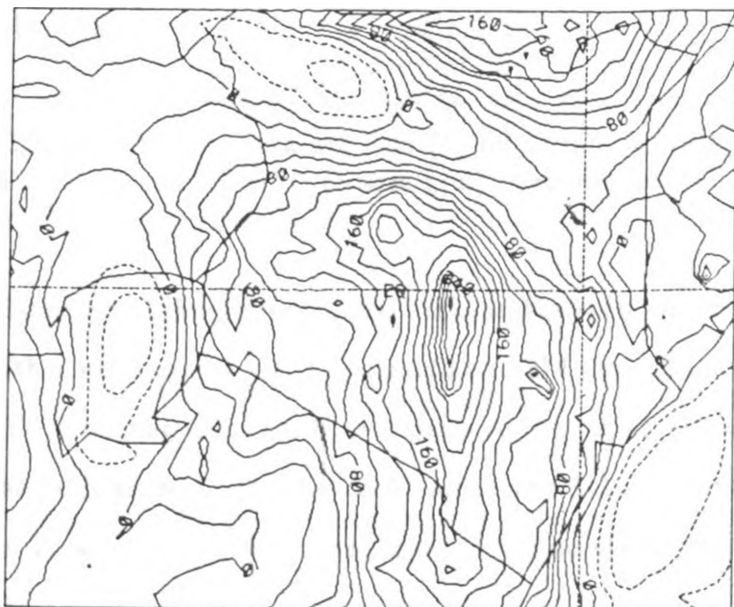
Figure 170: The vertical wind motion field (w) on terrain following coordinate 72.4 m above surface at 1600 UTC (fine grid). Contour interval is 0.2×10^{-3} m^{-1}. Case with no synoptic wind.

motion over this area at this period in time. Descending motions were seen over Lake Victoria and along the coast, giving rise to the lake breeze and sea breeze circulations both of which coupled with the upslope winds to flow towards the highest grounds in the model domain.

The potential temperature field during the morning hours are displayed in Figures 171 and 172. The temperature values ranged from 296.4 K over the ocean to 303.2 K
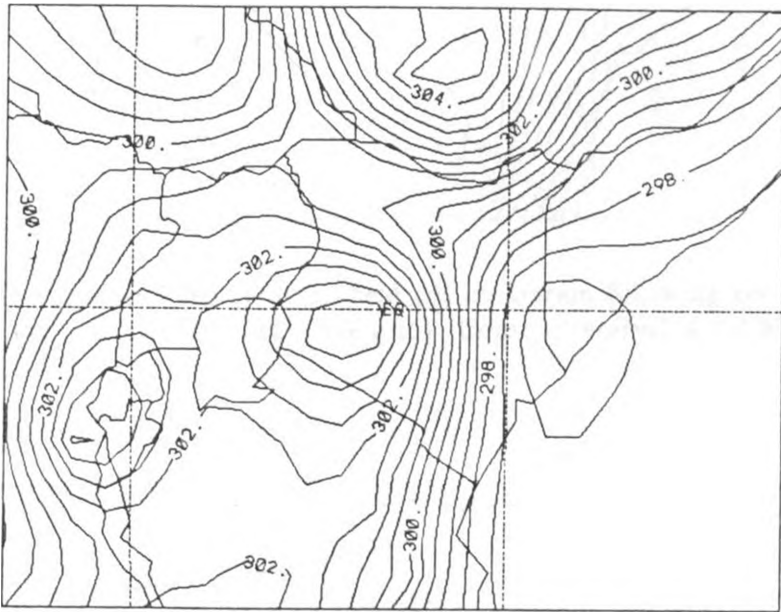
Figure 171: The potential temperature field (θ) on terrain following coordinate 72.4 m above surface at 0500 UTC (coarse grid). Contour interval is 0.5 K. Case with no synoptic wind.

over the highlands and Lake Victoria. The Turkana-Marsabit corridor was well depicted as a region with a well-mixed layer. Figures 173 and 174 show the potential temperature field at 1600 UTC ranging from 296 K over parts of the Indian Ocean to 305 K over the highlands. The fields showed relatively cooler areas over Lake Victoria, the Indian Ocean and over Lake Turkana with a well-mixed layer to the northeastern parts of the country and over the highlands.

The total water mixing ratio fields at 0500 UTC are shown in Figures 175 and 176. The values ranged from 11.6 g kg^{-1} to 18.8 g kg^{-1} with larger values concentrated along the coast and over the eastern to northeastern part of the country. Figures 177 and 178
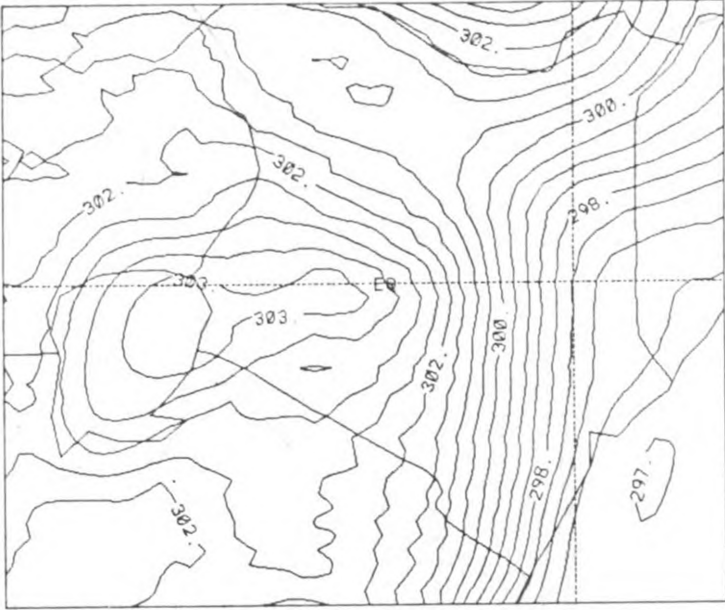
Figure 172: The potential temperature field (θ) on terrain following coordinate 72.4 m above surface at 0500 UTC (fine grid). Contour interval is 0.4 K. Case with no synoptic wind.
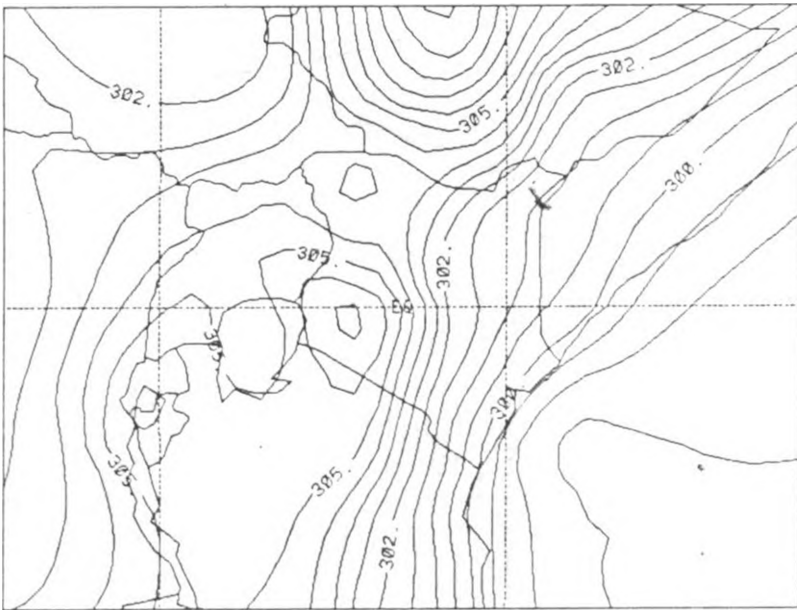
Figure 173: The potential temperature field on terrain following coordinate 72.4 m above surface at 1600 UTC (coarse grid). Contour interval is 0.7 K. Case with no synoptic wind.
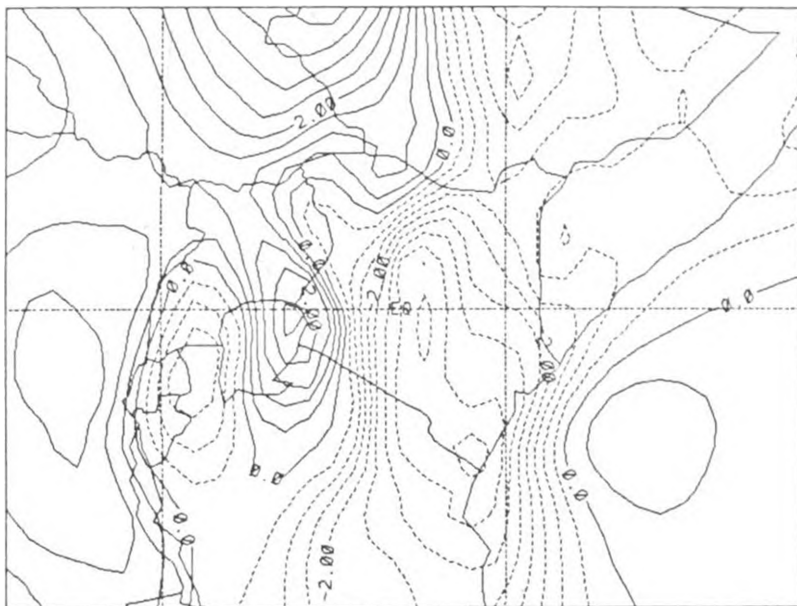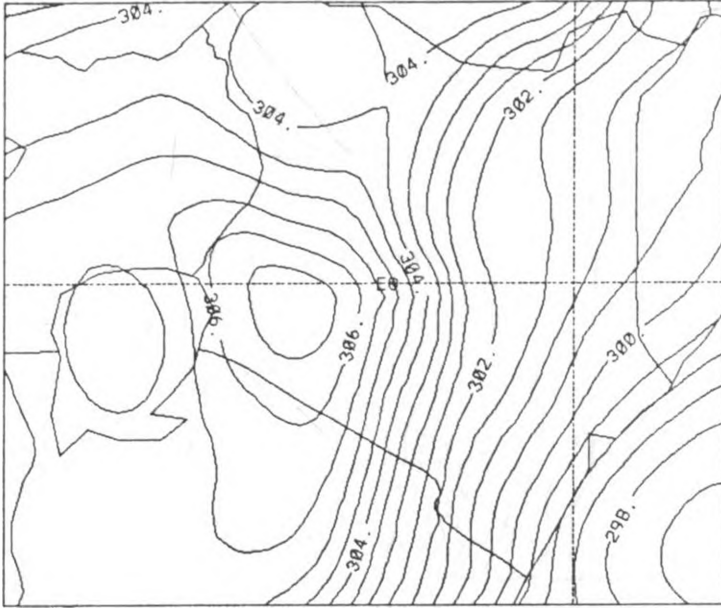
Figure 174: The potential temperature field on terrain following coordinate 72.4 m above surface at 1600 UTC (fine grid). Contour interval is 0.5 K. Case with no synoptic wind.
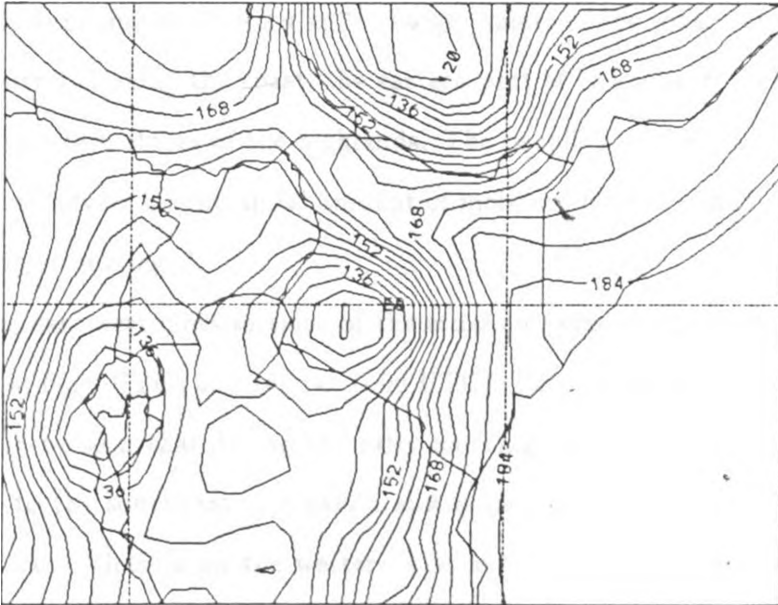
Figure 175: The total water mixing ratio field on terrain following coordinate 72.4 m above surface at 0500 UTC (coarse grid). Contour interval is 0.4 g kg^{-1}. Case with no synoptic wind.
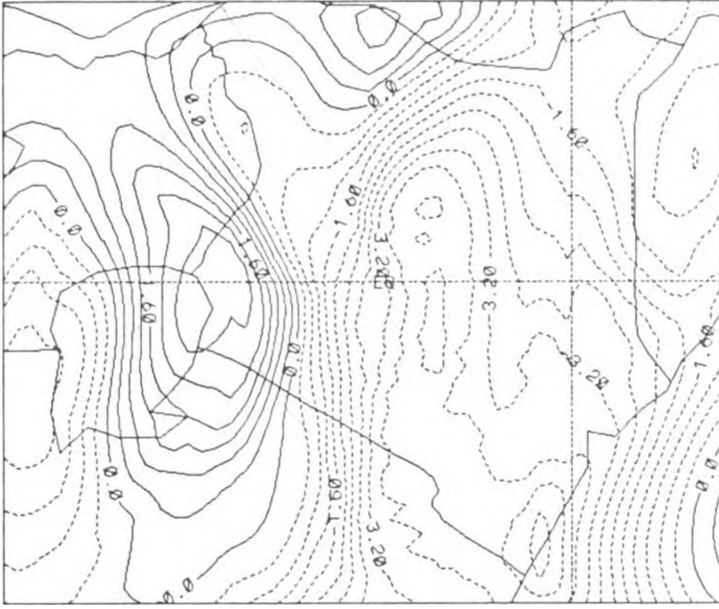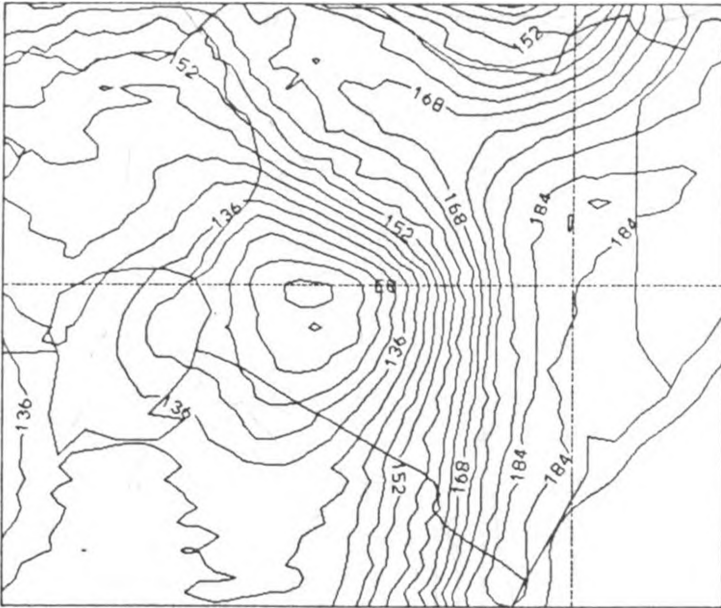
Figure 176: The total water mixing ratio field on terrain following coordinate 72.4 m above surface at 0500 UTC (fine grid). Contour interval is 0.4 g kg^{-1}. Case with no synoptic wind.

show the total water mixing ratio at 1600 UTC where the values increased from a minimum of 13.2 g kg^{-1} to a maximum of 19.2 g kg^{-1}. Larger values of the total water mixing ratio were still concentrated along the coast, the eastern part of the country (which is usually dry) and on the eastern slopes of the highlands. The coupling of the sea breeze with the upslope flow must advect a substantial amount of moisture farther inland from the coast than was previously envisaged.

The vertical east-west cross-sections of the zonal (u) wind component are illustrated in Figures 179 (at 0500 UTC) and 180 (at 1600 UTC). These fields are 50 km south of the equator. It could be seen that during the early morning the zonal winds (i.e., westerlies from highlands to the southwest of Uganda and easterlies from the Kenyan highlands) converged over Lake Victoria on the western side of the domain. Winds diverged from the high grounds in the middle of the domain and drained off towards the Indian Ocean to the east and to Lake Victoria to the west. There was also an off-shore wind at the coast (land-water boundary). The maximum value of the zonal wind was −0.49 m s^{-1} for the easterlies (dotted lines) and 0.7 m s^{-1} for the westerlies (solid lines). There was a
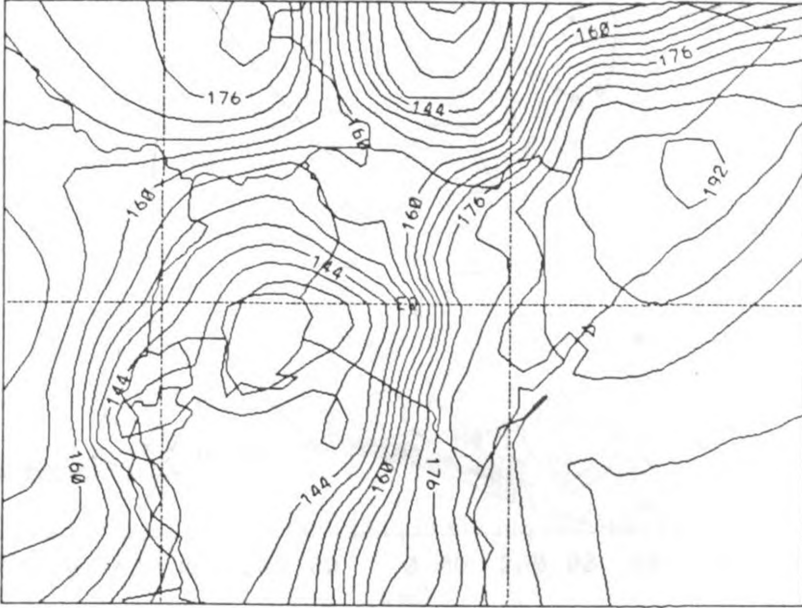
Figure 177: The total water mixing ratio field on terrain following coordinate 72.4 m above surface . at 1600 UTC (coarse grid). Contour interval is 0.4 g kg^{-1}. Case with no synoptic wind.
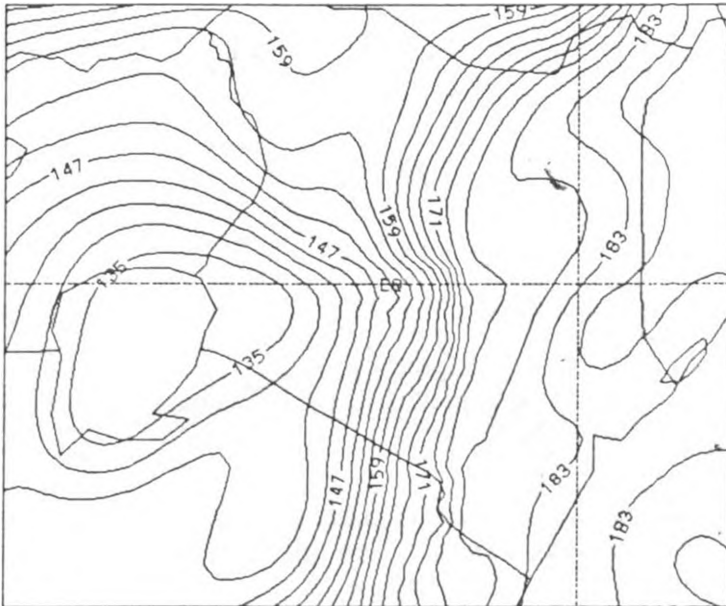
Figure 178: The total water mixing ratio field on terrain following coordinate 72.4 m above surface at 1600 UTC (fine grid). Contour interval is 0.3 g kg^{-1}. Case with no synoptic wind.
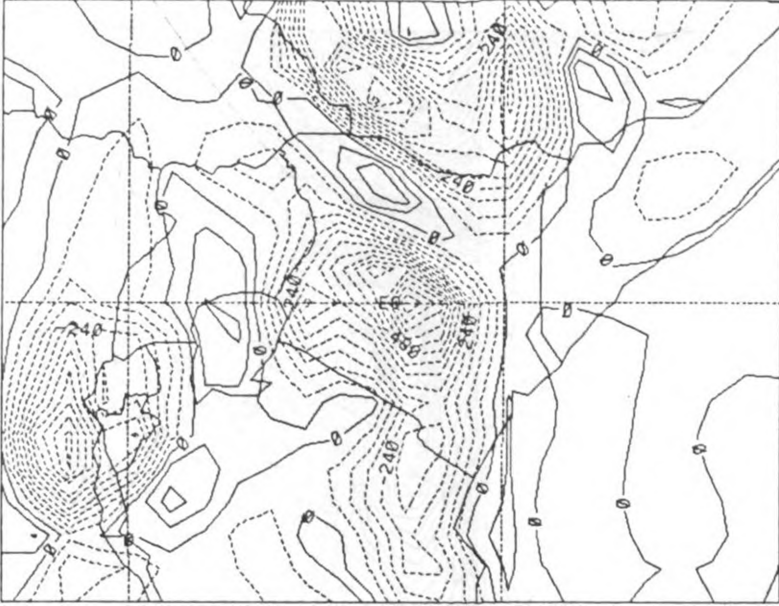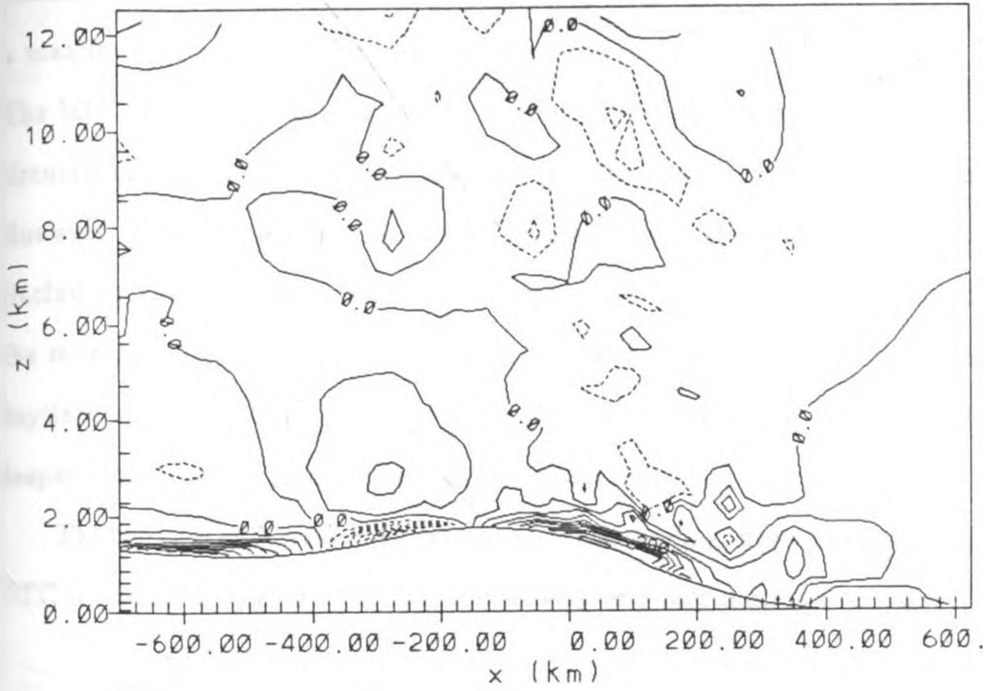
Figure 179: The vertical east-west cross-section of zonal wind (u) over Kenya at 0.5°S for 0500 UTC. Case with no synoptic wind.
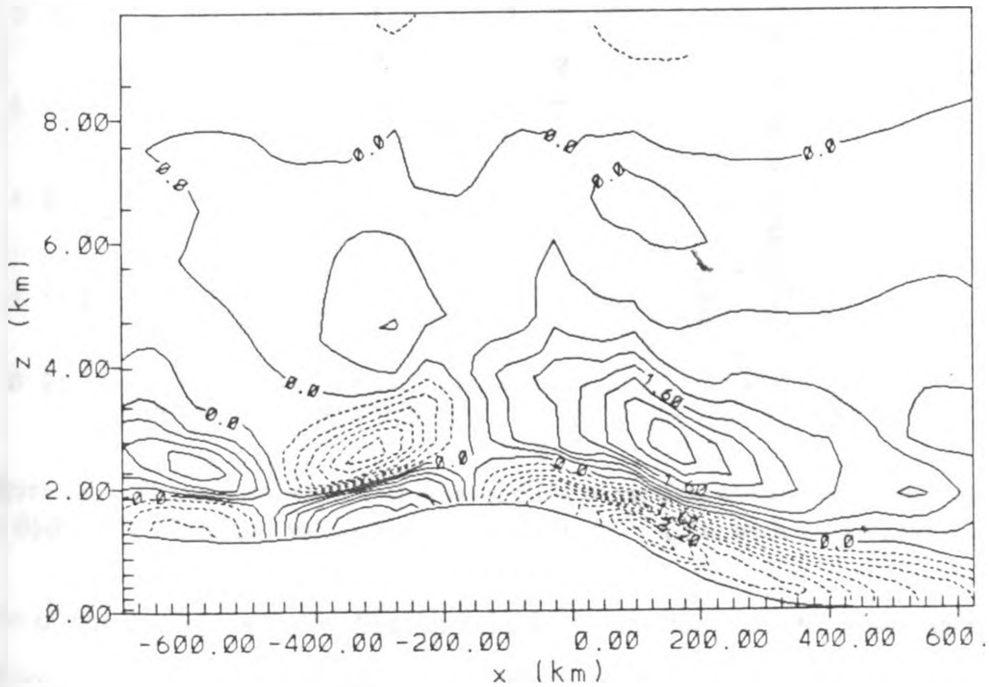
Figure 180: The vertical east-west cross-section of zonal wind (u) over Kenya at 0.5°S for 1600 UTC. Contour values are in units of m s^{-1}. Case with no synoptic wind.

reverse flow in the afternoon and early evening (Figure 180) where the easterlies attained a maximum speed of -4.8 m s^{-1} and a corresponding value for westerlies of 2.6 m s^{-1}. The lake and sea breeze circulations coupled with upslope winds. These low-level wind circulations occupied a shallow layer in the atmosphere of about 4.0 km above MSL. However, it can be seen by comparing Figures 179 and 180 that the afternoon circulations (including the sea breeze and the lake breeze circulations) occupied a deeper layer than the morning circulation (which included the land breeze circulation). This was because daytime solar insolation produced more vertical mixing which raised the boundary layer deeper than was the case at night and early morning.

The vertical east-west cross-section of the ascending/descending motion field at 0500 UTC is shown in Figure 181. The field illustrates rising motion over Lake Victoria to the
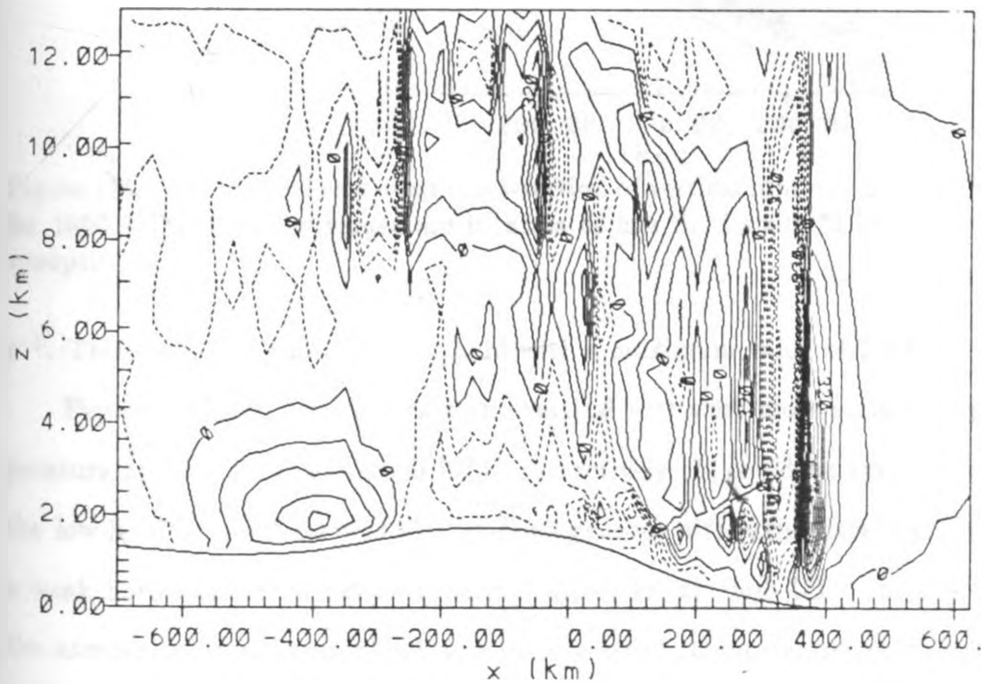
Figure 181: The vertical east-west cross-section of vertical motion (w) over Kenya at 0.5°S for 0500 UTC. Contour values are in units of m s^{-1}. Case with no syoptic wind.

west of the domain, a descending (or subsidence) motion over the land area and a rising motion over the ocean with relatively strong updrafts and downdrafts at the land-water interface at the coast. The maximum value of descending motion was 0.48 cm s^{-1} with a corresponding value of rising motion of 0.8 cm s^{-1}. Figure 182 depicted a reverse situation

of vertical wind at 1600 UTC with subsidence over the large water bodies (Lake Victoria and the Indian Ocean). The maximum value of descending motion attained was −2.7 cm
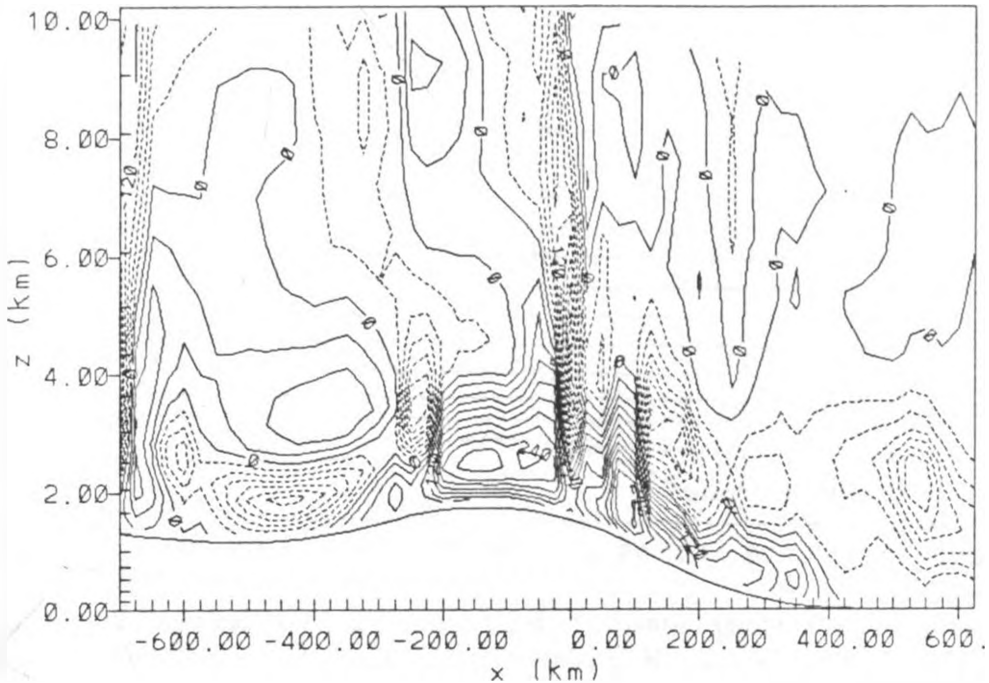
Figure 182: The vertical east-west cross-section of vertical motion (w) over Kenya at 0.5°S for 1600 UTC. Contour values are in units of m s^{-1}. Labels *1.0×10^{-4}. Case with no synoptic wind.

s^{-1}. There was rising motion over land with a maximum value of 3.3 cm s^{-1}.

Figures 183 and 184 illustrate the vertical east-west cross-section of potential temperature at 0500 UTC and 1600 UTC, respectively. It could be seen that at 0500 UTC the low-level atmosphere was almost homogeneous although there was an indication of a weak horizontal temperature gradient. However, at 1600 UTC the low level layers of the atmosphere were well-mixed and there existed strong temperature gradients in the horizontal near the surface. These temperature gradients were responsible for the upslope flow with the sea and lake breeze circulations.

Finally, Figures 185 and 186 show the vertical east-west cross-sections of total water mixing ratio at 0500 UTC and at 1600 UTC, respectively. The values in both figures ranged from 18.0 g kg^{-1} near the surface, decreasing to a minimal value at about 7.8 km height above MSL. Both figures show that there was a deeper layer of moisture over the Indian Ocean than over land and Lake Victoria. It has been suggested and verified that
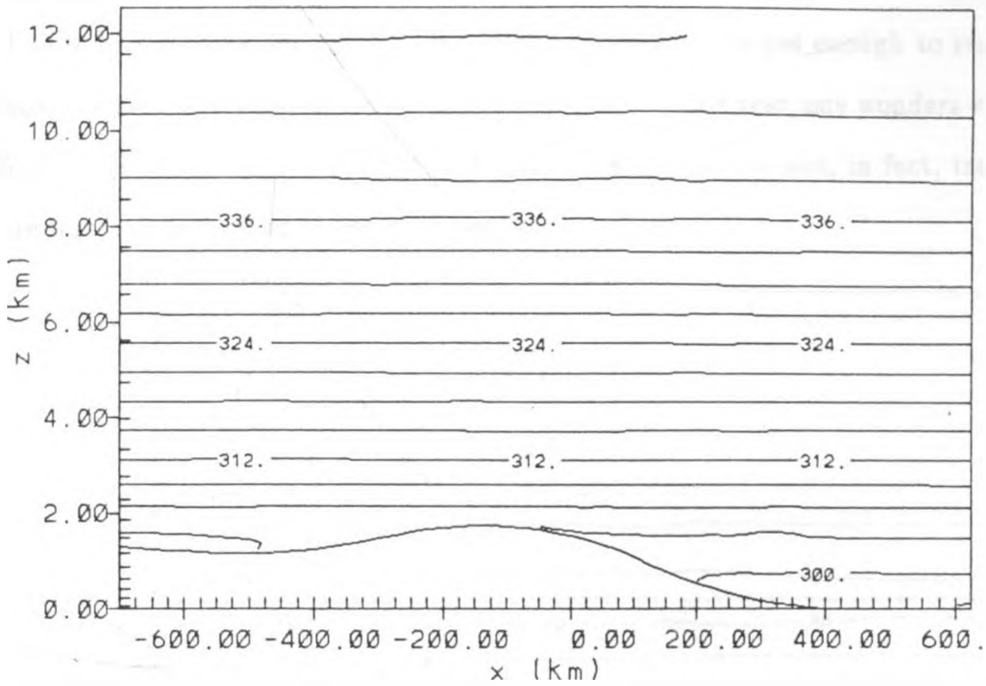
Figure 183: The vertical east-west cross-section of potential temperature field over Kenya at 0.5°S for 0500 UTC. Contour values are in units of K. Case with no synoptic wind.
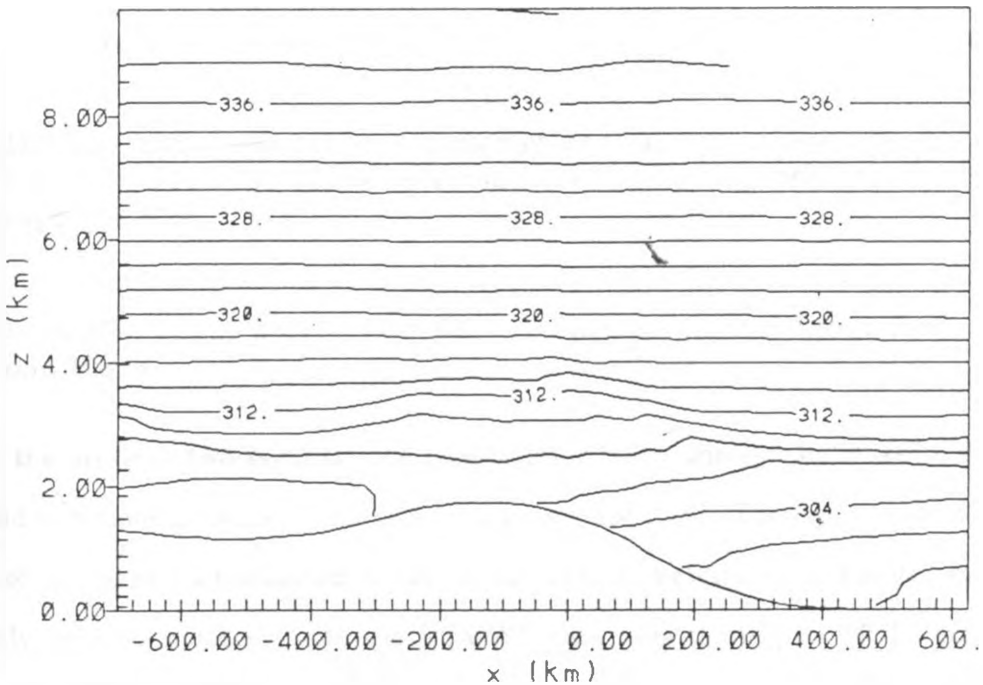
Figure 184: The vertical east-west cross-section of potential temperature field over Kenya at 0.5°S for 1600 UTC. Contour values are in units of g kg^{-1}. Labels *1.0×10^{-1}. Case with no synoptic wind.

Lake Victoria is responsible for transporting large amounts of moisture to the highlands than the sea breeze along the coast whose inland penetration is not enough to reach the highlands and influence weather there (e.g., Okeyo, 1987). However, one wonders whether the effect of the sea breeze coupling with the upslope winds does not, in fact, transport moisture further inland than is presently realized.
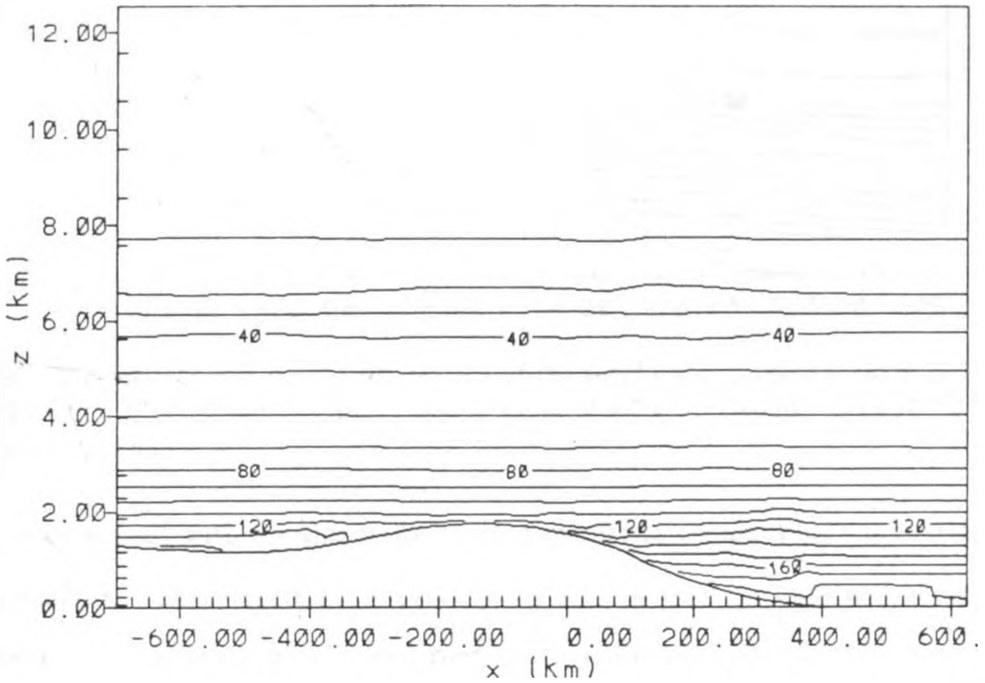
Figure 185: The vertical east-west cross-section of the total water mixing ratio over Kenya at 0.5°S for 0500 UTC. Contour values are in units of g kg^{-1}. Labels *1.0×10^{-1}. Case with no synoptic wind.

8.3 Discussion of the Interaction Between Mesoscale and Large-Scale Monsoon Flows

In the previous two sections, the results from the "variably" initialized ECMWF data and the "homogeneously" initialized data were discussed. The former looked at the effects of the large-scale monsoon winds on the weather patterns over Kenya. Included implicitly in the simulations with the ECMWF data were the impact of the mesoscale systems embedded in the large-scale flow (and seen in the fine grid fields). These mesoscale systems superimpose their influence on the synoptic-scale flow. The nested grid enabled fine resolutions which brought out the impact of the mesoscale phenomena. The latter
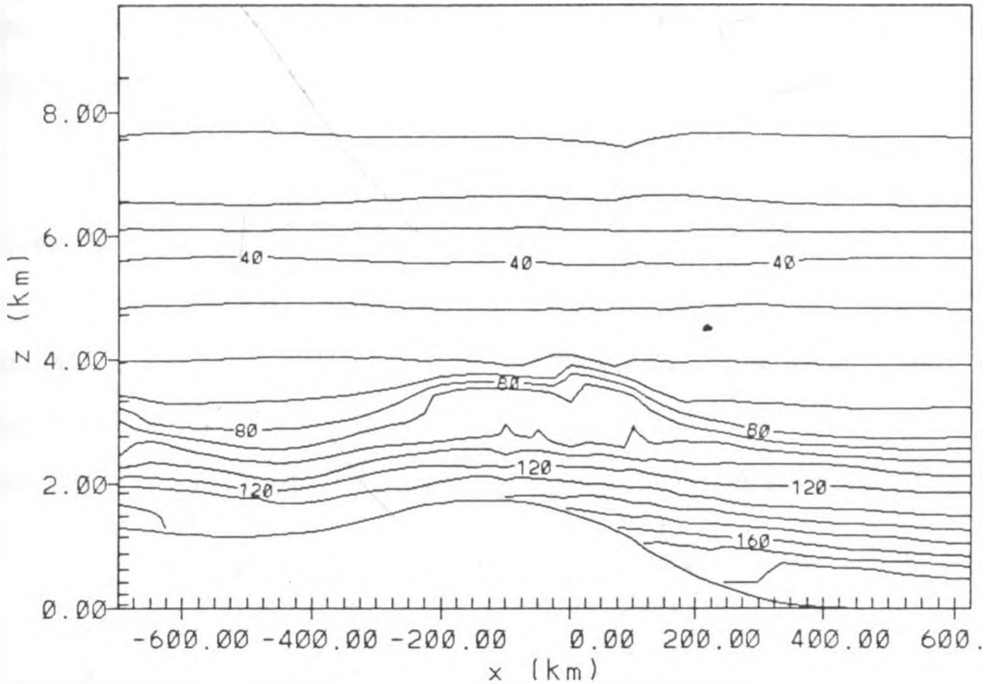
Figure 186: The vertical east-west cross-section of the total water mixing ratio over Kenya at 0.5°S for 1600 UTC. Contour values are in units of g kg^{-1}. Labels *1.0×10^{-1}. Case with no synoptic wind.

simulations only dealt with the thermally-induced mesoscale circulations, eliminating the monsoon winds, but including terrain, sea-surface temperature of the day, land percentage over the study site, and a constant land roughness parameter. The object of the latter simulations was to find out the influence of the mesoscale system on the diurnal weather patterns over the country in the absence of the synoptic scale monsoonal flows.

This chapter will discuss the interaction between the mesoscale and large-scale monsoon flows over Kenya by drawing attention to the results of the dry simulations (Experiments 1 and 2) in the previous two sections. This section also aims to emphasize the importance of the large-scale monsoon flow on the weather of the region; as the determinant for the location and movement of the convective or convergence zones and also by advecting a substantial amount of moisture into the area. The convective precipitation results generated by the model using the ECMWF data shall be discussed to further highlight the interactive nature of the monsoon flow with the local features. This discussion will look at the weather patterns first at the coast, then at the eastern slopes of the highlands, over the highlands followed by the Lake Victoria trough region, and the

Turkana-Marsabit corridor. Kenya provides a large variety of orographic features and precipitation patterns.

6.3.1 The Coastal Region

Along the coast (Mombasa, Malindi, Lamu; see Figure 32) there were land and sea breeze circulations (see Figures 156 and 158) and the large-scale southeasterly monsoon current which maintains almost a constant flow during the "Long Rains" season. Figures 187 and 188 show these large-scale winds at 0500 UTC and 1400 UTC, respectively, at low levels. It may be noted that during the afternoon the southeast monsoon flow veered
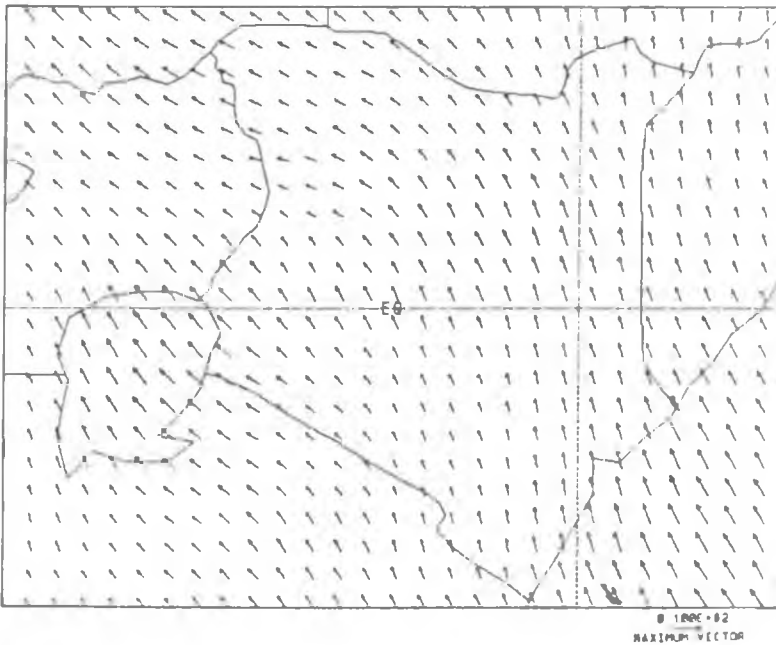
Figure 187: Wind vectors at 122 m above surface at 0500 UTC. Case with synoptic wind.

to become almost easterly over the northern half of Kenya because of the development of a strong low pressure zone to the west of Kenya, in Uganda and southern Sudan (see Figures 94, 99, and 101). Upslope flow to the Kenyan highlands could also play a role in veering the large-scale winds.

During late night and early morning the land breeze coupled with the downslope winds from the eastern slopes of the Kenyan highlands (Figures 156, 157, 160, and 164 to 179) and decerated the large-scale southeasterlies at the coast. There occurred a horizontal

0.811E+01
MAXIMUM VECTOR
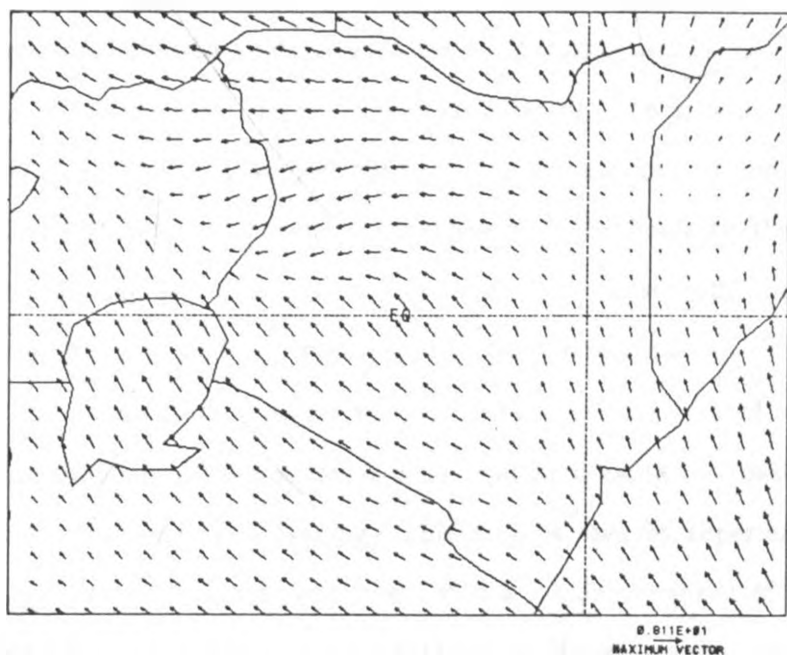
Figure 188: Wind vectors at 122 m above surface at 1400 UTC. Case with synoptic wind.

velocity convergence at lower levels with possible precipitation. This effect was seen in the perturbation Exner function field at lower levels (Figures 93 and 94) which displayed low pressure cells; one at the coast and another over the southern slopes of the Kenya highlands lying astride the border with Tanzania. These low pressure cells could initiate a convergence between the southeasterly monsoon wind and the downslope drainage wind (shown in Figures 156, 157, and 179) during late hours of the night and the early morning period. This interaction may be quantitatively determined if we superimpose Figure 187 (depicting large-scale easterlies at low levels) on Figure 157, which illustrates mesoscale circulation at the same time (0500 UTC or 8:00 a.m. local time). For instance, the westerly zonal wind component had a maximum of 1.0 m s^{-1} (see Figure 160) and a northerly wind component attained a maximum speed of 0.5 m s^{-1} in the morning (see Figure 164). The two wind components gave a resultant northwesterly wind vector with a speed of 1.1 m s^{-1}, which would resist the prevailing large-scale southeasterly flow that had a maximum strength of 10.0 m s^{-1} at 0500 UTC as depicted in Figure 187. Although the resistance was weak, there was low level convergence and subsequent precipitation where this interaction occurred, as will be verified later when displaying results for moist

convection. This low level convergence at the coast is also illustrated in Figures 38 and 39 of the observational analysis fields at 03 Z and 06 Z, respectively.

During the afternoon when the sea breeze couples with the upslope winds (Figures 158, 162, 166, and 180) the low pressure cells had advected northwards; one to the eastern part of Kenya and the other sat over the southwestern highlands to the east of Lake Victoria (Figures 98 and 99). Thus, as the southeasterly monsoon flow approaches the coast during the afternoon and late evening, they were accelerated in the low levels by the sea breeze (coupled with the upslope winds). These scenarios created a divergence at lower levels which minimized the possibility of precipitation along the coast in the course of the afternoon period and early evening. This may be seen by superimposing Figure 51, showing large-scale easterlies at low levels with a maximum speed of 8.38 m s^{-1} at 1600 UTC (7:00 p.m. local time), on Figure 158 depicting mesoscale circulation at the same time. The mesoscale flow registered a maximum westerly zonal wind speed of 2.4 m s^{-1} (Figure 162) and a maximum northerly speed of 2.4 m s^{-1} (Figure 166). Thus, the prevailing large-scale southeasterlies with a maximum strength of 8.38 m s^{-1} at low levels, would encounter a resistance of 2.4 m s^{-1} from a westerly mesoscale wind component plus another resistance of 2.4 m s^{-1} from a northerly mesoscale wind component (or a resultant opposing wind vector of 3.4 m s^{-1}) over the domain. Again, in places where this interaction occurred, active weather resulted as will be seen in the experiments with moist convection.

6.3.2 Eastern Slopes of the Kenyan Highlands

On the eastern and southern slopes of the Kenya highlands (Nairobi, Limuru, Thika, Muranga, Narok, etc.) the downslope winds (Figures 156, 157, 160, 164, and 179) retarded the southeasterly monsoon winds at lower levels during late night to early morning hours. The effect created a low-level convergence and possible active convective weather during these hours. However, during the afternoon and early evening the southeasterly monsoon current interacted with upslope wind (Figures 158 and 180) at lower levels. The upslope winds strengthened or accelerated the large-scale southeasterly winds causing divergence in the lower levels of the atmosphere, but the strong insolation realized during daytime

together with orographic lifting released convective instability and possible precipitation in the afternoon.

6.3.3 The Kenyan Highlands

Over the Kenya highlands (Kericho, Nakuru, Eldoret, Kitale, Nanyuki, etc.) the downslope winds drained off late at night and early morning to all directions (see Figures 156, 157, 160, 164, and 179). This drainage flow created a divergence zone over the highlands and this situation resulted in minimal convective weather activity. However, during the afternoon to early evening, the Lake Victoria breeze coupled with the upslope wind to converge with the southeasterly monsoon current which was, in turn, accelerated at lower levels with the upslope winds from the eastern and southern slopes of the Kenyan highlands (Figures 158, 162, and 166). This situation produced a strong convergence over the highlands and the possibility of precipitation. It may be noted that the observed surface large-scale flow field at 15 Z (Figure 42) showed a strong confluence over the highlands, thereby reflecting the effect of the mesoscale forcing on the large-scale flow.

6.3.4 The Lake Victoria Region

Around Lake Victoria (Kisumu, Homa Bay in Kenya; Musoma and Mwanza in Tanzania) during late night hours and early morning, there was a land breeze towards Lake Victoria which was coupled with downslope winds from the Kenya highlands (see Figures 156, 157, 160, and 164). This scenario accelerated the southeasterly monsoon current at lower levels (causing low-level divergence) to flow downhill into the Lake Victoria trough region producing no precipitation over the eastern side of Lake Victoria during this period. The land breeze from the western part of the Lake (over Bukoba in Tanzania; see Figure 32) and from the northern shores (over Entebbe and Kampala in Uganda) converged with the southeasterly monsoon winds during late night to early morning causing precipitation over these areas. However, during the day and early evening, the lake breeze (on the eastern shores of the lake) coupled with the upslope winds to converge (over Kericho district in the model) with the large-scale monsoon current accelerated at lower levels by the upslope winds from the eastern and southern slopes of the Kenya highlands. Although the

vertical motion fields (Figures 189 at 0500 UTC and 190 at 1400 UTC) showed subsidence (due to large-scale down-currents into the Lake Victoria Basin) over the eastern side of Lake Victoria, this region received a substantial amount of rainfall on this day. It was
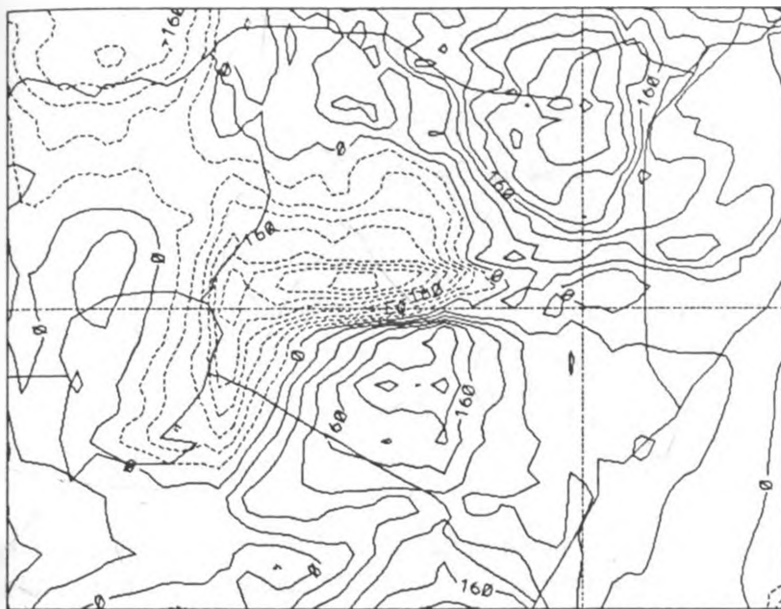
Figure 189: Vertical velocity field at 122 m above surface at 0500 UTC. Contour values are in units of m s^{-1}. Labels *1.0×10^{-4}. Case with synoptic wind.

therefore suspected that a strong convection occurred over the Nandi/Kericho highlands and the resultant deep precipitating convective clouds drifted towards the Lake advected by the large-scale easterlies (Okeyo, 1982; 1987). It could be noted that there was more subsidence over the lake at 1400 UTC than at 0500 UTC because the lake was cooler than the land in the afternoon.

Figures 191 and 192 at 0500 UTC and Figures 193 and 194 at 1400 UTC show the relative vorticity field at lower levels over Kenya. The relative vorticity was positive over much of the domain (in the region of rising motion) except on the eastern side of Lake Victoria where negative vorticity was registered over an area experiencing down-currents from the highlands. The relative vorticity over the area of study was seen to decrease slightly in the course of the simulation. The maximum value of positive relative vorticity over Kenya was 0.9×10^{-4} s^{-1} at 0500 UTC with a corresponding value of 0.8×10^{-4} s^{-1} at 1400 UTC.
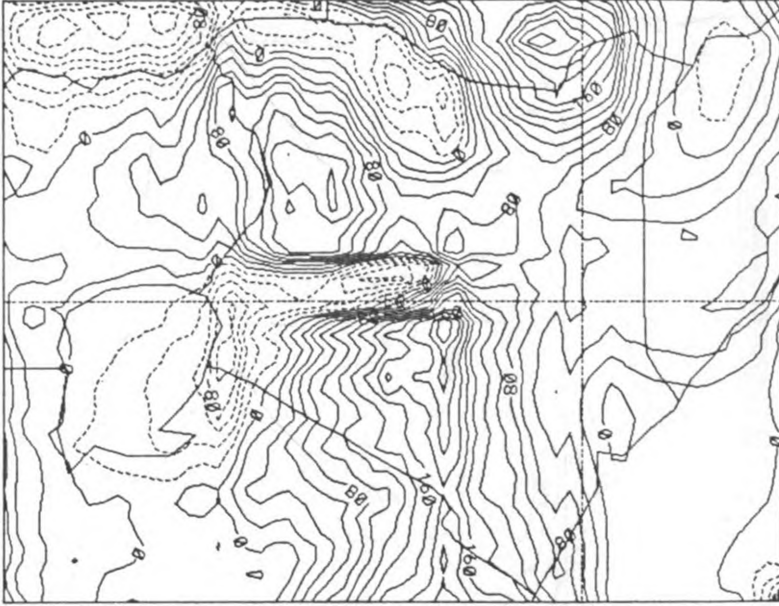
Figure 190: Vertical velocity field at 122 m above surface at 1400 UTC. Contour values are in units of m s^{-1}. Labels *1.0×10^{-4}. Case with synoptic wind.
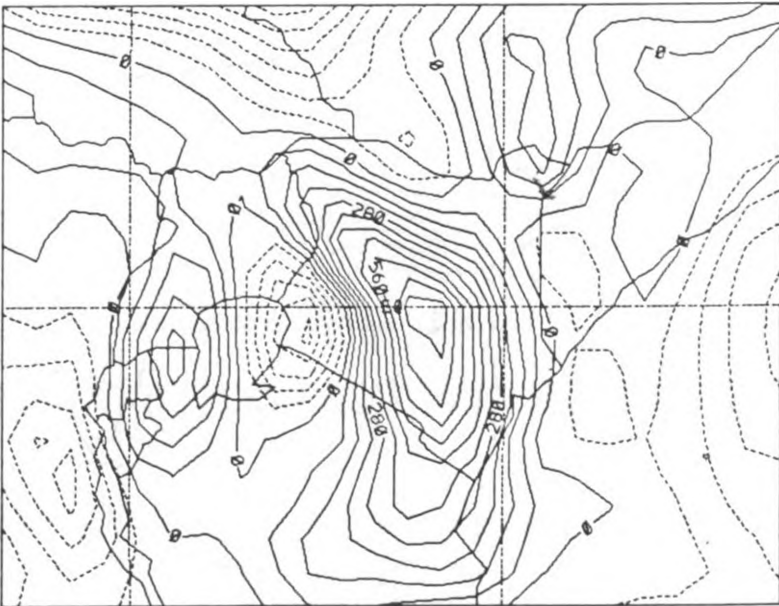
Figure 191: Relative vorticity field at 122 m above surface at 0500 UTC (coarse grid). Contour values are in units of s^{-1}. Case with synoptic wind.
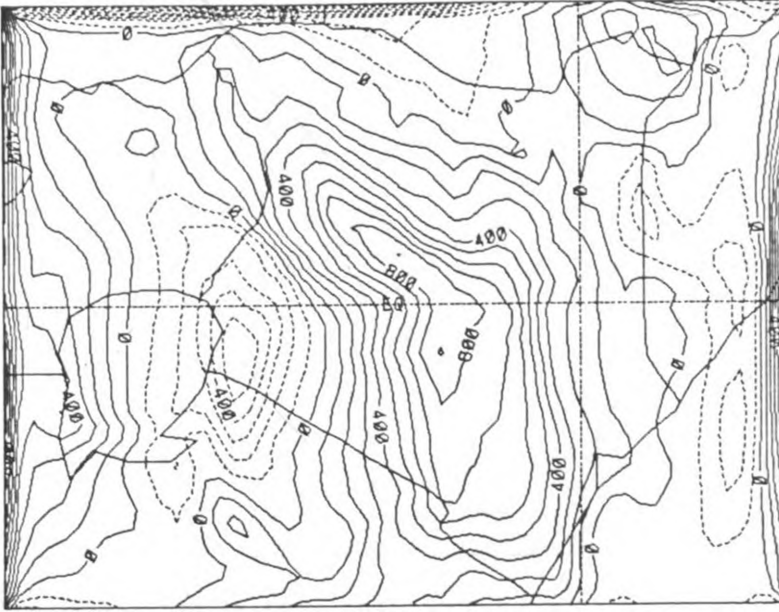
Figure 192: Relative vorticity field at 122 m above surface1 at 0500 UTC (fine grid). Contour values are in units of s^{-1}. Case with synoptic wind.
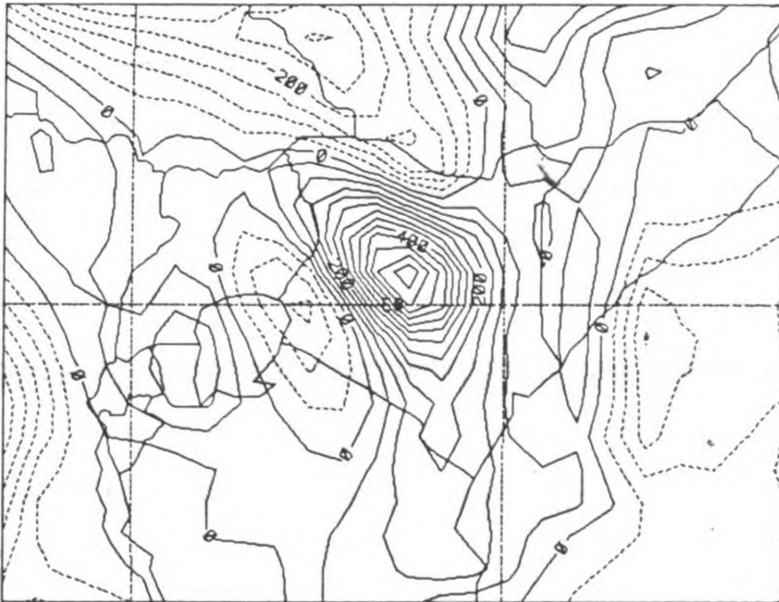
Figure 193: Relative vorticity field at 122 m above surface at 1400 UTC (coarse grid). Contour values are in units of s^{-1}. Case with synoptic wind.
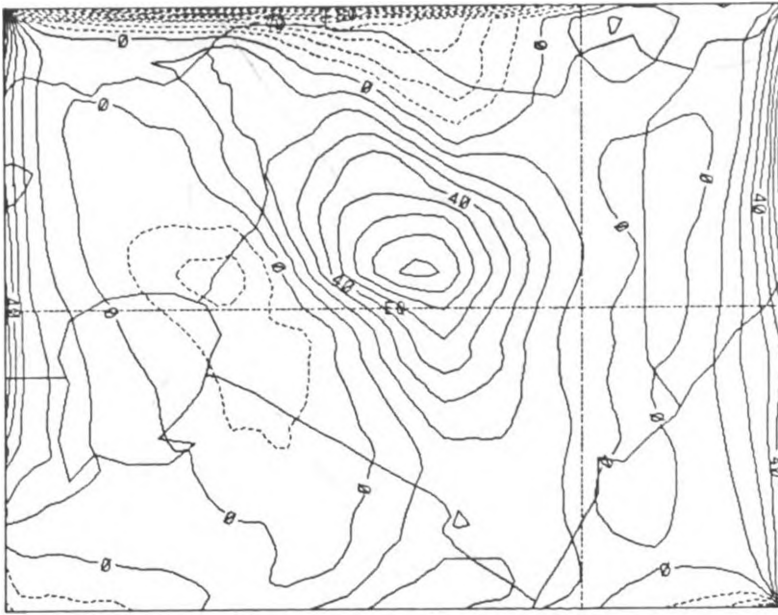
Figure 194: Relative vorticity field at 122 m above surface at 1400 UTC (fine grid). Contour values are in units of s^{-1}. Case with synoptic wind.

6.4 Results From Experiment 3: The Case With Moist Convection

To emphasize the diurnal weather pattern caused by the scale-interaction between the large-scale monsoon current, breeze circulations at the coast and at Lake Victoria, upslope/downslope winds due to orographic barriers etc., convective precipitation among other parameters was generated in the model. Tropical cumulus convection is an important element in an overall heat balance which modifies the tropical weather. Precipitation in the tropics drives tropical circulations by the release of latent heat. Thus, latent and sensible heating from clouds have a positive effect on the model forecasts. The Convective PrecipitationRate is normally associated with DeepConvection and was used in this study to indicate locations of precipitation at a specified time period in the course of the simulation.

Areas of convective precipitation along the coast caused by the convergence between the land breeze/downslope winds with the monsoon current discussed above are depicted in Figures 195 and 196 during the morning at 0400 UTC (or 7:00 a.m. Kenya Local Time) and in Figures 197 and 198 for 0500 UTC. There was also convective precipitation over most parts of Lake Victoria (except on the eastern side) due to the convergence between the land

Figure 195: Convective precipitation rate at 0400 UTC (coarse grid). Contour values are in units of m ms^{-1}. Labels $^*1.0\times10^{-3}$. Case with synoptic wind.
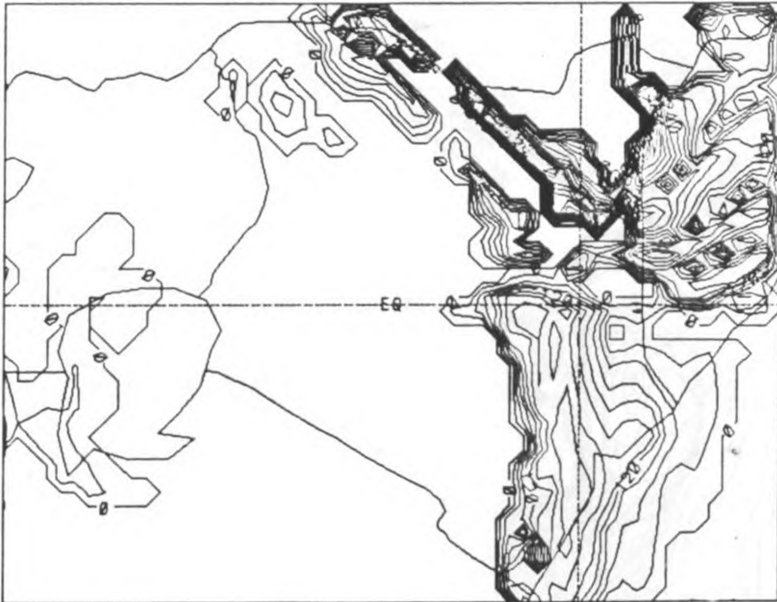
Figure 196: Convective precipitation rate at 0400 UTC (fine grid). Contour values are in units of m ms^{-1}. Labels $^*1.0\times10^{-3}$. Case with synoptic wind.

175
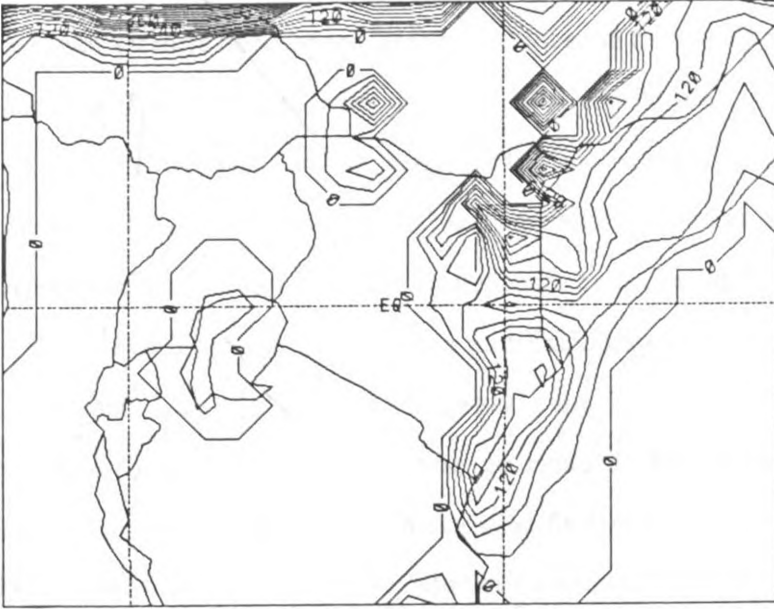
Figure 197: Convective precipitation rate at 0500 UTC (coarse grid). Contour values are in units of m ms^{-1}. Labels *1.0×10^{-3}. Case with synoptic wind.
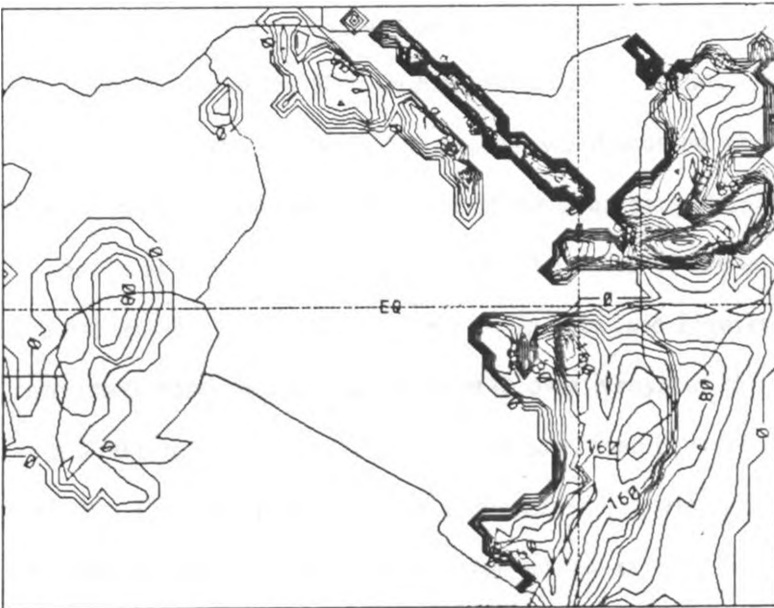
Figure 198: Convective precipitation rate at 0500 UTC (fine grid). Contour values are in units of m ms^{-1}. Labels *1.0×10^{-3}. Case with synoptic wind.

breeze from northern and western shores of the lake) with the large-scale southeasterly monsoon current. As mentioned above, there was no convective precipitation on the eastern portion of Lake Victoria because the large-scale monsoon currents pouring downhill into the Lake Victoria Trough region were accelerated at low levels by the downslope drainage winds (which coupled with the land breeze at the land-water interface) producing low-level divergence on the eastern side of the lake. There was convective precipitation in the Turkana-Marsabit corridor due to the convergence of the downslope drainage winds along this gap from Kenya highlands to the south and Ethiopian highlands to the north (see Figs. 156, 157, 160, and 164) with the large-scale southeasterly monsoon current during late night to early morning hours. It may be recalled that Figure 187 at 0500 UTC does not show any low-level divergence in the wind field over the Turkana-Marsabit area (hence, the presence of convective precipitation) although in Figure 188 at 1400 UTC the low-level divergence in the wind vectors over this area is more evident. The maximum modeled convective precipitation rate over Kenya at 0400 UTC was 0.60 mm s^{-1} with a corresponding value of 0.38 mm s^{-1} at 0500 UTC. During the afternoon at 1000 UTC (1:00 p.m. Kenya Local Time) the convective precipitation belt was slowly spreading westwards (driven by the monsoon current) and had now covered a large part of the eastern and southern slopes of the Kenyan highlands where insolation and orographic lifting released convective instability during the day as was discussed above. Convective precipitation was fairly widespread over most parts of the country; precipitation occurred in a northwest-to-southeast belt across the country to the north of the equator and over a locality on the northern shores of Lake Victoria in Uganda (see Figures 199 and 200). The maximum convective precipitation rate registered over Kenya at this time was 0.30 mm s^{-1}, down from 0.60 mm s^{-1} at 0400 UTC. The accumulated convective precipitation for 8 hours (from 0300 UTC to 1000 UTC) is depicted in Figures 201 and 202. The maximum accumulated convective precipitation over Kenya at this time was 6.4 mm. One can easily observe that the eastern side of Lake Victoria had accumulated minimal convective precipitation.

Figure 199: Convective precipitation rate at 1000 UTC (coarse grid). Contour intervals are in units of m ms^{-1}. Labels *1.0×10^{-3}. Case with synoptic wind.

Figure 200: Convective precipitation rate at 1000 UTC (fine grid). Contour intervals are in units of m ms^{-1}. Labels *1.0×10^{-3}. Case with synoptic wind.

Figure 201: Accumulated convective precipitation at 1000 UTC (coarse grid). Contour values are in units of mm. Case with synoptic wind.
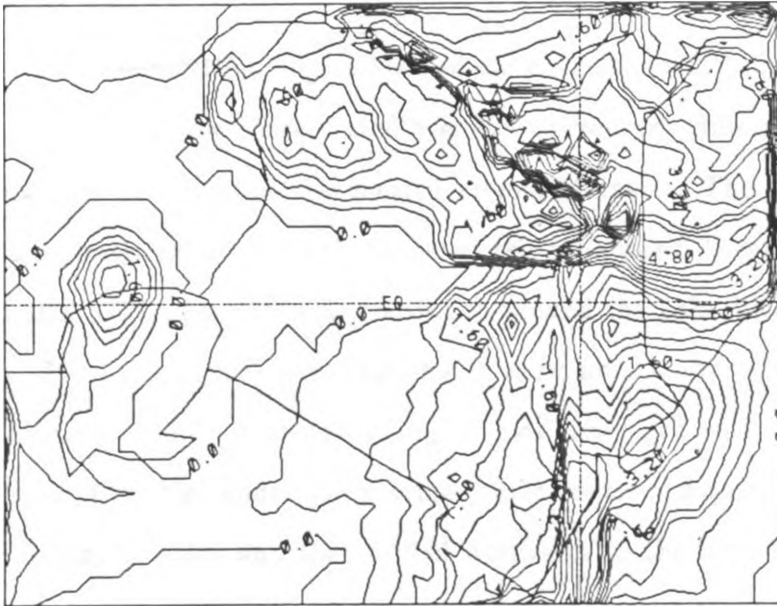
Figure 202: Accumulated convective precipitation at 1000 UTC (fine grid). Contour values are in units of mm. Case with synoptic wind.

The locations of the afternoon convection at 1200 UTC (Figures 203 and 204) show that the zone of convective precipitation continued to spread westwards over the country. There is precipitation over Kitale, Eldoret, Nakuru, etc. which are towns situated in

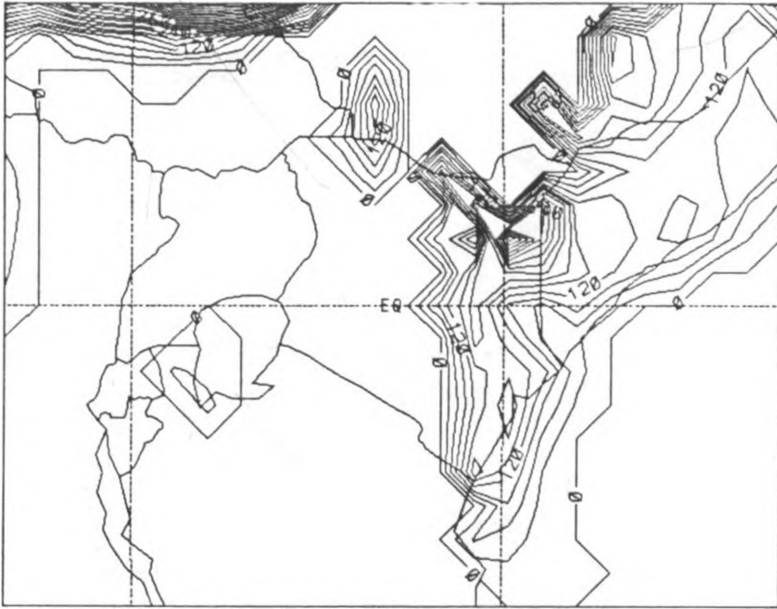Figure 203: Convective precipitation rate at 1200 UTC (coarse grid). Contour values are in m ms^{-1}. Labels *1.0×10^{-3}. Case with synoptic wind.

the Kenya highlands. Convective precipitation had moved southwards from the Turkana-Marsabit corridor and was now concentrated over the Cherangani Hills and Mt. Elgon area. Some convective precipitation was located around Marsabit. The maximum convective precipitation rate registered by the model at this time was 0.32 mm s^{-1}, up from 0.30 mm s^{-1} at 1000 UTC. There was no convection around the Lake Victoria region at this time of day. The eastern side of the lake should show some convection at this time. The strong lake breeze coupled with the upslope winds converged with the large-scale monsoon currents over the highlands. The ensuing convective cloud formations, therefore, occurred over the high grounds and then drifted westwards in the large-scale monsoon current towards the lake causing rainfall. It may be recalled that the model produced subsiding motion over this region due to the down-currents of the large-scale monsoon winds flowing over the highlands into the Lake Victoria Basin area. The subsiding motion

Figure 204: Convective precipitation rate at 1200 UTC (fine grid). Contour values are in m ms^{-1}. Labels *1.0×10^{-3}. Case with synoptic wind.

(on the leeward side of the high grounds) is then not associated with precipitation, and hence, the model registers minimum convective precipitation over this region; although records show that the eastern side of the lake in Kenya is normally very wet and large amounts of rain were recorded over Kisumu and Kisii on this particular day (see Figure 47). Another speculation could be that the fine resolution (horizontal grid spacing of 25 km by 25 km) was not sufficient to resolve precipitation on this leeward side of the large-scale downcurrent from the Kenyan Highlands.

Figures 205 to 212 show the locations and movement of convective complexes from 1300 UTC to 1600 UTC. By looking at these fields one easily notes that deep convection was widespread and experienced over large portions of the country. Larger areas of active convection were to the southern half of the country as compared to the northern section. Convection from the western part of Kenya drifted westwards into eastern Uganda and spread across most parts of that country with time. Eastern and central Uganda received a substantial amount of convective precipitation especially at 1500 UTC (see Figures 209 and 210). One also notes that convective precipitation over the eastern side of Lake Victoria was more likely to come from the north and northeast as opposed to the east.
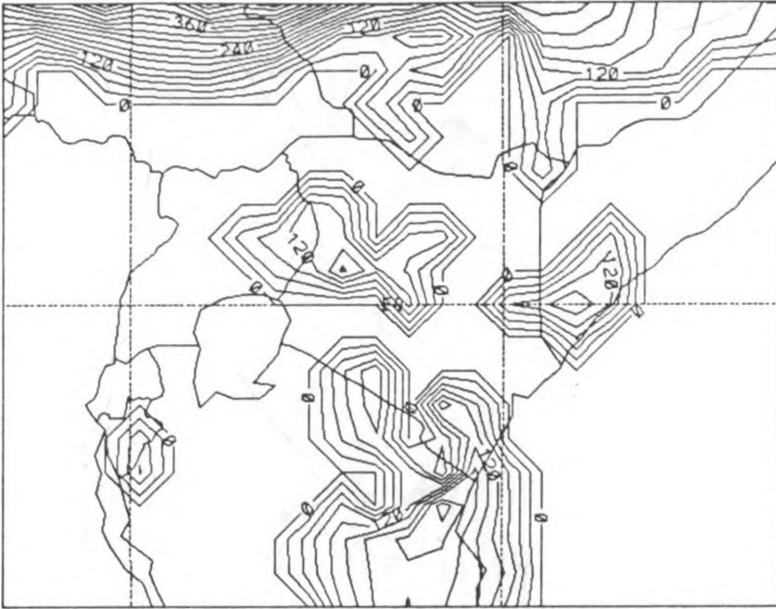
Figure 205: Convective precipitation rate at 1300 UTC (coarse grid). Contour values are in units of m ms^{-1}. Labels *1.0×10^{-3}. Case with synoptic wind.
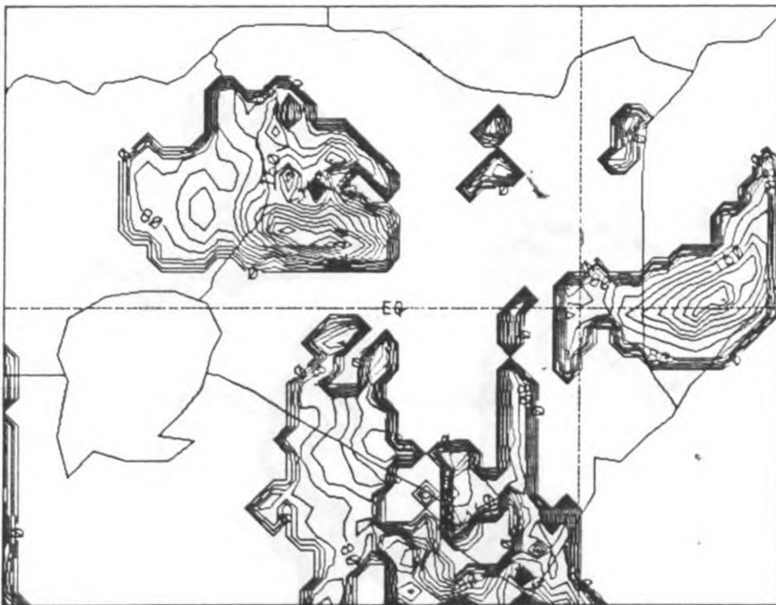
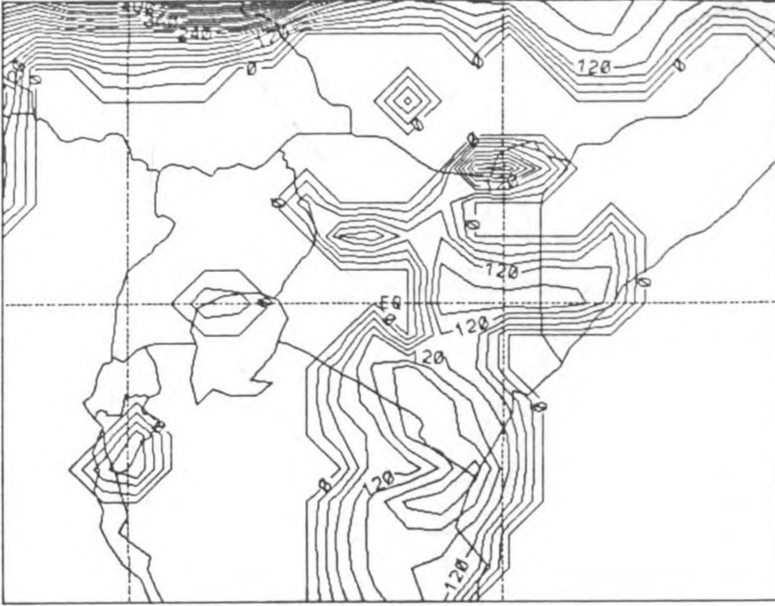Figure 206: Convective precipitation rate at 1300 UTC (fine grid). Contour values are in units of m ms^{-1}. Labels *1.0×10^{-3}. Case with synoptic wind.
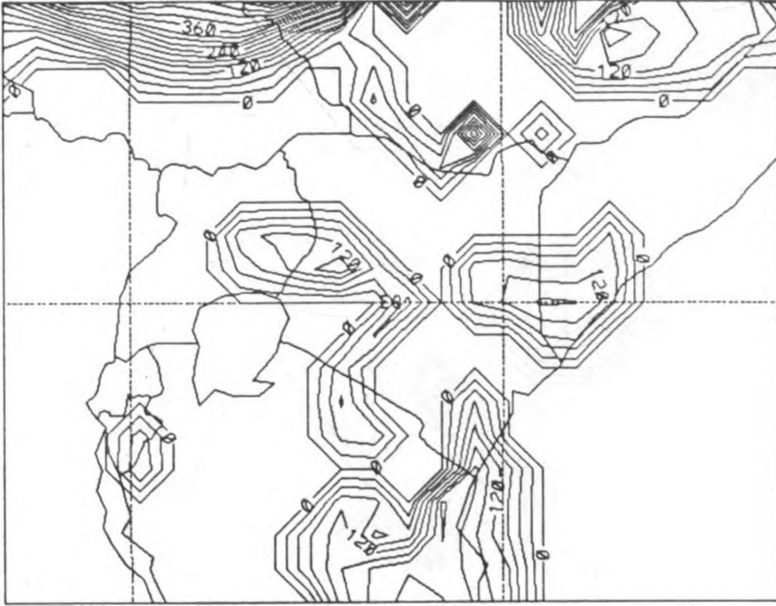
Figure 207: Convective precipitation rate at 1400 UTC (coarse grid). Contour values are in units of m ms^{-1}. Labels *1.0×10^{-3}. Case with synoptic wind.
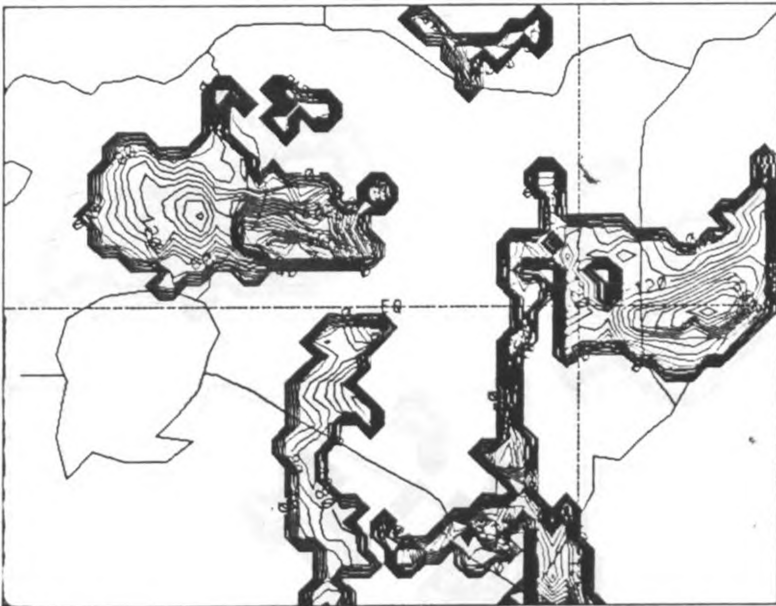
Figure 208: Convective precipitation rate at 1400 UTC (fine grid). Contour values are in units of m ms^{-1}. Labels *1.0×10^{-3}. Case with synoptic wind.
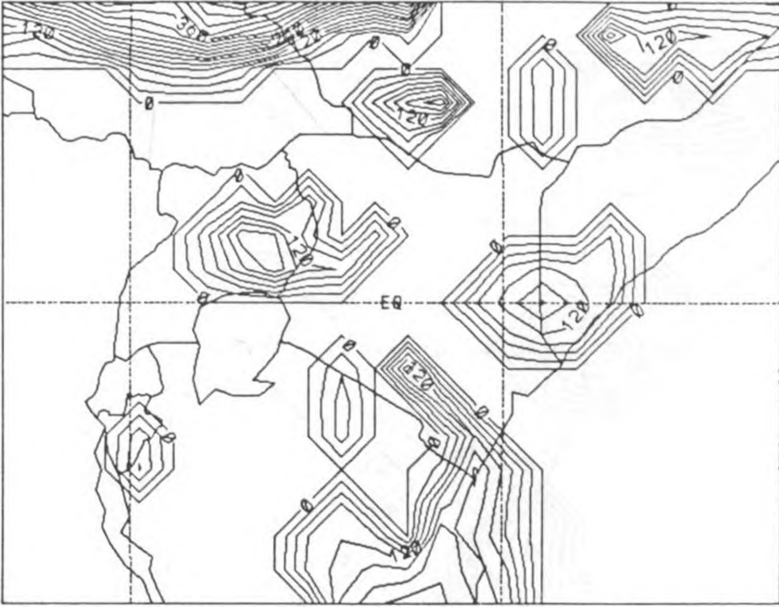
Figure 209: Convective precipitation rate at 1500 UTC (coarse grid). Contour values are in units of m ms^{-1}. Labels *1.0×10^{-3}. Case with synoptic wind.
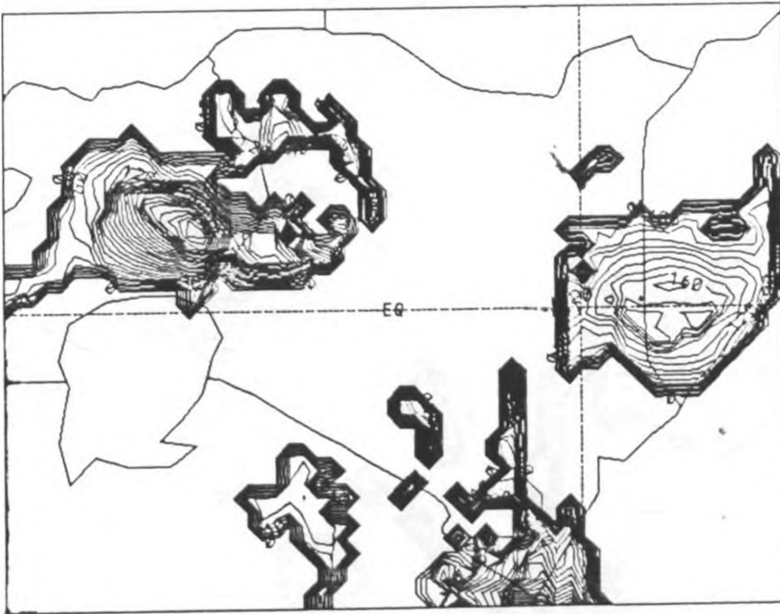
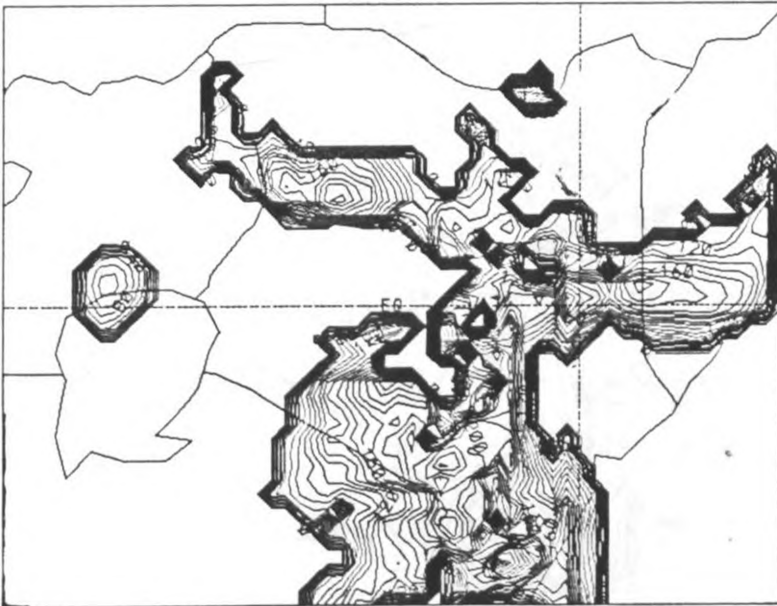Figure 210: Convective precipitation rate at 1500 UTC (fine grid). Contour values are in units of m ms^{-1}. Labels *1.0×10^{-3}. Case with synoptic wind.

Figure 211: Convective precipitation rate at 1600 UTC (coarse grid). Contour values are in units of m ms^{-1}. Labels $*1.0 \times 10^{-3}$. Case with synoptic wind.

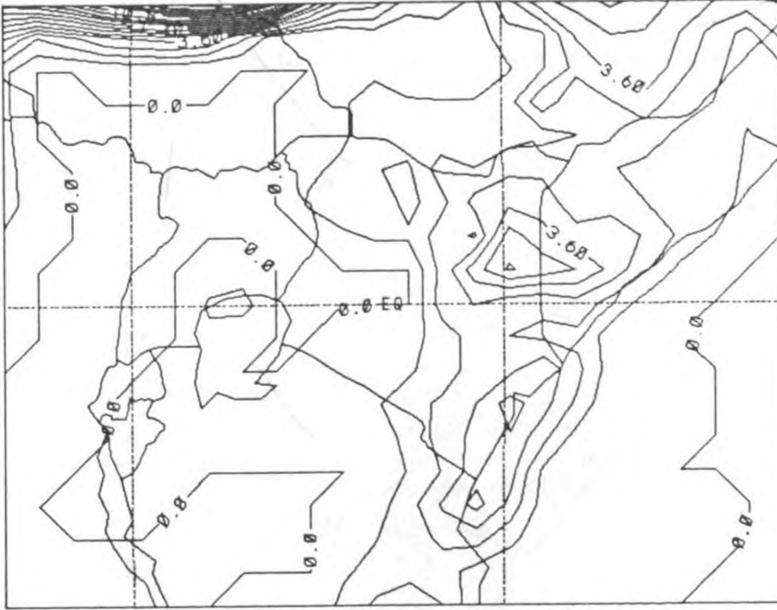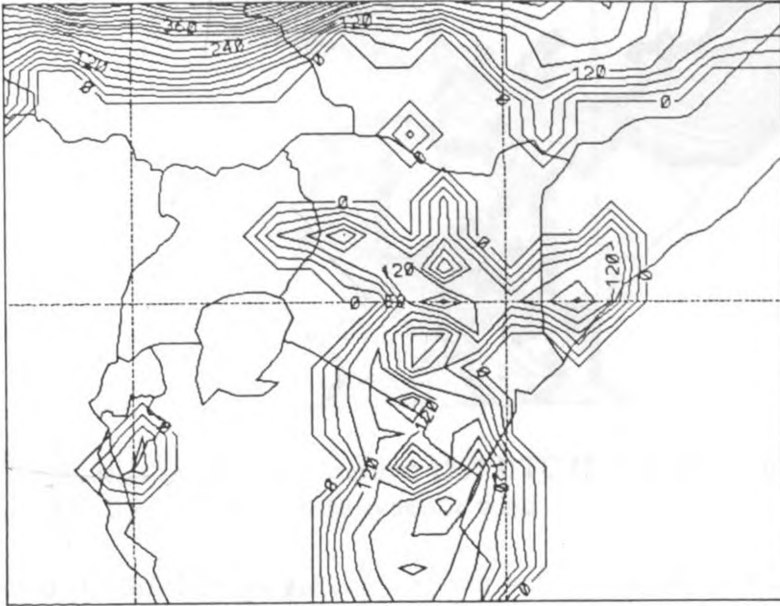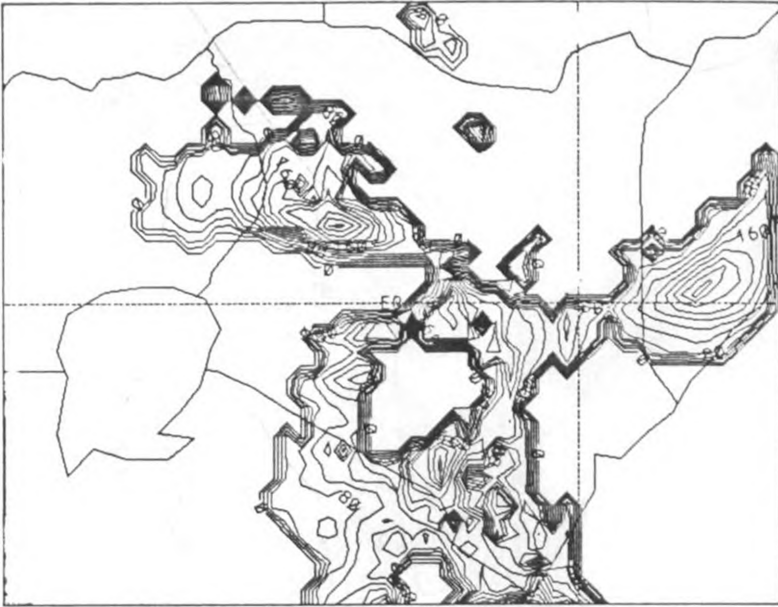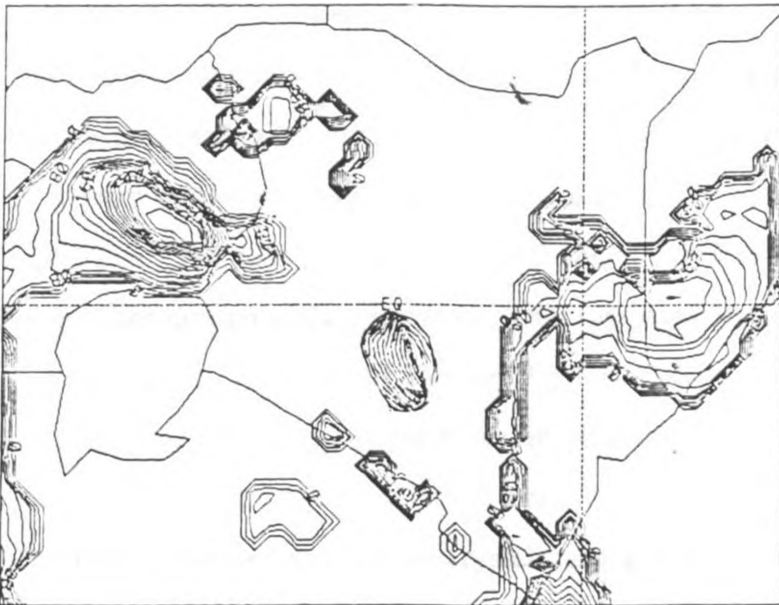Figure 212: Convective precipitation rate at 1600 UTC (fine grid).

When one observes the modeled wind field at 1400 UTC (Figure 188) it can be seen that part of the large-scale monsoon current which veered to become easterly to northeasterly (over the portion of the country starting immediately above the equator) converged with the other part which maintained a steady southeasterly course. The convergence zone occurred to the north of Lake Victoria, right from Kenya to Uganda. The veering winds to the north of the equator over Kenya did so because of the pressure fall over Uganda and southern Sudan, and also because of the strong upslope northerly winds that occurred on the northern-facing slopes of the Kenya highlands during the afternoon to early evening period (see Figures 158, 162, and 166). The veering winds to the northern part of Lake Victoria had definitely a strong meridional (north to south) wind component which drifted the generated convection to the eastern side of Lake Victoria. Convection on the eastern part of Kenya was displaced southwards towards the northern tip of the Kenyan coast but that over the highlands died with time. Convection was maintained at the southern coast of Kenya throughout the simulation; this scenario could have been in part due to an active ITCZ over the area with warmer sea surface temperatures (301 K) recorded by the model over the same area in the initial field.

The convective precipitation rate at 1600 UTC (or 7:00 p.m. local time) had a maximum value of 0.38 mm s^{-1} over Kenya which decreased thereafter (but increased over Uganda). The accumulated convective precipitation is displayed in Figures 213 and 216 and helped to show that there was indeed widespread convective weather activity over most parts of the country on this particular day. The maximum value over the domain at this time was 10.2 mm. The same field at 2400 UTC (Figures 215 and 216) showed a maximum value over the domain of 20.0 mm/day. This compared well with observed rainfall along the coast, eastern slopes of the Kenyan Highlands, and some parts of the Kenyan Highlands. However, the model underestimated rainfall over a portion of the highland areas where the observed rainfall was 21–30 mm.

Results of the model-generated pristine ice crystals and graupel (hailstones) from the Explicit Microphysics Parameterization showed a negligible amount over much of the domain; indicating the need to increase resolution for this type of parameterization.
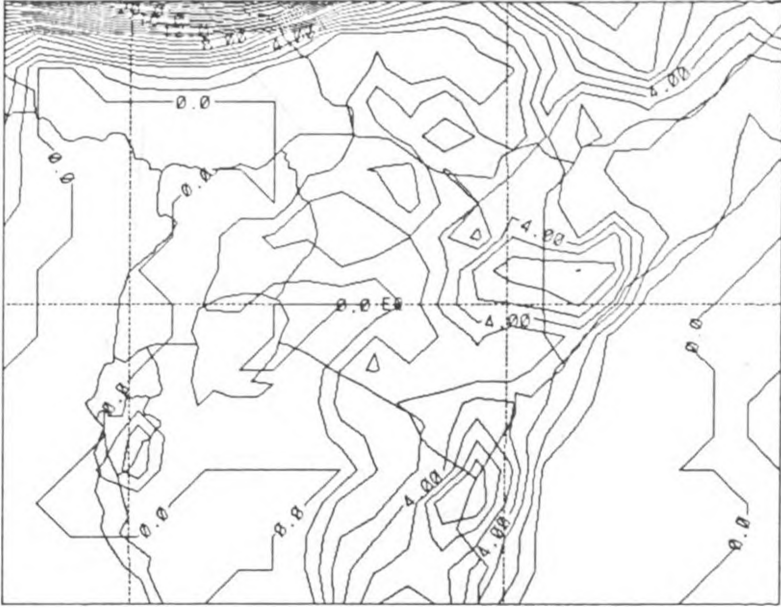
Figure 213: Accumulated convective precipitation at 1600 UTC (coarse grid). Contour intervals are in units of mm. Case with synoptic wind.
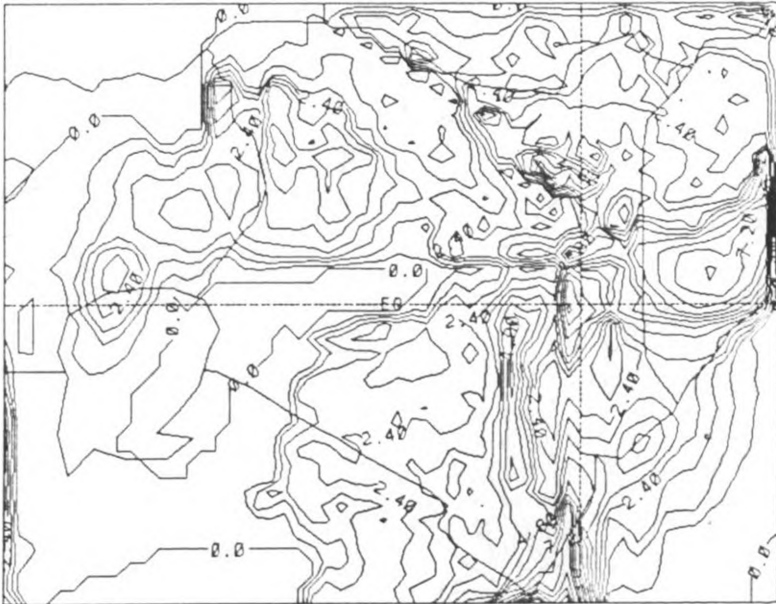
Figure 214: Accumulated convective precipitation at 1600 UTC (fine grid). Contour intervals are in units of mm. Case with synoptic wind.
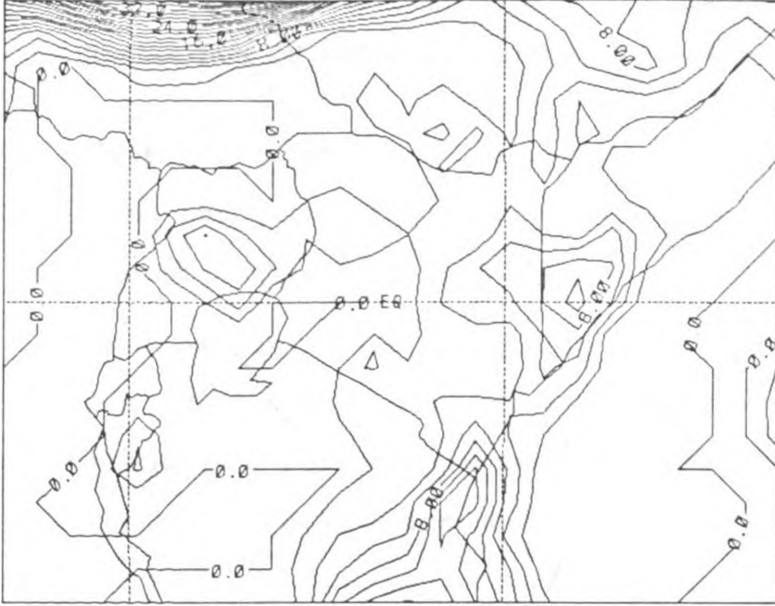
Figure 215: Accumulated convective precipitation (coarse grid). Contour intervals are in units of mm. Case with synoptic wind at 2400 UTC
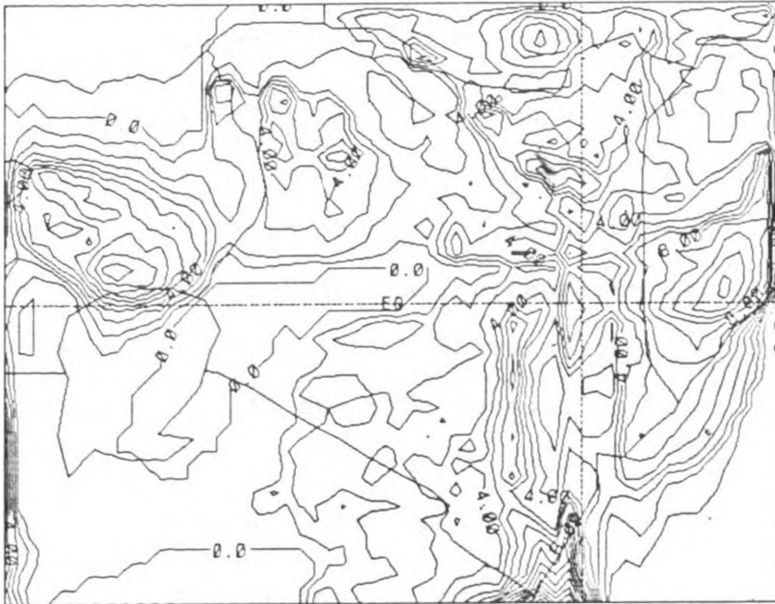
Figure 216: Accumulated convective precipitation (fine grid). Contour intervals are in units of mm. Case with synoptic wind at 2400 UTC

Chapter 7

7.0   COMPARISON OF MODEL RESULTS AGAINST AVAILABLE OBSERVATIONS

The validation of a model using observations can be categorized into (i) subjective evaluation or (ii) point and pattern quantitative validation.

In the subjective evaluation or verification method, one or more of the predicted fields are qualitatively compared against observations of a related phenomena (Pielke, 1974a). In the latter method, point by point correspondence between model prediction and observation of the same meteorological parameter provides test of the model skill (Keyser and Anthes, 1977). Because of the sparse network of observational analysis over Kenya the subjective evaluation method was applied in this study. It may be noted that Pibal data and satellite cloud imageries for the two radiosonde ascents at Nairobi (Figures 33 and 34) were not available to assist in this validation (see also first paragraph of chapter 5)

In this section comparison was made between the period of occurrence of Convective Precipitation Rates (CPR) over an area (Experiment 3) and the period of occurrence of observed rainfall from a selected sample station representing the area. The observed diurnal cycle of rainfall (measured from automatic raingauges) for sample stations in the study domain on the case study day are displayed in Figures 217(a) to 217(f).   The locations of these stations are shown in Figure 32.

The justification for the comparison by subjective evaluation i that the CPR represent locations of deep convection where low level convergence occurred as a result of the scale-interaction between

Figure 217(a): Histogram showing observed hourly rainfall (mm) at Malindi on 14th April, 1985
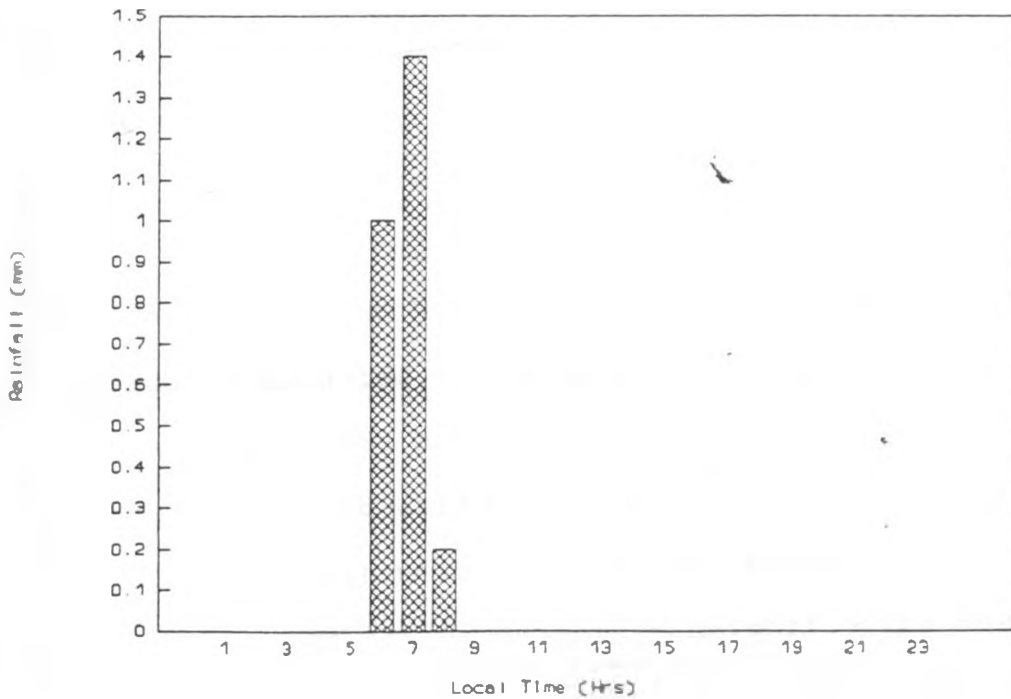
Figure 217(b): Histogram showing observed hourly rainfall (mm) at Marsabit on 14th April, 1985

the large-scale monsoonal winds and the local mesoscale circulations giving rise to precipitation over the same areas.

For instance, Figures 195 to 198 show that modeled precipitation from deep convection occurred over the coastal. strip, Eastern slopes of the Kenya highlands, in the Turkana-Marsabit channel (and Western parts of Lake Victoria) at 0400 UTC (7:00a.m local time) and at 0500UTC(8.00a.m local time). On the other hand, the histogram for observed hourly rainfall in Figure 217 (a) show that at Malindi (a sample station at the Coastal Region and 19.8m AMSL) there was rainfall between 5.00a.m and 9.00a.m. Similarly, Figure 217 (b) for observed hourly rainfall at Marsabit (1345. m AMSL and situated on the eastern side of the Turkana-Marsabit Channel) show that rainfall occurred in the morning period (between 5.00a.m to 9.00a.m).

There is therefore, a close agreement between the periods of occurrence of model-generated CPR and observed showers over the areas represented by the Stations.

The diurnal cycle of rainfall observed from Dagoretti Weather Station in Nairobi is depicted in Figure 217 (c). This station is situated on the eastern fringes of the Kenya Highlands at 1798m AMSL. Figure 217(c) shows that observed rainfall occurred during late-night to early morning (1.00 a.m to 8.00a.m) with more rainfall concentrated in the evening period (between 19h or 7p.m to midnight). The observed early morning rains are due to the interaction between the downslope local winds (see Figures 156 and 157) and the prevailing southeasterly monsoon winds (see figure 187).
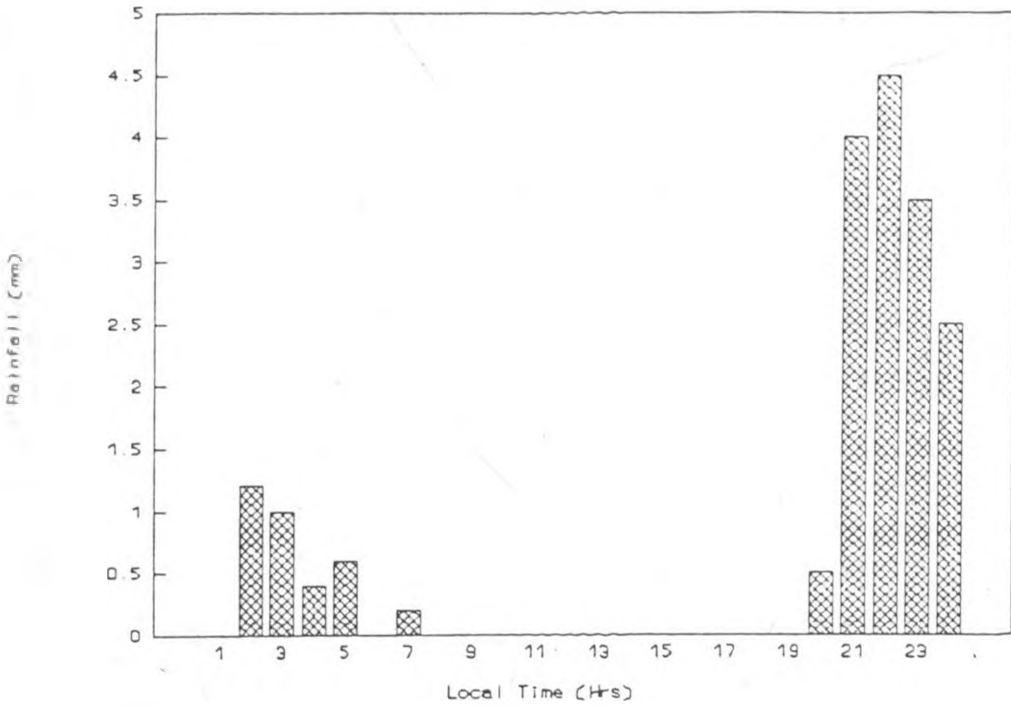
Figure 217(c): Histogram showing observed hourly rainfall (mm) at Dagoretti on 14th April, 1985
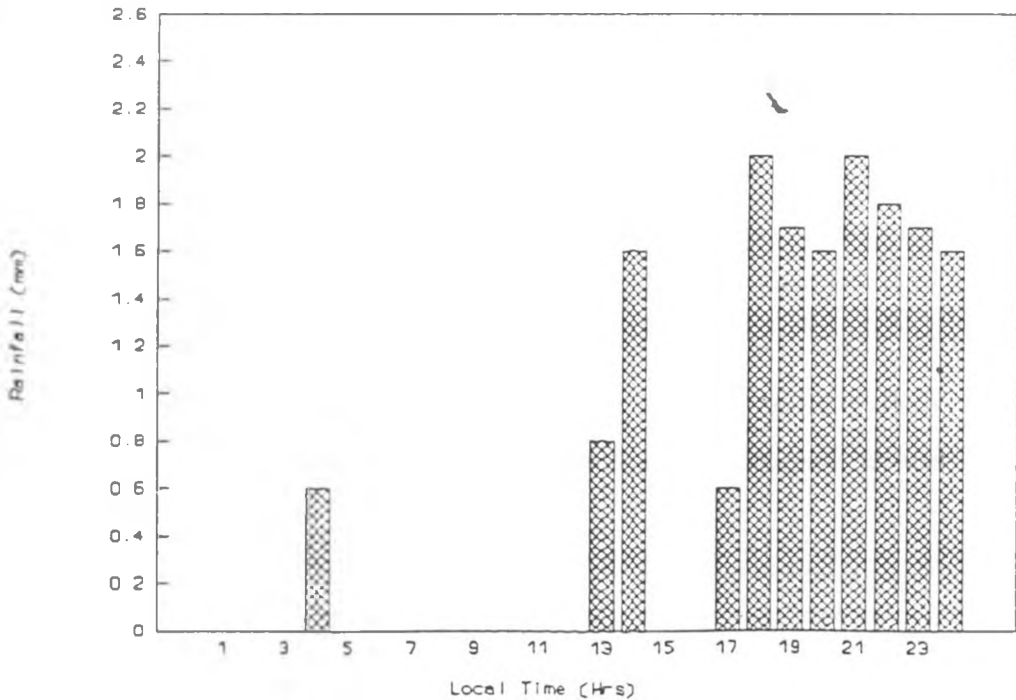
Figure 217(d): Histogram showing observed hourly rainfall (mm) at Eldoret on 14th April, 1985

It can be noted that the model did not simulate the morning rainfall over Nairobi (Figures 195 to 198). This may be explained by considering the fact that the modified Kuo scheme (1965, 1974) as used in RAMS was designed for deep clouds that go above 500mb i.e the tall cumulus "towers" (see Chapter 2 section 2.8). It can therefore be assumed that the morning rains observed over Nairobi emanated from Mid-level clouds whose top was at or just below the 500mb level. Therefore convection in the morning was not as strong as was the case in the afternoon.

The afternoon showers (7pm to Mid-night) resulted from deep convection and strong vertical overturning of the atmosphere induced by daytime solar insolation. The period of occurrence of the afternoon rains in Figure 217 (c) compares favourably with the period of occurence of modelled CPR in for instance Figures 211 and 212 at 1600UTC (or 7.00pm local time).

The observed hourly rainfall at the Highland Station of Eldoret (2083 m AMSL) is illustrated in Figure 217 (d). The diurnal cycle of observed rainfall shows that the observed showers were concentrated in the afternoon period between 17 h (5.00pm local time) to Mid-night; although the rains started earlier at 13h (1.00p.m local time) with trace rains at 4.00p.m. This scenario tallies well with the depictions in Figures 205 to 212 which show the occurrence of strong model-generated showers over the Highlands in the Eldoret/Kitale area during the afternoon period.

Figures 217(e) and 217(f) show observed hourly rainfall at Kisii (1707m AMSL) and Kakamega (1585m AMSL), respectively. These Stations are located in the Lake Victoria Trough   Region and are hence subject to the Lake influence. At Kisii (Figure 217(e) the rainfall occurred between 12h (Noon, local time) and Mid-night with breaks between 17h, 18h and 21h local times. At Kakamega
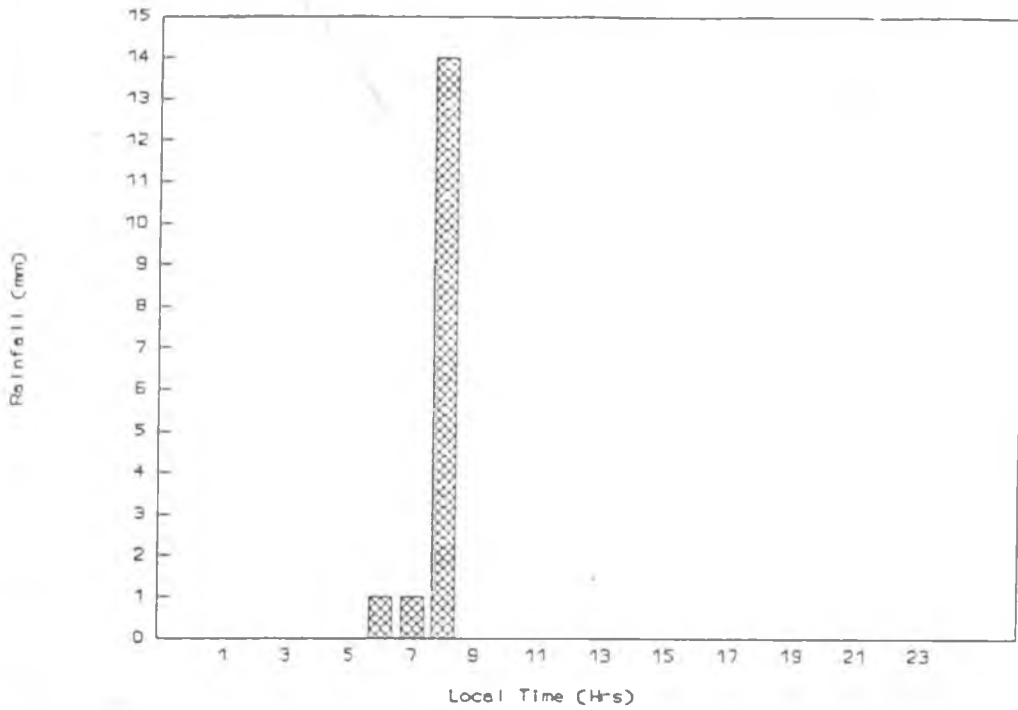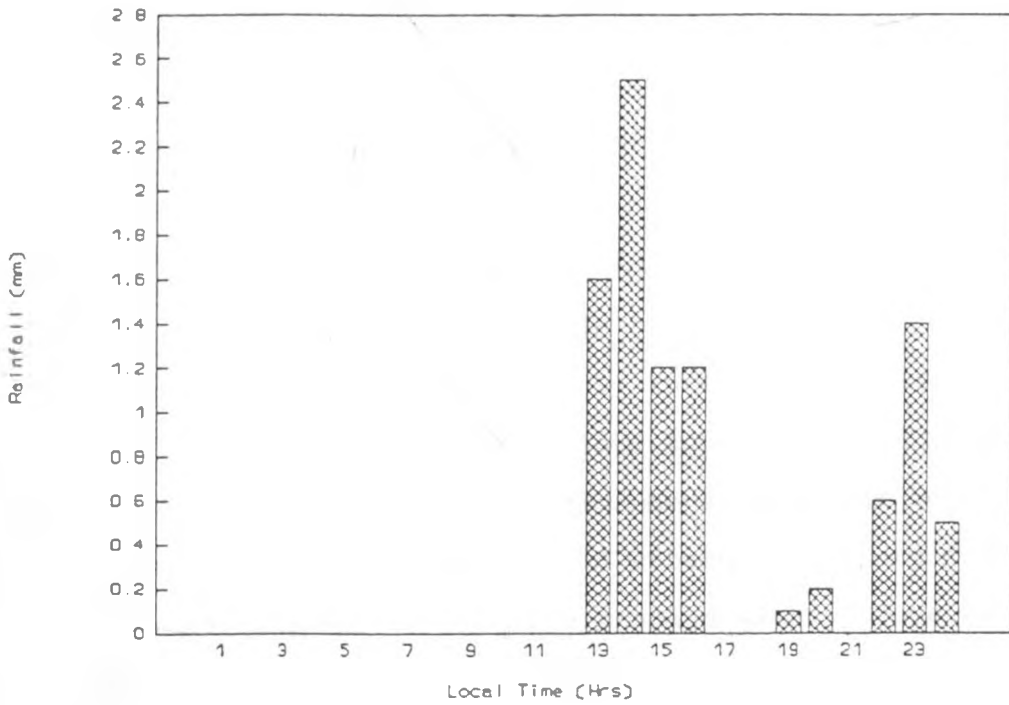
Figure 217 (e): Histogram showing observed hourly rainfall (mm) at Kisii on 14th April, 1985
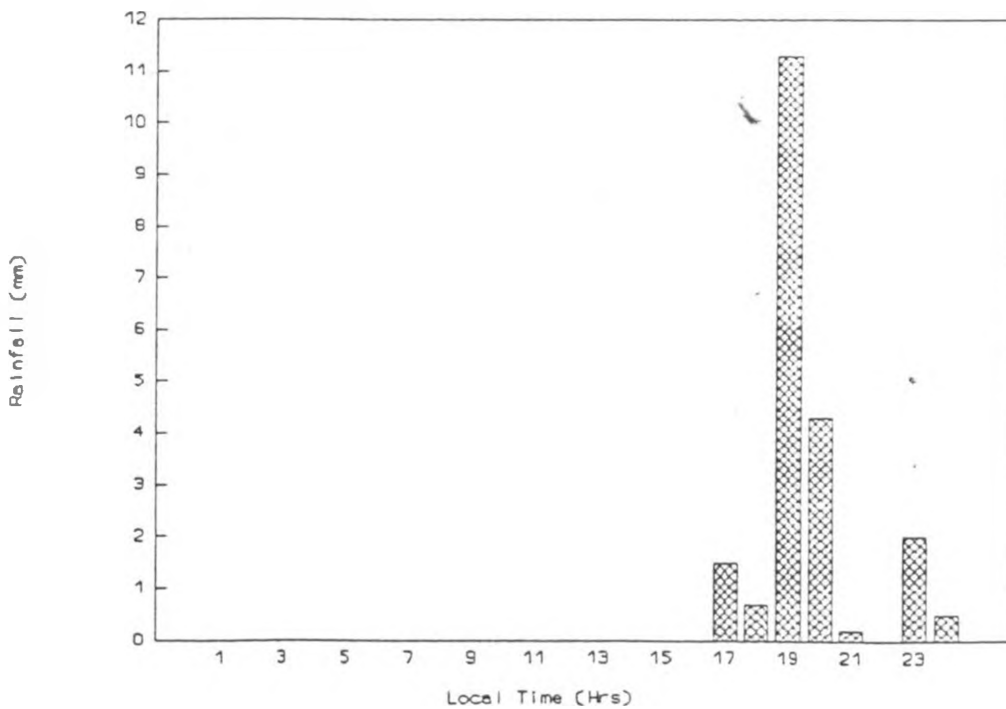
Figure 217 (f): Histogram showing observed hourly rainfall (mm) at Kakamega on 14th April, 1985

(Figure 217 (f)) the rain showers were recorded between 16h (4.00pm local time) and Mid-night; with a break at 22h (10.00pm) local time. Although Figures 205 to 212 clearly show modeled CPR over Kakamega area in the afternoon period, the same is not true over the Kisii area. Lack of modeled CPR over the Kisii area to support the observed rainfall can be attributed to the fact that the Kuo (1965, 1974) cumulus parameterization scheme simulated precipitation only in those areas where deep convection occurred (i.e where cloud tops were over 500mb).

In this case deep convection developed over the highlands as a result of the interaction and subsequent strong convergence between the Lake Victoria breeze coupled with upslope winds with the southeasterly monsoon winds (see Figures 199, 200, 203, and 204). The ensuing precipitating cloud ensemble drifted towards the Lake (and over Kisii) in the large-scale easterlies and hence the observed rainfall.

It may be concluded that the close agreement or correspondence between the periods of occurrence of observed rainfall at selected Stations over the study domain and the periods of occurrence of modeled CPR from deep convection over the same locations helps to validate the model-generated results against the observations.

However, there is need to adjust the model to simulate precipitation from mid-level clouds.

Chapter 8

SUMMARY, CONCLUSIONS, AND SUGGESTIONS FOR FUTURE WORK

8.1 Summary of the Work Done

Chapter 1 of this work reviewed the relevant literature and scope of the study. This included a discussion on the role of weather forecasting in socio-economic activities. It also highlighted the advantages of limited-area model over the traditional methods of synoptic chart analysis and the large-scale models with coarse grid-mesh in predicting tropical weather systems. The aims and objectives of the study were outlined including a definition of the study site.

Chapter 2 dealt with the formulation of the numerical model used in the study. It discussed various schemes in the model together with the options and techniques which were used to solve the different governing equations in the limited-area model adopted for this study.

Details of the acquisition of the data used in the study, together with the various processes which were used to prepare the data in order to obtain the initial values for the model simulations, were discussed in Chapter 3. This included the assimilation of ECMWF data which was subjected to five stages of analyses to create the initial fields for the model simulations.

The design of the three experiments used in this investigation was discussed in Chapter 4. The first experiment dealt with the dry simulations of the large-scale flow fields while the second experiment involved dry simulations of the mesoscale circulations. Using the results of the above two experiments, the mesoscale circulations were superimposed on the prevailing large-scale southeast monsoon winds at low levels to determine possible

areas of convergence/divergence over the country through scale-interaction of the two systems. The third experiment dealt with moist simulations of convective weather systems over the country by generating precipitation in the convergence zones determined earlier and further depicted the diurnal patterns of precipitation over the country which occurred as a result of the scale-interactions between the large-scale and the mesoscale flows.

Chapter 5 discussed, through observational analyses, the synoptic conditions which prevailed on the case study day. The flow features observed were verified against the model-generated results as a way of testing the model skill in replicating observed weather situations over the country.

The model-generated results from the three experiments, together with a discourse on the scale-interactions between the local mesoscale circulations and the prevailing southeast monsoon winds at low levels, were presented in Chapter 6. The large-scale and mesoscale outputs were discussed in terms of the wind fields, pressure fields, temperature fields, and moisture fields. The major features from the results of the large-scale simulations were that:

(i) There was a shallow layer of strong southeasterly monsoon currents at low levels with an average depth of 4.0 km across the domain. A westerly current occupied the middle layers of the atmosphere (from about 6.0 km to 11.0 km height) with strong easterly winds aloft (from 12.0 km to 23.0 km heights).

(ii) The vertical profile of the large-scale vertical wind field showed a rising motion in the low level easterlies, including large parts of the mid-levels, subsidence motions in the layer between 13 km and 16 km heights with an isothermal layer in the upper atmosphere.

(iii) The middle level westerlies were observed to recede eastwards out of the model domain and were replaced by the easterly winds, thereby indicating a vertical transfer of easterly momentum aloft.

(iv) Features like the ITCZ (at 2.6 km or 741 mb), the East African Low Level Jet Stream (at 1.3 km or 861 mb level) and a maximum of zonal wind in the Turkana-Marsabit corridor indicative of the Turkana Jet Stream were clearly discernible from the outputs of the numerical simulations.

(v) The potential temperature structure in the horizontal portrayed the presence of a "cold pool" of air in the Turkana-Marsabit corridor indicative of a cold surge of air advected from the Indian Ocean and channelled through this gap between the Kenyan highlands to the south and the Ethiopian highlands to the north. The thermodynamic structure in the vertical showed a well-mixed layer in the lower and mid-levels of the atmosphere with an isothermal layer in the upper levels (above 15.0 km height). There was a substantial amount of moisture advected into the country. The moisture field extended to a height of 8.0 km in the vertical.

The second experiment involving mesoscale simulations clearly signified the influence and effects of the orographic barriers, the Lake Victoria, the Indian Ocean, the Turkana-Marsabit corridor, radiation, surface roughness, soil moisture and temperature on the local circulation patterns when the large-scale monsoonal flows were neglected. The model-generated results showed the following features:

(i) Wind vectors, zonal and meridional wind contours showed land-breeze circulations around Lake Victoria and along the Indian Ocean during late night and early morning hours (0 UTC to 0800 UTC). Coupled with these breeze circulations were the downslope drainage (katabatic) winds that flowed towards the lowlands from the high ground areas. The vertical wind field showed a rising motion over Lake Victoria, the Indian Ocean, and the Turkana-Marsabit corridor during the early hours of the day.

(ii) The lake-breeze and sea-breeze circulations coupled with the upslope (anabatic) winds were realized in the afternoon (from 0900 UTC) and early evening periods. The vertical wind field showed sinking motion over Lake Victoria, the Indian Ocean, and over the Turkana-Marsabit corridor; with rising motion over the rest of the domain.

(iii) Contours in the vertical east-west cross-sections of the vertical wind field revealed updrafts and downdrafts registered at the land-water interfaces. For instance, at 0500 UTC the maximum rising motion registered was 1.0 cm s^{-1} against a sinking motion of –0.5 cm s^{-1} whereas at 1600 UTC the updraft was 3.3 cm s^{-1} against downdrafts of –2.9 cm s^{-1}.

(iv) The vertical cross-section of the zonal motion field revealed the vertical extent of the mesoscale circulations to be on the average 4.0 km AMSL. The sea-breeze and lake-breeze circulations had a deeper vertical extent than the land breeze circulations. This difference was attributed to the fact that there is usually more solar insolation during the day which induces more vertical mixing of the atmosphere in the Planetary Boundary Layer than is the case at night or early morning hours.

(v) The thermodynamic structure in the vertical showed more well-mixed layers at low levels of the atmosphere at 1600 UTC as compared to the situation at 0500 UTC. There were strong horizontal temperature and pressure gradients at low levels which induced the mesoscale circulations over the domain.

(vi) The amount of low level ($\sigma_z = 122$ m) moisture recorded over the domain ranged from a minimum of 11.6 g kg^{-1} to a maximum of 18.8 g kg^{-1} at 0500 UTC with a corresponding range of 13.2 g kg^{-1} to 19.2 g kg^{-1} at 1600 UTC. The contour maxima of these low level moisture fields were recorded at the coastal region during the initial stages of model integration and were seen to move inland with time. The inland transfer of moisture was attributed to the advection by the sea-breeze (or lake-breeze) coupled with the upslope winds. In the vertical extent the moisture field showed a negligible value at 7.8 km height.

The results from the third experiment showed the space-time location of the precipitation generated in the convergence zones which were controlled and advected by the large-scale flow field. This revealed the diurnal characteristic patterns of weather over Kenya.

(i) The coastal region received convective precipitation during late night to early morning hours from the scale interaction between the land-breeze, coupled with the down slope drainage winds, with the prevailing on-shore southeast monsoon winds.

(ii) The western part of Lake Victoria received convective rainfall during the late night and early morning period from a convergence induced by the interaction between the land-breeze, coupled with the donwslope winds from the western highlands, and the prevailing southeast monsoon winds at low levels.

(iii) Convective precipitation over the Turkana-Marsabit corridor was caused by the convergence of the downslope drainage winds from the surrounding highlands with the large-scale southeast monsoon winds during the late night to early morning period.

(iv) It was found that the eastern slopes of the Kenyan highlands received minimum convective precipitation in the morning (from a weak convergence induced by the scale interaction between the downslope drainage winds and the prevailing monsoon current) and more precipitation in the afternoon due to orographic lifting and release of convective instability induced by solar insolation.

(v) There was intense precipitation over the Kenyan highlands brought about by a strong convergence between the lake-breeze, coupled with upslope winds from the lowlands, with the iarge-scale southeast monsoon currents during the afternoon period. The modeled results showed intense convective precipitation rates over the highlands, which continued to drift westwards to the Lake Victoria Basin. Hence, the eastern parts of Lake Victoria received convective rainfall generated over the Kenyan highlands and which was advected westwards to the Lake Basin by the large-scale southeasterlies.

Chapter 7 used subjective evaluation technique to validate the model by determining the close correspondence between the periods of occurrence of the observed rainfall and the modeled convective precipitation rates (CPR) over the study domain.

8.2 Major Conclusions

The results from the study clearly delineated the relative importance of both the large-scale and mesoscale systems in the determination and replications of the diurnal patterns of weather observed over Kenya. The major conclusions from the study comprised the following:

(i) The diurnal weather patterns could only be obtained in the numerical simulations by including the large-scale monsoon wind systems in the model runs. The coastal region, the eastern slopes of the Kenyan highlands, the Kenyan highlands, and the Lake Victoria region with the region in the Turkana-Marsabit corridor depicted diurnal weather patterns that were related to the scale-interactions between the local circulations, like the sea/land breeze and the lake/land breeze circulations, upslope/downslope drainage winds with the prevailing southeast monsoon wind current.

(ii) The local features (Lake Victoria, the Indian Ocean, orography, Turkana-Marsabit corridor, etc.) played some major role in the generation and control of the local mesoscale circulations in the absence of the large-scale forcings.

(iii) The large-scale monsoon winds played an important role in the transfer of a substantial amount of moisture inland and further controlled the space-time locations, movement and intensity of the convergence/divergence zones and precipitation activities over the country.

(iv) The study indicated that in the absence, or with scarcity, of observational data for model initialization and verification (which is more prevalent in the tropics, including Kenya) the ECMWF data, when subjected to certain physical and dynamical constraints, can be initialized by a limited-area model like RAMS and used to generate forecast products that are closer to observations.

(v) Finally, the limited-area modeling technique which was adopted in this study may be used to forecast daily weather activities including the extreme events like hailstorms, lightning, thunderstorms, flash floods, strong winds, dry/wet spells, etc., thereby reducing the severe socio-economic consequences of such weather events. The method can also be used in the planning and management of all weather dependent activities.

8.3 Suggestions for Future Work

This study had the precious opportunity to use the ECMWF data and the sophisticated RAMS model, but there is generally insufficient upper air data and observational

studies for Kenya including the surrounding region. This handicap posed some problems in the proper verification of model results and for model initialization (hence, the use of the ECMWF data). Efforts should be made to obtain more observational studies in order to validate model outputs against these observations to increase the model skill, and thereby improve the forecasts using numerical methods.

Scale-interaction between the large-scale synoptic flows and the mesoscale systems over Kenya still needs more study using nested grids with even finer resolutions than used in this study. Finer resolutions, for instance 10 km grid intervals in the horizontal with a vertical spacing of 20 to 25 m, will resolve mesoscale and convective scale systems better and bring out stronger updrafts/downdrafts, especially at the land-water interfaces in sea/land and lake/land breeze circulations. Finer resolutions will also help to simulate the convective rainfall that occurs over this region with more accuracy.

Other large-scale synoptic systems which control the space-time weather characteristics over Kenya include the extratropical frontal incursions and upper-air troughs seen in satellite imagery. The lee low over Mozambique channel affects weather over Kenya as its intensification means a dry spell over the country. Moreover, easterly waves have also been studied over Kenya (e.g., Flemming, 1980; Njau, 1982). Although the impacts of these large-scale systems may be reflected in the monsoonal winds, the contribution of each needs to be investigated independently when studying weather over Kenya by numerical methods. This calls for the extension of the work beyond the African boundaries.

Lastly, efforts should be made to invest more in high performance computing in order to enhance research in numerical weather prediction studies. These studies will in turn have a positive impact on the economy of Kenya through improvement in weather forecasting which is crucial to the proper planning and management of all the weather related activities, including mitigation of the severe socio-economic impacts resulting from hazardous weather events.

ACKNOWLEDGEMENTS

REFERENCES

Alusa, A.L., 1986: Some characteristics of hailstorms in the Kericho-Nandi Hills area of Kenya. Kenya Meteorological Department. Institute for Meteorological Training and Research. Research Report No. 2/86. September, 1986.

Alusa, A.L. and M.T. Mushi, 1974: A study of the onset, duration and cessation of the rains in East Africa. Pre-print Vol. I, International Tropical Meteorological meeting, Nairobi (Kenya). Massachusetts: American Meteorological Society, 133-140pp.

Alusa, A.L. and P.M. Gwage, 1979: The occurrence of dry spells during the East African Long rains. The role of water resources in development. Edited by J.B. Castelino and C.P.M. Khamala Nairobi; Kenya National Academy, 21-85.

Anyamba, E.K., 1984: *On the monthly mean lower tropospheric circulation and anomalous circulation during 1961/1962 floods in East Africa*. M.Sc. Thesis, Department of Meteorology, University of Nairobi.

Arakawa, A. and V.R. Lamb, 1981: A potential entrophy and energy conserving scheme for the shallow water equations. *Mon. Wea. Rev.*, 109, 18-36.

Asnani, G.C. and J.H. Kinuthia, 1979: Diurnal variation of precipitation in East Africa. Kenya Meteorological Department, Research Report No. 8/79, 1-58.

Barnes, S.L., 1973: Mesoscale objective map analysis using weighted time-series observations. NOAA Technical Memorandum ERL NSSL-62, National Severe Storms Laboratory, Norman, OK, 38pp.

Chaggar, T.C., 1977: Geophysical distribution of thunderstorm days over East Africa. EAMD Tech. Note No. 26.

Chen, C. and W.R. Cotton, 1983b: Numerical experiments with a one-dimensional higher order turbulence model: Simulation of the Wangara Day 33 case. *Bound.-Layer Meteor.*, **25**, 375-404.

Clark, T.L., 1977: A small-scale dynamic model using a terrain-following coordinate transformation. *J. Comput. Phys.*, **24**, 186-215.

Clark, T.L. and R.D. Farley, 1984: Severe downslope wind storm calculations in two and three spatial dimensions using anelastic interactive grid nesting: A possible mechanism for gustiness. *J. Atmos. Sci.*, **41**, 329-350.

Cotton, W.R., C.J. Tremback and R.L. Walko, 1988: CSU-RAMS – A cloud model goes regional. Proc. NCAR Workshop on Limited-area Modeling Intercomparison, Nov. 15-18, NCAR, Boulder, CO, 202-211.

Cotton, W.R. and G.J. Tripoli, 1978: Cumulus convection in shear flow – Three-dimensional numerical experiments. *J. Atmos. Sci.*, **35**, 1503-1521.

Cotton, W.R., M.A. Stephens, T. Nehrkern and G.J. Tripoli, 1982: The Colorado State University cloud/mesoscale model – 1982. Part II: An ice phase parameterization. *J. Rech. Atmos.*, **16**, 295-320.

Cram, J.M., 1990: *Numerical simulation and analysis of the propagation of a pre-frontal squall line*. Ph.D. dissertation, Department of Atmospheric Science, Colorado State University, Fort Collins, CO, 332pp. (Paper No. 471).

Das, P.K., 1984: The monsoons – A perspective. Golden Jubilee publication. Indian National Science Academy, New Delhi, 1984.

Davies, H.C., 1976: A lateral boundary formulation for the multi-level prediction models. *Tellus*, **102**, 405-418.

Estoque, M.A., 1962: The sea-breeze as a function of a prevailing synoptic situation. *J. Atmos. Sci.*, **19**, 244-250.

Estoque, M.A. and K. Nimomiya, 1976: Numerical simulation of Japan sea breeze snowfall. *Tellus*, **28**, 24-253.

Findlater, J., 1966: Cross-equational jetstream at low levels over Kenya. *Meteor. Mag.*, **95**, 353-364.

Findlater, J., 1967: Some further evidence of cross-equational jetstream at low levels over Kenya. *Meteor. Mag.*, **96**, 216-219.

Findlater, J., 1968: The month to month variation of mean winds at low levels over East Africa. Tech. Memo No. 12, Nairobi, Kenya, East African Meteorological Department.

Findlater, J., 1969: A major low level air current near the Indian Ocean during northern summer. *Q. J. R. Meteor. Soc.*, **95**, 362-380.

Findlater, J., 1971: Mean monthly air flow at low levels over western Indian Ocean. Geophysical Memoirs No. 115. London: Her Majesty's Stationary Office.

Flatau, P.J., G.J. Tripoli, J. Verlinde and W.R. Cotton, 1989: The CSU-RAMS cloud microphysics module: General theory and code documentation. Atmospheric Science paper No. 451, Colorado State University, Department of Atmospheric Science, Fort Collins, CO 80523.

Fraederick, K., 1972: A simple climatological model of the dynamics and energetics of the nocturnal circulation at Lake Victoria. *Q. J. R. Meteor. Soc.*, **98**, 332-335.

Gal-Chen, T. and R.C.J. Somerville, 1975a: On the use of a coordinate transformation for the solution of the Navier-Stokes equations. *J. Comput. Phys.*, **17**, 209-228.

Gal-Chen, T. and R.C.J. Somerville, 1975b: Numerical solution of the Navier-Stokes equations with topography. *J. Comput. Phys.*, **17**, 276-310.

Glover, J., P. Robinson and J.P. Henderson, 1954: Provisional maps of the reliability of rainfall in East Africa. *Q. J. R. Meteor. Soc.*, **80**, 602-607.

Griffiths, J.F., 1959: The variability of the annual rainfall in East Africa. *Bull. Am. Meteorol. Soc.*, **40**, No. 7, 361-362.

Johnson, D.H., 1962: Rain in East Africa. *Q. J. R. Meteor. Soc.*, **88**, 1-19.

Kagenyi, J.N., 1990: Use of vertical wind shears in tropical weather forecasting. Kenya Meteorological Department. *Presented, Proc. of the Second Technical Conferences on Weather Forecasting in Eastern and Southern Africa*, Nairobi, 3-7 September, 1991.

Keyser, D., and Anthes, R.A., 1977: The applicability of a mixed-layer model of the planetary boundary layer to real data forecasting. Mon. Wea. Rev. 105, 1351-1371.

Kiangi, P.M.R., M.M. Kavishe and J.K. Patnaik, 1981: Some aspects of the mean tropospheric motion field in East Africa during the long rain season. *Kenya J. of Science and Tech.* (A) (1981), **2**, 91-103.

Klemp, J.B. and D.R. Durran, 1983: An upper boundary condition permitting internal gravity wave radiation in numerical mesoscale models. *Mon. Wea. Rev.*, **111**, 430-444.

Kuo, H.L., 1965: On formation and intensification of tropical cyclone through latent heat release by cumulus convection. *J. Atmos. Sci.*, **22**, 40-63.

Kuo, H.L., 1974: Further studies of the parameterization of the effects of cumulus convection on large-scale flow. *J. Atmos. Sci.*, 1232-1240.

Mahrer, Y. and R.A. Pielke, 1977b: The effects of topography on sea and land breezes in a two-dimensional numerical model. *Mon. Wea. Rev.*, **105**, 1151-1162.

Majugu, A.W., 1983: Mean and seasonal diurnal variation of precipitation in East Africa. M.Sc. Thesis, Department of Meteorology, University of Nairobi, Kenya.

Mesinger, F. and A. Arakawa, 1976: Numerical methods used in atmospheric models. GARP Publications Series No. 14, WMO/ICSU Joint Organizing Committee, 64pp.

McCumber, M.C. and R.A. Pielke, 1981: Simulation of the effects of surface fluxes of heat and moisture in a mesoscale numerical model – Part I: Soil layer. *J. Geophys. Res.*, **86**, 9929-9938.

McPherson, R.D., 1970: A numerical study of the effects of a coastal irregularity on the sea-breeze. *J. Appl. Meteor.*, **9**, 767-777.

Molinari, J., 1985: A general form of Kuo's cumulus parameterization. *Mon. Wea. Rev.*, **113**, 1411-1416.

Nieuwolt, S., 1974: Interannual rainfall variability in Tanzania. Pre-print Vol. 1, International Tropical Meteorology meeting, Nairobi (Kenya). Massachusetts: American Meteorological Society, 252-257.

Ngara, T., 1978: *Some aspects of the East African low-level jet*. M.Sc. thesis, Department of Meteorology, University of Nairobi, Nairobi, Kenya.

Ngara, T. and G.C. Asnani, 1978: Five-c   oscillation in the East African low-level jet. *Nature* (London), **272**, 708-709.

Ogallo, L.J., 1980: *Time series analysis of rainfall in East Africa*. Ph.D. Thesis, Department of Meteorology, University of Nairobi, Nairobi, Kenya.

Ojany, F.F. and R.B. Ogendo, 1985: Kenya: A study in physical and human geography, Nairobi: Longmans, 1985.

Okeyo, A.E., 1982: *A two-dimensional numerical model of the lake-land and sea breezes over Kenya.* M.Sc. Thesis, Department of Meteorology, University of Nairobi, Kenya.

Okeyo, A.E., 1987: *Towards the development of a forecasting numerical model for Kenya.* Ph.D. Thesis, Department of Meteorology, University of Nairobi, Kenya.

Otengi, S.B.B., 1980: *Analysis of pentad rainfall for agricultural purposes in Kenya.* M.Sc. Thesis, Department of Meteorology, University of Nairobi, Nairobi, Kenya.

Perkey, S.J. and C.W. Kreitzberg, 1976: A time-dependent boundary scheme for limited area primitive equation model. *Mon. Wea. Rev.*, **104**, 744-755.

Pielke, R.A., 1974: A three-dimensional numerical model of the land and sea breezes over southern Florida. *Mon. Wea. Rev.*, **102**, 115-139.

Pielke, R.A. and Y. Mahrer, 1975: Technique to represent heated planetary boundary layer in mesoscale models with coarse vertical resolution. *J. Atmos. Sci.*, **32**, 2288-2308.

Pielke, R.A., 1986: *Extended abstracts of papers presented at the WMO/AMS/UCS international workshop on rain-producing systems in the tropics.* WMO Tropical Meteorology Programme (TMP) and Commission for Atmospheric Sciences (CAS), (San Jose, Costa Rica, 21-25 July, 1986).

Phillips, G., 1967: *Model School Atlas* (London, Phillips).

Pyuzza, N.D., 1983: A study of the mean upper tropospheric horizontal motion field in the near-equatorial region. M.Sc. Thesis, Dept. of Meteorology, University of Nairobi, Kenya.

Ramage, C.S. and C.V.R. Raman, 1972: Meteorological atlas of the international Indian Ocean expedition. Vol. 2, Upper Air. Washington: National Science Foundation, NSF-IOE-3.

Sansom, H.W. and S. Gichuiya, 1971: Hailstorms in the Kericho area. East African Meteorological Department, Kenya (Nairobi). Tech. Memo. No. 22, (1971).

Semazzi, F.H.M., 1979: *Numerical experiments on the dynamic-orographic influence in the tropics*. M.Sc. Thesis, Department of Meteorology, University of Nairobi, Nairobi, Kenya.

Semazzi, F.H.M., 1983: On the bounded derivative initialization method. Ph.D. Dissertation, Department of Meteorology, University of Nairobi, Kenya.

Thompson, B.W., 1957: Diurnal variation of precipitation in British East Africa. Tech. Memos. Nos. 8, 1-12 and 1-49, Nairobi: East African Meteorological Department.

Thompson, B.W., 1965: *Climate of Africa*. London: Oxford University Press.

Tremback, C.J. and R. Kessler, 1985: A surface temperature and moisture parameterization for use in mesoscale numerical models. *Proc. 7th Conf. on Numerical Weather Prediction*, June 17-20, Montreal, Quebec, American Meteorological Society, Boston, 355-358.

Tremback, C.J. and G.J. Tripoli and W.R. Cotton, 1985: A regional scale atmospheric numerical model including explicit moist physics and a hydrostatic time-split scheme. *Preprints, 7th Conference on Numerical Weather Prediction*, June 17-20, 1985, Montreal, Quebec, AMS.

Tremback, C.J., G.J. Tripoli, R. Arritt, W.R. Cotton and R.A. Pielke, 1986: The regional atmospheric modeling system. *Proc. Inter. Conf. Development and Application of Computer Techniques to Environmental Studies*, November, Los Angeles, California, P. Zannetti, Ed., Computational Mechanics Publications, Boston, 601-607.

Tremback, C.J., J. Powell, W.R. Cotton and R.A. Pielke, 1987: The forward-in-time upstream advection scheme: Extension to higher orders. *Mon. Wea. Rev.*, **115**, 540-555.

211

Tremback, C.J., 1990: *Numerical simulation of a mesoscale convective complex: Model development and numerical results.* Ph.D. Dissertation, Department of Atmospheric Science, Colorado State University, Fort Collins, CO, 247pp. (Paper No. 465).

Tripoli, G.J. and W.R. Cotton, 1980: A numerical investigation of several factors contribution to the observed variable intensity of deep convection over south Florida. *J. Appl. Meteor.*, **19**, 1037-1063.

Tripoli, G.J., and W.R. Cotton, 1982: The Colorado State University three-dimensional cloud/mesoscale model - 1982. Part I: General theoretical framework and sensitivity experiments. *J. de Rech. Atmos.*, **16**, 185-220.

Tripoli, G.J. and W.R. Cotton, 1989a: Numerical study of an observed orogenic mesoscale convective system. Part I: Simulated genesis and comparison with observations. *Mon. Wea. Rev.*, 117, 273-304.

Tripoli, G.J. and W.R. Cotton, 1989b: Numerical study of an observed orogenic mesoscale convective system. Part II: Analysis and governing dynamics. *Mon. Wea. Rev.*, **117**, 3305-328.